UNIVERSITY OF SOUTHAMPTON

FACULTY OF ENGINEERING, SCIENCE AND MATHEMATICS

School of Engineering Sciences

A Critical Evaluation and Development of the Operational Utility of Active Rotor Technology

by

Mark Peter Jones

Thesis for the degree of Doctor of Philosophy

September 2010

UNIVERSITY OF SOUTHAMPTON

ABSTRACT

FACULTY OF ENGINEERING, SCIENCE AND MATHEMATICS
SCHOOL OF ENGINEERING SCIENCES
Doctor of Philosophy
A CRITICAL EVALUATION AND DEVELOPMENT OF THE OPERATIONAL UTILITY OF ACTIVE-ROTOR TECHNOLOGY
by
Mark Peter Jones

Modern manufacturing techniques, materials, and design tools enable the modern helicopter designer to highly optimise the rotor; however the resulting optimum must be a compromise between the demands of axial and forward flight and those arising from conflicting requirements of the advancing and retreating sides of the rotor disc. Active technologies provide the opportunity to alleviate some of this design compromise by adapting the rotor to the specific requirements depending on the blade azimuth, the aircraft's location within the flight envelope, and the mission upon which it is engaged.

Three such active rotor technologies are considered here: air jet vortex generators, trailing edge flaps, and active trailing edges. The performance of each device is assessed through the adaptation of indicial aerodynamics methods within a rotor performance method and associated computer program. The results of these assessments are used to inform a critical evaluation of the operational utility of each technology, and their relative merits and weaknesses are compared.

The high-speed performance enhancement capabilities of the air jet vortex generators are confirmed; however when applied to a modern rotor design, which has already been optimised for the delay of retreating blade stall, the performance gains are predicted to be limited. Their overall utility is also found to be restricted in comparison to the other technologies as their unsuitability for higher harmonic control means that they are limited to only the performance enhancement application.

In contrast, the adaptability of trailing edge flaps to additional applications can be observed from the literature and is further demonstrated here through the prediction of their ability to reduce helicopter blade sailing. This novel application of the trailing edge flap is investigated using a new dynamics method with results obtained demonstrating promising results for a real case study.

Possible drawbacks of the trailing edge flap arise due to the exposure of its hinges, which can cause an increase in drag and also reliability issues in harsh environments. The active trailing edge aims to overcome these problems by eliminating the hinges, but only at the expense of deflection capability. A new model is thus presented which accurately models the active trailing edge and demonstrates that even a restricted deflection capability can be used to provide vibration reduction and performance enhancement capabilities of similar magnitudes to those demonstrated for the trailing edge flap.

Table of Contents

List of Figures

Declaration of Authorship

I, Mark Peter Jones, declare that the thesis entitled:

'*A Critical Evaluation and Development of the Operational Utility of Active Rotor Technology*'

and the work presented in the thesis are both my own, and have been generated by me as the result of my own original research. I confirm that:

- this work was done wholly or mainly while in candidature for a research degree at this University;
- where any part of this thesis has previously been submitted for a degree or any other qualification at this University or any other institution, this has been clearly stated;
- where I have consulted the published work of others, this is always clearly attributed;
- where I have quoted from the work of others, the source is always given. With the exception of such quotations, this thesis is entirely my own work;
- I have acknowledged all main sources of help;
- where the thesis is based on work done by myself jointly with others, I have made clear exactly what was done by others and what I have contributed myself;

parts of this work have been published as:

Jones M.P., Newman S.J., Vibration reduction of a Lynx aircraft via actively controlled trailing edge flaps, Proceedings of the 32nd European Rotorcraft Forum, 2006.

Jones M.P., Newman S.J., A method of reducing blade sailing through the use of trailing edge flaps, Proceedings of the American Helicopter Society 63rd Annual Forum, 2007.

Signed: ……..

Date:…….

Acknowledgements

My first and biggest thanks must go to my supervisor, Dr. Simon Newman, for all his help, guidance and support throughout both my post-graduate and under-graduate studies. His boundless enthusiasm demonstrated in under-graduate 'powered lift' lectures inspired me to follow a career in rotorcraft and I was therefore delighted when the opportunity arose to embark on a research project under his tutorship, from which this thesis is the result. His continued support, in difficult times, in the later stages of my research and throughout my lengthy write-up process has, in particular, been most gratefully received.

Thanks must also go to everyone involved in the Rotor Aeromechanics Defence Aerospace Research Partnership (DARP), for which the bulk of this research was conducted, and also to Qinetiq and the Sea King IPT for providing the opportunity to apply the blade sailing research to a real operational case study.

I am especially grateful to all those who have provided the opportunity for useful discussion into active rotor technology. These include the other DARP researchers from the various academic and industrial collaborators, particularly the staff at AgustaWestland: those who supported the research at the University of Southampton (N. Griffiths, A. Brocklehurst, A. Lord, and S. Spurway) and also the many others who have since, as my colleagues, provided ample opportunity for discussions which are sure to have influenced this thesis.

I would also like to extend my gratitude to all those at the University of Southampton who have shown remarkable patience in my long write-up period, especially Alessia Plutino for dealing with my numerous administrative issues!

Finally, thanks must go to my parents and all other family and friends for supporting me through but especially to Heather for her never-ending support and patience and for providing extra stimulus in the race to submit (which, of course, she won!). Hopefully now we can have those guilt-free fun weekends…

Thanks to you all.

Nomenclature

General Notation:

$a_{coriolis}$	Acceleration due to Coriolis
A_i, b_i	Constants used in circulatory indicial response functions
A_n	Fourier coefficient in Glauert (1947) form of vorticity distribution
B_l	Longitudinal cyclic pitch
B_n, B_c, B_m	Vortex strength factor (normal force, chord force, pitching moment)
c	Blade chord or Forcing vector fro blade sailing model
C	Sum of forcing terms for blade sailing model
C_c	Chord force coefficient
C_d	Drag coefficient
C_{d_0}	Viscous drag coefficient
$C_{f\delta}$	Drag term due to resolution of flap/ATE force (non-dimensional)
C_l	Lift coefficient
C_{l_α}	Lift slope
C_m	Pitching moment coefficient
C_{m_0}	Zero-lift pitching moment coefficient
C_n	Normal force coefficient
C_{n_1}	Critical value of normal force for dynamic stall onset
$C_{n_{min}}$	Minimum value of normal force coefficient
C_p	Pressure coefficient distribution
C_{pres}	Centre of pressure
C_T	Thrust coefficient
d	State vector for blade sailing model
dx	Blade segment
D	Decrement term in recurrence solution to Duhamel's integral
EI	Blade flapwise bending stiffness
f	Separation location
F	Shape factor for ATE deflection or Force per unit length
f_c	Camber line boundary condition due to camber and inflow

F_δ	Drag term due to resolution of flap/ATE force (dimensional)
g	Gravitational acceleration
k	Reduced frequency
K_{c_i}, K_{n_i}, K_{m_i}	Factors for normal force, pitching moment and chord force models
K_f	Kirchoff factor for trailing edge separation
K_{f_c}, K_{f_n}	New separation factors for normal and chord force coefficients
K_{f_i}, K_{fd_i}	Factors in new model for separation location
K_0, K_1, $K_{1,exp}$	Factors used for empirical representation of centre of pressure
L	Lift
L_n, L_c, L_p	Factors in normal force, chord force and centre of pressure equations
m	Blade mass per unit length
M	Mach number or Blade bending moment
M_{bp}, $M_{f,exp}$	Factors used for empirical representation of centre of pressure
r	Rotor blade radial location, or pitch rate
R	Rotor radius
s	Non-dimensional time (distance travelled in semi-chords)
S	Blade flapwise shear
S_1, S_2	Factors used in calculation of separation location
s_r	Rotor solidity
t	Time
T	Non-dimensional time constant or Blade tension
V	Freestream velocity
V_x	Vortex influence parameter
w_i	Induced perpendicular velocity due to bound vorticity
w_w	Perpendicular velocity due to inflow distribution
x	Chordwise coordinate (dimensional)
$\bar{x}$	Chordwise coordinate (non-dimensional with respect to blade chord)
x_h	Hinge location in linear chordwise coordinate
Y	Definition of aerofoil camber line
z	Rotor blade flapwise deflection
α	Angle of attack

α_1	Static stall angle of attack
α_{crit}	Critical lagged angle of attack for dynamic stall onset
α_{ds}	Angle of attack for dynamic stall
α_{f_i}	Parameter used in new model for separation location
α_{min}	Angle of attack at minimum normal force coefficient
β	Rotor blade flapping angle, or Prandtl-Glauert factor
γ	Bound vorticity distribution
δ	Flap/ATE deflection (positive down)
δ_0, δ_1	0/rev and 1/rev ATE deflection
$\delta(t)$	Dirac delta function
ΔC_m	Dynamic stall pitching moment correction
ε_0	Thin aerofoil integral for lift and pitching moment
η_d	Factor for non-ideal recovery of leading-edge pressure
θ	Blade pitch
θ_0	Collective pitch
λ_i	Induced downwash (non-dimensional)
μ (mu)	Advance ratio, Flight speed non-dimensionalised using the rotor tip speed.
μ_0	Thin aerofoil integrals for pitching moment
μ_x, μ_z	Tangential and perpendicular inflow velocities (non-dimensional)
μ_w	w_w/V
μ_{zD}	$\mu_z+\lambda_i$
ρ	Air density
ϕ	Indicial response function, or Wagner's function
ψ	Azimuth, or circular chordwise coordinate
ψ_h	Hinge location in circular chordwise coordinate
ω	Circular frequency
Ω	Rotor Speed

Time Constant Subscripts:

F	Boundary layer lag
m_1, m_2	Dynamic stall pitching moment lag
P	Pressure lag
r	Reattachment lag

V	Vortex formation time
VL	Vortex travel time
α	Angle of attack lag

Other Subscripts:

c, d, m, n	Normal force, chord force, pitching moment, drag force
C	Circulatory component
d, u	Upward and downward values for separation location
I	Impulsive (non-circulatory) component
j	Chordwise integration segment
US	Un-separated model value

Abbreviations:

/rev	Per rotor revolution
ACSR	Active Control of Structural Response
AJVG	Air Jet Vortex Generator
APA	Amplified Piezoelectric Actuator
ATE	Active Trailing Edge
AVG	Active Vortex Generator
BERP	British Experimental Rotor Program
BVI	Blade-Vortex Interaction
CFD	Computational Fluid Dynamics
CSD	Computational Structural Dynamics
DSV	Dynamic Stall Vortex
HHC	Higher Harmonic Control
IBC	Individual Blade Control
MIT	Massachusetts Institute of Technology
TEF	Trailing Edge Flap
TEV	Trailing Edge Vortex
UMARC	University of Maryland Advanced Rotor Code
VG	Vortex Generator

Chapter 1 Introduction

1.1 The Helicopter Design Challenge

"*The future of the helicopter … lies not in competition with the airplane, but in its ability to perform certain functions which the airplane cannot undertake*." [Klemin (1925)]

Dr. Alexander Klemin was referring to the main strength, indeed the entire reasoning for the existence, of the helicopter – the ability to fly efficiently and controllably at low speeds and, more particularly, in hover. This requirement however also serves to handicap the helicopter. The rotor can be designed for a very efficient hover capability; indeed many helicopter rotor designs are still driven by their axial flight performance using the Figure of Merit (*which is defined as the ratio between the rotor's ideal induced power and its actual total power*). The problems and engineering challenges really become apparent however when the aircraft moves into horizontal flight.

This defines the fundamental difference between a helicopter rotor and an aircraft propeller. Whilst a propeller experiences a predominantly axial flow, similar to a helicopter rotor in axial flight, the helicopter rotor in forward flight sees a large component of tangential flow which causes controllability problems which have to be overcome and now continue to present an almost hard limit to the maximum speed of the aircraft. Figure 1.1 shows how in forward flight the helicopter rotor experiences an asymmetry of flow depending on whether the blade is on the advancing side or retreating side of the rotor disc. If the blades were rigid and held at constant pitch around the azimuth the resulting asymmetry of lift, which is proportional to the square of the velocity, would produce a rolling moment, thus toppling the aircraft.

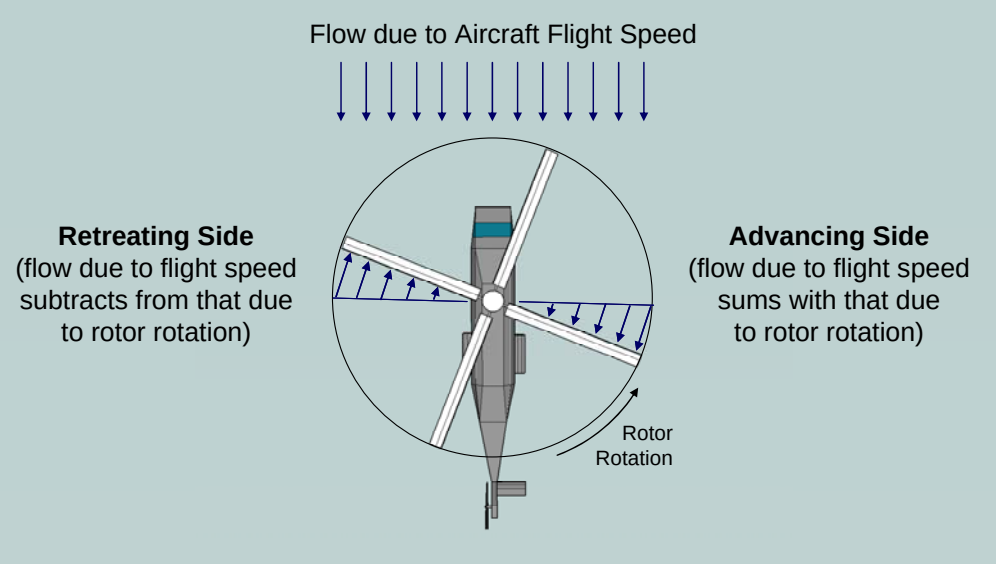

Figure 1.1: Flow asymmetry of a rotor in forward flight.

This problem was overcome by Juan de la Cierva [de la Cierva and Rose (1931)] through the introduction of the flapping hinge whereby a mechanical hinge connects the blade to the rotor hub thus ensuring that the moments are not transmitted. Control is then obtained through the use of collective and cyclic pitch, whereby the collective lever adjusts the mean angle of attack of the blades to set the overall thrust whilst the cyclic stick varies the pitch, once per revolution, around the azimuth to ensure that the blade deflection, or flapping, is such that the overall thrust vector is tilted to balance the other forces acting upon the helicopter (i.e. weight and drag) and to thus trim the aircraft. The application of cyclic pitch in this way therefore overcomes the natural tendency of the rotor to flap backward in forward flight due to the flow asymmetry. In addition, as the rotor is powered internally, some form of anti-torque is required to stop the fuselage from spinning. This is generally provided by a tail rotor or a ducted fan which is located on the tail of the aircraft and is also used for yaw control through the adjustment of its collective pitch which is controlled by the pilot's pedals.

1.1.1 Stall Boundaries

Although the trimming problem has been overcome at moderate speeds, the flow asymmetry continues to limit the forward speed of the helicopter. On the advancing side, the addition of the forward flight and rotor rotation components means that portions of flow over the blade approach the speed of sound far in advance of the aircraft flight speed. These high Mach numbers cause the blade to undergo shock induced separation and the rotor therefore encounters advancing blade stall.

On the retreating side however, in order to generate the blade flapping to give the forward disc tilt required for forward flight, the cyclic must be applied approximately 90 degrees in advance, i.e. on the retreating side around 270 degrees azimuth. This means that the blades encounter a higher angle of attack whilst also experiencing a low value of flow velocity due to the subtraction of the forward flight component from the rotor rotation component. The rotor will therefore suffer from retreating blade stall due to the combination of low speed and high angle of attack. As the blades are pitching predominantly at the frequency of the rotor rotation, this stall can be said to be occurring dynamically. This dynamic stall phenomenon has been shown to yield air flow physics and airloads which are markedly different from the static stall case, McCroskey et al (1981).

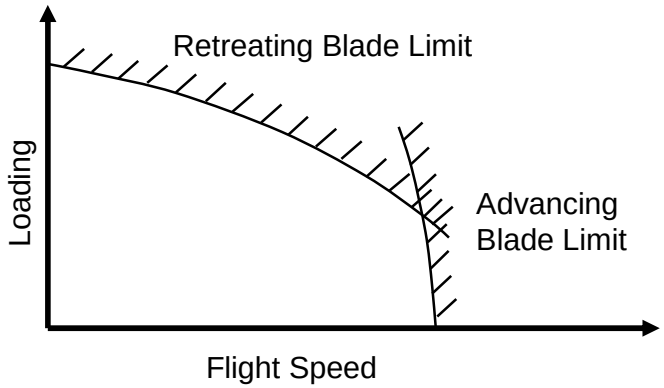

Figure 1.2: Flight envelope due to advancing and retreating blade stall limits.

Either advancing blade or retreating blade stall will occur depending upon the thrust loading of the rotor as shown in Figure 1.2. At higher blade loading the angle of attack limits are reached first and retreating blade stall will be encountered. At lower blade loading, higher speeds may be obtained until the Mach-dependent advancing blade limit is reached first. In practice, blade stall might not in itself define the flight envelope if the rotor system is designed to tolerate the loads associated with blade stall. In this case other parameters will define the limiting boundary with a common limitation being the power requirement, which may in some cases be reached prior to the stall boundary. On the other hand, the stall-induced loads may result in the stall boundary defining the flight envelope limitation; indeed the Cruise Guide Indicator on the Sea King monitors the control loads to inform the pilot of their proximity to the stall boundary. Furthermore rotorcraft in service with the UK military must conform to UK Def Stan 00-970 which stipulates that the flight envelope is defined by the retreating blade stall boundary. Regardless of whether or not it forms the flight boundary, if retreating blade stall can be delayed, then the associated rise in power, control loads and blade loads will also be delayed which suggests improvements in performance and a possible expansion of the

high blade loading portion of the flight envelope. Alternatively, for a given retreating blade stall boundary the delay may allow for a reduction in rotor speed which will instead delay the onset of advancing blade stall and may also come with the added benefit of a reduction in noise.

1.1.2 Rotor Induced Vibration

Another critical issue with rotorcraft is the high level of vibration in comparison to fixed wing aircraft. The helicopter suffers the same vibration sources as the fixed wing aircraft, i.e. the engines, transmission and fuselage aerodynamics; however it is the additional contribution of the rotors, particularly the main rotor, which dominates the vibration.

The prediction of vibration is a very complex problem. Assume for simplicity that the blades are rigid outboard of the flapping hinge. The variation in dynamic head alone results in 1 and 2/rev variations in forcing. The blade will flap in response to this forcing and then the conservation of angular momentum dictates that it must accelerate in the horizontal plane. This effect is known as the Coriolis acceleration and for a blade segment at rotor radius r and with mass m undergoing vertical motion due to the blade flapping through an angle of β, the acceleration due to Coriolis is given by:

$$a_{coriolis} = 2\Omega m r \beta\dot{\beta} . \qquad \textbf{1.1}$$

This acceleration is in the plane of the rotor rotation in what is referred to as the lead-lag direction, see Figure 1.3 (*lead is when the motion is in the rotor rotational direction and lag is in a direction opposed to this*). This acceleration can be large; indeed lead-lag hinges are included on fully-articulated rotor hubs in order to relieve the large chordwise bending moments which might otherwise occur.

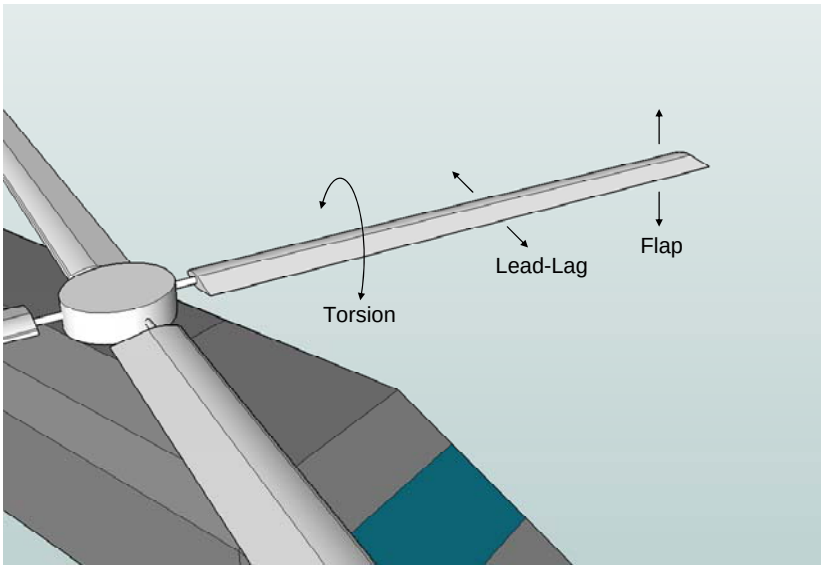

Figure 1.3: Degrees of freedom of the helicopter rotor blade.

As the Coriolis acceleration consists of the flapping displacement multiplied by the flapping velocity, simple trigonometric relations will reveal that the 0, 1 and 2/rev components of blade flapping will give Coriolis forces up to 4/rev. The lead-lag motion created by this forcing then impacts on the aerodynamic inflow into the blade which feeds back into the blade flapping and, through Coriolis, the lagging motion and again back into the aerodynamics. It is immediately apparent that even with just this basic feedback mechanism there are already multiple harmonic excitations of the rotor.

In reality the problem is decidedly more complex, as demonstrated in Figure 1.4. In terms of aerodynamics, the helicopter rotor operates close to, or at low speed in, its own wake and this creates aerodynamic forcing at many harmonics. This effect is exacerbated by the close proximity of the rotor to the fuselage, whose aerodynamic influence can impinge on the rotor leading to a further source of multi-harmonic dynamic inflow. In addition to the complex aerodynamic environment, modern rotor blades are also dynamically challenging. The elasticity of the blades must be considered, as limits imposed by strength, mass, and geometry requirements means that the blades are sufficiently flexible to impact on the solution. The normal modes of vibration are defined as single frequency eigen-solutions to the equations of motion and are generally calculated for the blades in vacuo, i.e. with no aerodynamics. For a given flight case, the aerodynamics and additional coupling terms are then applied as a forcing to the equations of motion, whose response is then given by a superposition of the normal modes. Such a modal approach is advantageous as only a limited number of modes are sufficient to provide the required accuracy and therefore the time integration of the modal equations of motion is computationally efficient. A modal analysis of the solution can also provide

further insight and guidance in the design process. Although the 'exact' solution is given by an infinite mode set, in practice only the elastic modes of natural frequencies low enough to impact on vibration and loads are considered, with at least 8-12 modes being typically used in prediction tools. The modes of modern blades are, however, highly coupled in flap and lag as well as the twisting, or torsion, degree of freedom (Figure 1.3), and the prediction of such modes can be challenging.

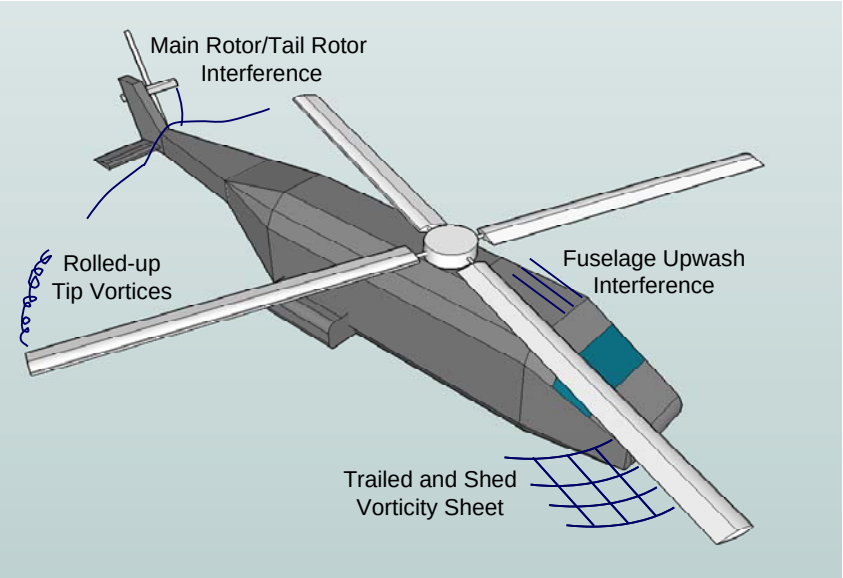

Figure 1.4: Complications due to helicopter aerodynamics.

It is, however, not only the blades themselves which must be considered. Most rotors also include a damper in the lead-lag direction to reduce the impact of ground resonance which may occur due to the coupling of rotor, fuselage and undercarriage modes. *(Rotor blade flapping is highly damped through aerodynamic effects but lead lag motion is poorly damped and requires additional damping to be incorporated.)* In flight these lag dampers can have a large impact on the vibration, and their non-linear behaviour adds further complication through the coupling of blade harmonic responses. Likewise, the control system which is used to alter the pitch of the blades provides another load path which can couple the individual blades and the response of the fuselage itself will cause a motion to be generated at the rotor hub which feeds back into the rotor system thus giving a further coupling.

1.2 Passive Design Improvements

From the previous discussions it is clear that achieving improvements in performance and vibration through passive means is becoming ever more challenging. This is particularly true in terms of pure maximum speed, where developments in the 1980s of both aerofoil

and planform shape under the British Experimental Rotor Program (BERP) enabled a modified Westland Lynx helicopter to achieve the helicopter World Speed Record of 249.1mph (Figure 1.5). The fact that this record has stood for 23 years demonstrates how little further improvement in speed capability is possible using the conventional helicopter configuration with passive blades.

Figure 1.5: Westland Lynx modified for the World Speed Record. Courtesy AgustaWestland.

Nevertheless, the development of ever more sophisticated numerical analyses can still provide further improvements in performance through passive design optimisation, this being well illustrated by the development of the latest generation BERP IV blade. Harrison et al (2008) discuss how the combination of improvements in the dynamic design process (see below) and the use of Computational Fluid Dynamics (CFD) to facilitate the design of high-lift, zero pitching moment aerofoils enabled the blade twist to be increased to 16 degrees. The use of such high twist enabled a 5% improvement in hover performance over the previous BERP III design through the minimisation of induced power. Furthermore, a combination of numerical analysis and wind tunnel testing also enabled the tip planform to be further optimised which, along with the newly developed aerofoil sections, provided power reductions of 10-15% in highly loaded

conditions along with an envelope expansion of up to 10 kts, although no improvement was provided at lower blade loading.

The reduction of rotor induced vibration through passive design is also benefiting from improvements in predictive capability and computer processing power. The latter in particular has enabled structural analysis and aeroelastic predictions of vibration to be coupled into a single process, which enables the use of structural optimisation for the minimisation of vibration [see, for example, Glaz et al (2009)]. As well as providing more flexibility in the allowable blade property distributions in the optimisation process, modern composite manufacturing techniques have also given rise to the use of aeroelastic tailoring [see, for example, Bao et al (2008)]. Aeroelastic tailoring seeks to make advantageous use of structural couplings between the flap, lag, and torsion degrees of freedom of the blade which, through interaction with the aerodynamics, can further improve its dynamic response. Such techniques were used along with structural optimisation in the dynamic design of the BERP IV blade, as discussed by Moffatt and Griffiths (2009). However, with the emphasis of design on improving the hover performance, the resulting large amount of twist meant that the requirement on the dynamic design was simply to maintain the control load and vibration levels of the existing BERP III blade. Using the modern techniques discussed above this and some further improvement was achieved, as shown in Figure 1.6.

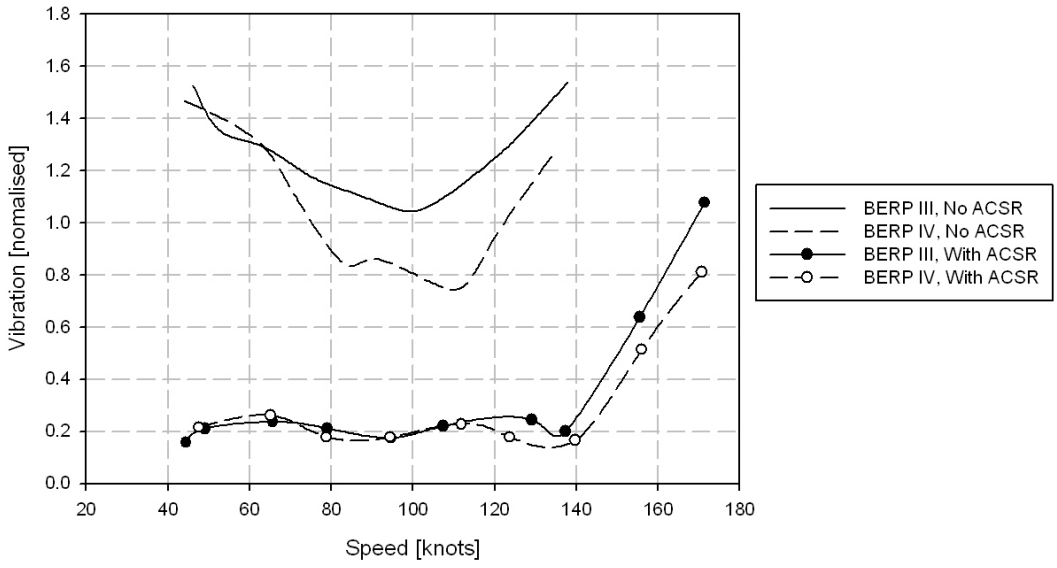

Figure 1.6: Comparison of EH101 vibration with BERP III and BERP IV main rotor blades with Active Control of Structural Response (ACSR), a fuselage-based active vibration control sytem, either on or off, based on Harrison et al (2008).

The results presented in Figure 1.6 show that even using the most up-to-date design processes, the vibration could be reduced by a maximum of 30% at medium flight speeds but with little to no improvement at low and high-speed flight. Perhaps without compromising so much for performance enhancement this could have been improved, however the results are a long way from those achieved using the Active Control of Structural Response (ACSR) system, Harrison et al (2008). This system uses actively controlled actuators located between the gearbox and the fuselage to cancel the vibratory forcing from the main rotor using feedback from accelerometers in the fuselage, and clearly this active control is substantially more effective at reducing vibration than using passive design alone.

Two key reasons exist for the limited effectiveness of passive design. The first is that the process is still hampered by a limited prediction capability. Standard design tools of sufficient efficiency for use in the design and optimisation process give poor prediction of the phasing of the high-frequency loads which are all-important for vibration prediction, with such problems well highlighted by Hansford and Vorwald (1998). More recently, some good correlations for the UH-60 helicopter have been obtained through the coupling of CFD with Computational Structural Dynamics (CSD); however obtaining good results for a well understood flight-tested aircraft is significantly easier than predicting *a-priori* for a new design. Also, these techniques are so computationally expensive that they are of only limited use in the design process, and the lower fidelity but highly efficient methods such as those used in the current research must continue to be pursued, albeit with considerable input from the higher fidelity aerodynamics methods. With the limited accuracy in vibration prediction an optimiser might find a design which uses vibration reduction mechanisms which cannot be relied upon in reality, and therefore the ability to create a passive blade designed for minimum vibration is compromised. The second reason for the limited effectiveness of passive design is the simple variability of vibration. In their optimisation design study Glaz et al (2009) highlight how the source of vibration varies considerably across the flight speed range, and that no single design is optimum for both the high-speed and low-speed cases. In addition, most modern helicopter designs are offered with a wide range of fuselage configurations and installed equipment but still using the same rotor system. This, together with manufacturing variability, means that the important components of vibratory loads, and the coupling of the rotor-fuselage dynamics, can vary considerably from airframe-to-airframe within a supposedly common fleet.

The variability and unpredictability of vibration in rotorcraft are what makes it such an attractive proposition for an active system able to adapt, on-line, to the specific aircraft and flight condition. This is well demonstrated by the 'ACSR-ON' results presented in Figure 1.6. Similarly, the variation of the aerodynamic environment both with flight speed and around the azimuth would also suggest that the adaptation of the blade within flight could also prove beneficial from a performance standpoint. The location of active devices on the rotor itself therefore suggests that the many compromises which clearly exist in both the aerodynamic and dynamic design goals of a helicopter rotor blade could be minimised. In this way the performance and loads could be optimised at source rather than using a fuselage-based system to cancel the loads generated by the rotor. Furthermore, if the aerodynamics of the rotor can be used to advantage the vibration reduction might be achieved using lighter, more efficient systems. This may also reduce fatigue of hub and control system components whilst also enhancing performance and providing the possibility of further applications such as noise reduction.

Unsurprisingly then, in the last decade there has been a proliferation in the literature of papers concerning a wide variety of technologies which may be said to fall under the title of 'Active Rotors'. Three such active rotor technologies are considered in this dissertation, Air Jet Vortex Generators (AJVGs), Trailing Edge Flaps (TEFs), and the closely related Active Trailing Edge (ATE).

1.3 Air Jet Vortex Generators

The production of longitudinal helical vortices, i.e. with the vortex core passing in a streamwise direction, over an aerofoil re-energises the boundary layer through mixing with the freestream and therefore has been shown to considerably enhance the stall characteristics with little to no drag penalty. Static vortex generators have long been used on fixed wing aircraft. They consist of geometrical shapes which protrude from the aerofoil surface into the flow in order to produce the required vorticity.

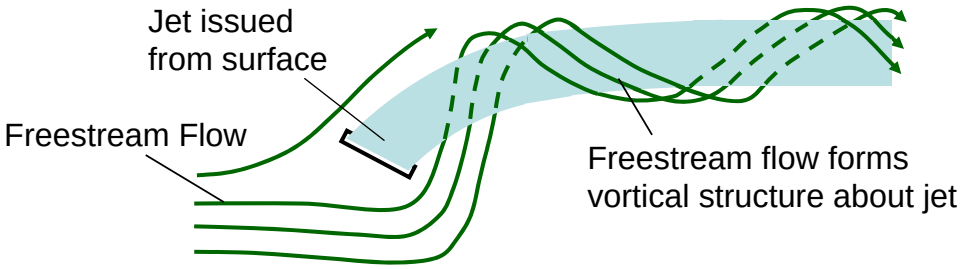

Figure 1.7: Helical vortex formation around a jet. Based on the water jet observations of Rao (1998) with jet pitch and skew angles of 30 and 45 degrees respectively.

Air Jet Vortex Generators (AJVGs) perform the same function by blowing air from the aerofoil surface into the boundary layer in order to produce a similar vortical structure, as shown in Figure 1.7. AJVGs do not have the profile drag penalty associated with static vortex generators and have the added advantage that they may be switched on and off. The system power requirements can therefore be minimised by only switching on the jets when their use is advantageous. Furthermore, the pulsing of the jets has been shown to yield further increases in the lift benefits whilst reducing the total mass flow requirements.

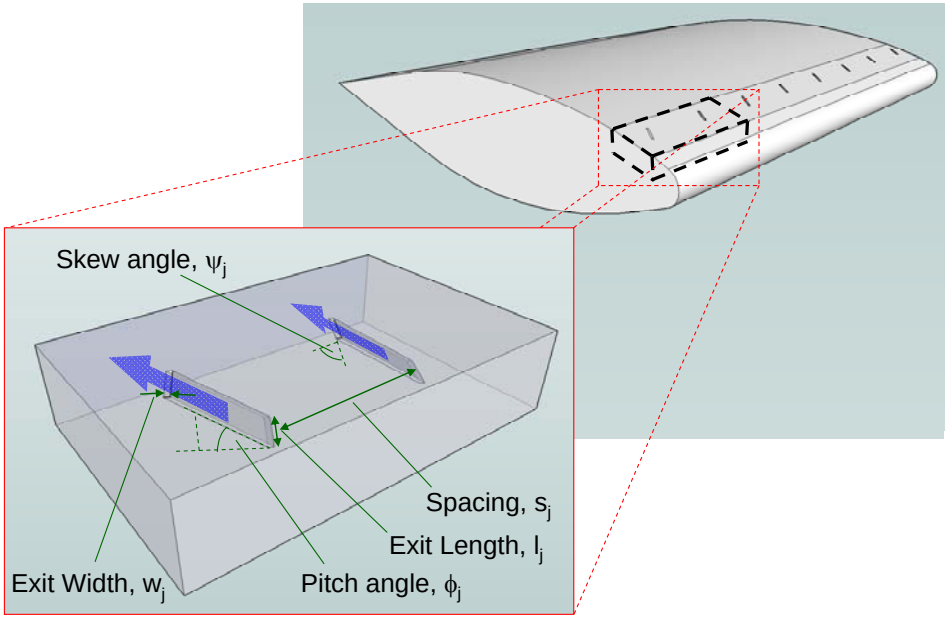

Figure 1.8: Schematic of Air Jet Vortex Generators.

Figure 1.8 shows a typical geometry for a set of AJVG nozzles. A pressurised chamber supplies air to a set of flow control valves which release the air through these nozzles. The latter have built in pitch and skew angles which must be optimised to give the greatest effect on the stall characteristics by ensuring the maximum production of vorticity at the required height above the aerofoil surface whilst also minimising the drag penalty. The following sections present a background of the development of AJVGs, starting with static vortex generators before moving on to firstly steady and then to pulsed AJVGs.

1.3.1 Static Vortex Generators

The use of static vortex generators (VGs) was first suggested by Taylor (1947) for use in the diffuser section of wind tunnels. These vortex generators protrude into the flow to produce longitudinal vortices. A typical shape can be envisioned as a half delta, as shown

in Figure 1.9, which is inclined in order to produce a vortex along its edge much like that created by a delta-winged aircraft. Since then there has been a significant amount of investigation into the formation and downstream propagation of the resulting vortices, with a view to understanding and maximising the effectiveness of such devices.

Schubauer and Spangenberg (1960) tested a number of different static VGs against a range of adverse pressure gradients. They found that although the devices varied in effectiveness, their overall influence was similar, and the overall result was basically equivalent to a reduction in the effective pressure gradient. Pearcey (1961) then provided a thorough investigation into the design and optimisation of vortex generators.

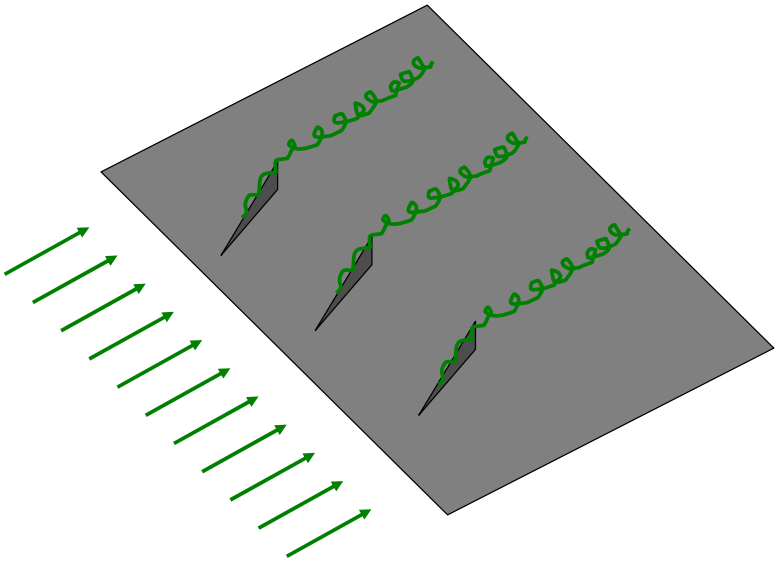

Figure 1.9: Half-delta static vortex generators.

In the 1980s researchers at Imperial College published a succession of papers describing experimental investigations into the modification of the turbulent boundary layer structure due to embedded longitudinal vortices. Mean flow and turbulence measurements were presented for a single vortex, Shabaka et al (1985), and for a vortex pair, Mehta and Bradshaw (1985), and Mehta (1984) suggested the need for sophisticated turbulence models if the experimental results were to be produced numerically.

Perhaps because of this requirement much of the research into the topic continued to be experimentally based, with good examples being the work conducted by Eaton and colleagues at Stanford University. Pauley and Eaton (1988) provided a detailed report of the flowfield due to vortices embedded in a two-dimensional boundary layer, whilst Shizawa and Eaton (1992) reported turbulence measurements due to a longitudinal vortex in a three-dimensional boundary layer. Numerical studies into vortex-boundary-layer

interaction have also been performed with early examples being Liandrat et al (1985) and Sankaran and Russell (1990) and a more recent example being the large-eddy simulation of You et al (2006).

This is only a selection of the literature available on the use of static VGs and there has clearly been a large amount of optimisation and understanding developed. However, Carr and McAllister (1983) found that although static VGs significantly delayed static stall, in the dynamic pitching environment the trailing edge separation was delayed but leading edge stall was induced, and little appreciable improvement in the dynamic loads was observed. In addition, static VGs are known to give a drag penalty due to their protrusion into the flow and therefore have a detrimental effect in conditions away from stall. The use of variable pitch active vortex generators (AVGs) as investigated, for example, by Shizawa and Endo (2007) could perhaps overcome some of these problems; however the parasitic drag due to the surface area of the devices could still be significant at low angles of attack.

1.3.2 Steady Air Jet Vortex Generators

Air Jet Vortex Generators (AJVGs) were first demonstrated by Wallis (1952) as a means of delaying turbulent boundary layer separation whilst reducing the drag penalty associated with static VGs. A spanwise series of jets blowing normal to the surface were installed at the 50% chord location of a NACA 2214 aerofoil. The interaction of the jets with the freestream produced pairs of counter-rotating vortices, Figure 1.10, which enhanced the mixing of the high-energy freestream flow with the boundary layer. Although the jets were found to have a favourable effect through the delay of boundary layer separation, they were found to be less effective than static VGs as the produced vorticity was more quickly dissipated.

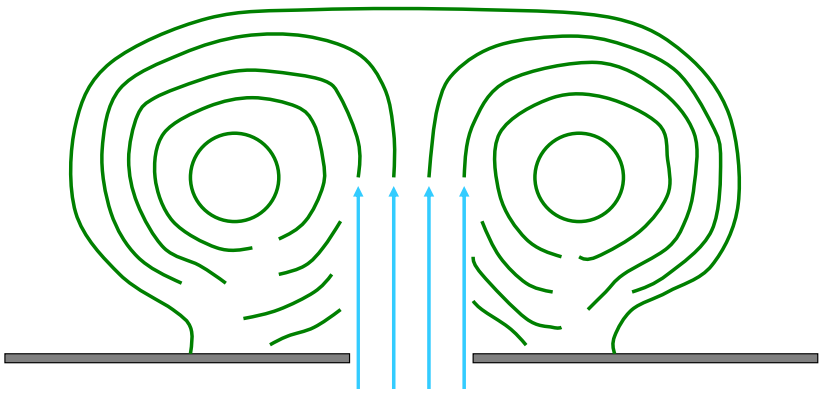

Figure 1.10: Counter-rotating vortex pair from a wall-normal blowing Air Jet Vortex Generator.

Wallis (1956) addressed this issue by inclining the jets such that they had a cross-stream component. The inclined jets were compared to wall-normal jets and were found to produce a stronger set of co-rotating vortices, Figure 1.11, which delayed the boundary layer separation as effectively as static vortex generators, a result later confirmed by Pearcey (1961).

Johnston and Nishi (1990) investigated experimentally an array of steady jets, circular in cross-section, pitched at 45 degrees. When pointing in the upstream direction the jets were ineffective but when an angle of skew was included such that the jet had a cross-flow component, see Figure 1.8, they were effective in reducing the stalled region through the production of longitudinal vortices. However, evidence was given for substantial spanwise variation, and the jets had much more effect on re-attachment than detachment. Compton and Johnston (1992) later investigated the development of the vortices as they travelled downstream using a hotwire. It was found that the vortices produced were qualitatively similar to the weak vortices produced by smaller static vortex generators. Maximum vorticity was found to be dependent on the jet skew angle (with the optimum being around 45 degrees from the freestream) and on the Velocity Ratio (VR), defined as the ratio between the jet and freestream velocities. The dependency of the AJVG effectiveness on jet velocity, orientation and location was also confirmed by Selby et al (1992), who also concluded that the boundary layer control was achieved much more efficiently than was possible with slot blowing.

Zhang (1993) studied numerically the effects due to velocity ratio and skew angle. The jets were found to be most advantageous when the resulting longitudinal vortex was located at the edge or outer region of the boundary layer. The vortex strength and the resulting heat transfer were found to be stronger if the skew angle was between 0 and 45 degrees. Further investigation into the effects due to the velocity ratio was also performed experimentally for both counter-rotating [Zhang (1999)] and co-rotating [Zhang (2003)] AJVG arrays.

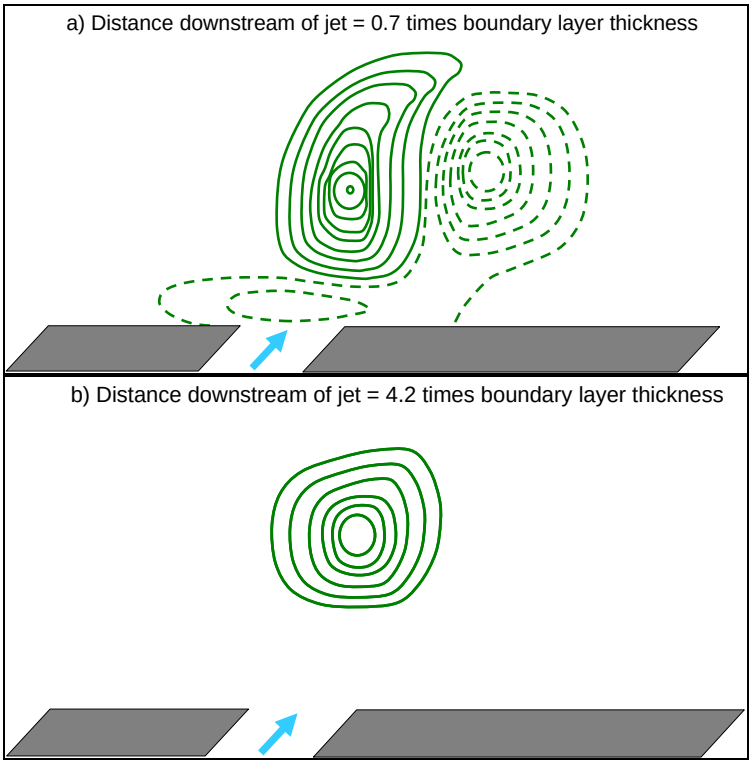

Figure 1.11: Co-rotating vortices from skewed and pitched jets. The secondary vortex is split and dissipated, which for an AJVG array leaves a set of co-rotating primary vortices further downstream. Sketch based on PIV contours of Rixon and Johari (2003).

Henry and Pearcey (1994) published a numerical investigation, the results from which were supported by the experimental data of Compton and Johnston (1992) in terms of the downstream decay of vorticity. Jet parameters were varied to maximise the overall skin friction which implies a delay in separation. Optimum jet pitch and skew angles were estimated to be 30 degrees and 60 degrees respectively. Increases in the jet velocity ratio increased the strength of the generated vortices; however it also caused them to move more quickly away from the surface when in the counter-rotating configuration. This result was also confirmed by Akanni and Henry (1995) through a comparison of co-rotating and counter-rotating AJVG arrays. They found that counter-rotating arrays were more effective immediately downstream, but co-rotating vortices remained closer to the surface for longer and were therefore more effective farther downstream.

Innes et al (1995) studied the use of AJVGs on a 2-dimensional, 3 element aerofoil and showed a significant increase in the maximum lift coefficient. Following this there have been significant studies at City University into the optimisation and application of AJVGs to wind turbine blade aerofoils. Building on the numerical results of Henry and Pearcey (1994) experiments demonstrated increases in the static stall angle of attack of up to 6 degrees for 17% thick [Oliver (1997)] and 21% [Vronsky (1999)] thick aerofoil sections.

Following this promising work on wind turbine sections, attention has been diverted to the thinner aerofoils associated with rotorcraft. Lewington (2001) presented numerical results for jet spacing and velocity ratio optimisation for both co- and counter-rotating jets. The co-rotating jets were found to perform significantly better farther downstream, this being presumed to be due to the vortex lifting in the counter-rotating case, as previously demonstrated by Akanni and Henry (1995). For the co-rotating array, an optimum velocity ratio of 2 together with a jet spacing of approximately 4 times the boundary layer thickness (at the jet exit) was defined. An experimental study using a flat plate validated some of the skin friction variation results, and a test of a NACA 23012C equipped with the optimised jet geometry was again found to successfully delay stall by up to 6 degrees angle of attack, thus enhancing the maximum normal force by 25%.

Rixon and Johari (2003) investigated the flowfield created by steady AJVGs using PIV techniques. Jets pitched and skewed at 45 and 90 degrees respectively were investigated using velocity ratios of 1, 2 and 3. The circulation, peak vorticity, and the wall-normal and spanwise locations were all found to increase linearly with the jet velocity ratio. The circulation and peak vorticity decreased with distance downstream for VRs of 2 and 3, whilst the lower VR case displayed different behaviour as it failed to penetrate beyond the log region of the boundary layer. In all cases the vortices were found to drift significantly to the extent that the time-averaged data was affected.

Singh et al (2005, 2006) performed a dynamic pitching experiment of an RAE 9645 aerofoil with steady blowing AJVGs located at 12% and 62% chord and found that blowing only from the front row of jets produced the best results (for the same total mass flux), with a delay in the formation of the dynamic stall vortex and reduced pitching moment divergence and lift hysteresis. The experiment was to highlight the possibility of using such jets to delay the retreating blade stall of rotorcraft. The authors warned however that the experiments were performed at low Mach number and that the effects due to compressibility, varying Mach number, and skewed flow may affect their use in the real rotorcraft environment.

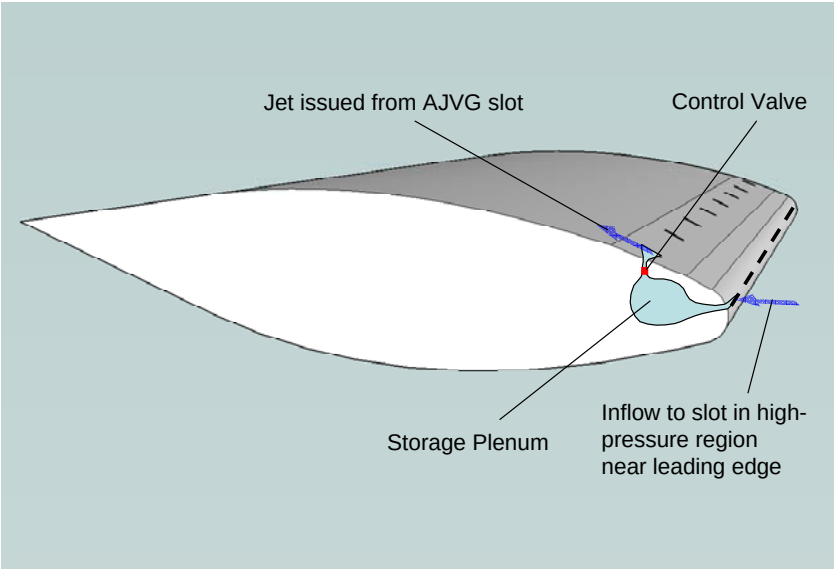

Figure 1.12: Sketch of a self-supplying AJVG system suggested by Krzysiak (2008).

A recent contribution to the viability of AJVGs involves a method for reducing the system requirements of an AJVG array. Krzysiak (2008) performed low- and high-speed wind tunnel tests of a self-supplying AJVG system whereby the flow was supplied from the overpressure region towards the leading edge of the lower surface, Figure 1.12. The set-up was shown to successfully delay separation without the need for a separate supply of high-pressure fluid.

1.3.3 Pulsed Air Jet Vortex Generators

A significant amount of evidence has therefore been gathered to show that steady blowing AJVGs reduce flow separation by re-energising the boundary layer through the production of streamwise vorticity. Another approach to active flow control involves oscillatory blowing [see, for example, Seifert and Pack (1999)] whereby spanwise vorticity may be introduced into the boundary layer through its interaction with a jet starting impulse. Such methods are attractive because they reduce the mass flow requirements, or even eliminate it altogether in the case of synthetic jets. [*Synthetic jets use a sub-surface oscillating membrane to promote alternate sucking and blowing through an orifice, see Hassan (2001)*]. McManus et al (1994) first introduced the concept of pulsing the AJVGs to obtain these benefits whilst maintaining the advantages of vortex generators. An experiment was undertaken which used pulsed AJVGs to reduce the separation of the boundary layer in an adverse pressure gradient created by a rearward slope. Two tunnel speeds were used, and a variety of velocity ratios and frequencies were tested. Flow visualisation revealed that the pulsed jets did indeed create large spanwise turbulent structures which enhanced the mixing to reduce the separation. An operating frequency of 30Hz and a velocity ratio of 2 were found to be optimum, and when

compared to steady jets at the same overall flow rate, pulsed jets were found to be considerably more effective in separation control.

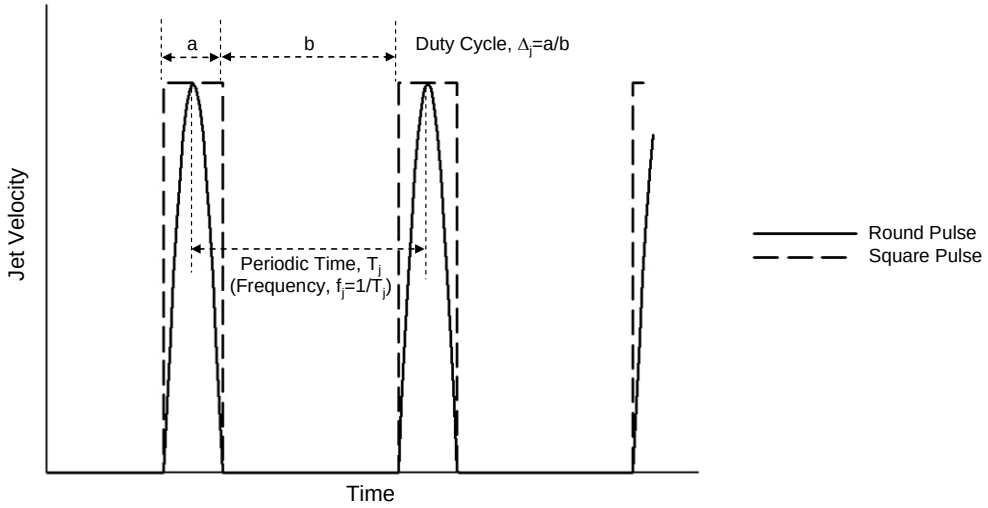

Figure 1.13: Definition of pulsed air-jet vortex generator flow parameters.

Following this, McManus et al (1995) presented results for a flat plate with a leading edge flap. A single circular pulsed AJVG was located on the leading edge flap and static pressure distributions were measured. The study found that the single jet could influence a spanwise region of at least 7.5 times the jet diameter. For moderate angles of attack the AJVG enhanced the suction over the front portion of the main element but resulted in less effect at the higher angles of attack, giving the notion that the jet becomes ineffective if the flow separates upstream of its location. Effectiveness was found to be dependent on both the velocity ratio and the total mass flow rate, suggesting that the dependency on velocity ratio can be used to reduce the duty cycle (see Figure 1.13) and, therefore, the mass flow requirements.

Further results for a model with a leading edge flap are presented in a later paper [McManus et al (1996)]. Stall was again shown to be delayed through the formation of large-scale turbulent eddies, and changes to both lift and drag coefficients were delayed by up to 5 degrees in angle of attack. The Strouhal number, based on the optimum pulse frequency of the jets and the frontal area of the model, was found to be close to that based on the natural shedding frequency of an equivalent bluff body, identifying a possible link to the underlying flow physics of separated flows. Two jets were used to study the effects due to jet spacing. Approximately two-dimensional pressure fields could be obtained with the jets separated by as much as 40 times the jet diameter, thus reducing the overall mass flow requirements of a large span wing/blade.

Magill and McManus (2001) investigated the applicability of pulsed AJVGs to fighter aircraft through experimentation with a model of a fighter aircraft with a swept wing and an aerofoil suitable for compressible flow experiments. The model experiments confirmed that the AJVGs enhanced the lift with little drag penalty for the fighter aircraft wing in low speed, high angle of attack conditions and were even more effective when used together with high-lift devices (leading- and trailing-edge flaps). However, the optimum jet geometry obtained from the 2-dimensional experiments was found not to be applicable to the more complicated 3-dimensional geometry of the fighter wings. The aerofoil section tests also revealed that the jets continued to be effective up to supercritical Mach numbers (defined by the upper-surface flow accelerating to sonic speeds) but reduced in effectiveness thereafter.

Hasegawa et al (2001a) studied the downstream development of the longitudinal vortices due to pulsed AJVGs using flow visualisation of a flat plate experiment. It was observed that as the jet pulse is initiated, regions of positive and negative vorticity elongate along the pitch angle of the issuing jet. When the jet pulse finishes, the positive vortex is split and attenuates the negative vortex, thus suppressing the creation of a vortex pair. This attenuation assures that the upward movement of the vortices is suppressed and the mixing between boundary layer and freestream can continue further downstream.

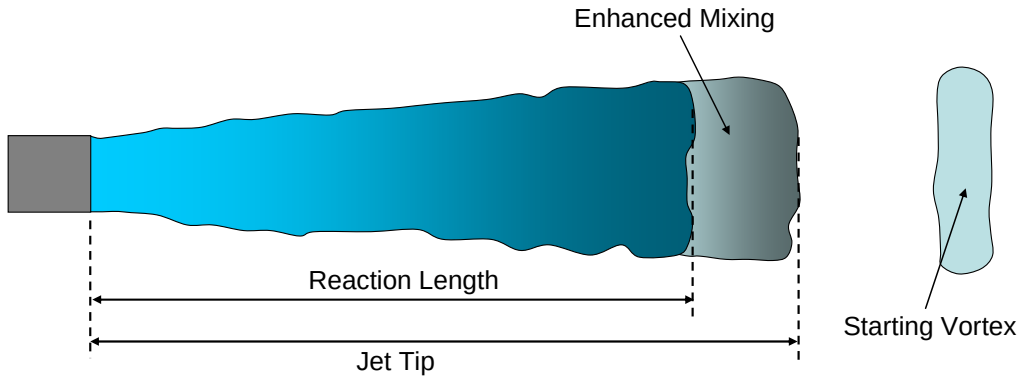

Figure 1.14: Schematic of an impulsively started jet showing the faster moving detached starting vortex. Reproduced from Johari et al (1997).

Johari and Rixon (2003) have also studied the longitudinal vortices. Using particle-image-velocimetry (PIV), vorticity contours were plotted, the total circulation calculated and the movement of the centres of vorticity traced. The counter-rotating vortex pairs observed for the steady jets were once again obtained. Peak values of longitudinal vorticity and circulation were found to be higher for pulsed jets than steady jets however the phase averaged values were lower than that of the steady jets. The greater influence of pulsed jets for a given mass flow was therefore put down to the longitudinal vortices

moving further into the boundary layer through the generation of a starting vortex ring by the jet. The influence of the starting vortex ring (Figure 1.14) on the penetration of a pulsed jet into a cross flow has also been studied by Johari et al (1999).

To investigate the use of AJVGs in suppressing the laminar boundary layer separation in low-pressure turbines, Postl et al (2004) performed a Direct Numerical Simulation (DNS) study of a flat plate with an imposed streamwise pressure distribution, as measured for a low pressure turbine blade. When using pulsed jets, the delay in separation was attributed not only to the entrainment of high energy fluid into the boundary layer by the streamwise vorticity but also to the early transition of the boundary layer, a result later confirmed by Gross and Fasel (2007).

Scholz et al (2006, 2008) considered using pulsed AJVGs to eliminate leading edge slats such that typical high-lift, three-element configurations could be replaced with a more simple two-element design, with the AJVGs used in place of the slat to prevent separation over the main element. A 2-dimensional single-element wind tunnel model was designed to approximate the pressure distribution and boundary layer behaviour of a typical 2-element design. The model was also given a reversible nose which could be inverted to change the position of the AJVG orifices, which essentially put them approximately on or upstream of the leading edge separation location. With the further aft location the AJVGs did not prevent separation, but did increase the post-stall lift coefficient. This, therefore, represented a post-stall flow control scenario during which a small dependency on actuation frequency was observed, thus supporting the evidence presented by McManus et al (1996) who suggested an influence of the Strouhal number of the natural shedding frequency. With the AJVGs located further forward, stall was effectively delayed by up to 2.5 degrees. In this case the frequency has no influence and the mass flux became the dominant factor.

The study of an AJVG on a flat plate by Ortmanns and Kahler (2007) showed that the distributions of the turbulent fluctuations in the boundary layer were hardly affected by the jet, therefore confirming that the mixing is dominated by the large-scale momentum transport as previously expected. Furthermore Kostas et al (2007, 2009) tested experimentally the effects due to the duty cycle and pulse frequency of both co-rotating and counter-rotating jet arrays and found that with a sufficiently high pulse frequency, essentially quasi-steady flow structures were formed.

1.3.4 The Potential Application of Air Jet Vortex Generators

From the evidence presented above, the most efficient stall delay using AJVGs appears to be achieved by choosing the parameters which correctly position the maximum possible vorticity within the boundary layer in a similar way to that achieved using static vortex generators. In addition, post-stall coefficients may also be influenced through interaction with the natural shedding frequency of the aerofoil, as is done using synthetic jets, whilst separation delay of laminar boundary layers may be achieved by using pulsing to encourage an early boundary layer transition. Using these mechanisms, a number of applications have been considered for AJVGs. Examples include:

- Stall delay for a reduced part count and stage weight of Low Pressure Turbines (LPTs) of turbomachinery [Bons et al (2001)]
- Stall delay and enhanced pressure recovery of diffusers [Liu and Nishi (2007)].
- Stall delay and enhanced manoeuvrability of fighter aircraft [Magill and McManus (2001)].
- Replacement of the leading edge slat in high-lift, 3-element configurations [Scholz et al (2008)].
- Performance enhancement of wind turbines [Oliver (1996)].

Previously it was mentioned that researchers at City University, London have been considering the use of AJVGs for helicopter rotor performance since at least 2001 [Lewington (2001)]. Most of the research however has concentrated on the experimental and numerical prediction of the effects due to AJVGs on the airload coefficients of typical aerofoils, and although it is expected that AJVGs could considerably delay retreating blade stall, little has been done to assess the effects on the overall rotor performance. An initial study has been presented by Kenning et al (2004); however the modifications made to the performance code were very basic and could not be expected to be capable of properly capturing the complex unsteady effects due to AJVGs. A key aim of the current research is thus to develop a model, based on a recent series of wind tunnel tests, which can more accurately represent the effects due to AJVGs. The model must be simply implemented and rapidly calculated to be used effectively in typical rotor performance codes. Using the newly developed model, the overall impact of AJVGs on the performance of an advanced helicopter rotor will be investigated and an assessment of the operational implication will be performed.

1.4 The Trailing Edge Flap and Active Trailing Edge

Trailing Edge Flaps (TEFs) are aerodynamic control surfaces located at the trailing edge of the blade. Two main types have been considered in the past, these being the servo-flap and the integral flap. The servo flap (see Figure 1.15) is generally of small chord and is placed behind the blade such that its main effect is on the pitching moment of the blade with which it may interact at relatively low deflection magnitudes. However, these flaps suffer from aerodynamic penalties, their mechanisms are exposed to the environment and they require the blade to be reasonably soft in torsion.

Figure 1.15: The Kaman H-2 Seasprite helicopter and a close up of its servo-flap primary control system. Photographed by the author at the USS Midway Aircraft Carrier Museum, 2009.

The second type, which is to be the focus of this dissertation, is the integral lift flap, as shown in Figure 1.16. These flaps are an integral part of the blade such that at zero deflection their profile becomes flush with the main blade contours and therefore the aerodynamic penalties are considerably reduced in comparison to the servo-flap. In addition, by having a greater influence on the lift coefficient the integral flap is better suited to interacting with the flapping modes which are most associated with vibration without the need for a soft-in-torsion blade. However, in order to give the required lift

perturbations, the flap chord, spanwise extent, and deflection requirements may be expected to be larger.

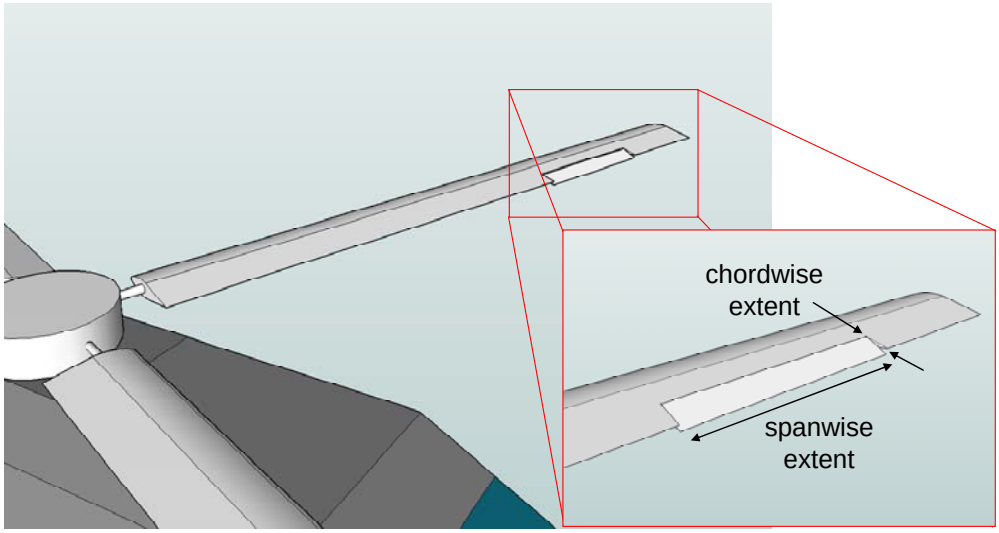

Figure 1.16: Geometry of an integral trailing edge flap.

The American company Kaman have advocated using Trailing Edge Flaps (TEFs) for primary control as an alternative to the more traditional use of blade root actuation. The first production helicopter to use such a system was the Kaman H-2 Seasprite shipborne utility helicopter, shown in Figure 1.15, which first flew as early as 1959 [Endres and Gething (2002)]. Such systems however have not been widely adopted by other helicopter manufacturers. The system allows a simplification of the rotor hub but the external servo-flap has a clear drag penalty. In addition, the exposure of the hinges of both the flap and the push-rod mechanism gives rise to concerns over maintainability in the harshest environments. Also of importance is that in order to give the servo-flap sufficient control authority, the rotor blade is designed to be soft in torsion. Wei (2002) presents some of the challenges that this makes for the rotor design engineer. In a blade in which there is already a large compromise between limit loads, vibration, fatigue loads, stability, and aerodynamic efficiency, a further compromise and constraint may be undesirable.

Stuller (1992) however quoted Kaman as saying "*...but today we have got microchips and the ability to put intelligence and more precise control in the rotor heads, blade and servos*." In other words, with the development of materials technology and digital control systems, the ability to operate flaps at high frequency with low power consumption has given rise to the possibility of using TEFs for control at higher harmonics. The use of higher harmonics, whereby control is applied to the blade at frequencies greater than the rotor rotation frequency, has been suggested to provide, for example, improvements in

vibration, noise, performance, and fatigue life. The use of TEFs for this higher harmonic control has also been suggested to obtain the benefits at much reduced power requirements compared to higher harmonic control at the blade root. Actively controlled TEFs have therefore been prolific in the literature over the last two decades revealing a large number of numerical studies which have been supported by a range of both model- and full-scale experimental tests.

1.4.1 Numerical Studies

Some early research into TEFs was performed by researchers at McDonnell Douglas/Boeing who examined the impact of TEFs on Blade Vortex Interaction (BVI). BVI occurs when a blade passes close to a vortex generated by a previous blade passage. The velocities induced by closely passing vortices result in significant changes to the pressure distribution around the aerofoil and the corresponding lift and pitching moment response, see Figure 1.17. These interactions therefore result in increases in both noise and vibration and are responsible for the distinctive cracking sound, known as blade slap, associated with helicopters in low-speed descending flight or abrupt turns where the rotor is more likely to be operating within its own wake. Hassan et al (1992, 1994) considered the benefits available from both leading edge and trailing edge flaps through the modification of loads due to a Blade Vortex Interaction (BVI). The numerical results suggest that the trailing edge flap can successfully alleviate the unsteady loading, and therefore the noise, due to a BVI. The deflection of the flap however is relatively large (up to 10 degrees) and must be controlled according to the chordwise location of the vortex. Such precise control and large deflections could prove difficult to implement.

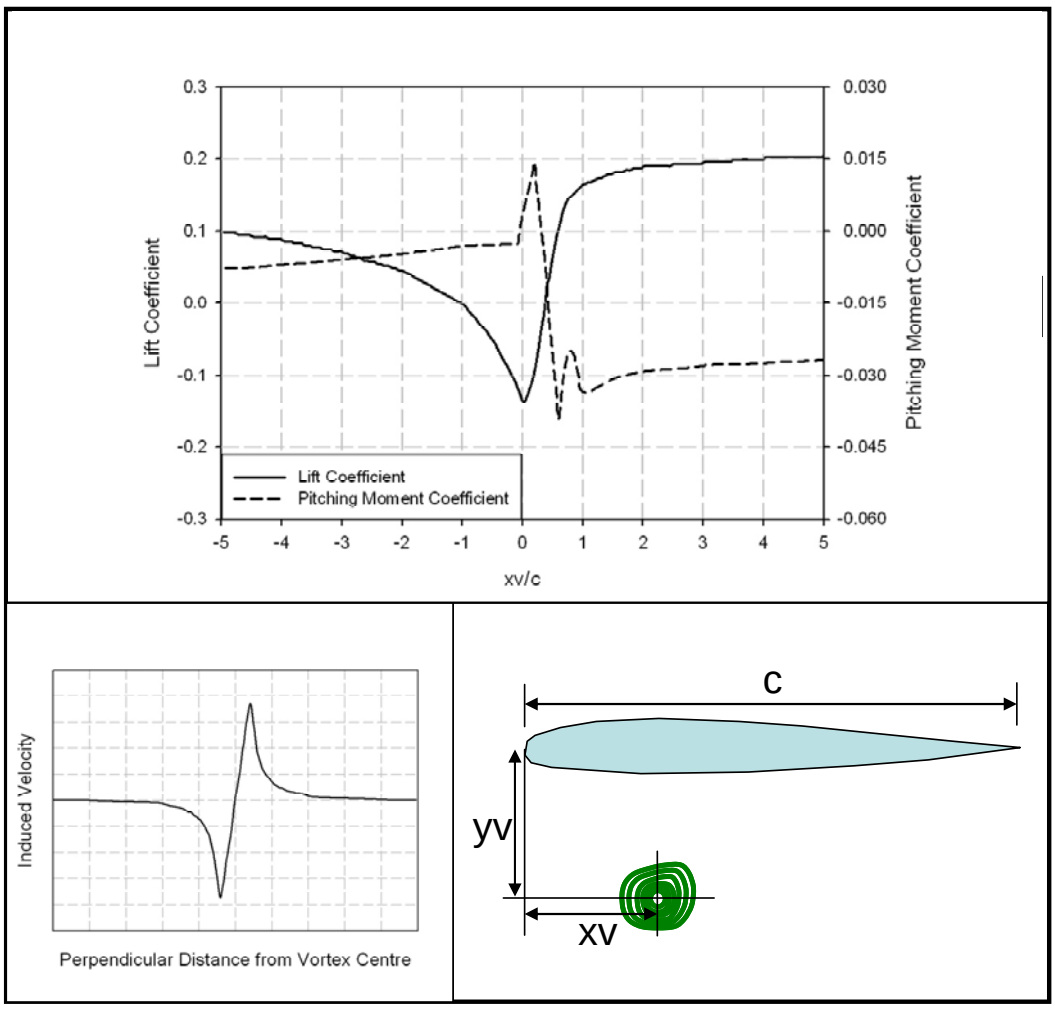

Figure 1.17: Effect on lift and pitching moment coefficients due to a parallel blade vortex interaction. Coefficient variations based on Hassan et al (1994).

To overcome these limitations, Charles et al (1996) considered using higher harmonically controlled TEFs for BVI reduction. The theory here is that by applying control inputs at higher harmonics, the distance and orientation between blades and vortices can be altered for a reduced acoustic signature. This method therefore does not depend on sensing a vortex encounter at the blade but instead depends on a more global form of noise feedback from, for example, a skid mounted microphone.

Straub and Hassan (1996) then performed a conceptual design of a full-scale active TEF system for the MD-900 helicopter and highlighted the importance of a variety of aerodynamic and dynamic design parameters, all of which must be accurately modelled such that the most efficient design can be achieved. Straub and Merkley (1997) also performed the conceptual design of an actuation system for the primary control of an AH-64 aircraft and concluded that with improvements in actuation technology, the full manoeuvre envelope might be achieved with active trailing edge flaps.

Millott and Friedmann (1992, 1994) and Friedmann and Millott (1995) were amongst the first to consider the reduction of vibration using active trailing edge flaps and to compare the approach to conventional individual blade control (IBC), where the entire blade is pitched at higher harmonics at the root, see for example Nguyen and Chopra (1990). Significant reductions in vibration were achieved using both methods; however the use of trailing edge flaps enabled a similar level of vibration reduction at a much reduced power requirement. The torsion stiffness of the blades was found to have a significant impact on results obtained and on the optimum spanwise location of the flap. The practical implementation of such an active flap system was also discussed by Millot and Friedmann (1993).

Milgram and Chopra (1995) also considered the use of TEFs for vibration reduction using the University of Maryland Advanced Rotor Code (UMARC). Open loop control inputs were shown to yield significant reductions in vibration and strong interactions with the 3rd flap mode and 1st torsion mode were noted. However, a reduction in the blade torsion stiffness was found to result in a decrease in effectiveness of the flap, a result which is not in agreement with Millott and Friedmann (1992), thus highlighting how the geometric design of the flaps must be tailored to the specific rotor to which they are being applied. Following on from this work, Milgram and Chopra (1998a) performed a parametric study of an integral trailing edge flap. The authors concluded that the amount of vibration reduction was reasonably independent of flap length, chord, and radial position, as an alteration to the flap deflection schedule could account for any changes however some benefit was found in locating the flap away from the node of the second flap mode (see Figure 1.18) whilst a small chord gave lower power requirements. Therefore any flap of reasonably large deflection capability should give large reductions in vibration; however more careful design of the system can yield significant reductions in actuation load, deflection and power requirements.

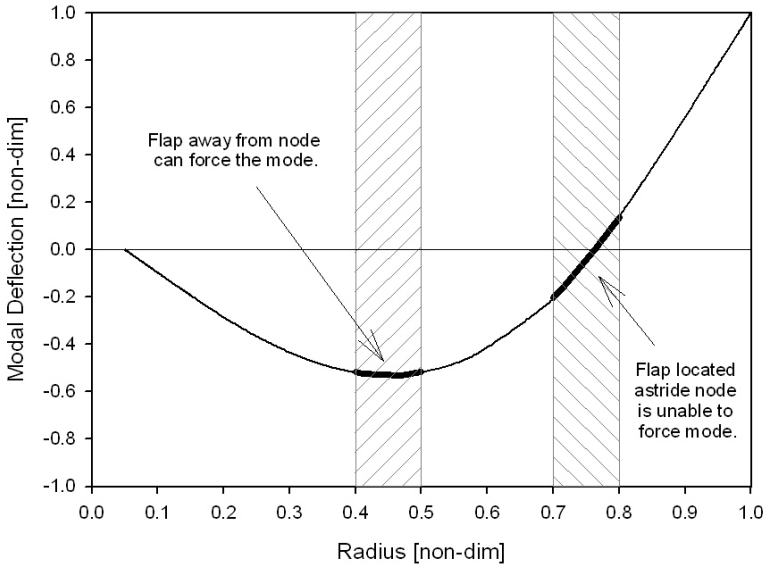

Figure 1.18: Example of a flap located at a modal node unable to force the mode.

Milgram and Chopra (1996, 1998b) also compared their analytical results to data from a wind-tunnel experiment. The baseline rotor (no flap actuation) was found to be in good agreement with the analytical prediction in terms of modal frequencies and the flapwise bending moment and torsion moment however the in-plane bending loads were found to be poorly predicted. The comparison also revealed that the effect of the flap on the flapwise bending moments was over-predicted. Clearly care needs to be taken in making strong conclusions from such analytical studies. In general it would appear that the effects of the flap on the out-of-plane loads are realistic although the precise magnitude may not be adequately predicted. The poor prediction of even the baseline rotor in-plane loads suggests that any prediction of reductions in these loads using the flaps should be viewed with some caution.

To improve on the fidelity of the earlier work of Millott and Friedmann (1992), Myrtle and Friedmann (1997a, 1997b, 2001) developed a semi-empirical aerodynamic modelling technique which could be written in state-space form for use in aeroelastic simulation codes. This model was tested within a fully coupled dynamic formulation. The importance of including compressibility effects and unsteady effects were highlighted since flap deflection requirements were shown to change. With the flap geometry chosen to make use of the servo-effect, it was found that greater flap deflections were required for higher blade torsion frequencies, as larger alterations to the pitching moment were required to enable the desired angle of twist of the stiffer blade. Myrtle and Friedmann (1998) have also discussed some practical considerations such as the flap configuration, the stability of a blade with a free flap, and the conceptual design of a suitable actuator.

A free-wake model was later incorporated into the program, as reported by de Terlizzi and Friedmann (1999), and was used to provide further evidence that the flaps actuated at frequencies of 2-5 times the rotor rotation frequency (2-5/rev) could successfully reduce the BVI induced vibration of a four-bladed rotor.

Kobiki et al (1999) presented the design and aeroelastic analysis for an on-blade active flap. Flap locations were sensibly chosen according to the shapes of the modes that were of most relevance to fuselage vibration. Flap spanwise and chordwise sizes were then determined to minimise the actuation requirements. Using only 1 degree of actuation, the optimum design was shown to give significant reductions in the out-of-plane loads, but at high-speed this was at the expense of the in-plane loads. The effect of the flap system on blade stability was also investigated and the important parameters of flap natural frequency and the centres of gravity of the flap and blade were identified.

Cribbs and Friedmann (2001) looked into the effects of actuator saturation and suggested the best way in which the maximum deflections should be used. Clipping the optimum signal was demonstrated to be a poor method, which is to be expected as this method would result in significantly different harmonics being input. Scaling the signal would preserve the harmonics and this method was indeed found to give better results. The best results were achieved using an adjustment to a control weighting, included in the cost function, to give a local optimum subject to the deflection constraint. This method therefore ensures that the most important input harmonics are preserved.

Chan and Brocklehurst (2001) used a rotor prediction program to predict the stall delay capability of TEFs. A prescribed once per revolution (1/rev) deflection of the flap (Figure 1.19) was used to provide the effect of variable camber. This deflection schedule provides an increase in the maximum lift coefficient on the retreating side whilst an un-cambered section is maintained on the advancing side to avoid a drag rise. The method was predicted to delay stall by up to 20knots with associated power reductions of 10% using downward flap deflections of 9 degrees.

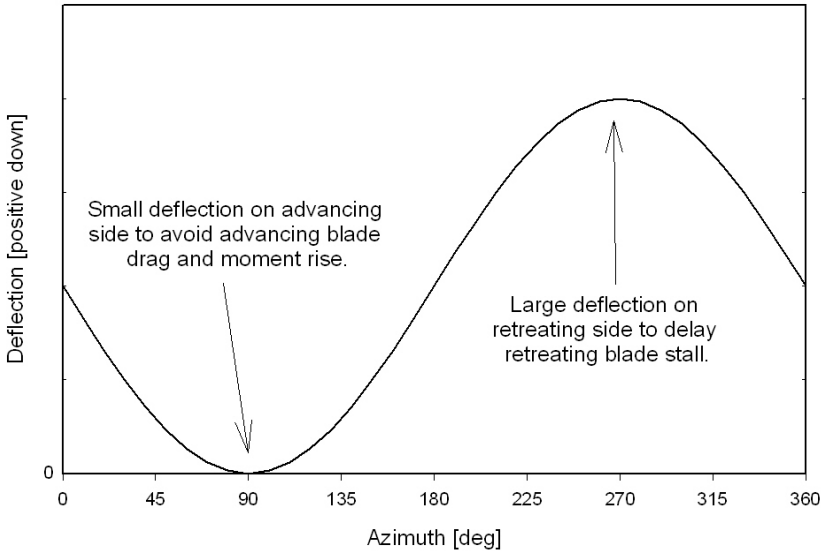

Figure 1.19: Prescribed trailing edge flap deflection used by Chan and Brocklehurst (2001).

Depailler and Friedmann (2002) considered the reduction of dynamic stall induced vibration. Without the application of deflection constraints the controller allowed large (15 degree) deflections on the advancing side which in reality would cause large shock-induced loads. Such physics are not accounted for in the modelling and therefore these results should be viewed with caution. With the application of a constraint the controller kept the deflection on the advancing side very small whilst larger deflections on the retreating side were shown to delay the onset of dynamic stall which in turn reduced vibration through the reduction of the stall-induced loads. The application of the constraint therefore forced the controller to use a control strategy which was similar to the open-loop type control being considered by Chan and Brocklehurst (2001) for the delay of retreating blade stall.

The research group led by Friedmann went on to consider the effects due to TEFs on both noise and performance. Patt et al (2005) considered the prediction of noise increases due to the use of an actively controlled flap for the reduction of BVI-induced vibration. The reduction of vibration was always found to be accompanied by a noise penalty, although dual flaps were found to yield lower noise penalties due to smaller deflection requirements. Following on from this, Patt et al (2006) used a combined cost function to reduce noise and vibration simultaneously. A dual flap system was found to be effective, however the reduction in both noise and vibration were less significant when obtained simultaneously. Liu et al (2006a, 2006b, 2008a) predicted reasonable reductions in main rotor power by using flaps with a higher harmonic control algorithm which compared

favourably with results obtained using an offline optimiser. The flight cases studied were however already far into stall. Furthermore, the drag model used for the effects due to the trailing edge flaps was only rudimentary, particularly as high Mach effects can be expected at the flight conditions being modelled. The results here should therefore be viewed with caution.

Straub and Charles (1999, 2001a) compared the rotor performance programs CAMRAD/JA and CAMRAD II for the modelling of rotors equipped with trailing edge flaps. The comparisons showed that although the more basic CAMRAD/JA code was useful for initial sizing studies, the higher fidelity CAMRAD II gave more accurate predictions of the blade loads. This together with the use of more advanced aerodynamic models and the inclusion of a model for the flap dynamics also allowed for more accurate modelling and sizing of the system as a whole.

Leconte et al (2001) also investigated the optimum flap size and locations for vibration reduction. Particular emphasis is given to the comparison between 15% and 25% chord flaps, with the former expected to rely predominantly on moment forcing and the latter on lift forcing. In practice the comparative influence of lift and pitching moment was found to be dependent more on the flight condition and blade dynamic design. The smaller chord flaps, whilst using greater deflections, were found to provide the same overall effects for lower actuator power. Flaps located further inboard were observed to be more effective at low speed whilst the most outboard flap was more effective at high-speed. The authors concluded that it was therefore advantageous to incorporate numerous flaps which could be best optimised according to the flight condition.

Shen and Chopra (2001, 2003) performed a numerical study of the stability of coupled actuator-flap-blade systems using linear stability methods. The coupled stability of the system must be considered as the dynamic and aerodynamic design can lead to potentially unstable coupling, as illustrated in Figure 1.20. The study found that while aerodynamically balancing flaps can reduce actuator loads, it can have a destabilising effect on the system. Similarly, flaps with centres of gravity aft of the hinge can suffer from flutter. Results indicated that the critical damping ratios of the coupled response modes were affected by the flap mass and the stiffness of the control system, actuator and blade.

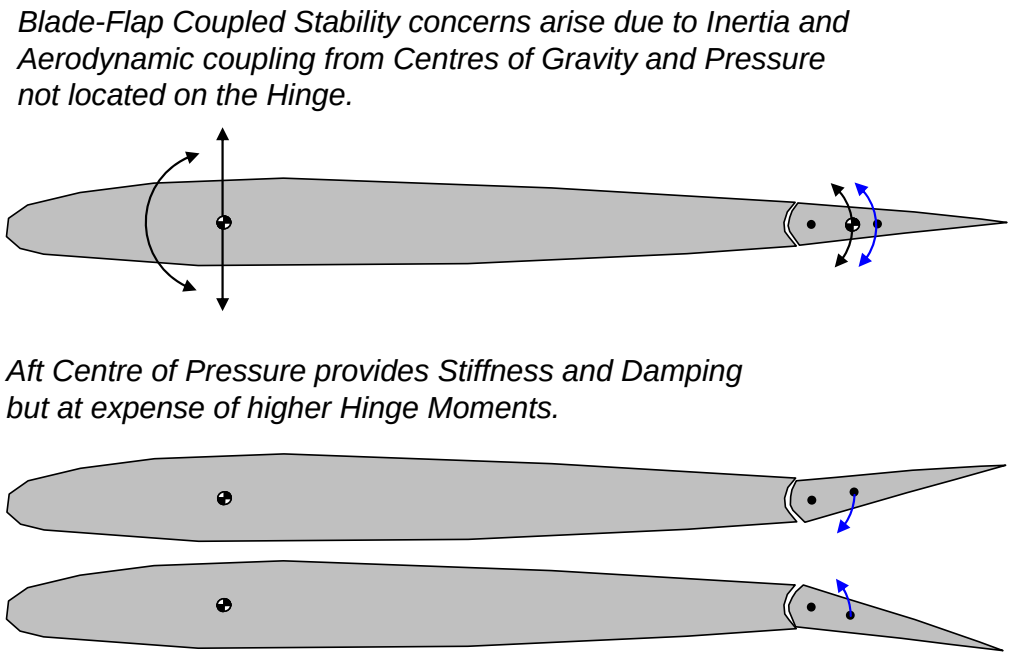

Figure 1.20: Stability concerns of a trailing edge flap.

Using the previously developed models, Shen and Chopra (2002, 2004, 2006) considered using flaps for both primary (flight) and secondary (noise, vibration) control such that the conventional swashplate might be eliminated to give substantial weight savings. Only steady-state forward flight cases were considered, however the flaps were shown to obtain trim using half peak-to-peak deflections of around 7 degrees. Aerodynamic balancing of the flaps was used to reduce the required actuator power and higher harmonics could be superimposed onto the primary 1/rev deflections to give the simultaneous reduction of vibration, albeit with additional deflection requirements. Malpica and Celi (2007) also investigated the control power available from trailing edge flaps when being used for primary flight control of a swashplateless rotor. Flap position was predicted to have little effect but a greater spanwise extent was found to improve handling qualities. Increasing the blade pitch index (the set collective pitch) and decreasing the blade torsion stiffness gave greater control, but this is done to the detriment of the trailing-edge flap-torsion coupling stability.

Many recent studies have considered ways of improving the vibration reduction capability of active flap systems. Viswamurthy and Ganguli (2004) considered the use of up to four flaps mounted near the blade tip. When compared to the use of a smaller number of flaps of the same total length, multiple flaps were found to give the same vibration with reduced deflection requirements thus leading to a lower actuation power requirement. Viswamurthy and Ganguli (2006) continued by explicitly modelling the hysteresis associated with a piezoelectric actuator. The results suggested that the non-

linearity thus introduced led to a deterioration of the controller performance in terms of achievable vibration reduction. This result suggests that if an actuation system with non-linearities is used then the best results may be achieved if a local feedback displacement controller is used to position the active flaps. Viswamurthy and Ganguli (2007) also performed an optimisation for the spanwise location of dual flaps. Two optimal design points were recognised, one with slightly better vibration reduction, the other with reduced actuation requirements. The solution providing better vibration reduction can be associated with using direct lift forcing of the flap modes whilst the second solution was more dependent on the servo-effect. It might therefore be hypothesised that if a blade of greater torsion stiffness were to be used the servo-effect design may no-longer be so effective such that a single optimum design based on the flapping modes will remain.

Zhang et al (1999, 2004) investigated using a hybrid active/passive design process whereby the blade structural properties could be optimised to obtain the maximum efficiency from the actively controlled flap. The hybrid optimisation resulted in deflection requirements being significantly reduced compared to those for designs where flaps are applied to either a baseline or passively optimised blade. Reduction in control effort was observed to be achieved by moving the blade flap and torsion natural frequencies closer to the actuation frequencies. It should be noted however that some large increases in the passive hub loads were observed and that the only constraints applied were on natural frequencies and autorotation capability. The entire study was also conducted with a single flap location; very different results might be obtained if the flap placement were to be included in the optimisation. Glaz et al (2008a, 2008b) also considered adding actively controlled flaps to passively optimised rotor blades. The passive optimisation, like the deflection of the flaps, was found to yield conflicting optimums for noise, vibration and performance such that if improvements in all three parameters were required, the obtained benefits would be greatly reduced.

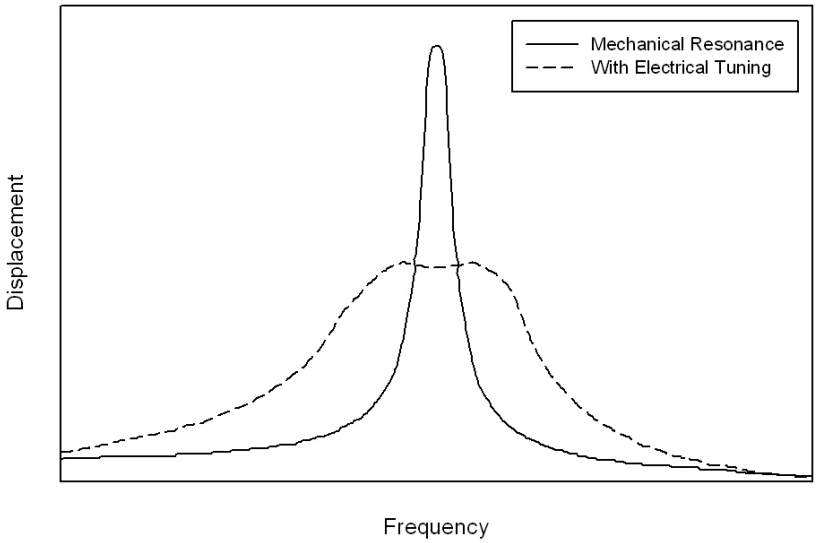

Figure 1.21: Flap displacement capability enhancement using mechanical and electrical tailoring, reproduced from Kim et al (2004).

Kim et al (2004, 2005, 2007) proposed the use of a resonance actuation system for vibration reduction whereby multiple flaps are used, with each one having a natural frequency electronically tuned to be an integer harmonic of the rotor rotation frequency. Mechanical tuning alone can increase the deflection capability but results in a deflection peak of low bandwidth and the possibility of stability concerns. The use of electrical tuning with the mechanical approach can provide a peak of greater bandwidth, Figure 1.21, and a system of increased stability margins. Bench tests are promising, with results suggesting the resonant flap system can achieve over 3 times the deflection of non-resonant systems. The authors claimed the system was fully robust however a full flap-actuator-blade stability analysis has not been carried out and is required to confirm that the system is stable. In addition, the tuning of the flap frequencies for vibration reduction and using smaller actuators would make the design less amenable to other, off-design, purposes such as performance enhancement.

Recently Falls et al (2006, 2007) investigated using tabs to actuate the trailing edge flaps. Various designs were investigated and were shown to provide the necessary control to obtain rotor trim. However, at certain levels of flap stiffness, the flap-tab combination did show the tendency to go unstable. Although this method suggests promise in reducing actuation requirements, the extra level of complexity would probably mean it is unlikely to be adopted.

As well as noise, vibration and performance, numerous other uses for TEFs have also been proposed. Stevens and Smith (2001) investigated using flaps for fault interrogation whereby small flap deflections were input at discrete frequencies and the response recorded using embedded strain gauges. The frequency response function was then used by a damage detection algorithm to predict both stiffness and inertial faults. Kim et al (2003, 2006) also considered the use of multiple flaps for the reduction of blade bending moments and control loads at high speed. A 1/rev input signal was used to 'straighten' the blade which at an advance ratio of 0.35 achieved blade flapwise bending moment reductions of up to one third. For a blade with highly cambered aerofoils, control load reductions of up to 80% we achieved. Celi (2003) investigated the use of trailing edge flaps, present for secondary control purposes, to stabilise and control a blade which has had a pitch-link failure. Using flap inputs up to the second harmonic resulted in the blade obtaining similar rigid flap and pitch dynamics to the other pitch-link controlled blades. The study showed that the flaps could be used in such an emergency if sufficient actuation authority were available. One further use of the flaps is to artificially enhance the stability margins of a blade. Konstanzer (2005) used decentralised control, with individual blade feedback sensors, to demonstrate reductions in vibration and simultaneously enhancement of the stability margins of the blade lagging modes. Roget and Chopra (2003, 2004, 2008) developed a controller which uses separate inputs for each blade to provide the capability to reduce vibration caused by dissimilar blades. The methodology was developed and tested using UMARC, which predicted significant improvements in the vibration reduction of dissimilar blades when compared to a standard Higher Harmonic Control (HHC) approach. The numerical results were later reinforced by wind tunnel testing of a model rotor with active flaps. The wind tunnel testing confirmed simultaneous reductions of the 1/rev and N/rev hub loads of around 40-50%, although non-controlled harmonics of the hub loads were observed to increase.

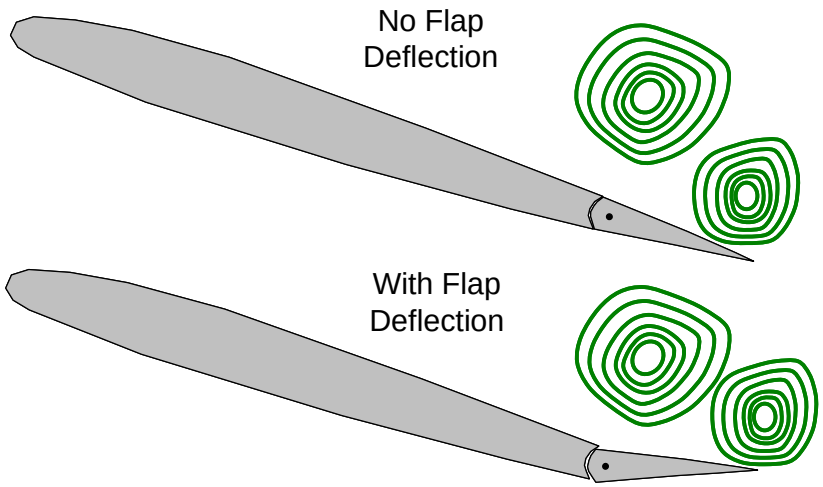

Figure 1.22: Simplified representation of the flow physics calculated by Feszty et al (2004). Diagram shows approximate vorticity contours. The upward deflection of the flap during dynamic stall can promote closer interaction of the trailing edge and dynamic stall vortices leading to the early detachment of the former.

Most of the papers discussed above were based on efficient rotor codes with reduced order aerodynamics models. More recently however some papers have emerged which have demonstrated the use of CFD to predict the influence of trailing edge flaps on helicopter rotors. Feszty et al (2004) investigated the interaction of the TEF with the dynamic stall process. Without TEF deflection, large nose-down pitching moments were found to be caused not only by the Dynamic Stall Vortex (see the following chapter) but also by the formation of a secondary vortex at the trailing edge. Upward deflections of the flap during the dynamic stall process were found to move the position of the trailing-edge vortex so that it would be washed downstream earlier due to its interaction with the dynamic stall vortex, see Figure 1.22. Deflections greater than 10 degrees were required to give a significant impact, although these deflections were on the retreating side where the dynamic head, and thus the required actuator force, was lower. Davis et al (2005) reviewed this approach further, but also considered the use of downward flap deflections to reduce the proportion of rotor disc entering dynamic stall. Both methods were found to reduce blade shears and vertical moments and to increase the aerodynamic damping.

Related to this research is a series of papers published by Gerontakos and Lee (2006, 2007a, 2007b, 2008) on an experimental investigation into the alleviation of dynamic stall using trailing edge flaps. Gerontakos and Lee (2006) initially considered the effects of both upward and downward flap deflections. Only upward deflections were demonstrated to have a beneficial influence on the pitching moment associated with dynamic stall. The flap was found to have only a small influence over the dynamic stall vortex which, unlike the data of Feszty et al (2004), suggested that the reduction in nose-down pitching moment was due to the increased suction on the underside of the flap. Further

optimisation of the 1/rev signal was reported by Gerontakos and Lee (2007a) before the use of higher harmonics for dynamic stall alleviation of a NACA 0015 aerofoil was considered [Gerontakos and Lee (2007b)]. The use of 2/rev inputs was found to be most successful displaying reductions in the nose-down pitching moments and the areas of negative pitch damping. 3/rev inputs gave slight improvements, whilst 4/rev inputs were found to be detrimental. Finally, PIV results reported by Gerontakos and Lee (2008) confirmed that, since the trailing edge vortex observed by Feszty et al (2004) was not in evidence, the reduction of the nose-down pitching moment was due to the increased suction on the under-side of the trailing edge flap. These conflicting results therefore suggest that the interaction of flaps with dynamic stall is complex and dependent on the particular aerofoil and flow conditions under consideration.

Gagliardi and Barakos (2006, 2009) used CFD to investigate the application of plain and slotted flaps to hovering rotors of medium twist (7 degrees). It was found that the slotted flap with constant deflection could produce the performance associated with an equivalent rotor of 13 degrees of twist whilst a plain flap with constant deflection recovered the performance equivalent to 10 degrees of twist. However, the flap was located far inboard (48% span) which would make it less ideal for other purposes and used a large chord and deflection (32% and 10 degrees respectively) which may be beyond the capability of some actuators.

Altmikus and Knutzen (2007) performed a simulation of a steady forward flight condition using coupled CFD-CSD. The paper presents a comparison between the analytical prediction and flight test data for the passive blade and then goes on to present the performance benefits predicted by the numerical method by using a purely 2/rev flap actuation input. The use of a single input perhaps highlights the current weakness of the coupled CFD/CSD methods, which are often too expensive to be used for an optimisation process.

Mishra et al (2007) also developed a coupled CFD-CSD analysis incorporating an integral trailing edge flap to investigate its use for vibration reduction. Following validation against wind-tunnel experiments, an optimum deflection schedule was shown to give reductions in the fixed-frame vibratory hub loads. Later Mishra et al (2009) used the same methods to assess the effectiveness of trailing edge flaps in mitigating the effects due to dynamic stall. The coupled CFD-CSD solver was found to give good agreement with flight test data for a standard (flapless) UH60 rotor and with unsteady deflections of a trailing edge flap from a fixed wing. With confidence in the solver thus obtained, it was

used to show that with the right phasing and amplitude a 1/rev flap deflection can be used to alleviate the dynamic stall effects, leading to a 30% reduction in the blade's vibratory torsion response. With a similar input schedule it was also shown that a rotor trim could be obtained at a higher thrust condition, thus suggesting that an expansion of the flight envelope is possible.

1.4.2 Practical Implementation and Actuation

Clearly a large amount of numerical analysis has been completed. This has been supported by practical implementations, which were made possible through the development of suitable actuation schemes. Dawson et al (1995) and Straub (1995) first performed wind tunnel tests using a model rotor equipped with trailing edge flaps. In order to yield sufficient actuation authority a selection of cams were used to investigate specific flap deflection schedules at individual harmonics and a limited number of phases. This open-loop testing meant that the full capability of an active system could not be realised, but it did provide an early validation of the potential benefits available from TEFs. Substantial reductions in vibratory hub loads were found to be possible and noise alleviation was also predicted, albeit with accompanying increases in blade loads. However, the results from 2/rev inputs aimed at improvements in rotor performance were inconclusive, due to the limited accuracy of the measurement equipment.

The ability to demonstrate the full closed-loop potential of the active flap in a rotor system is dependent upon the availability of low-mass actuators capable of being accurately controlled at high frequencies with sufficient authority in terms of both deflection and load operating in high centripetal acceleration fields. A series of such actuators have been developed at the Massachusetts Institute of Technology (MIT). Spangler and Hall (1990) first tested a piezoelectric bimorph actuated flap (Figure 1.23) in a wind-tunnel, and verified modelling tools to speculate on scaling the design to full-scale applications. Hall and Prechtl (1996) improved on the design by using a tapered bimorph actuator with a flexure link to the flap. The development and validation of a state-space model was also reported and was used to suggest that such an actuation system could provide up to 5 degrees of deflection for a full-scale system.

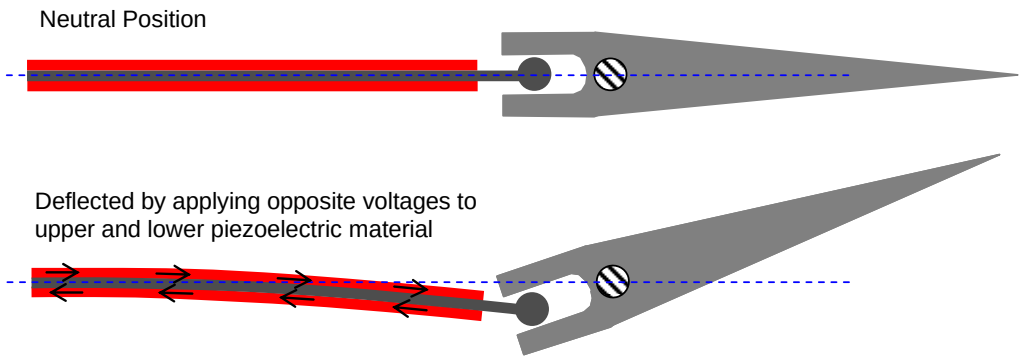

Figure 1.23: Diagram of a piezoelectric bimorph actuated flap.

A significant amount of model-scale research, including the development and testing of model rotors and suitable actuators, has also been undertaken at the University of Maryland and the development of this research up to October 2000 is discussed by Chopra (2000). Like the early research at MIT, much of the initial research has been conducted using piezoelectric bimorphs to actuate the flaps. The earliest work revealed disappointing deflection capabilities under the significant centrifugal loads associated with the rotating system. A Froude-scale rotor was manufactured for investigations into the origin of the losses and the results of this work, which was conducted in parallel with analytical methods, was reported by Ben-Zeev and Chopra (1996). Results demonstrated that friction at the flap-blade interface was mostly responsible for the loss in deflection capability and that the use of thrust bearings greatly improved performance. Koratkar et al (1997) later showed that the Froude-scale rotor achieved flap deflections of up to 8 degrees, and that these deflections and the corresponding response of the vibratory hub loads were in good agreement with analytical predictions.

The bimorph actuation technology was therefore considered to be of sufficient maturity for the testing of model rotors equipped with bimorph actuated flaps. Fulton and Ormiston (2001) modified existing rotor blades to incorporate flaps with a length of 12% of the rotor radius. The rotor was tested at reduced rotor speed due to the limitations of the actuation system and because of structural weakening necessary to incorporate the active sections in pre-existing rotor blades. Nevertheless, the flaps were shown to have significant authority over the blade flap and torsion response, particularly when actuated close to the natural frequencies of the various modes. Wind-tunnel tests by Fulton and Ormiston (1998) showed significant reductions in single harmonics of the blade bending moments due to open-loop flap actuation. Another important result of this work was the unexpected occurrence of control reversal, whereby the effect on lift due to the twisting of the blade exceeded the direct-lift effect of the flap. This highlights the important influence of the blade torsion stiffness on the effectiveness of the trailing edge flaps.

At the University of Maryland, Koratkar et al (1999) used the analytical tools correlated against the earlier Froude-scaled rotor to design a Mach-scaled rotor which was to be tested on both a hover stand and in the wind tunnel. The rotor was at first tested with open-loop control [Koratkar et al (2002a)] during which sufficient flap deflections and authority over the vibratory hub loads were demonstrated. Following this, the work culminated in full closed-loop tests for the simultaneous reduction of the fixed-frame hub vibratory thrust, rolling moment and pitching moment [Koratkar et al (2002b)] using the neurocontrol algorithm presented by Spencer et al (1999). Reductions of the order of 80% were demonstrated for advance ratios from 0.1 to 0.3 thus validating the feasibility of using trailing edge flaps for this purpose. More recently, Bao et al (2006) have reported further progress on model rotor testing using piezoelectric bimorph actuated flaps for primary as well as secondary control. To obtain the necessary control power, the flap was of much greater spanwise length than the previous models, and the research to date has focussed on achieving the required deflections. Copp and Chopra (2008) have reported that, with a series of modifications, the goals have been obtained and that testing is in progress.

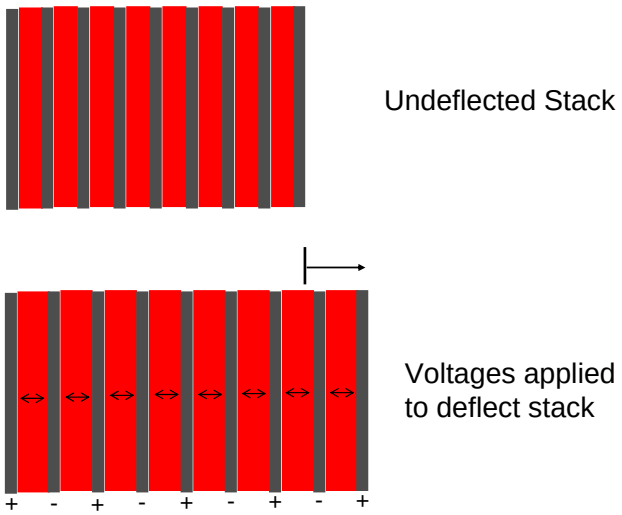

Figure 1.24: Diagram of a piezoelectric stack actuator. Note: Exaggerated displacement.

The research group at the University of Maryland have also investigated the use of piezoelectric stacks for the actuation of flaps, Figure 1.24. Piezoelectric stacks exhibit lower displacement, but higher force characteristics than the bimorph actuators. The small displacement is insufficient to actuate the flaps directly and therefore a mechanism is required to convert some of the force into extra displacement, however a well-designed mechanism coupled to a high efficiency piezoelectric stack can give greater mass specific

energy than the bimorph actuators. Samak and Chopra (1996) first looked at using an amplified stack actuator to control a flap. The displacement obtained was significantly less than predicted, which demonstrates the importance and difficulty in designing an efficient amplification mechanism. Spencer and Chopra (1996) then applied a stack actuator using L-arm amplification to a trailing edge flap which was tested on a wing section in the wind tunnel. (*The L-arm mechanism is a basic lever where an L-shaped component is rotated by pushing the end of the short arm with the piezoelectric stack to give a larger displacement at the end of the longer arm.*) The losses were less significant than for the device of Samak and Chopra (1996), though were still greater than predicted. Chandra and Chopra (1997) demonstrated a greatly improved design in the wind tunnel. This design had a greater level of integration between the stack and the mechanism, which again used an L-arm amplification mechanism but with an elastic hinge providing the rotation. Lee and Chopra (2001) then demonstrated an improved actuator for the actuation of a full-scale flap (although the flap was small in spanwise extent). The actuator used an integrated double L amplification mechanism (*where the first L-arm is used to push a second lever*). The results were encouraging with the actuator displaying sufficient performance both in the wind-tunnel and under centrifugal loading during a spin test.

Straub et al (1997b, 2001b) at Boeing have developed a 'biaxial' amplified stack actuator for use in the full-scale MD-900 rotor blade. Continuous testing and improvements led to a doubling of the actuator performance such that with the inclusion of the latest piezoelectric stack technology the actuator was deemed to provide sufficient authority for the full-scale application.

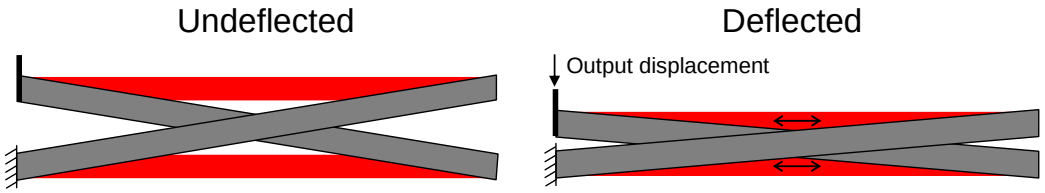

Figure 1.25: Diagram of the X-frame actuator developed by Prechtl and Hall (1997).

Following their work on bimorph actuators, the researchers at MIT also developed an amplified stack actuator. Prechtl and Hall (1997) conducted an actuator survey and used the conclusions to design a new actuator for maximum specific energy. The actuator used two parallel piezoelectric stacks within an inert amplification frame, the arrangement of which has led to the actuator being named the 'X-frame'. The actuator has been used in a design for a model-scale active rotor blade based on the CH-47 rotor. The design is presented in detail by Prechtl and Hall (1998), with particular emphasis placed on aspects

of the design required to overcome the challenging acceleration environment. The blade was then tested on a hover stand by Prechtl and Hall (2000). Data collected demonstrated that closed-loop control successfully reduced multiple harmonics of vibration with both single and multiple flap deflection harmonic inputs.

The X-frame actuator has clearly been shown to have a high efficiency and has therefore drawn interest from Boeing for use in the MD-900 active rotor blade. This has prompted further development and testing, with Hall et al (2000) presenting the testing of an improved double X-frame with two such actuators operating in opposition to negate the need for an external preload. Spin testing and dynamic shake testing has been conducted to evaluate its performance in representative operational environments during which the actuator was found to provide adequate characteristics for the actuation of the full-scale blade.

Figure 1.26: The Boeing Smart Material Actuated Rotor Technology (SMART) active flap equipped rotor during whirl tower testing. Image reproduced from Straub et al (2004).

The prolonged development of piezoelectric actuators described above eventually led to a workable solution for use in a full-scale rotor test by Boeing. Straub and Kennedy (2005) presented the development and whirl tower testing of the Smart Material Actuated Rotor Technology (SMART) active rotor blades suitable for the MD-900 helicopter, see Figure 1.26. The whirl tower tests achieved 7 hours of successful flap operation during which the system was shown to have significant authority over the vibratory thrust of the rotor. The system was then tested further in a wind-tunnel, as discussed by Straub et al (2009).

Elsewhere, a number of projects have considered the use of the Amplified Piezoelectric Actuator (APA) range offered by the French CEDRAT Company. These actuators consist of a piezo stack around which is wrapped a metallic or composite frame. This frame preloads the stack (which has a very limited tensile limit) and also amplifies the stroke. Clearly the stack must elastically deflect the frame and therefore losses are inevitable. However the simplicity of the scheme means that a well-designed actuator can be light, giving an actuator with a high overall specific energy capability.

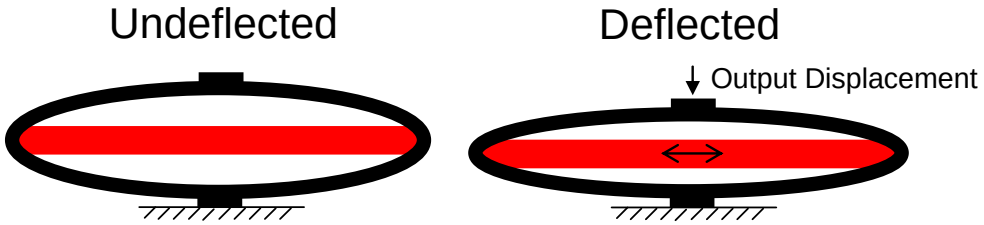

Figure 1.27: Diagram of an Amplified Piezoelectric Actuator as manufactured by the French CEDRAT Company.

Leconte and des Rochettes (2002) presented the results of centrifugal and aerodynamic tests of a model-scale active flap module utilising CEDRAT actuators. The centrifugal problems reported by Chopra were largely overcome by replacing discrete hinges by a flexible 'blade'. With the selection of an APA actuator with suitable characteristics the aerodynamic loading requirements were also shown to be satisfied. The success of these tests led to a similar active flap design being used in a model rotor developed jointly by ONERA and DLR under the Active Blade Concept (ABC) project. Mainz et al (2005) have discussed the rotor blade design and manufacture in detail whilst Crozier et al (2006) and Delrieux et al (2007) have presented results successfully demonstrating vibratory load and noise reduction.

Another project to use an APA actuator is the Smart Hybrid Active Rotor Control System (SHARCS) led by Carleton University and introduced by Nitzsche et al (2005). This

project is a co-operation between academia and industry of Canada, Italy and Greece and aims to test a model rotor equipped with active devices in the wind tunnel. The planned rotor blades are to incorporate an active pitch link, active tip anhedral and, of relevance here, an active trailing edge flap. The flap is included primarily to influence the dynamic stall characteristics of the blade, whilst the active tip and pitch link are to be employed primarily for noise and vibration reduction respectively. Ghorashi et al (2006) have presented the preliminary design of the blade, with further updates from Feszty et al (2008). The active flap uses two APA actuators to deflect the trailing edge flap by up to 4 degrees. The use of two actuators in this way allows a push-pull configuration such that the flap would fail to the neutral position, unlike the ABC rotor where an unloaded flap would be in a deflected position.

Much like the incorporation of the X-frame actuators into the Boeing full-scale test rotor, the experience gained in Europe in the CEDRAT-type actuators has led to them being used by Eurocopter Deutschland in a full-scale flight test vehicle. Full-scale flap units were first tested in the wind-tunnel by Schimke et al (1998). These flap units were incorporated into a highly modified blade design based on the EC145 main rotor blade, Figure 1.28, as discussed by Dieterich et al (2006). In contrast to the single large flap of Boeing's SMART rotor, the BK117 blades incorporate three much smaller flaps, each actuated by two EADS designed actuators of the CEDRAT type. The use of three flaps suggests a much more flexible system, ideal for both noise and vibration reduction. A modified BK117 equipped with these rotor blades started flight testing in 2005. The ability of the system to reduce vibration has therefore been proven in flight with some preliminary test results being presented by Roth et al (2006). Following the flight test experience, Jänker et al (2006) related how ECD are continuing to improve the system with optimised actuators and reduced control system size and mass. The results of this study should result in a system which is much more feasible for operational use.

Figure 1.28: Image of the Eurocopter Deutschland active flap equipped blade during whirl tower testing. Image reproduced from Roth et al (2006).

Another successful full-scale application has been led by ATIC who demonstrated the first full-scale active rotor on a whirl tower, with the results presented by Hasegawa et al (2001b). Following this success, JAXA are looking towards demonstrating noise reduction in the wind tunnel and work is progressing on a new actuation system with ongoing development and testing presented by Kobiki et al (2007, 2008). An analytical investigation determined the properties required for noise reduction purposes, setting a requirement for 6 degrees of deflection. The full-scale system was then tested under typical operational conditions on the bench and in the wind-tunnel, during which it was demonstrated that 6 degrees of deflection could be obtained at up to 27.5 Hz.

The discussion in this section has clearly focussed on the actuation of flaps using piezoelectric actuators as this method is favoured and used by all three full-scale test rotors. Generally, the existing evidence suggests that piezoelectric actuators have shown the most promise, however other actuation methods have also been investigated. Alternative methods suggested in the literature include the Terfenol-D based magnetostrictive actuator of Fenn et el (1996), the bending-torsion coupled beam of Bernhard and Chopra (1999), the piezo-hydraulic actuator of Sirohi and Chopra (2002), the tab actuated flap of Falls et al (2006), the magnetostrictive and electrostrictive hybrid hydraulic actuators of John et al (2007) and the Pneumatic Artificial Muscles (PAM) of Wereley et al (2008).

In addition, other researchers have looked into alternative piezoelectric methods. The induced shear tube of Centolanza et al (2002) appeared to have little to no advantage over the amplified stack, but the C-block actuators of Clement et al (1999) and the single crystal stacks of Szefi et al (2006) show promise of further improving the capability of the piezoelectric-based actuators.

Sikorsky Aircraft are also pursuing an active flap test program. Chaudhry et al (2009) have discussed the development of the active rotor blade which was based on the existing Schweizer 434 blade with a highly modified section incorporating an electromagnetic actuator developed by Hamilton-Sundstrand Claverham. The small scale of the rotor allowed testing of both primary and secondary blade control at reduced cost; however it also meant that only a single flap could be used, whereas the authors suggested that in a future system the incorporation of multiple flaps would be likely.

1.4.3 Active Trailing Edges

Despite the vast array of research discussed above, and although the first test flight occurred several years ago, there is still no active rotor system in production. In order for this to happen, an active rotor system must be both operationally and economically viable within a realistic range of operational environments. Therefore any penalties which might be associated with an active system must be kept to a minimum. All of the practical demonstrations introduced above make use of discrete trailing edge flaps incorporating some form of hinge. The reliability of such mechanisms in harsh environments may therefore come into question; see for example Ahci and Pfaller (2008). Such concerns are based on the fact that parts of the control mechanism, particularly the hinges, are exposed to the environment, which in adverse conditions could lead to malfunction due to the ingestion of sand, dust or ice.

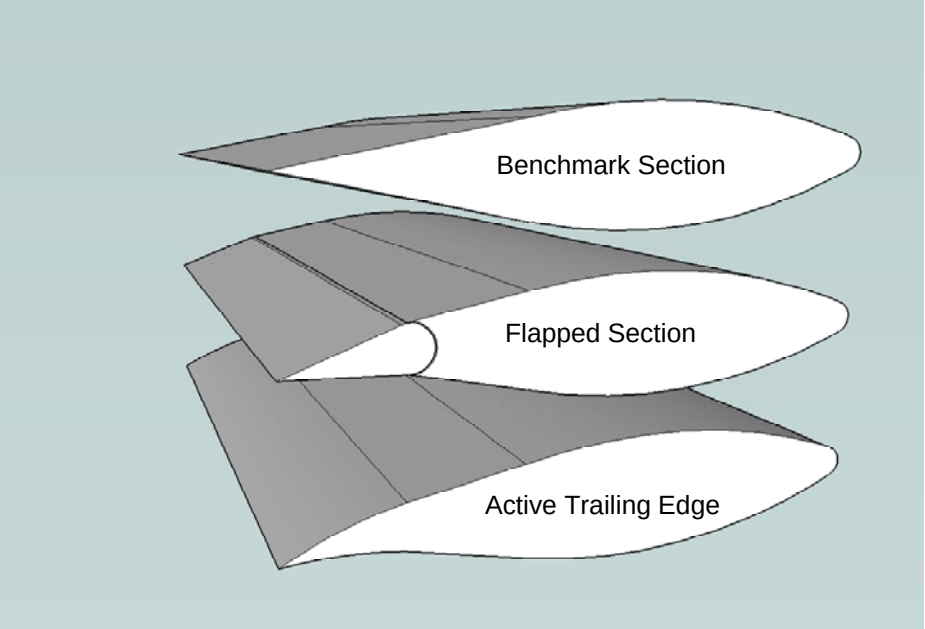

Figure 1.29: Flapped and Active Trailing Edge blade sections.

The integral flap design has given rise to the concept of an Active Trailing Edge (ATE) whereby the hinges are eliminated but the trailing edge shape is 'morphed', as illustrated in Figure 1.29. Clearly with the elimination of the hinge, the smooth aerodynamic profile of the trailing edge may be maintained which gives the possibility of a reduction in any drag penalties. In addition, as the change in camber is introduced smoothly without a discontinuity at the hinge, there will be subtle differences in the aerodynamic effects due to TEFs and ATEs which must be considered.

The research into the use of ATEs in the rotorcraft context has seen significantly less emphasis when compared to the TEF, possibly due to doubts over whether sufficient deflection capability can be achieved whilst ensuring that the trailing edge is strong enough to withstand the limit loads. The viability of an active camber aerofoil concept has however been investigated by Gandhi et al (2008), who presented a structural optimisation using finite element analysis. This design concept was then successfully validated using bench-top tests of a prototype. However, much of the research into ATEs has been conducted at Eurocopter following their flight test of the TEF system. Janker et al (2007) discussed improvements being made to the existing flap system, but also discussed the application of structural morphing and the associated advantages. Ahci and Pfaller (2008) have presented some detailed optimisation of active trailing edge structures, including effects of the interface regions (between active and passive spanwise regions), using finite element methods. Following this, Grohmann et al (2008) presented further details of the design including the development of aerodynamic coefficient polars.

1.5 Research Aims

A review of the prospects of vastly improving the current state of helicopter performance and vibration through passive design of the main rotor blades has suggested that the possible gains are limited due to the existence of conflicting requirements not only over the flight envelope, but also around the azimuth. The situation for vibration reduction is further exacerbated as *a-priori* predictions continue to be unreliable, particularly if made using methodologies of sufficient efficiency to be of use in a design and optimisation process.

The incorporation of active devices into the rotor blades suggests that they may be further optimised in-flight according to the particular flight condition or azimuth location. This capability can remove some of the compromises currently made in the design of the rotor blades. Furthermore, an actively controlled device can also overcome some of the limitations in the modelling as their off-design capability is significantly increased over a passive design.

The literature review has highlighted three active technologies which have been proposed for use on helicopter rotor blades, and this dissertation aims to analyse the operational utility of these systems. The first is the Air Jet Vortex Generator (AJVG) array. This technology has been demonstrated to provide significant delays in stall that are valid in both the static and dynamic cases. The influence of such an enhancement on the overall capability of the rotorcraft has however seen little research. This dissertation therefore presents an evaluation of the performance enhancement capability due to the installation of an Air Jet Vortex Generator array. To enable the investigation, the modification of an aerodynamic model is required such that it is capable of adequately predicting the effects due to the AJVGs to give the investigation sufficient validity. Using the new method the effect of the AJVGs on the rotor performance is predicted, which is in turn used to analyse their operational effectiveness.

The second technology, the Trailing Edge Flap (TEF) has, in contrast to the AJVGs, seen a high level of development both in industry and academia to the point of being proven in flight test. However, a TEF system has not yet been incorporated into a production rotor blade, and if this is to happen then the cost of the active system must be fully justified by its operational benefits, and its reliability and maintainability must be maximised. One potential application of the TEF which can significantly contribute to its operational benefit is its application to the blade sailing phenomenon. Blade sailing refers to the large

blade responses that can occur during the engagement or disengagement of the rotor in high-wind conditions, such as those found on a ship at sea, or on an oil rig, and can significantly restrict the environment within which the aircraft can safely operate. This dissertation therefore presents the predicted effectiveness of the TEF in reducing the blade sailing during a real operational scenario and builds upon the research presented by the author at the American Helicopter Society [Jones and Newman (2007)]. The dissertation therefore provides further evidence to the effectiveness of the TEF when applied to the blade sailing problem and gives a further justification for the selection of the TEF for incorporation into the next-generation rotor blade.

Finally, some of the most recent literature has considered replacing the Trailing Edge Flap with the Active Trailing Edge technology in order to reduce drag and to greatly improve on its reliability and maintainability. However, such gains come with the possibility of a reduction in the deflection capability. The final aim of the dissertation is therefore to analyse the operational effectiveness of an ATE system of limited deflection capability in order to analyse whether the possible advantages of this technology are worthwhile in comparison to the Trailing Edge Flap.

The evaluation of the ATE and AJVG systems has required significant development of the aerodynamic predictive capability. In order to understand how these devices have been modelled, some background into the physics and modelling of rotorcraft aerodynamics is required, and this is provided in Chapter 2. Following this the investigation into the utility of the AJVGs is presented in Chapter 3. Chapter 4 contains a general discussion on the utility of the Trailing Edge Flap in the rotorcraft context, but primarily focuses on its application to the blade sailing problem. The investigation into the latest technology of Active Trailing Edges is then covered in Chapter 5 before some overall conclusions, including comparisons of the technologies, are made in Chapter 6 along with some recommendations for future research.

Chapter 2 The Modelling of Unsteady Aerodynamics

2.1 Introduction

In this chapter consideration is given to the existing methods of which use will be made in the modelling of the active technology. The evaluation of the effectiveness of Active Trailing Edges for vibration reduction is a key aim of this research such that the inclusion of blade dynamics in the simulation is vital. This requirement essentially determines the kind of aerodynamic methodology to be used. We have seen from the literature that some significant advances have been made in coupling Computational Fluid Dynamics methods to rotor dynamics simulations, but that the resulting simulations are still in their infancy and are computationally expensive. The modelling of active devices using such techniques must therefore be considered to be a substantial research task in its own right. In the design and evaluation of new technologies therefore, lower fidelity, but significantly more efficient methods, remain to be much more suitable.

The current research has therefore made use of the AgustaWestland rotor performance program r150. The use of this program was primarily due to its availability but also because it has a reasonable vibration prediction capability which has enabled the author to investigate the devices impact on this important aspect of rotor performance as well as the effects on rotor power and efficiency. The interaction of the helicopter with its own wake, highlighted in the previous chapter, clearly shows that the flow field in which the helicopter operates is highly three-dimensional in nature. However, most rotor performance analysis programs, including r150, calculate the aerodynamic coefficients using a blade-element lifting-line approach. This method consists of discretising the blade into a finite number of spanwise elements. At each location the inflow velocities are determined which through calculation of angle of attack and Mach number are used to calculate the two-dimensional aerodynamic coefficients (lift, drag, pitching moment). The calculated lift distribution is then used to determine the spanwise change in bound circulation strength from which a trailed vorticity sheet, sometimes referred to as the near-wake, is defined. Similarly, the calculated aerodynamic loads are used to determine the blade dynamic response and can also be used to provide information for the determination of a far wake structure which may range in fidelity from a constant downwash velocity through to free-wake methods such as that discussed by Bagai and Leishman (1995). The inflow to each blade segment is then determined through the superposition of contributions from the far and near wakes, the blade motions and the aircraft motion. From the inflow the two-dimensional blade loads are determined and the calculation continues in a time-stepping manner.

It is the calculation of the two-dimensional aerodynamic coefficients in response to the inflow which is to be the focus of this chapter as such a model will have to be capable of representing the effects due to the active devices. However, for a helicopter travelling in forward flight, as a rotor blade passes around the azimuth, the inflow velocity and angle of attack change substantially due, not only to the influence of the wake, but also for the need to maintain trim. The changes due to the cyclic pitch occur at the frequency of rotor rotation which, for medium-sized helicopters is in the region of 4-5Hz, whilst changes in the inflow due to the blade dynamic response or the close proximity of a vortex from a preceding blade can be much more rapid. The resulting time-dependence of the inflow results in the aerodynamic loads being substantially different from those in the equivalent quasi-steady conditions and the method used to calculate the two-dimensional coefficients must capture these flow physics.

If the flow remains attached then the aerodynamic loads will exhibit changes in both phase and magnitude compared to the quasi-steady equivalent which must be modelled if the blade loads and the corresponding performance are to be adequately predicted. On the other hand, if the rotor is more highly loaded and the blade is passing in and out of stall then the phenomenon known as dynamic stall occurs and the modelling task becomes significantly harder. Dynamic stall exhibits markedly different flow physics to the static case such that the airload response bears little resemblance to the quasi-steady equivalent. Furthermore, the response changes significantly with frequency and with mean angle of attack, indeed it is the light stall conditions found closest to the flight envelope boundary which prove to be the toughest to predict.

Most rotor performance programs, including the one to be used here, model these effects using indicial methods. Such methods have evolved over many years and the author does not seek to reinvent the wheel in this respect, instead making alterations to an existing model in order to sufficiently account for the main effects due to the devices. The model forming the basis for the current research is the Third Generation method, as described by Beddoes (1991), which is an evolution of the widely used Leishman-Beddoes model described by Leishman and Beddoes (1986,1989). The choice of this model was governed by its inclusion of two particular features, namely its integration of the camber-line boundary condition and the explicit modelling of the trailing edge separation (see below). These features make the model ideally suited to enable modifications for the representation of effects due to Active Trailing Edges and Air Jet Vortex Generators respectively, as will become clear in subsequent chapters.

This chapter introduces the main characteristics associated with unsteady aerodynamics but with the discussion centred on its modelling using the indicial methods employed by the Third Generation Model. It is therefore intended to provide the reader with the knowledge required to understand the alterations which have been made to the model in order to adequately capture the effects due to the active devices and to justify its use for this purpose. Section 2.2 presents the physics and modelling of the attached flow regime before dynamic stall is discussed in section 2.3.

2.2 Unsteady Aerodynamics for Attached Flow

2.2.1 Thin Aerofoil Theory for Steady Incompressible Flow

A derivation of the steady-state aerodynamic loads based on the incompressible thin aerofoil theory will first be presented as it forms the asymptote for the circulatory loads in the unsteady case, as is to be discussed in section 2.2.2. It should be noted that knowledge of this theory is particularly required to understand how the Active Trailing Edges are to be modelled.

Thin aerofoil theory for steady, incompressible flow consists of replacing an aerofoil of assumed infinitesimal thickness by a vortex sheet from which the load distribution can be calculated according to Joukowsky's theorem; see, for example, Fung (1955):

$$dL = \rho V \gamma(x)\, dx \qquad \textbf{2.1}$$

where ρ is the fluid density, V is the freestream velocity and $\gamma(x)$ is the vorticity sheet defined along the aerofoil coordinate, x, see Figure 2.1. The pressure distribution can therefore be found if the distribution of the bound vorticity strength can be calculated.

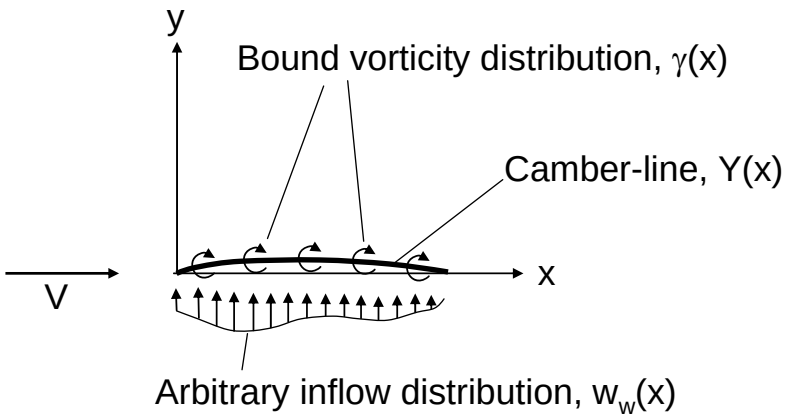

Figure 2.1: Steady flow over a two-dimensional aerofoil of infinitesimal thickness, adapted from Fung (1955).

This is achieved through application of the boundary condition of zero perpendicular flow across the camber-line whilst also satisfying the Kutta condition that the flow leaves the trailing edge smoothly and therefore that $\gamma(c) = 0$, where c is the aerofoil chord.

Therefore, if the camber-line of an aerofoil is given by $Y(x)$, then the streamline boundary condition on the aerofoil, which stipulates that the slope of the aerofoil camber-line defines a streamline of the fluid, is given by:

$$\frac{\left(w_i(x) + w_w(x)\right)}{V} = \frac{dY}{dx} \qquad \textbf{2.2}$$

where w_i is the induced velocity due to the bound vorticity and w_w is the wind (inflow) velocity (both in the y-direction, see Figure 2.1). For an aerofoil of small camber, i.e. making the assumption that the vorticity lies approximately on the x-axis, the induced velocity due to the bound vorticity is:

$$w_i(x) = \int_0^c \frac{\gamma(\xi)\,d\xi}{2\pi(\xi - x)}. \qquad \textbf{2.3}$$

To facilitate the calculation, Glauert (1947) expressed the vorticity distribution as an infinite series:

$$\gamma(\psi) = 2V\left(A_0 \cot\frac{\psi}{2} + \sum_1^\infty A_n \sin n\psi\right) \qquad \textbf{2.4}$$

where the chordwise variable, ψ, has been introduced such that:

$$x = \frac{c}{2}\left(1 - \cos\psi\right). \tag{2.5}$$

Substituting equation 2.4 into equation 2.3 results, after some manipulation, in:

$$\frac{w_i(\psi)}{V} = \left(-A_0 + \sum_1^\infty A_n \cos n\psi \right). \tag{2.6}$$

Substitution into equation 2.2 gives:

$$-A_0 + \sum_1^\infty A_n \cos n\psi = f_c(\psi) \tag{2.7}$$

where the boundary condition due to the camber and inflow have been combined into a single function as:

$$f_c = \frac{dY}{dx} - \frac{w_w(x)}{V}. \tag{2.8}$$

The left-hand side of equation 2.7 is clearly a Fourier series and the coefficients may be determined using the usual method of orthogonality to obtain:

$$-A_0 = \tfrac{1}{\pi}\int_0^\pi f_c d\psi \tag{2.9}$$

$$A_n = \tfrac{2}{\pi}\int_0^\pi f_c \cos n\psi d\psi. \tag{2.10}$$

Substituting equation 2.4 into equation 2.1 and dividing by the dynamic pressure and the chord gives the pressure coefficient distribution as:

$$\Delta C_p = \frac{dL}{\frac{1}{2}\rho V^2 c} = \frac{2\gamma(x)dx}{Vc} = 4\left(A_0 \cot\frac{\psi}{2} + \sum_1^\infty A_n \sin n\psi \right) d\bar{x} \tag{2.11}$$

where $\bar{x} = x/c$. Chordwise integration may then be used to obtain the lift and pitching moment coefficients. At this point the usefulness of the Glauert (1947) form for the vorticity distribution becomes particularly apparent as the integration ensures that most of the terms of the series have zero contribution such that the lift and pitching moment (about the quarter chord) coefficients are given by:

$$\begin{aligned} C_l &= \pi\left(2A_0 + A_1\right) \\ C_m &= -\frac{\pi}{4}\left(A_1 - A_2\right). \end{aligned} \tag{2.12}$$

By substituting the Fourier coefficients this can alternatively be expressed as:

$$C_l = 2\pi\varepsilon_0$$
$$C_m = \mu_0 - \frac{\pi}{2}\varepsilon_0 \qquad \textbf{2.13}$$

where:

$$\varepsilon_0 = -\frac{1}{\pi}\int_0^{\pi} f_c\left(1-\cos\psi\right)d\psi$$
$$\mu_0 = -\frac{1}{2}\int_0^{\pi} f_c\left(1-\cos 2\psi\right)d\psi\ . \qquad \textbf{2.14}$$

The integral ε_0 therefore represents the effective angle of attack, indeed for the case with zero camber and a uniform upwash due to an applied angle of attack, α, it can be shown that $\Delta f = -\alpha$ and $\varepsilon_0 = \alpha$. In practice the linear lift slope of 2π can be replaced by experimentally derived, Mach dependent values and the pitching moment coefficient can be similarly factored for effects due to compressibility.

2.2.2 Unsteady Effects

If an aerofoil is experiencing an unsteady inflow, then the lift, and therefore the bound vorticity, is changing with time thus suggesting that vorticity must be shed from the trailing edge of the aerofoil, Figure 2.2. This shed vorticity wake convects downstream away from the aerofoil; however the 'near' shed wake influences the inflow to the aerofoil in a similar manner to the trailed wake and can have a significant impact on the response of the circulatory loads following a perturbation.

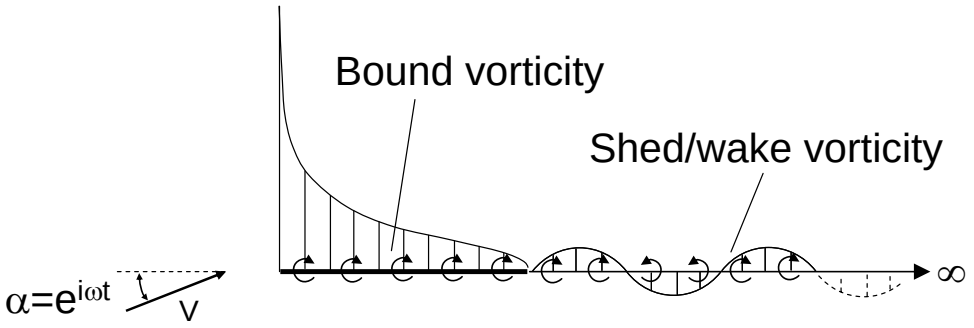

Figure 2.2: Representation of the bound and shed/wake vorticity of a harmonically pitching aerofoil, based on Leishman (2000).

Furthermore, the motion of the aerofoil requires an acceleration of the fluid in the immediate vicinity which in turn exerts a pressure force on the aerofoil. As the pressure wave convects away from the aerofoil the force is very quickly reduced towards zero,

indeed in the incompressible case the load is instantaneous and gives rise to the so-called apparent mass effects.

The response to a perturbation of the aerofoil force and moment coefficients can therefore be modelled as the sum of a circulatory component, which grows towards the quasi-steady value derived in the previous section, and a non-circulatory load which decays towards zero from the initial impulse value. Consider, for example, the incompressible case for which Theodorsen (1935) calculated the aerodynamic response of an aerofoil undergoing harmonic pitching and plunging motions. The apparent mass, or impulsive, response is instantaneous and consists of terms containing the first and second time derivatives of the aerofoil motion whilst the circulatory response consists of the quasi-steady value multiplied by a frequency dependent term known as Theodorsen's function. This function is generally expressed in terms of a non-dimensional frequency known as the reduced frequency which is defined as:

$$k = \frac{\omega c}{2V} \qquad \textbf{2.15}$$

where ω is the frequency in radians per second and c and V are the chord and velocity respectively. For a rotor blade pitching at n times its rotation frequency, Ω, the reduced frequency is therefore given by:

$$k = \frac{n\Omega c}{2\Omega r} = \frac{nc}{2r}. \qquad \textbf{2.16}$$

A 1/rev pitching motion will therefore result in a reduced frequency of around 0.15 near the blade root and 0.05 near the tip with higher harmonics of pitching factored accordingly. Theodorsen's (1935) result for the response of the lift coefficient to a sinusoidal pitch oscillation is plotted against the reduced frequency in Figure 2.3. Taking the root of the blade as an example, even for a 1/rev pitching motion, with a reduced frequency of around 0.15, the amplitude of the lift response has reduced by around one-fifth compared to the quasi-steady value. It is also clear that pitching at higher harmonics due to, for example, the blade torsion response will result in aerodynamic loads with a significant phase lead.

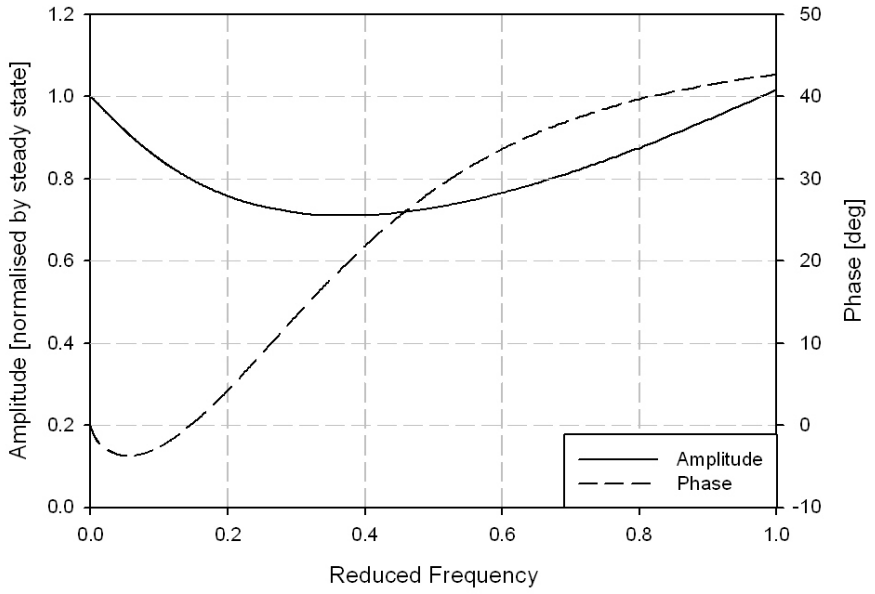

Figure 2.3: Lift response to a sinusoidal pitch oscillation as predicted by Theodorsen (1935).

Being in the frequency domain, Theodorsen's results are of limited use for rotorcraft analyses as the time-varying velocity in forward flight means that the reduced frequency is not well defined. A more useful derivation is that of Wagner (1925) who obtained the solution to the aerodynamic response of a thin aerofoil to a step change in angle of attack. Such a response is called the indicial response and the associated theory is often referred to as indicial aerodynamics. Wagner's (1925) result for the chordwise distribution of the pressure coefficient, in the notation of Leishman (2000), is:

$$\frac{\Delta C_p\left(\bar{x},s\right)}{\alpha} = \frac{4c}{V}\delta\left(t\right)\sqrt{\left(1-\bar{x}\right)\bar{x}} + 4\phi\left(s\right)\sqrt{\frac{1-\bar{x}}{\bar{x}}}\,. \qquad \textbf{2.17}$$

Alternatively, this can be expressed in the ψ domain as:

$$\frac{\Delta C_p\left(\psi,s\right)}{\alpha} = \frac{4c}{V}\delta\left(t\right)\frac{1}{2}\sin\psi + 4\phi\left(s\right)\cot\frac{\psi}{2}\,. \qquad \textbf{2.18}$$

The first term is the non-circulatory (apparent mass) contribution, which is again instantaneous and thus makes use of the Dirac delta function. The second term is the circulatory contribution which is written in terms of the function, ϕ, known as Wagner's function, which defines the growth of the circulatory response in terms of the non-dimensional time, s, defined as:

$$s = t\frac{2V}{c}. \qquad \textbf{2.19}$$

Note that as Wagner's function grows asymptotically to a value of 1 the final pressure distribution equals that given by the thin aerofoil theory of the previous section, see equation 2.1, where for zero camber and a simple angle of attack input, $A_0 = \alpha$ and $A_n = 0$ for n>0. Good approximations to Wagner's function, for example Jones (1940), can be obtained using formulas consisting of a number of exponential terms of the form:

$$\phi(s) \approx 1 - \sum_i A_i e^{-b_i s}\ . \qquad \textbf{2.20}$$

Such exponential forms enable the result to be more easily manipulated and approximations to Wagner's result can therefore be used, with the appropriate chordwise integration, to calculate the response of the lift and pitching moment coefficients to an arbitrary, time varying, angle of attack using Duhamel's integral; indeed, for a sinusoidal input, the use of Wagner's function will provide the same result as Theodorsen such that Theodorsen's function can in fact be written in terms of Wagner's function [see, for example, Fung (1955)].

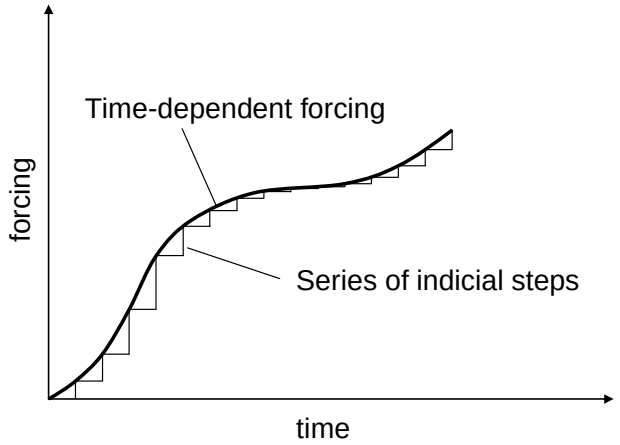

Figure 2.4: Representation of an arbitrary function by a series of step inputs.

Consider then an arbitrary, time-varying forcing given by:

$$\alpha(s) = \alpha(0) + \int_0^s \frac{d\alpha}{d\sigma}(\sigma)\, d\sigma\,. \qquad \textbf{2.21}$$

This may be rewritten as the superposition of a series of step functions, as illustrated in Figure 2.4, such that:

$$\alpha(s) = \alpha(0)1(s) + \int_0^s \frac{d\alpha}{d\sigma}(\sigma)1(s-\sigma)\,d\sigma \qquad \textbf{2.22}$$

where *1(s-σ)* is the unit step function. The response to a unit step input is referred to as the indicial admittance, which in this case is Wagner's function, and the circulatory response to this forcing may therefore be written as:

$$C_l(s) = 2\pi\left[\alpha(0)\phi(s) + \int_0^s \frac{d\alpha}{d\sigma}(\sigma)\phi(s-\sigma)\,d\sigma\right] = 2\pi\alpha_E\,. \qquad \textbf{2.23}$$

The term in brackets is Duhamel's integral and may be viewed as an equivalent forcing which is denoted with a subscript capital E. This forcing is an equivalent steady-state condition which returns the same instantaneous response. The use of exponential approximations for the indicial admittance means that the integration through time for the equivalent forcing may be obtained very efficiently with relatively large time steps using the recurrence solution method. The method, see, for example, Beddoes (1976) or Leishman (2000), consists of the instantaneous forcing minus the sum of some 'decrement' or 'deficiency' terms, one for each exponent term in the indicial response function (in this case the approximation to Wagner's function). The decrement terms are updated at each time step to account for the aerodynamic history according to:

$$\begin{aligned} \alpha_E(s) &= \alpha(s) - \sum_i D_i(s) \\ D_i(s) &= D_i(s-\Delta s)e^{-b_i\Delta s} + A_i\left(\alpha(s) - \alpha(s-\Delta s)\right)\sqrt{e^{-b_i\Delta s}}\,. \end{aligned} \qquad \textbf{2.24}$$

Although Wagner's result provides an analysis method to calculate the aerodynamic response to an arbitrary angle of attack variation, the boundary condition along the chordline will not necessarily be well represented by a simple angle of attack as the inflow to the blade will typically include both pitching and plunging motions and will often be highly non-uniform due to the influence of a closely passing vortex from a previous blade. Solutions for the response to particular examples of non-uniform inflow have been sought, such as Küssner's (1935) calculation of the response to a sharp-edged gust, however a methodology for the calculation of the response due to an arbitrary inflow distribution is provided by the reciprocal (or reverse flow) theorems. Heaslet and Spreiter (1952) state the theorem for lift as:

"The lift in steady or indicial motion of a wing having arbitrary twist and camber is equal to the integral over the planform of the product of the local angle of attack and the loading per unit angle of attack at the corresponding point of a flat-plate wing of identical planform in flight in the reverse direction".

For the two-dimensional case being considered here the theorem gives the result:

$$C_{l_1} = \int_2 \alpha_1 \left(\frac{\Delta C_{p_2}}{\alpha_2} \right) dx_2 \qquad \textbf{2.25}$$

where ΔC_{p_2} is the pressure distribution resulting from the angle of attack α_2, and α_1 defines the boundary condition (camber and inflow distribution) for which the lift coefficient is required. Wagner's result for the indicial response to angle of attack can therefore be used, along with the reverse flow theorem, to calculate the lift response for arbitrary boundary conditions containing non-uniform distributions of camber and inflow.

Thus, if a step change in the camber/inflow distribution is given by Δf_c, then $\alpha_1 = -\Delta f_c$ and from substitution of equation 2.17 into equation 2.25 the resulting response of the lift coefficient is given by:

$$\Delta C_l = -\frac{c}{V}\delta(t)\int_0^{\pi} \Delta f_c \sin^2\psi \, d\psi + 2\pi\varepsilon_0\phi(s). \qquad \textbf{2.26}$$

A similar reverse flow theorem, based on the pressure distribution due to a pitch rate perturbation, exists and therefore the pitching moment coefficient can be similarly calculated. Thus, for the incompressible case the unsteady aerodynamic loads can be calculated for an arbitrary inflow and camber-line variation.

2.2.3 Modifications for Compressibility

Unfortunately, an exact result for the entire indicial airload response in compressible flow does not exist. However, the asymptotic steady-state circulatory values can be calculated using linear theory, or in practice can be derived from experimental data, whilst the initial impulse values are given by piston theory, see Lomax (1952).

Unlike for incompressible flow, the finite sound speed means that the non-circulatory load is no longer an instantaneous impulse and the decay of this load must be modelled. This is done by replacing the Dirac delta function with an exponential decay using a

Mach-dependent time constant. Likewise, the compressibility of the fluid affects the growth of the circulatory loading and therefore Wagner's function is replaced by a Mach-dependent equivalent which is usually of the form:

$$\phi_C(s) = 1 - \sum_i A_i e^{-b_i \beta^2 s} \qquad \textbf{2.27}$$

where use has been made of the Prandtl-Glauert factor which is defined as:

$$\beta = \sqrt{1 - M^2} \ . \qquad \textbf{2.28}$$

The coefficients A_i and b_i are derived from experiment and higher-fidelity Computational Fluid Dynamics methods. Similarly the decay of the non-circulatory response is modelled by:

$$\phi_I(s) = e^{-s/T_I} \ . \qquad \textbf{2.29}$$

Here the time constant, T_I, can either be set according to experimental data or can be calculated based on the gradient of the initial response according to the exact linear theory of Lomax (1952). Such methods are discussed in detail by Leishman (1988, 2000), where separate time constants are derived for various forms of loading (camber-line boundary conditions) including pitch, pitch-rate and sharp-edged gusts using solutions obtained from the reverse flow theorems based on the exact linear theory of Lomax (1952). The various responses to the different sources of inflow can then be summed due to the principle of superposition.

2.2.4 Attached Flow Modelling in the Third Generation Model

The third generation model, however, attempts to account for a non-uniform inflow, which may arise due to an arbitrary motion and/or gust/vortex encounter, through numerical integration of the boundary condition. The asymptote for the circulatory response is calculated based on thin aerofoil theory. The lift and pitching moment coefficients were shown in section 2.2.1 to be dependent only upon the first three Fourier coefficients, A_0, A_1 and A_2. These coefficients are calculated by numerically integrating along the chord of the aerofoil whereby it is split into ten segments such that the size of each segment is equal in the ψ domain, i.e. $\Delta\psi=\pi/10$. The numerical integration is then used along with equations 2.9 and 2.10 to give the coefficients as:

$$A_0 = \frac{1}{\pi}\sum_{j=1}^{10}\left[\frac{\pi}{10}\times\mu_w\left(\psi_j\right)\right]$$
$$A_1 = \frac{2}{\pi}\sum_{j=1}^{10}\left[-\mu_w\left(\psi_j\right)\times\left(\sin\psi_{2,j}-\sin\psi_{1,j}\right)\right] \quad \textbf{2.30}$$
$$A_2 = \frac{2}{\pi}\sum_{j=1}^{10}\left[-\mu_w\left(\psi_j\right)\times\left(\tfrac{1}{2}\sin 2\psi_{2,j}-\tfrac{1}{2}\sin 2\psi_{1,j}\right)\right]$$

where $\psi_{j,}$ ψ_{1j} and ψ_{2j} are the values of ψ at the midpoint, beginning and end of segment j respectively and the inflow has been made non-dimensional by the freestream velocity:

$$\mu_w = w_w/V\ . \quad \textbf{2.31}$$

The thus calculated Fourier coefficients are then used to give the asymptotic values for the circulatory lift and pitching moment coefficients according to equation 2.12 along with appropriate compressibility corrections.

Now consider the impulsive, or non-circulatory, terms. These components are based around the compressible derivation by Lomax (1952) which gives the local pressure wave system resulting at the instant a perturbation is applied. The result to be used here is for the instantaneous difference in pressure coefficient across the aerofoil due to a step change in the inflow velocity:

$$\Delta C_p\left(\psi, s=0\right) = \left(\frac{4}{M}\right)\Delta\mu_w\left(\psi\right). \quad \textbf{2.32}$$

This uniform loading is only valid at the instant the perturbation is applied and the subsequent dissipation of the non-circulatory loading and growth of the circulatory loading leads to a complicated non-uniform and rapidly changing pressure distribution as the pressure perturbation propagates to and around the leading and trailing edges of the aerofoil. Leishman and Beddoes (1986) therefore hypothesised that the decay of the non-circulatory load should be given a weighting such that the load decays quicker at the leading and trailing edges and suggested a weighting given by $\sin\psi$. In the 3rd generation model this weighting is applied to the flow perturbation itself, thus being analogous to applying the reverse flow theorem in the incompressible case (equation 2.26). The 'exact' response to a step change in angle of attack has been calculated for the short time period [valid for non-dimensional time values of $0 \le s \le 2M/\left(1+M\right)$] by Lomax (1952) and the result may also be found in Leishman (2000). Therefore, to

investigate the validity of the weighting used in the 3rd generation model, the author has calculated numerically, for a range of Mach numbers, the average pressure distribution as calculated by Lomax (1952) over the time slice for which the exact result is valid. For each time step the modelled circulatory load has been subtracted such that the results approximate only the non-circulatory loading. The thus obtained average distributions are compared to the assumed form in Figure 2.5.

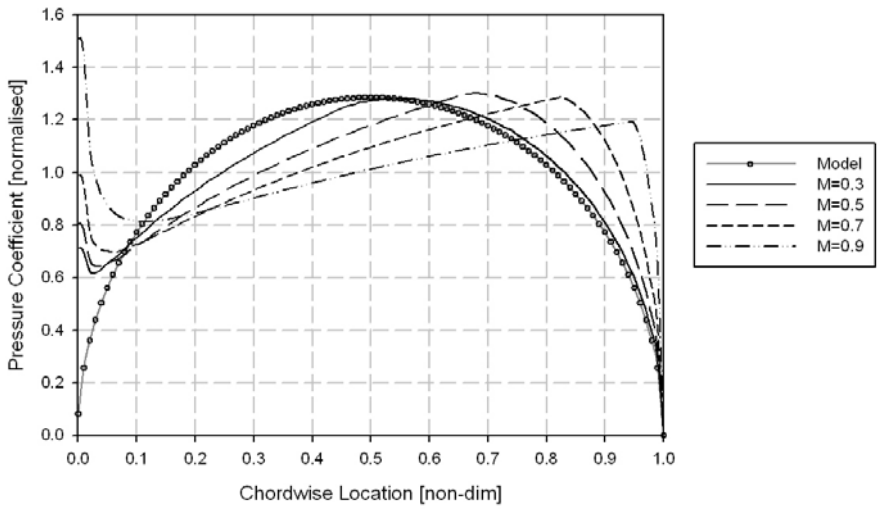

Figure 2.5: Comparison of time-averaged non-circulatory pressure distributions calculated by Lomax (1952) to the shape assumed in the Third Generation model.

Clearly the assumed form is most accurate for the lower Mach numbers which appear to be converging towards the analytical incompressible result and is less suited to higher Mach numbers but is still reasonable. The weighting for the pitching moment can be similarly obtained using the reverse flow theorems and this weighting is approximated in the 3rd generation model by $\frac{1}{4}\left(\sin 2\psi - \sin\psi\right)$. The comparison of this weighting to the time-averaged shape obtained from the solution of Lomax (1952) is shown in Figure 2.6 and again the approximation is reasonable over the Mach number range but particularly at low Mach numbers.

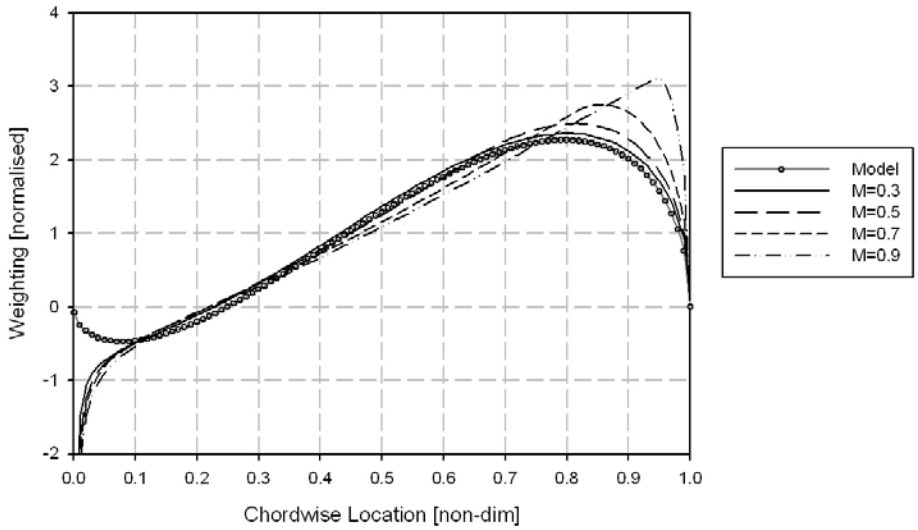

Figure 2.6: Comparison of time-averaged non-circulatory pitching moment weighting calculated by Lomax (1952) to the shape assumed in the Third Generation model.

Therefore, using the assumed average pressure distribution for the indicial response to angle of attack, the non-circulatory response to an arbitrary boundary condition can be obtained using the reverse flow theorems, with the resulting chordwise integrals again being evaluated numerically. The initial and final values of the response provided by the non-circulatory and circulatory contributions are then used with appropriate experimentally-derived indicial admittance functions to integrate the solution using the recurrence method, see Leishman and Beddoes (1986). The integration of the boundary condition therefore means that the same model and time constants are used regardless of the form of the forcing.

To demonstrate the accuracy of the approach, the author has used the model, albeit with the number of segments increased to 100 (as will be explained in Chapter 5), to predict the lift response to a blade-vortex interaction. The result is compared to that presented by Leishman (2000) using an Euler finite-difference method in Figure 2.7 from which the comparison is good, suggesting that the application of the 3rd generation model to the prediction of loads due to non-uniform inflow is justified and this, therefore, supports its use for the prediction of effects due to the arbitrary camber deflection shapes of Active Trailing Edges.

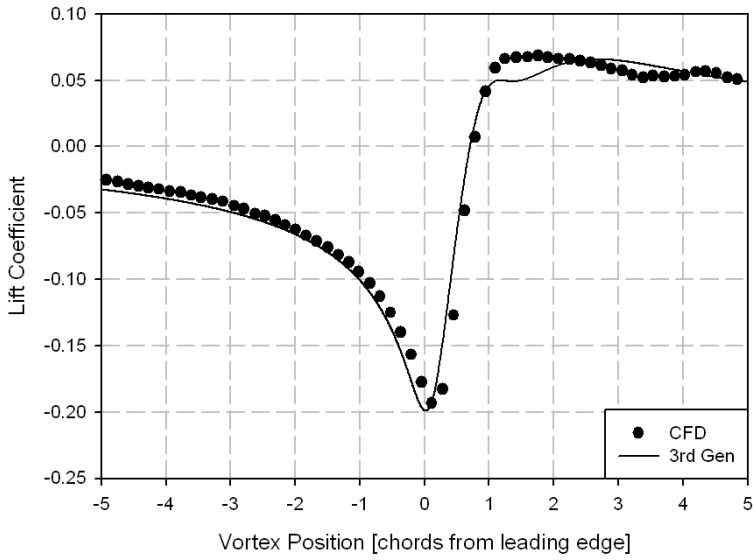

Figure 2.7: Third Generation model prediction of lift response during a blade-vortex interaction compared to the CFD (Euler) results presented by Leishman (2000). The case is for a Mach number of 0.65 and non-dimensional vortex strength of 0.2 located 0.26 chords below the aerofoil.

Thus far, only the lift and pitching moment coefficients have been mentioned. The pressure drag, however, is obtained through resolving the unsteady normal and chord force coefficients through the appropriate angle, as shown in Figure 2.8.

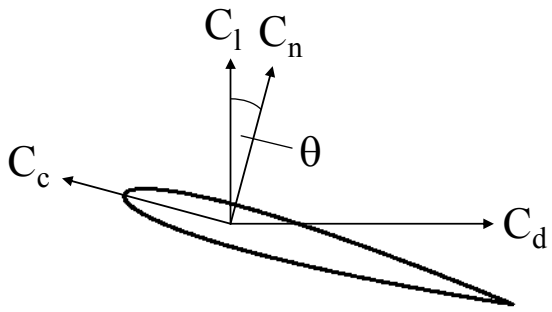

Figure 2.8: Resolution of normal and chord force coefficients into lift and drag coefficients.

Once the viscous drag coefficient, C_{d_0}, is added, the total drag coefficient may therefore be calculated as:

$$C_d = C_n \sin\theta - C_c \cos\theta + C_{d_0} . \qquad \textbf{2.33}$$

The unsteady chord force is estimated using the instantaneous equivalent angle of attack for the circulatory lift coefficient as:

$$C_c = \eta_d C_{l_c} \alpha_E \quad \textbf{2.34}$$

where α_E is the equivalent angle of attack, C_{l_c} is the circulatory component of the lift coefficient and η_d is an input coefficient for the non-ideal recovery of the leading edge pressure (typically given a value of approximately 0.95). See Leishman (1987) for more information of the derivation of the unsteady drag.

2.3 Unsteady Aerodynamics of Separating Flow

2.3.1 Characteristics of Dynamic Stall

The motion of an aerofoil or an unsteady inflow has an even greater influence if the aerofoil is passing in and out of stall as shown in Figure 2.9. In particular, in comparison to the quasi-static case, the delay in the reaction of the surrounding flow will cause the aerofoil to exhibit a lift overshoot whereby both the stall angle and the maximum lift coefficient are significantly increased. In addition, the generation and release of a vortex from the leading edge of the aerofoil has a significant influence, particularly over the pitching moment coefficient which shows a much larger nose-down (negative) value than observed in the static case.

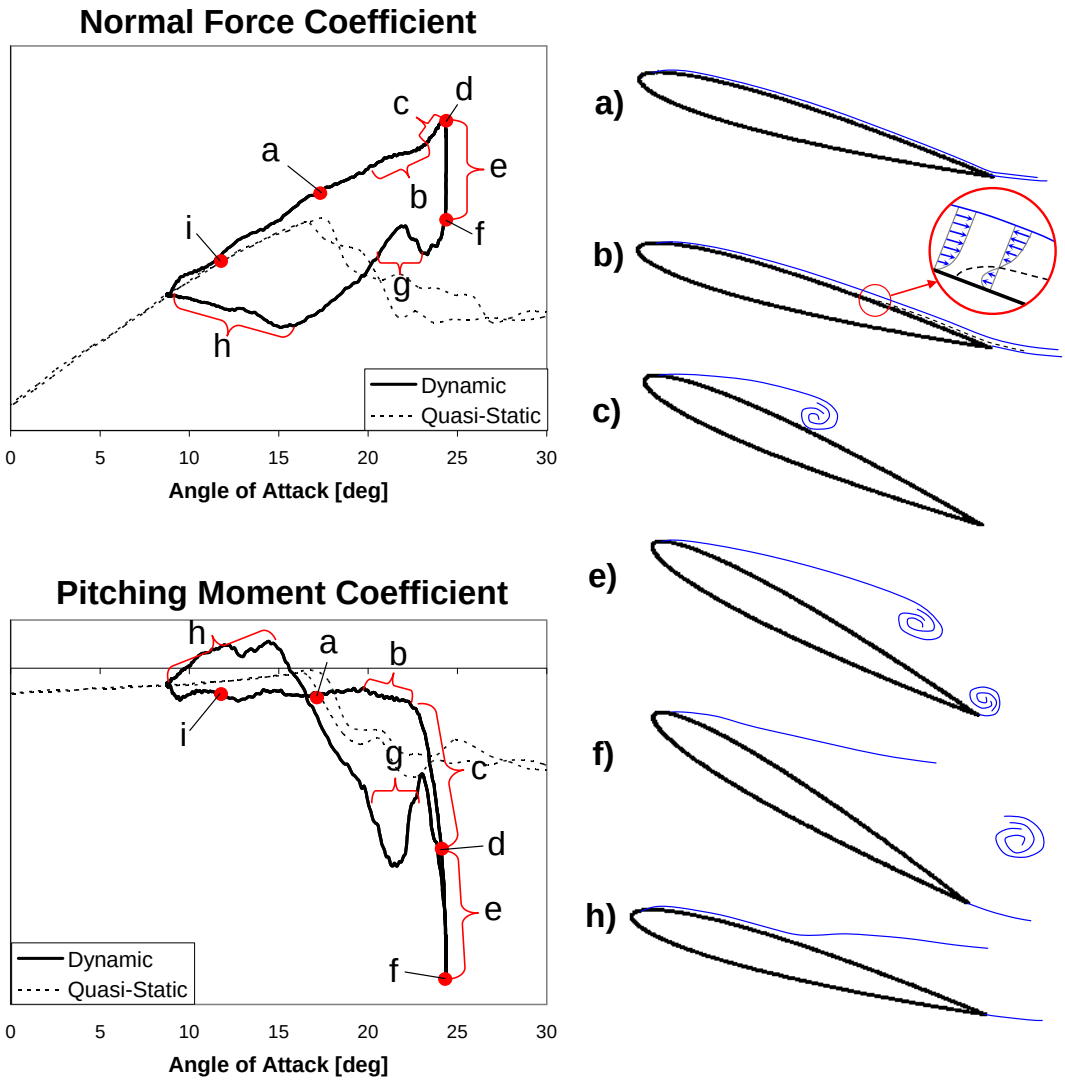

Figure 2.9: Dynamic stall features, description in main body of text. Based on Carr et al (1977) with modifications of Singh (2007).

The following discussion is based on that presented by Carr et al (1977) with modifications included by Singh (2007). The nature of dynamic stall can change considerably with the pitch rate, mean angle of attack and Mach number however the main features remain similar and are highlighted here as they are clearly reflected in the modelling methodology presented in the following section. The discussion here will also help to explain the main features observed in the Air Jet Vortex Generator data, the modelling of which is presented in the next chapter. Note that the letters in *Italic* in the following text refer to the labels of Figure 2.9.

As the aerofoil passes up through the static stall angle of attack, *a*, the flow remains attached and the lift coefficient continues to follow the attached flow lift slope. As the angle of attack continues to increase, the boundary layer begins to react and a region of flow reversal is initiated at the trailing edge and grows upstream towards the leading

edge, *b*, until it eventually covers the entire upper surface of the aerofoil. The reverse flow region, however, is only observed over a thin layer near the surface and the effect on the normal force and pitching moment is minimal.

As the angle of attack increases further a vortex, referred to as the Dynamic Stall Vortex (DSV), begins to form near the leading edge of the aerofoil. Shortly prior to stall a peak in the suction near the leading edge is reached before the commencement of dynamic stall is defined by the collapse of this leading pressure peak and the dynamic stall vortex begins to move downstream, *c*. As the vortex migrates downstream it increases in strength and this can cause the lift to increase at a greater rate. The motion of the vortex also causes the pressure distribution to change sufficiently to cause an increasingly nose-down pitching moment thus defining the point of moment divergence (or moment stall).

The lift begins to decrease when a significant portion of the flow has separated from the aerofoil and the peak in lift, *d*, occurs when the vortex is at approximately the mid-span location, thus defining the point of lift divergence (or lift stall). As the vortex continues to move downstream, *e*, the nose-down pitching moment continues to increase. Feszty et al (2003) suggest that the suction of the DSV can also cause the formation of a trailing edge vortex (TEV) due to flow from the high pressure lower surface and that the TEV contributes to the nose-down pitching moment before it is shed along with the DSV. In any case, the maximum nose-down pitching moment is obtained when the DSV is approximately at the trailing edge and full stall is encountered as the DSV is shed from the aerofoil, *f*. Following this, secondary, and even tertiary, vortices may be formed and shed from the leading edge giving further, but weaker, oscillations in the lift and pitching moment, *g*.

Reattachment, *h*, begins during the down-stroke once the aerofoil has passed below the static stall angle of attack. The reattachment process is slow and the flow only returns to nominally attached flow conditions once the aerofoil is well into the up-stroke, *i*.

In summary, the loads associated with a dynamically pitching aerofoil are significantly different to those generated in the quasi-static case. The finite time taken for the flow to react to the motion of the aerofoil means that the separation of the boundary layer is significantly delayed and a large overshoot in lift results. The characteristics of the loads are also clearly dominated by the generation of the Dynamic Stall Vortex, particularly the pitching moment which shows a large nose-down value which is far in excess of that seen in the quasi-static case. These features must be modelled if the performance of a

helicopter rotor is to be adequately predicted. The theory behind one such method will therefore be presented in the following section as it will be adapted to account for the influence of the active technology.

2.3.2 Modelling Flow Separation

The Third Generation dynamic stall model is conceptually very similar to that of the Second Generation model presented by Leishman and Beddoes (1986, 1989). The following outline of the theory is therefore based on these references; however minor alterations made for the Third Generation model are also included. The model is semi-empirical in nature and therefore depends heavily on experimentally-derived, Mach dependent coefficients, as will become clear below.

For a static aerofoil, the lift coefficient reduces as flow separation occurs from a location which starts at the trailing edge and moves upstream as the angle of attack is increased. The effect on the lift coefficient may be approximated using Kirchoff's approximations which apply a factor to the attached-flow value based on the flow separation location. Leishman and Beddoes (1989) approximate the separation point in the static case using formulas of exponential form. In the Third Generation model, the formulas have been slightly altered such that the separation point, f, is equal to 0.6 when the aerofoil is at the stall angle of attack α_1. The separation location (non-dimensional, with respect to blade chord) is therefore given by:

$$\begin{aligned} \alpha \le \alpha_1 \Rightarrow f &= 1 - 0.4\exp\left(\frac{\alpha - \alpha_1}{S_1}\right) \\ \alpha > \alpha_1 \Rightarrow f &= 0.02 + 0.58\exp\left(\frac{\alpha_1 - \alpha}{S_2}\right) \end{aligned} \qquad \textbf{2.35}$$

where α_1, S_1 and S_2 are empirical, Mach dependent values for the given aerofoil. Note that the validity of these equations, with respect to both the clean aerofoil and one equipped with air jet vortex generators, will be discussed in the next chapter.

According to Kirchoff, the normal force coefficient may then be approximated by:

$$C_{n_C} = C_{n_{C,US}} \times \frac{1}{4}\left(1 + \sqrt{f}\right)^2 = C_{n_{C,US}} K_f \qquad \textbf{2.36}$$

where the subscript *US* denotes the un-separated value resulting from the attached flow calculations described in the previous section. Leishman and Beddoes (1989) also suggested empirically derived formulas for the variation of the centre of pressure and chord force coefficient with the separation location. These formulas have since been modified such that in the Third Generation model the centre of pressure location is given by:

$$C_{pres} = \frac{C_{m_C}}{C_{n_C}} = K_0 + K_1\left(1 - f^{K_{1,\exp}}\right) + K_2\left(f - M_{bp}\right)\exp\left[\frac{-\left(f - M_{bp}\right)^2}{M_{f,\exp}}\right] \qquad \textbf{2.37}$$

and the chord force coefficient is given by:

$$C_c = C_{c_{US}}\left(1 - 0.8\frac{C_{pres}}{C_{pres,0}}\right)K_f^{1.5} \qquad \textbf{2.38}$$

where:

$$C_{pres,0} = K_0 + K_1 + K_2\left(f - M_{bp}\right)\exp\left[\frac{-\left(f - M_{bp}\right)^2}{M_{f,\exp}}\right]. \qquad \textbf{2.39}$$

The coefficients K_0, K_1, K_2, $K_{1,exp}$, $M_{f,exp}$ and M_{bp} are empirical, Mach dependent inputs for the given aerofoil and are set to obtain the best possible representation of the stall characteristics in steady-state conditions.

However, in unsteady conditions the occurrence of stall, and the variation of the separation location, is progressively delayed as the rate of change of the forcing increases. This delay in separation must therefore be accounted for in the model. From unsteady pitching experiments, it has been observed that a rate-independent criterion for dynamic stall (associated with the detachment of the Dynamic Stall Vortex) is provided by the attainment of a critical value of pressure near the leading edge of the aerofoil; see Leishman and Beddoes (1989). Furthermore, the attainment of this pressure peak was seen to lag behind the peak in the normal force coefficient, with the lag varying approximately linearly with the pitch rate. The onset of stall can therefore be modelled by applying a first order lag to the normal force coefficient and comparing the obtained value to a critical value of normal force denoted by C_{n_1}. The lag is applied using the recurrence solution to Duhamel's integral, in a similar way to the attached flow response, such that a decrement is calculated and subtracted from the instantaneous value at each

time step. The onset of dynamic stall therefore occurs when $C_n' > C_{n_1}$ where the pressure lagged value for the normal force coefficient is given by:

$$C_n' = C_{n_{US}} - D_P(s)$$
$$D_P(s) = D_P(s-\Delta s)\exp\left(\frac{-\Delta s}{T_P}\right) + \left(C_{n_{US}}(s) - C_{n_{US}}(s-\Delta s)\right)\sqrt{\exp\left(\frac{-\Delta s}{T_P}\right)}. \quad \textbf{2.40}$$

Furthermore, if it is assumed that the trailing edge separation location is similarly affected by this pressure lag (this will be justified below) then an equivalent, pressure lagged, angle of attack may be defined as: $\alpha' = C_n' / C_{l_\alpha}$

$$\alpha' = C_n' / C_{l_\alpha}. \quad \textbf{2.41}$$

This lagged angle of attack may then be used instead of the instantaneous value in equation 2.35 to give a pressure lagged separation point denoted by f'.

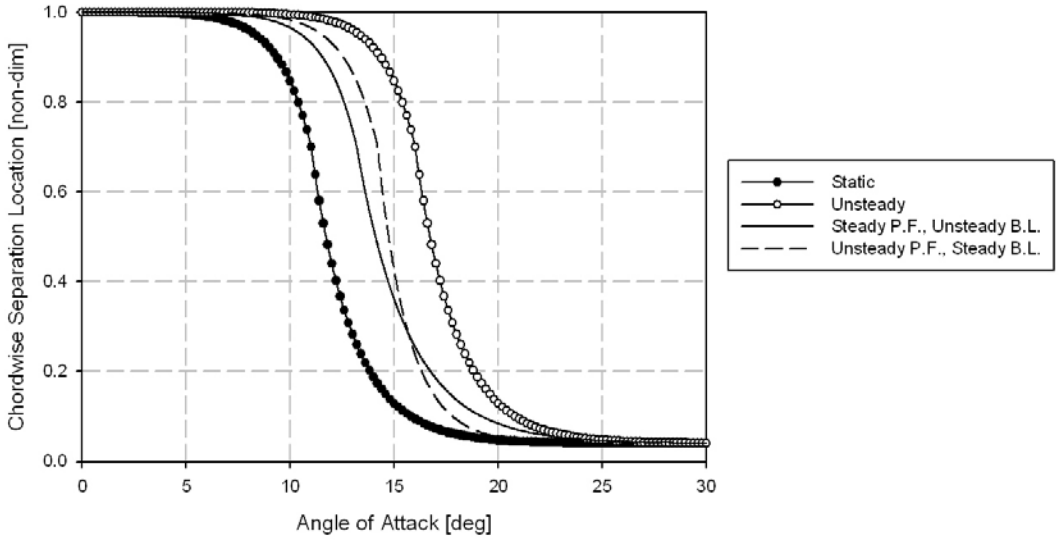

Figure 2.10: Sketch demonstrating cumulative effects on separation location due to pressure lag (predicted by unsteady potential flow, P.F.) and boundary layer lag (predicted by unsteady boundary layer, B.L.) as calculated by Scruggs (1974).

Experiments reveal, however, that the pressure lag alone is insufficient to account for the lag in the separation location. A coupled potential flow-boundary layer code, Scruggs (1974), has been used to investigate, independently, the effects due to the unsteady potential solution and the unsteady boundary layer. These results were used by Leishman and Beddoes (1986) to show that the above methodology accounted for the lag due to the pressure distribution as predicted by the potential flow solution but that a further lag is

required to account for the additional effect of the boundary layer which in turn lags behind the pressure distribution, as shown in Figure 2.10. The resulting effect on the boundary layer separation location is accounted for in the model by applying a further first order lag such that:

$$f'' = f' - D_F \qquad \textbf{2.42}$$

where D_F is a decrement term with time constant T_F calculated in the same way as D_P (see equation 2.40).

The pressure- and boundary layer-lagged separation location could now be substituted into the steady-state formulas for the loading coefficients to obtain the unsteady loading coefficients. This, however, would only account for the effects due to trailing edge separation, whereas the stall characteristics in the unsteady case are dominated by the presence of the Dynamic Stall Vortex (DSV) which is built up and then released from the leading edge, as discussed in the previous section.

The additional lift and pitching moment due to the vortex is accounted for in the Third Generation model using further modifications to the separation location, with separate adjustments being made to the normal force and pitching moment values. In the case of the normal force coefficient, the value of f'' is increased to synthesise a delay in separation whilst for the pitching moment f'' is decreased to provide the nose-down pitching moment associated with the DSV. It has been found from experiment that the non-dimensional time, T_{VL}, taken for the vortex to travel from the leading edge to the trailing edge is mostly independent of aerofoil and Mach number and that the build-up and release of further vortices (secondary and tertiary vortex shedding) is governed by a similar time scale. Therefore a DSV influence parameter, V_x, is defined using a sinusoidal form, based on the ratio of a non-dimensional time counter s_v (started when the stall onset criterion is met) and the time constant T_{VL}:

$$\begin{aligned} s_v = 0 &\Rightarrow V_x = 0 \\ s_v \le T_V &\Rightarrow V_x = \left[\sin\left(\tfrac{\pi}{2}\left(s_v/T_V\right)\right)\right]^{1.5} \\ s_v > T_V &\Rightarrow V_x = \left[\cos\left(\pi\left(s_v - T_V\right)/T_{VL}\right)\right]^2 . \end{aligned} \qquad \textbf{2.43}$$

This sinusoidal form accounts for not only the primary DSV but also any secondary or tertiary shed vorticies. Note that additional flexibility is provided in the model for the build-up time of the first DSV using the time constant T_V. Clearly however, in the static case, the DSV is not present, whilst its strength grows as the pitch rate is increased. Also, the strength diminishes with each shed vortex. To account for this behaviour, the modifications to the separation locations are made in proportion to $f'' - f'$, i.e. proportional to the effect of the boundary-layer lag, which increases with pitch rate. This value also tends to zero as the aerofoil either becomes fully stalled or starts to decrease in incidence, at which point the modifications due to the stall vortices are stopped. With the inclusion of separate factors, B_1 and B_2, for the normal force and pitching moment effects, the modifications to the separation locations used in the normal force and pitching moment calculations are therefore given by:

$$\begin{aligned} f_n'' &= f'' + B_n\left(f'' - f'\right)V_x \\ f_m'' &= f'' - B_m\left(f'' - f'\right)V_x . \end{aligned} \qquad \textbf{2.44}$$

Incorporating these corrections gives the final circulatory airload coefficients, including unsteady trailing- and leading-edge separation effects as:

$$\begin{aligned} C_{n_C} &= C_{n_{C,US}} \times 0.25\left(1+\sqrt{f_n''}\right)^2 = C_{n_{C,US}} K_f \\ C_{pres} &= K_0 + K_1\left(1 - f_m''^{K_{1,\exp}}\right) \\ &\quad + K_2\left(f_m'' - M_{bp}\right)\exp\left[\frac{-\left(f_m'' - M_{bp}\right)^2}{M_{f,\exp}}\right] \\ C_{pres,0} &= K_0 + K_1 \\ &\quad + K_2\left(f_m'' - M_{bp}\right)\exp\left[\frac{-\left(f_m'' - M_{bp}\right)^2}{M_{f,\exp}}\right] \\ C_c &= C_{c_{US}}\left(1 - 0.8\frac{C_{pres}}{C_{pres,0}}\right)K_f^{1.5} . \end{aligned} \qquad \textbf{2.45}$$

Finally, the total coefficients are found through the summation of the circulatory and impulsive (non-circulatory) components, which are assumed to be unaffected by flow separation, such that the output of the model is given by:

$$C_n = C_{n_C} + C_{n_I} \qquad \textbf{2.46}$$

$$C_m = C_{n_C} C_{pres} + C_{m_I}$$
$$C_d = C_{n_C} \sin\theta - C_c \cos\theta + C_{d_0} .$$

This outline has provided an overview of the theory; however in practice the model includes various other empirical corrections, including adjustments to the time constants at various stages of the cycle. In particular, the value of α_1 is altered for decreasing incidence to delay reattachment and a separate value of f'' for the calculation of the pitching moment is added so that it is not affected by empirical corrections to the normal force value. Many such corrections are discussed by Leishman and Beddoes (1986).

2.4 Chapter Summary

An introduction to unsteady aerodynamics has been provided. In particular, the capability of the Third Generation model, of which use is to be made in the modelling of the active devices, to predict the unsteady airload response to an arbitrary change in the chordline boundary condition has been demonstrated. This gives confidence in the application of the method to the modelling of effects due to Active Trailing Edges. The main flow separation features associated with dynamically pitching aerofoils have also been briefly discussed and the theory behind a model developed to predict such effects has been presented in some detail. The model has been demonstrated to explicitly include effects due to trailing edge separation which the literature has shown to be heavily influenced by the operation of Air Jet Vortex Generators. In the following chapters, adaptations to the model will be used to approximate the effects due to the active rotor technologies such that their operational utility, in the context of a conventional rotorcraft, can be assessed.

Chapter 3 Air Jet Vortex Generators

3.1 Overview

In this chapter, the feasibility of using Air Jet Vortex Generators (AJVGs) to enhance the capability of an advanced helicopter rotor will be considered. The literature has revealed that extensive experimental and numerical investigations into the effects due to AJVGs on the aerodynamic performance of 2-dimensional aerofoils have been performed. The results of these tests confirm that both static and dynamic stall can be delayed considerably using arrays of jets positioned near the leading edge of the aerofoil. Little has been done, however, in the analysis of the advantage provided to a rotor system as a whole due to the enhanced stall characteristics. This chapter therefore seeks to quantify the merits of the system such that the operational utility of AJVGs can be assessed. In order to perform this task, an efficient method for the approximation of the aerodynamic effects due to AJVGs is required. The first half of this chapter will present the modifications made to the indicial aerodynamics model in order capture the effects due to AJVGs. Following this, the new model will be used in a critical analysis of the suitability of AJVGs for enhancing the capability of the main rotor of a modern helicopter.

3.2 Steady State Modelling of Air Jet Vortex Generators

Various analytical models for the effects due to unsteady aerodynamics, and dynamic stall in particular, have been developed over the past decades for the clean aerofoil. An implementation of one such model, the 3rd generation method [Beddoes (1991)], was readily available to the author and therefore the method for capturing effects due to AJVGs has been based on this model. As discussed in the previous chapter, this method explicitly models the dynamics of the trailing edge separation which the AJVGs are predominantly influencing through interaction with the boundary layer and is therefore ideally suited to the purpose.

The adequacy of the existing methodology for the modelling of the integrated airload coefficients (lift, drag and pitching moment) in the static case will first be considered. In particular the model must provide sufficient flexibility to capture the subtle differences in the movement of the trailing edge location with and without the AJVGs in operation. One immediately identified limitation of the model is that the force and moment coefficients are dependent upon the separation location alone. This means that the method explicitly assumes that the pressure distribution and the resulting integrated airloads are independent of angle of attack unless at least some trailing edge separation has occurred. Additionally, it is assumed that the relation between the normal force

coefficient and the trailing edge separation location is independent of both the aerofoil shape and the Mach number. In reality, as will be demonstrated below, these assumptions are unreasonable and the result is that the model gives poor results for the static coefficients of even the basic aerofoil and has been found to be totally inadequate for an aerofoil equipped with AJVGs.

This section therefore introduces a method which incorporates the angle of attack dependent coefficients of the first generation model into the third generation model which is coupled with a new model for the relation between the integrated airloads and the separation location. The modelling of the separation location itself has also been altered as the smooth profiles used in the existing model could not adequately represent the profiles observed during static aerofoil tests of the AJVGs carried out at City University, Prince (2008). The new model is based on observations from experimental results of tests performed at the University of Glasgow and City University [Coton (2008), Prince (2008)] and although developed primarily to capture the effects due to AJVGs it also improves the basic aerofoil modelling. Note that the experimental results used throughout this dissertation are for an AJVG array with jets pitched at 30 degrees and skewed at 60 degrees operated with a pulsing frequency of 71Hz and a duty cycle of 50%; Prince (2008).

3.2.1 Separation Location Model

The results from the static tests displayed trailing edge separation characteristics which could not be adequately represented using the existing equations (see Figure 3.1) and therefore these have been replace by a set of superimposed polynomials. The separation location is therefore given by:

$$
\begin{aligned}
&f = 1 \\
&\alpha > \alpha_{f_1} \rightarrow f = f + K_{f_1}\left(\alpha - \alpha_{f_1}\right) + K_{f_2}\left(\alpha - \alpha_{f_1}\right)^2 \\
&\alpha > \alpha_{f_2} \rightarrow f = f + K_{f_3}\left(\alpha - \alpha_{f_2}\right) + K_{f_4}\left(\alpha - \alpha_{f_2}\right)^2 \\
&\alpha > \alpha_{f_3} \rightarrow f = f + K_{f_5}\left(\alpha - \alpha_{f_3}\right) + K_{f_6}\left(\alpha - \alpha_{f_3}\right)^2
\end{aligned}
\qquad \textbf{3.1}
$$

where $K_{f_{1-3}}$ and $\alpha_{f_{1-3}}$ are Mach and aerofoil dependent constants. Superimposing the polynomials in this way ensures that the efficient interpolation between Mach number and aerofoil is maintained. Note that, for simplicity, throughout this section of the dissertation the symbol α is used throughout. In reality this may be replaced by $\left|\alpha - \alpha_0\right|$

, where α_0 is the zero-lift angle, to account for aerofoil camber and negative pitch angles (such that the coefficients would be multiplied by the appropriate sign for positive or negative pitch).

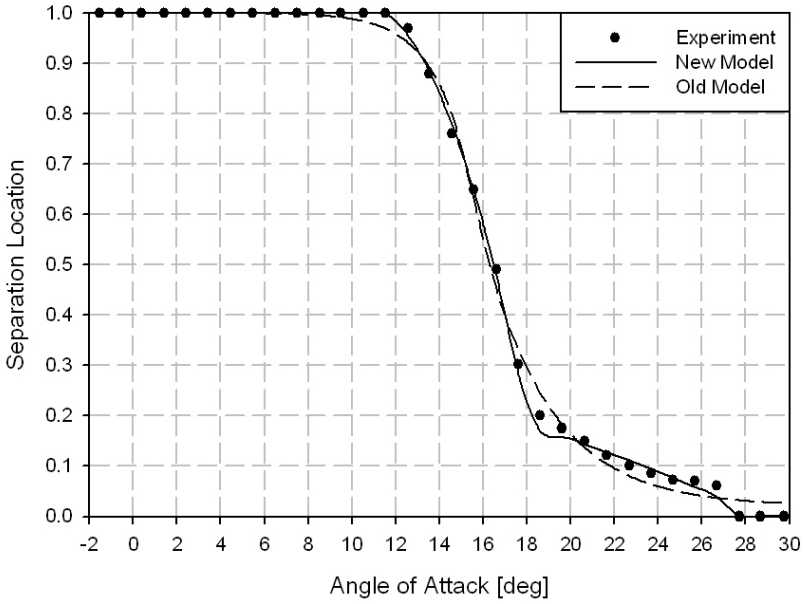

Figure 3.1: Separation Location prediction by Old and New Models.

A comparison of the prediction of the separation location by the old and new models is shown in Figure 3.1. The experimental data is from the wind tunnel tests at City University, Prince (2008) of the RAE 9645 aerofoil without AJVGs. The new model proposed here is clearly an improvement. In particular, note that the flow is fully attached until almost 12 degrees. The fact that the old model does not capture this was found to have a large effect on the pitching moment prediction. Also note that the flow stays partially attached until a sudden forward movement at around 27 degrees. This effect is also much better captured with the new model and again was found to influence the overall airload prediction.

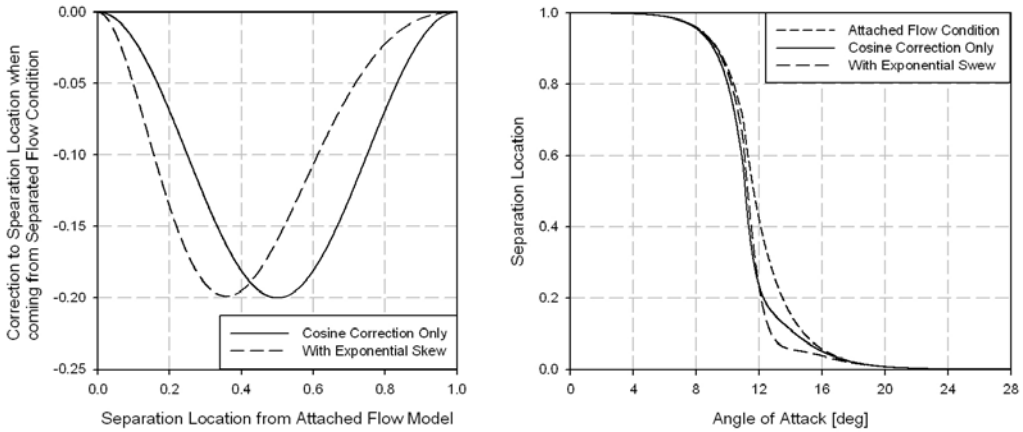

Figure 3.2: Correction to Separation Location Applied when Returning from a Separated Flow Condition showing the correction (left) and the overall effect against angle of attack (right).

With the operation of air jet vortex generators the trailing edge separation location displayed a large amount of hysteresis. If the aerofoil is brought from a separated flow state to the desired angle of attack then the separation location has been observed to be further forward than if the aerofoil was brought from an attached flow condition. A correction, which is applied only when the aerofoil is returning from a separated state, has therefore been devised. When either fully attached or fully separated the correction must be equal to zero, and to ensure a smooth curve the derivative of the correction should also be zero at these points. The correction may therefore be given the form:

$$f = f + K_{fd_1}\left[\cos\left(2\pi\left(1-f\right)\right)-1\right] \qquad \textbf{3.2}$$

where K_{fd_1} is a constant. This correction is demonstrated in Figure 3.2 for $K_{fd_1} = -0.2$. This form implies that the greatest correction is applied when $f = 0.5$, however the wind tunnel results suggested that the hysteresis effect is generally more prominent for small amounts of separation and therefore a 'skew' was applied using an exponential weighting such that the correction became:

$$f = f + K_{fd_1}\left[\cos\left(2\pi\left(1-f\right)\right)-1\right]\exp\left(K_{fd_2}\left(1-f\right)\right). \qquad \textbf{3.3}$$

Note that if this correction results in $f < 0$ then the separation location is set to zero. The overall effect is shown in Figure 3.2.

3.2.2 Separation Independent Model

The 1st generation model of Beddoes (1976) incorporates empirical relations for the variation of the pitching moment and drag coefficients up until stall. The models are of a form such that they incorporate Mach number and aerofoil dependent coefficients which may be interpolated to ensure continuity between Mach number and also allow for interpolation between two aerofoil sections such that portions of a blade which are being blended between two known aerofoil sections may be modelled. In order to improve the prediction of pre-stall airload coefficients by the 3rd generation model, it is proposed that 1st generation style empirical relations are reinstated.

Consider first the pitching moment model. A pitching moment angle of attack, α_{m_1}, is defined by:

$$\begin{aligned} |\alpha| \le \alpha_1 &\rightarrow \alpha_{m_1} = |\alpha| \\ |\alpha| > \alpha_1 &\rightarrow \alpha_{m_1} = \alpha_1 \end{aligned} \qquad \textbf{3.4}$$

and a second angle of attack, α_{m_2}, is defined by:

$$\begin{aligned} \alpha_{m_1} \le K_{m_1} &\rightarrow \alpha_{m_2} = 0 \\ \alpha_{m_1} > K_{m_1} &\rightarrow \alpha_{m_2} = \alpha_{m_1} - K_{m_1} \end{aligned} \qquad \textbf{3.5}$$

where K_{m_1} is one of the Mach and aerofoil dependent constants. The resulting pitching moment including the zero-lift value is then given by:

$$\begin{aligned} s_{sep} > 1.9 &\rightarrow C_m = C_{m_0} \\ s_{sep} \le 1.9 &\rightarrow C_m = K_{m_2}\alpha_{m_1} + K_{m_3}\alpha_{m_2}^2 + C_{m_0} \end{aligned} \qquad \textbf{3.6}$$

where s_{sep} is the non-dimensional separation time started when $\alpha > \alpha_1$. The proposed modification to the 3rd generation model is to apply this same model to account for variations in the pitching moment up to the onset of trailing edge separation. The model is kept the same such that the coefficients used in the first generation model may be used, however, in order to merge the model with the separation dependent variation; the author has replaced the use of s_{sep} with the square of the separation location such that the un-separated pitching moment coefficient at low angles of attack is given by:

$$C_{m_{C,US}} = \left(K_{m_2}\alpha_{m_1} + K_{m_3}\alpha_{m_2}^2\right)f^2 + C_{m_0} \quad \textbf{3.7}$$

where f is the trailing edge separation location.

Models have also been introduced for the variation of the normal and chord force coefficients prior to trailing edge separation onset. In the 1st generation model, the drag coefficient rather than the chord force coefficient is explicitly modelled and so the old model cannot be directly applied as for the pitching moment coefficient. The forms used for the empirical variations, therefore, are simple second order polynomials. As the separation dependent modelling supersedes the model at higher angles of attack this was found to be adequate. (The results presented later in this chapter should justify this statement). The use of single polynomials also ensures that an interpolation of the coefficients is possible. The models for the variation of the un-separated normal and chord force coefficients at low angles of attack are therefore given by:

$$C_{n_{C,US}} = \left(K_{n_1} + K_{n_2}\alpha + K_{n_3}\alpha^2\right)f^2 \quad \textbf{3.8}$$

$$C_{c_{US}} = \left(K_{c_1} + K_{c_2}\alpha + K_{c_3}\alpha^2\right)f^2. \quad \textbf{3.9}$$

The use of the new pre-stall model will now be demonstrated using the City University wind tunnel results [Prince (2008)] for a clean (no AJVGs) RAE9645 aerofoil. For fitting to the experimental results, each data point is multiplied by the value of f^2 relevant for that angle of attack and then the coefficients of equations 3.7, 3.8 and 3.9 may be found using a standard technique such as least squares fitting.

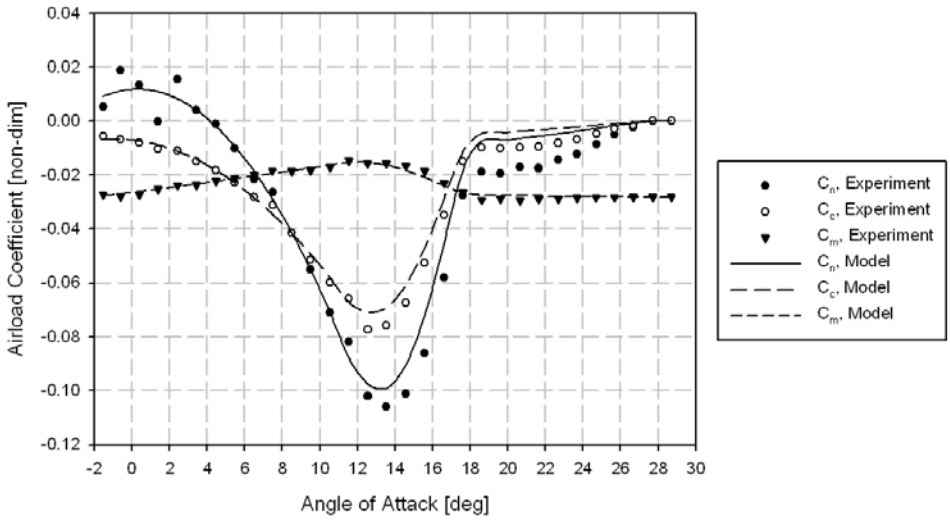

Figure 3.3: Prediction of Separation Independent Coefficient Change

Fitting of the coefficients for the RAE 9645 aerofoil is shown in Figure 3.3. Note how the coefficients rapidly decrease after 12 degrees as the separation model (see following section) is expected to take over.

3.2.3 Prediction by Old Model of Effects due to Separation

The separation behaviour in the static tests at City University will now be compared to that predicted using the existing 3rd generation model such that the deficiencies can be highlighted. The dependence of the circulatory normal force coefficient on trailing edge separation for a static aerofoil is given by the model as:

$$C_n = K_f C_{n_{C,US}}$$
$$K_f = \frac{1}{4}\left(1+\sqrt{f}\right)^2 . \qquad \textbf{3.10}$$

The response, K_f, due to the separation location is therefore independent of both Mach number and aerofoil. Figure 3.4 plots the experimental normal force data as well as that predicted by equation 3.10 using the experimental separation location.

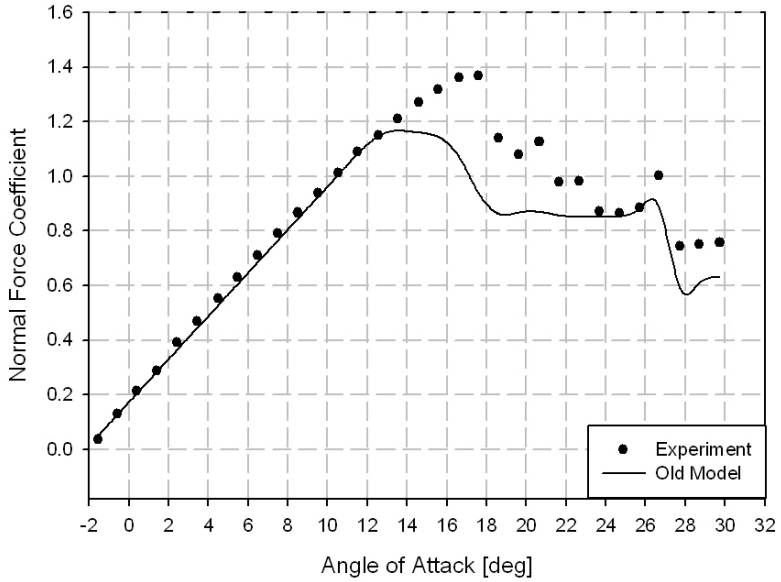

Figure 3.4: Old model Prediction of Normal Force Coefficient

Clearly the stall prediction is early as the normal force predicted by the model reduces at a lower angle of attack than the experimental data. Dividing the normal force by the un-separated value and plotting against the separation location results in Figure 3.5.

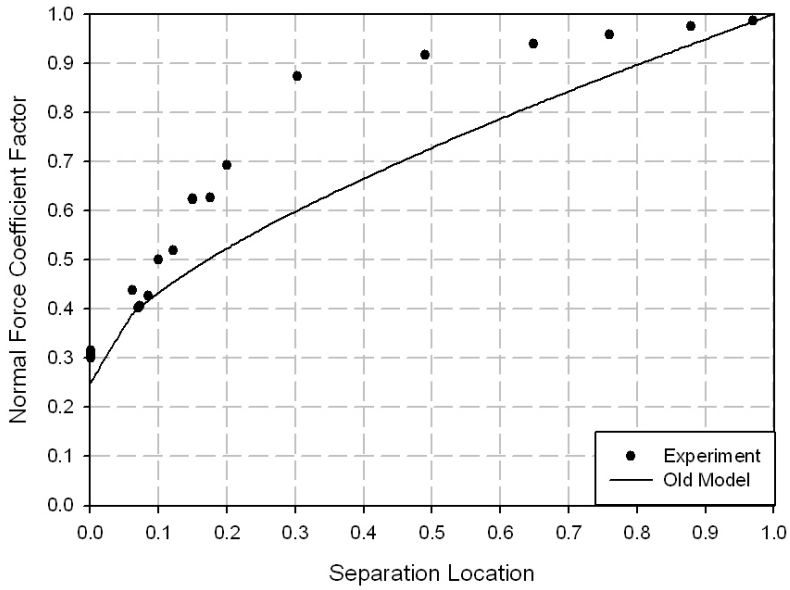

Figure 3.5: Old Model Prediction of Normal Force Coefficient Factor

The factor applied to the normal force due to trailing edge separation location is clearly well predicted once the flow is fully separated. However the model significantly under-predicts the normal force when the separation location is at approximately 30%. In other words, for this particular aerofoil and Mach number combination, the experiment shows that lift is maintained for much larger amounts of separation than the model predicts.

Now let us consider the chord force which is given in the static case by the 3rd generation model as (see chapter 2):

$$C_c = C_{c_{US}} \left(1 - 0.8 \frac{C_{pres}}{C_{pres,0}} \right) K_f^{1.5} . \qquad \textbf{3.11}$$

Figure 3.6 shows results using this model against the experimental data. Experimental values for K_f and C_{pres} are used in this equation along with an appropriate value for η_d.

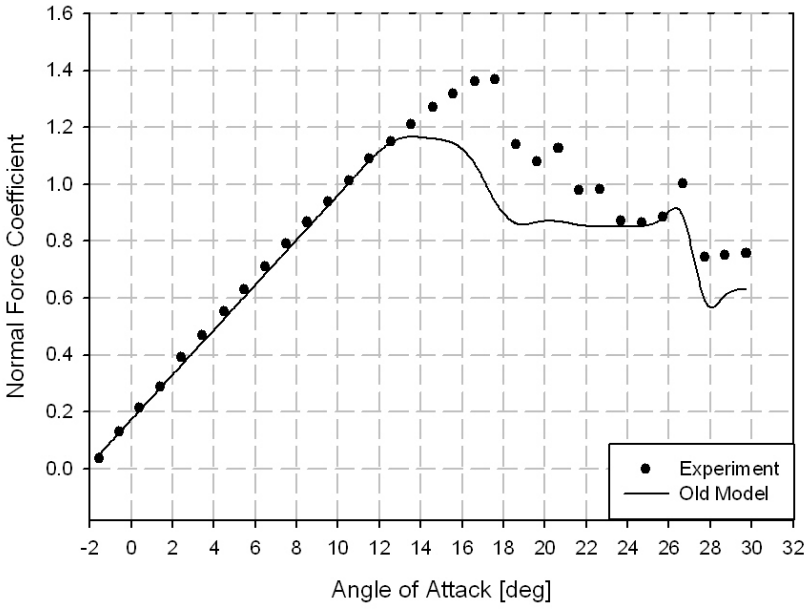

Figure 3.6: Old model prediction of Chord Force Coefficient

Clearly the stall is again predicted to occur too early due to the dependence on the factor K_f. Once again dividing the data by the un-separated value and plotting against the separation location results in Figure 3.7. From this figure it is clear that the pressure chord force, as well as the normal force, is maintained for greater amounts of separation than is predicted by the model.

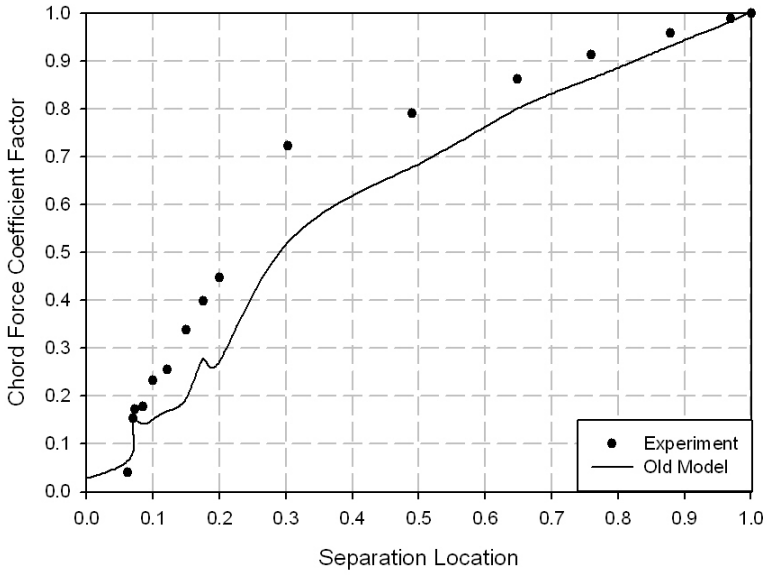

Figure 3.7: Old Model Prediction of Chord Force Coefficient Factor

Recall the equation used by the existing model for the centre of pressure location:

$$C_{pres} = K_0 + K_1\left(1 - f^{K_{1,\exp}}\right) + K_2\left(f - M_{bp}\right)\exp\left[\frac{-\left(f - M_{bp}\right)^2}{M_{f,\exp}}\right]. \qquad \textbf{3.12}$$

Performing a best fit for the various input parameters of this equation against the experimental test data and plotting the results against the separation location results in Figure 3.8.

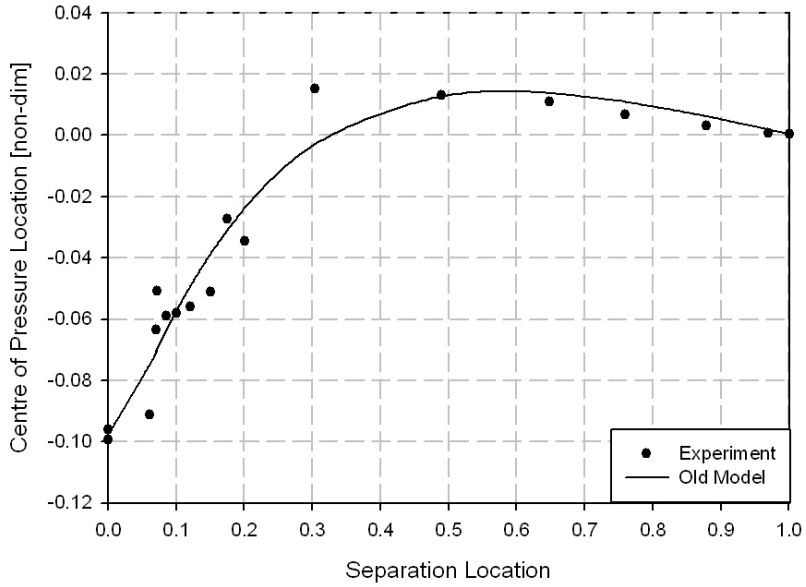

Figure 3.8: Old Model Prediction of Centre of Pressure Location

The curve fit appears to be better than those for the normal and chord force coefficients, however the main rearward movement of the centre of pressure is predicted to occur sooner, and is gentler, than the experiment suggests. Attempts to improve on the location of the main movement (at approximately $f = 0.3$) result in a worse curve fit elsewhere.

Clearly more representative equations for the integrated airload response to trailing edge separation are required. The equations should be more general in nature such that the alteration of a set of coefficients is sufficient to account for changes in Mach number, aerofoil and even the operation of air jet vortex generators.

3.2.4 New Model for Effects due to Separation

Given the deficiencies of the existing model highlighted above, new forms for the representation of the response of the integrated airload coefficients to the separation location will be suggested. Consider first the normal force coefficient. We seek a

replacement for the trailing edge stall factor, K_f, and therefore to guide the model development we seek to plot this value for the experimental data. Firstly, so that the model is continuous between the fully attached flow variation presented in the previous section and the trailing edge separation variation presented here, the pre-stall variation given by equation 3.8 is subtracted from the experimental values of C_n at each angle of attack. Following this, each value is divided by the normal force predicted by the linear model. The resulting factors at each angle of attack for the normal and chord forces respectively are therefore given by:

$$K_{f_n} = \left(C_{n_{\exp}} - C_{n_{C,US}}\right) / \left(C_{l_\alpha}\alpha\right) \quad \textbf{3.13}$$

$$K_{f_c} = \left(C_{c_{\exp}} - C_{c_{US}}\right) / \left(C_{l_\alpha}\alpha\sin\alpha\right). \quad \textbf{3.14}$$

The variation of $1-K_f$ with $1-f$ can now be plotted, as shown in Figure 3.9.

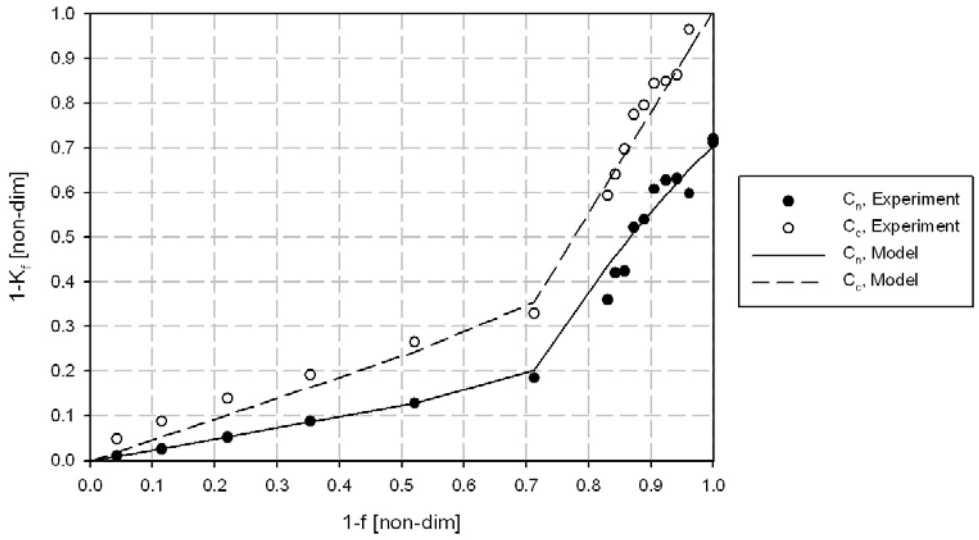

Figure 3.9: New Model Prediction of Normal and Chord Force Factors

From Figure 3.9, it can be seen that there are two distinct regions which are almost linear in nature. The variation can therefore be approximated by the superposition of 2 polynomials in a manner similar to equations 3.4 and 3.5 for the separation independent pitching moment. The new model for the variation of the normal force coefficient factor is therefore given by:

$$\begin{aligned} f_{n_2} \le 0 &\rightarrow \left(1-K_{f_n}\right) = L_{n_1} f_{n_1} + L_{n_2} f_{n_1}^2 \\ f_{n_2} > 0 &\rightarrow \left(1-K_{f_n}\right) = L_{n_1} f_{n_1} + L_{n_2} f_{n_1}^2 + L_{n_3} f_{n_2} + L_{n_4} f_{n_2}^2 \end{aligned} \quad \textbf{3.15}$$

where:

$$\begin{aligned} f_{n_1} &= 1 - f \\ f_{n_2} &= 1 - f - L_{n_5} \end{aligned} \qquad \textbf{3.16}$$

and the coefficients $L_{n_{1-5}}$ are Mach and aerofoil dependent constants. Similarly the chord force factor is given by:

$$\begin{aligned} f_{c_2} \le 0 \rightarrow \left(1 - K_{f_c}\right) &= L_{c_1} f_{c_1} + L_{c_2} f_{c_1}^2 \\ f_{c_2} > 0 \rightarrow \left(1 - K_{f_c}\right) &= L_{c_1} f_{c_1} + L_{c_2} f_{c_1}^2 + L_{c_3} f_{c_2} + L_{c_4} f_{c_2}^2 \end{aligned} . \qquad \textbf{3.17}$$

where:

$$\begin{aligned} f_{c_1} &= 1 - f \\ f_{c_2} &= 1 - f - L_{c_5} . \end{aligned} \qquad \textbf{3.18}$$

Now consider the centre of pressure location, which can be modelled using a similar method. The centre of pressure movement due to trailing edge separation is approximated from the experimental results by:

$$C_{pres,\exp} = \left(C_{m_{\exp}} - C_{m_{C,US}}\right) \Big/ \left(C_{n_{\exp}} - C_{n_{C,US}}\right). \qquad \textbf{3.19}$$

This can once again be plotted against $1 - f$ as shown in Figure 3.10.

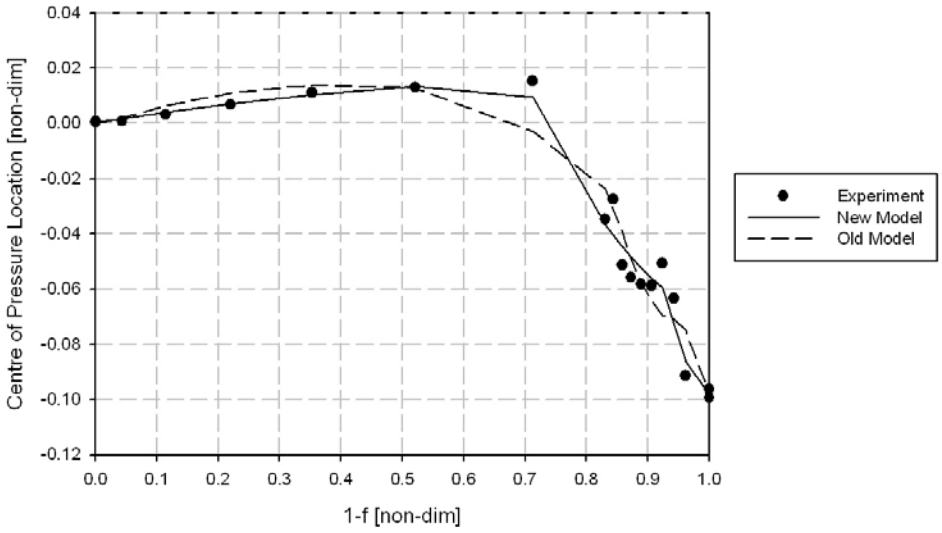

Figure 3.10: New Model Prediction of Centre of Pressure Location

In this case the result can be adequately represented by the superposition of 3 polynomials such that the centre of pressure location is given by:

$$\begin{aligned} C_{pres} &= L_{p_1} f_{p_1} + L_{p_2} f_{p_1}^2 \\ f_{p_2} > 0 \rightarrow C_{pres} &= C_{pres} + L_{p_3} f_{p_2} + L_{p_4} f_{p_2}^2 \\ f_{p_3} > 0 \rightarrow C_{pres} &= C_{pres} + L_{p_5} f_{p_3} + L_{p_6} f_{p_3}^2 \end{aligned} \qquad \textbf{3.20}$$

where:

$$\begin{aligned} f_{p_1} &= 1 - f \\ f_{p_2} &= 1 - f - L_{p_7} \\ f_{p_3} &= 1 - f - L_{p_8} \,. \end{aligned} \qquad \textbf{3.21}$$

From Figure 3.10 it is clear that the fit is not as successful as in the force coefficient factors but there is certainly an improvement over the existing method, particularly in the delay of the centre of pressure movement until larger amounts of separation have occurred.

3.2.5 Overall Coefficient Prediction

In summary, the overall integrated airloads for a static aerofoil are given by the new model as:

$$\begin{aligned} C_{n_C} &= C_{n_{C,US}} + \left(1 - K_{f_n}\right) C_{l_\alpha} \alpha \\ C_c &= C_{c_{US}} + \left(1 - K_{f_c}\right) C_{l_\alpha} \alpha \sin\alpha \\ C_{m_C} &= C_{m_{C,US}} + C_{pres} \left(1 - K_{f_n}\right) C_{l_\alpha} \alpha \,. \end{aligned} \qquad \textbf{3.22}$$

The prediction of the coefficients for the RAE 9645 aerofoil using the old and new models is shown against the experimental data in Figure 3.11 through Figure 3.13.

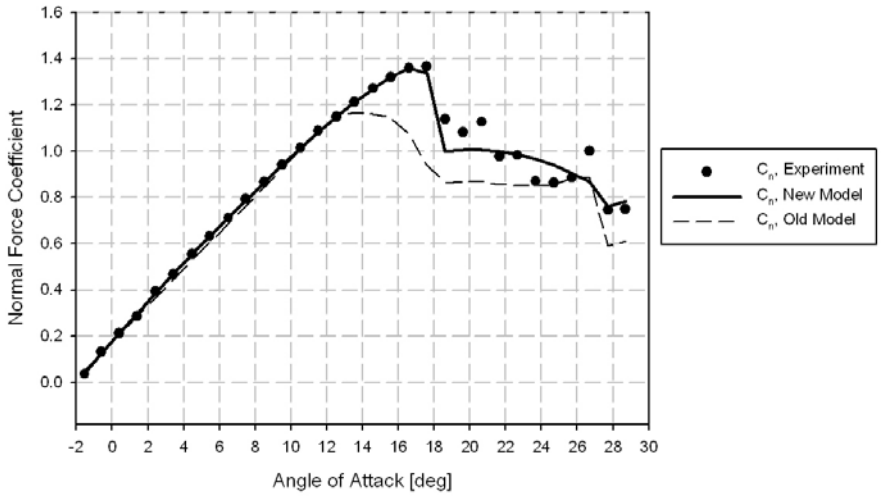

Figure 3.11: Prediction of Static Normal Force Coefficient using Old and New Models.

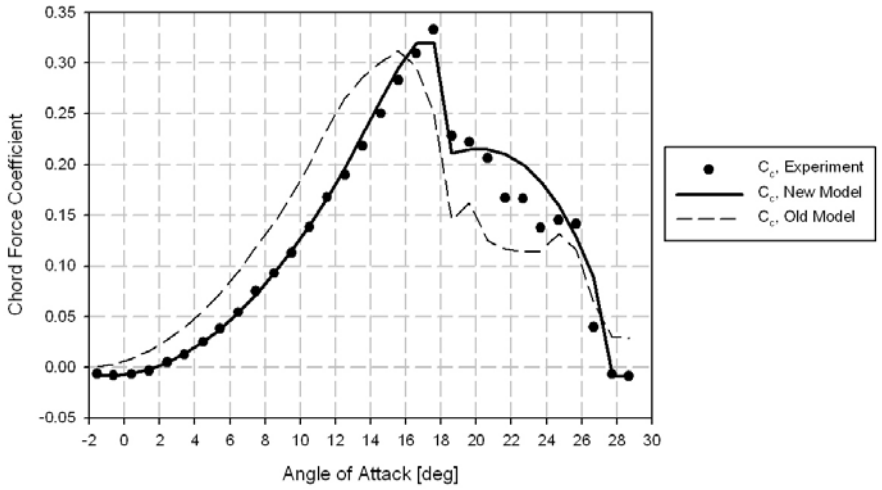

Figure 3.12: Prediction of Static Normal Force Coefficient using Old and New Models.

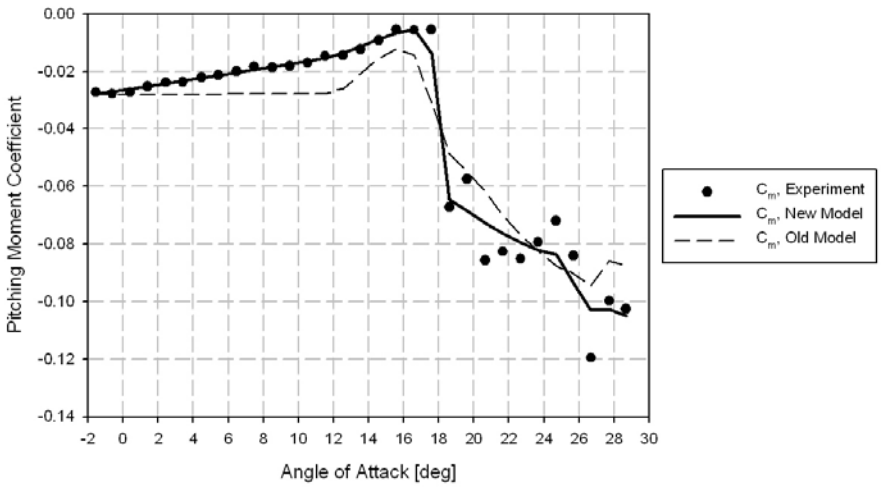

Figure 3.13: Prediction of Static Pitching Moment Coefficient using Old and New Models.

There is a clear improvement in the prediction using the new model and the need for the inclusion of models for the variation in the coefficients prior to the onset of trailing edge separation is clear to see, particularly for the pitching moment and chord force coefficients. Also the greater flexibility of the new model in terms of response to the trailing edge separation is clear as the correlation in the stall behaviour is improved.

3.2.6 Static Coefficients with Air Jet Vortex Generators

Although the new model was developed with regard to the data from the Air Jet Vortex Generator tests, all the data used to explain the development of the model in the previous sections was for the aerofoil without AJVGs in operation. This enabled the new model to be compared to the old model, however in this section the results will be presented for the cases with AJVGs in operation.

Firstly, consider the trailing edge separation location. Data for the RAE9645 aerofoil with and without AJVGs in operation are presented in Figure 3.14 along with the representations using the new model.

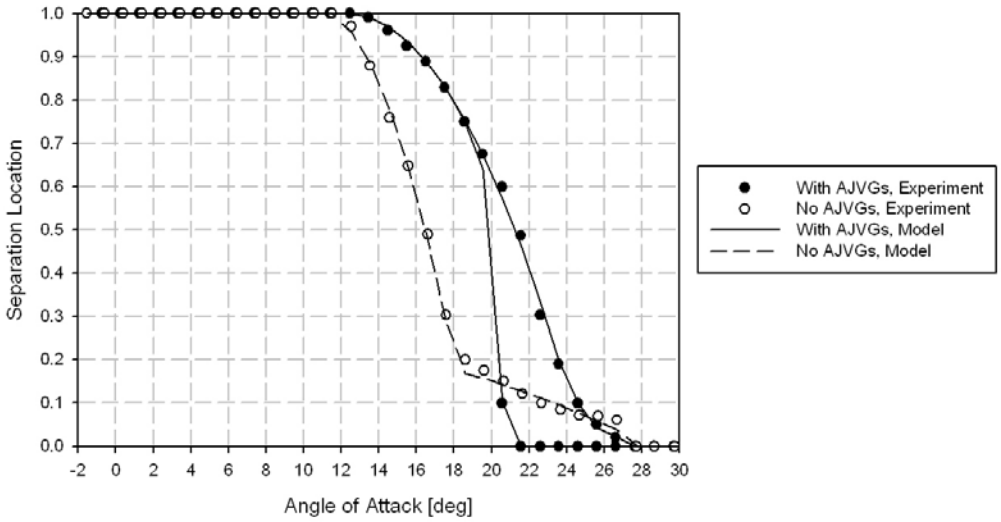

Figure 3.14: Prediction of separation location with and without AJVG operation. Note hysteresis in AJVG data and its prediction by the model.

With the AJVGs operating, the onset of trailing edge separation is only slightly delayed however the subsequent forward movement of the separation location is much more gradual with respect to angle of attack. In the non-blown case the separation location is at 20% chord within 6 degrees of the trailing edge separation onset as opposed to 12 degrees with the AJVGs in operation. It is also interesting and revealing to note that the two appear to coalesce near 10% chord, close to where the jets are located. The reduced

effectiveness of the AJVGs when returning from a stalled state is also displayed through the hysteresis in the blown result. Overall it is clear to see that the AJVGs significantly delay the forward movement of the separation location with regard to angle of attack and that the new model performs well in modelling the differences including the hysteresis effect.

Consider now the modelling of the separation independent changes to the coefficients. The AJVGs work by delaying separation through re-energising the boundary layer. Clearly these effects should have little influence on the coefficients at lower angles of attack. The delay in the separation however means that the transition of the new model from the separation-independent component to the separation-dependent component is also delayed as the domination of the f^2 terms (see equations 3.7 to 3.9) occurs at higher angles of attack. These effects are demonstrated in Figure 3.15 through Figure 3.17 where the model is also shown to correlate well with the experimental data both with and without AJVGs.

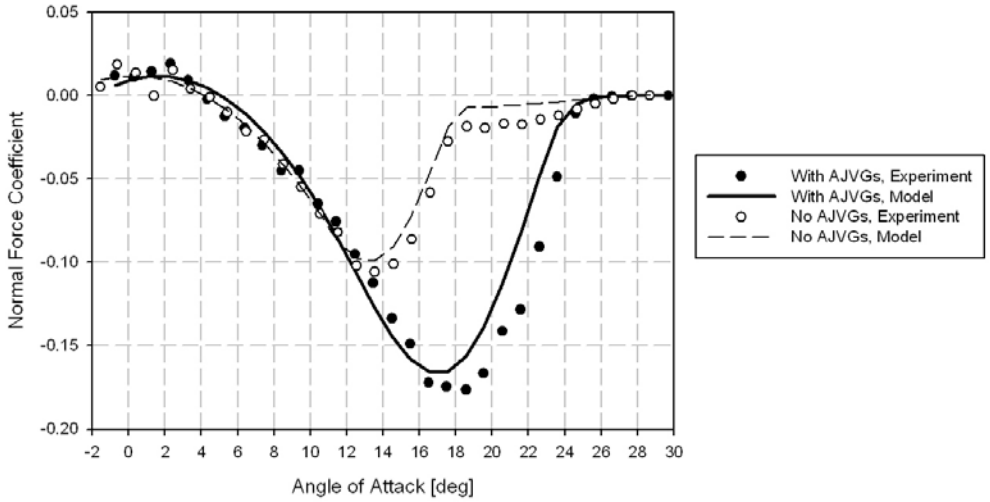

Figure 3.15: Prediction of separation independent normal force coefficient change.

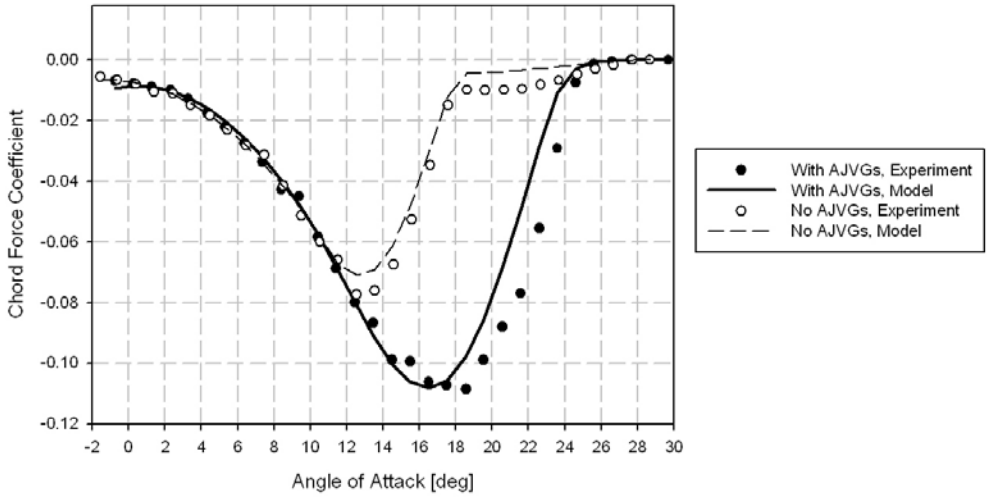

Figure 3.16: Prediction of separation independent chord force coefficient change.

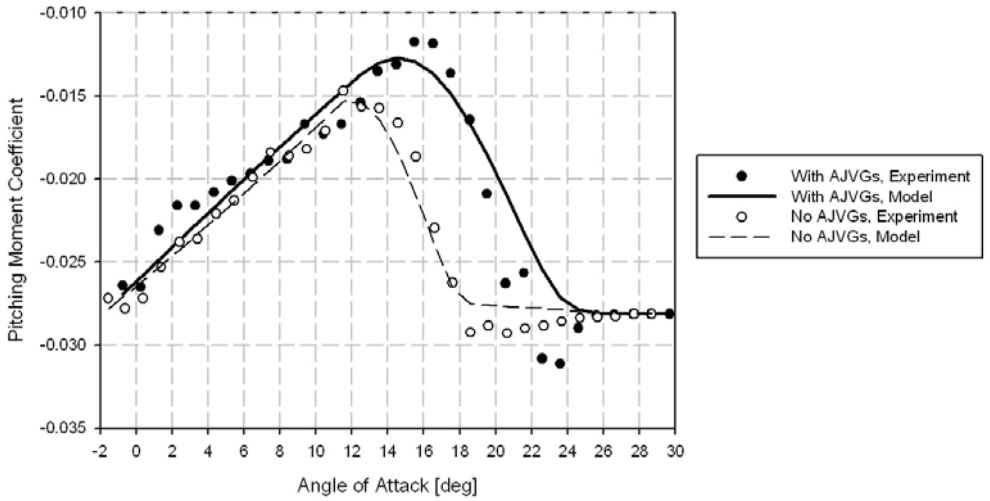

Figure 3.17: Prediction of separation independent pitching moment coefficient change.

The responses of the normal and chord force coefficient factors to the trailing edge separation are shown in Figure 3.18 and Figure 3.19 respectively. Unlike for the non-blowing case, when AJVGs are operating, the response of the normal and chord force coefficient factors is almost linear until the separation location reaches the jets. This means that the separation has more effect initially but the final drop in the coefficients only occurs once the flow is almost entirely separated. The flexibility of the new model means that these differences in the response to the separation location may be captured. Note that there is an anomalous point in the test data when $f \approx 0.2$ and that no attempt has been made to model this. The reason for this is that this anomaly did not show up in the dynamic tests and any attempt to model it in the static case led to decreased correlation in the dynamic pitching cases.

Data for the centre of pressure movement is shown in Figure 3.20. The forward movement of the centre of pressure with partial amounts of separation is clearly reduced with the use of AJVGs. The break in the pitching moment is also delayed until a larger degree of separation has occurred. However, once the separation point approaches the location of the jets the rearward movement of the centre of pressure occurs more rapidly than for the clean aerofoil. Once again the observed differences with and without AJVGs are well captured using the new model.

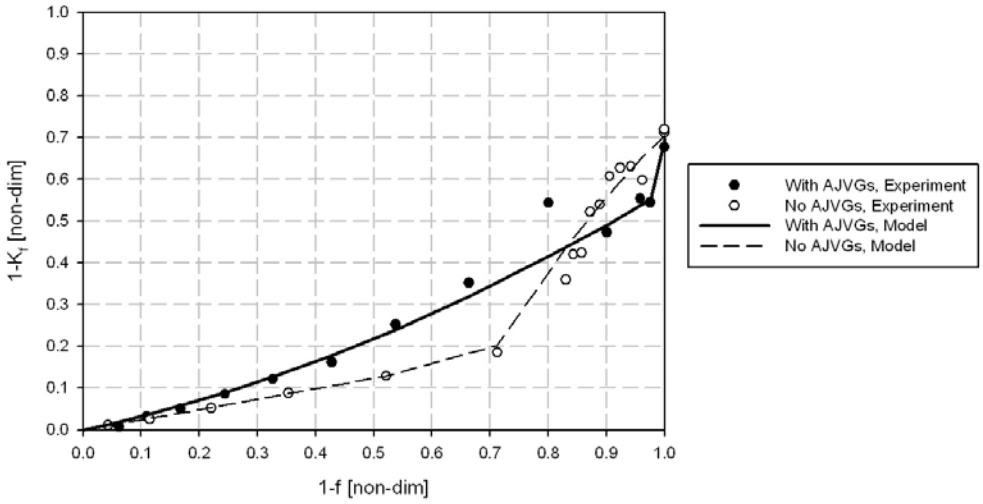

Figure 3.18: Prediction of normal force factor with and without AJVGs.

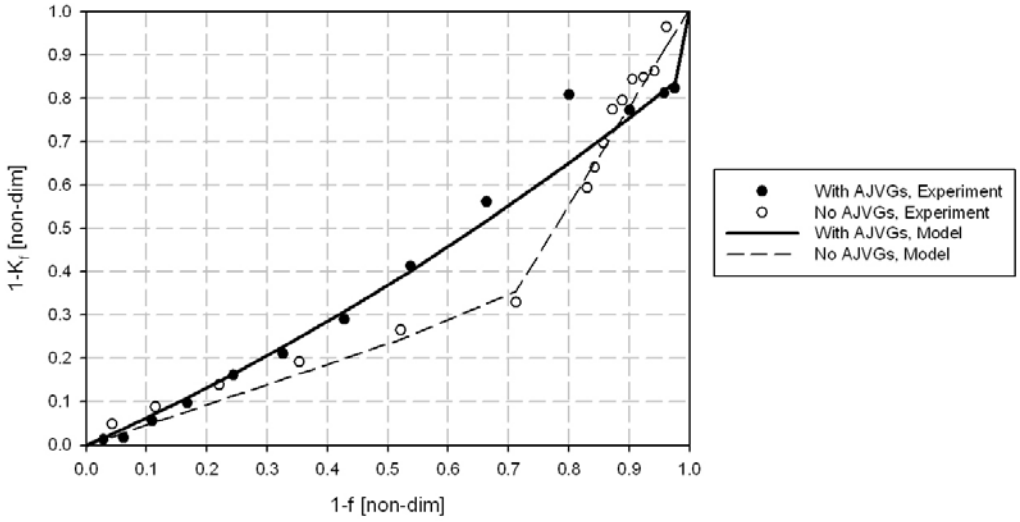

Figure 3.19: Prediction of chord force factor with and without AJVGs.

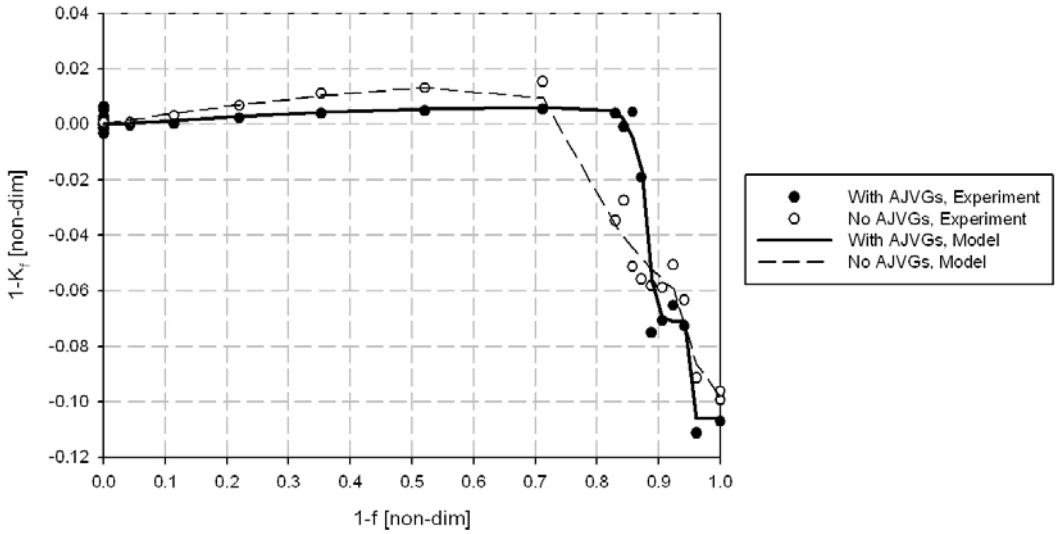

Figure 3.20: Prediction of centre of pressure location with and without AJVGs.

Equations 3.22 for the total coefficients leads to the plots of the normal and chord force coefficients and the pitching moment coefficient in Figure 3.21 through Figure 3.23 from which the difference made by the AJVGs is immediately clear. Up until stall of the clean aerofoil, the characteristics are very similar. With the operation of AJVGs, however, the stall is delayed by around 3 degrees of angle of attack and is also gentler up until the separation location approaches the region in which the jets are located. At this point a more dramatic drop in both the normal and chord force coefficients occurs. The break in the pitching moment coefficient is correspondingly delayed and initially decreases slowly with angle of attack as the movement of the separation location is delayed.

As noted earlier, there are anomalous data points in the normal and chord force coefficients between 23 and 24 degrees angle of attack. Similar effects were not observed in the dynamic pitching test results and any attempt to model them in the static case led to bad correlation in the dynamic cases. For this reason these points were purposely excluded from the static data modelling. With the exception of these points however the new model has been shown to be capable of representing the integrated airload coefficients of a static aerofoil with or without the operation of Air Jet Vortex Generators.

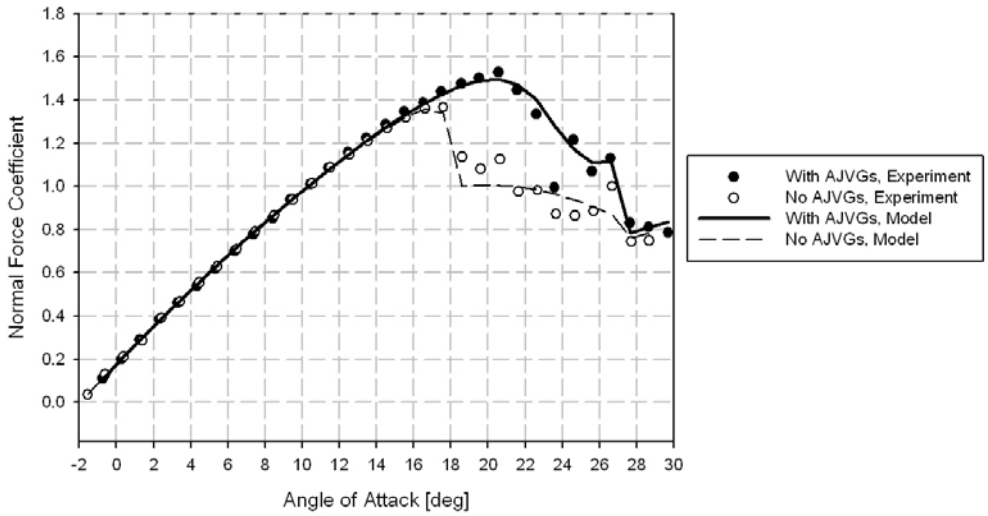

Figure 3.21: Normal force coefficient with and without AJVGs.

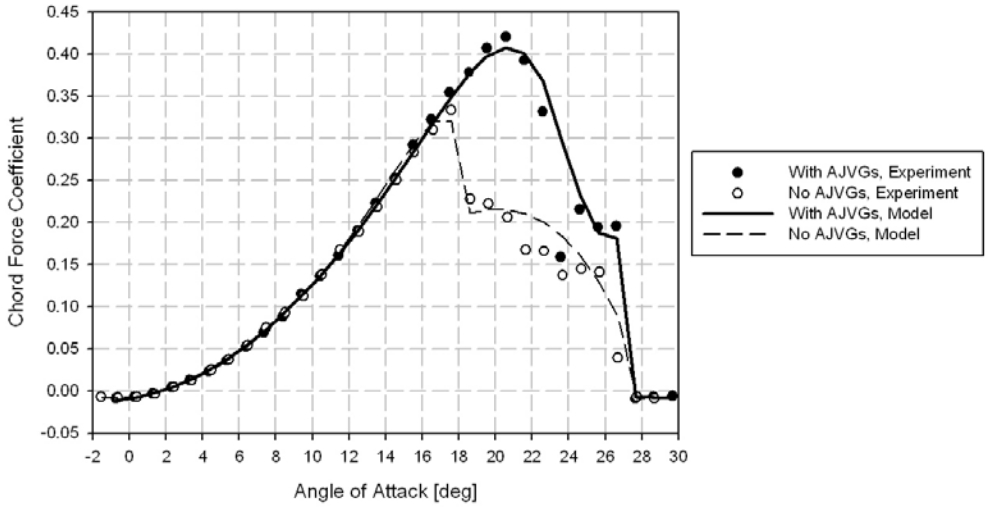

Figure 3.22: Chord force coefficient with and without AJVGs.

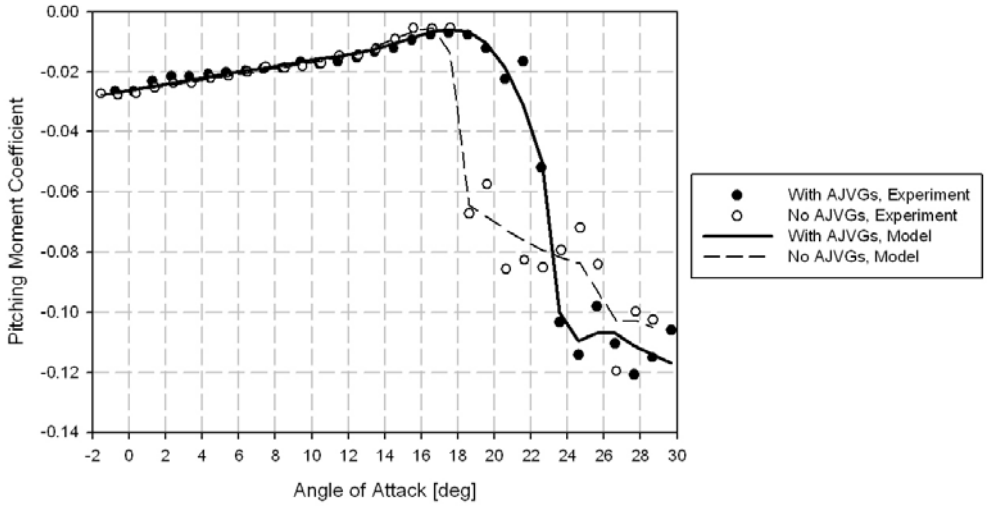

Figure 3.23: Pitching moment coefficient with and without AJVGs.

3.3 Unsteady Modelling of Air Jet Vortex Generators

The modifications to the static aerofoil representation presented in the previous section maintained the explicit modelling of the separation location central to the 3rd generation model. The advantage of this method over the use of look-up tables is that the 3rd generation methodology for the modelling of unsteady effects remains applicable as the steady value of the separation location may be taken as input, from which a lagged value is calculated. This lagged value is then substituted into the steady equations for the calculation of the integrated airloads.

A new unsteady model is therefore derived by incorporating the new steady model into the existing 3rd generation unsteady formulation by replacing the old equations for the separation location with the new equations and likewise with the old and new coefficient models. However, the static corrections alone did not adequately model the effects observed in the results from the dynamic pitching experiments performed at the University of Glasgow [Prince (2008), Coton (2008)] and therefore this section discusses the additional modifications made to the model to improve the correlation in the dynamic pitching cases.

3.3.1 Suggested Alterations from University of Glasgow

The University of Glasgow wind tunnel tests were conducted at very low Mach numbers and it has been shown in the past that, at these low Mach numbers, the performance of the 3rd generation dynamic stall model is poor and two major changes have been suggested by researchers at the University of Glasgow which vastly improve the modelling. These changes are to be used here and will therefore be discussed in turn.

The first change is an alteration to the criteria for the onset of dynamic stall. A full discussion of the shortcomings of the old criteria and the development of the new criteria can be found in Sheng et al (2006). Briefly, the old criteria used a critical value of C_n denoted by C_{n_1} which was found to correspond to the Evans-Mort correlation of peak suction and adverse pressure gradient for the static aerofoil, Evans and Mort (1959). For a dynamically pitching aerofoil the leading edge pressure coefficient is reduced such that the achievement of the critical value of normal force is delayed. This delay is incorporated into the model by the introduction of a first order lag with time constant T_P.

At low Mach number, however, the lag was found to be insufficient and the reliance on the Evans-Mort criterion introduced significant subjectivity. For these reasons a new model was sought.

The new model is based around a lagged angle of attack for which a model has been developed based upon experimental observations of dynamic stall onset. It has been noted that the dynamic stall onset angle increases linearly with reduced pitch rate, r, above some critical value of reduced pitch rate, r_0, such that the critical angle of attack defining the onset of dynamic stall is given by:

$$\alpha_{ds} = \alpha_{ds,0} + \left(T_\alpha \frac{180}{\pi} \right) r \,. \qquad \textbf{3.23}$$

Therefore if a lagged angle of attack, α', is defined using a first order lag with time constant T_α then the dynamic stall angle is exceeded when the lagged angle of attack exceeds $\alpha_{ds,0}$. For pitch rates of less than r_0, the stall angle is assumed (based on experimental observations) to have a linear variation between the static stall angle, α_1, and $\alpha_{ds,0}$. Overall then the stall onset occurs when $\alpha' \geq \alpha_{crit}$ where:

$$\begin{aligned} \alpha_{crit} &= \alpha_{ds,0} && r \geq r_0 \\ \alpha_{crit} &= \alpha_1 + \left(\alpha_{ds,0} - \alpha_1 \right) r / r_0 && r < r_0 \,. \end{aligned} \qquad \textbf{3.24}$$

The effect of the angle of attack delay is also applied to the trailing edge separation by replacing the static angle of attack with an effective dynamic angle of attack given by:

$$\alpha_f = \alpha' - \Delta\alpha_1 \qquad \textbf{3.25}$$

where:

$$\begin{aligned} \Delta\alpha_1 &= \alpha_{ds,0} - \alpha_1 && r \geq r_0 \\ \Delta\alpha_1 &= \left(\alpha_{ds,0} - \alpha_1 \right) r / r_0 && r < r_0 \,. \end{aligned} \qquad \textbf{3.26}$$

The above alterations have been included in the unsteady model; however it is important to check that these dynamic stall criteria are relevant for the RAE 9645 aerofoil with and without the AJVGs operating. Dynamic stall onset angles have been collated from the dynamic ramp test data from the University of Glasgow experiment [Prince (2008), Coton (2008)] and are plotted against reduced pitch rate in Figure 3.24.

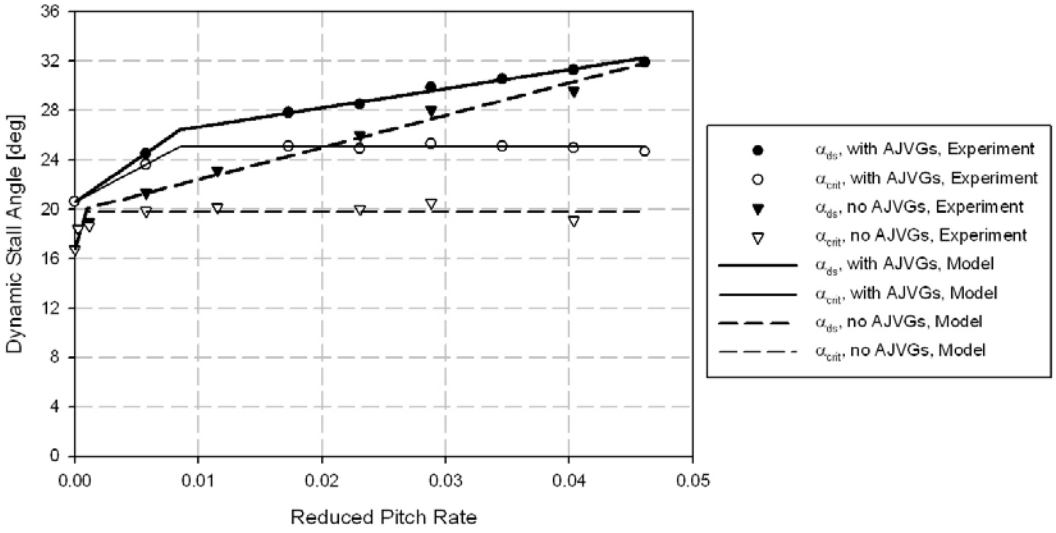

Figure 3.24: Dynamic Stall Angles for Blown and Non-Blown Aerofoils

Note that in both cases, a straight line fit for the dynamic stall angle above the critical rate is possible. The model presented above, using a first order lag, is therefore reasonable for the RAE9645 aerofoil both with and without AJVGs. Note from the data that the dynamic stall angle when using AJVGs is always higher. The advantage is greatest when the aerofoil is pitching at the critical reduced frequency (r_0) for the with AJVG data, however the advantage decreases as the pitch rate increases until there is little to no difference at the highest tested pitch rate. This fact highlights the importance of frequency for the operation and use of air jet vortex generators.

The second modification to the dynamic stall model, as suggested by Sheng et al (2007), concerns the reattachment process. In the original 3rd generation model, this was achieved simply through further lagging of the boundary layer response. However at low Mach and Reynolds numbers this methodology has been found to be insufficient. The reattachment process was identified by Sheng et al (2007) to occur in two phases. Firstly a convective process occurs which removes the stalled flow, which is then followed by the re-establishment of the attached boundary-layer. In the original model it is only really the second process which is modelled.

The start of the convective process was found to be heralded by a rise in suction somewhere near 2.5% chord while the end of the process corresponded closely to the attainment of a minimum value of normal force coefficient, $C_{n_{\min}}$, following which the boundary-layer recovery commences. The incidence at which the suction rise (start of the convective process) occurs was observed to be independent of reduced pitch rate (to a

first order) and in the static case coincided with the attainment of $C_{n_{\min}}$. Additionally the angle of attack, $\alpha_{\min}$, at which $C_{n_{\min}}$ occurred was found to vary approximately linearly with the reduced pitch rate such that:

$$\alpha_{\min} = \alpha_{\min_0} + \left(\frac{180}{\pi} T_r\right) r \,. \qquad \textbf{3.27}$$

Therefore the convective process may be approximated by assuming initialisation to occur when the aerofoil passes through $\alpha_{\min_0}$ and completion to occur after a non-dimensional time T_r. During the convective process the normal force behaves according to the lift curve slope at initialisation, following which the boundary layer is allowed to reattach. The calculation of T_r is performed by plotting the value of $\alpha_{\min}$ against the reduced frequency and calculating the gradient of a best-fit line. Data from the ramp down tests of the RAE 9645 aerofoil with and without AJVGs is plotted in Figure 3.25.

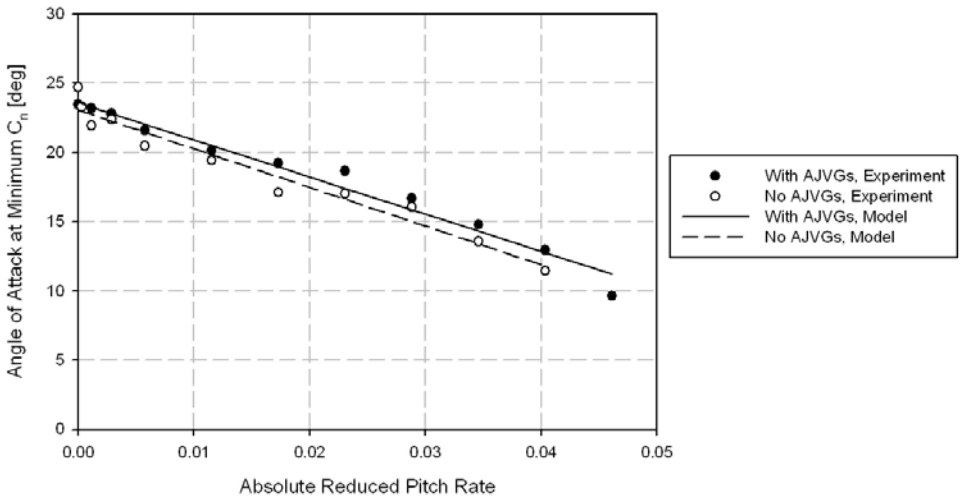

Figure 3.25: Reattachment time constant calculation.

The linear correlation is not as close as for the dynamic stall angle but is deemed to be sufficient for the current purpose. Also note that the use of AJVGs results in little to no overall effect on the reattachment convection process as there is little difference in either $\alpha_{\min_0}$ or in T_r. This reinforces the hysteresis seen in the static aerofoil separation location plots. Note that the reduced pitch rate is well defined for ramp tests but less well defined for sinusoidal or arbitrary pitching motions. The instantaneous pitch rate in the model has therefore been replaced by a pressure lagged pitch rate with time constant T_r. Given that the stall onset criterion has in the past been linked closely to the attainment of

a leading edge pressure, the use of a pressure lagged reduced pitch rate to define the stall characteristics seems reasonable and has indeed led to good results.

3.3.2 Further Alterations to the Dynamic Stall Model

The inclusion of the University of Glasgow modifications alone was found to be insufficient for modelling the aerofoil both with and without AJVGs and therefore the author has made some further modifications to the model which will be discussed in this section.

Consider first the time constant T_F. Values for this parameter have been approximated from the ramp test data from the University of Glasgow experiments and plotted against pitch rate as shown in Figure 3.26. It is clear that the value of the time constant is decreasing with reduced pitch rate and so the constant value input to the model has been replaced by a linear variation. The linear fit as shown in Figure 3.26 exhibits less correlation than the models in the previous section, although it is a clear improvement over a constant value model.

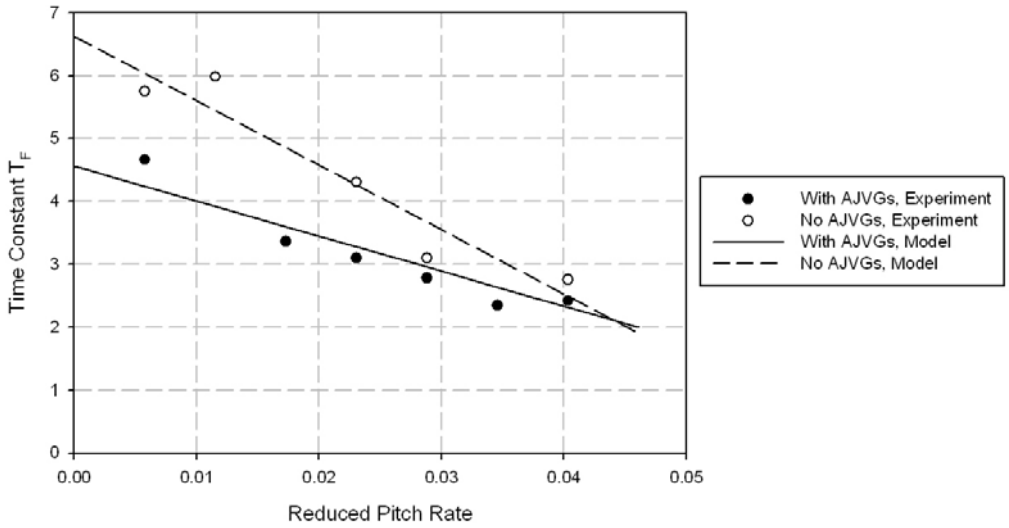

Figure 3.26: Boundary Layer Delay Time Constant

The incorporation of all the modifications discussed to this point into the 3rd generation method enabled the normal force coefficient of the dynamically pitching RAE9645 aerofoil without the AJVGs operating to be reasonably represented. Consider first the test results for various mean angles of attack with a superimposed sinusoidal pitch variation with amplitude of 8 degrees at a frequency of 1.97 Hz. The results are presented for the various values of mean angle of attack in Figure 3.27. The correlation is generally reasonable, particularly at higher mean angles of attack, however reattachment occurs

early in the light stall (lower mean angle of attack) cases and the overall post-stall drop in normal force coefficient in these cases is under-predicted.

Figure 3.28 shows three different pitch frequency cases for a constant mean angle of attack of 16 degrees. For the lower frequency cases the reattachment is slightly early, however, for the highest frequency case, it is too late. Apart from these differences the reproduction may be considered to be reasonable for the current purpose and therefore no further modifications were made to the model for the normal force coefficient of the clean (no AJVG) aerofoil.

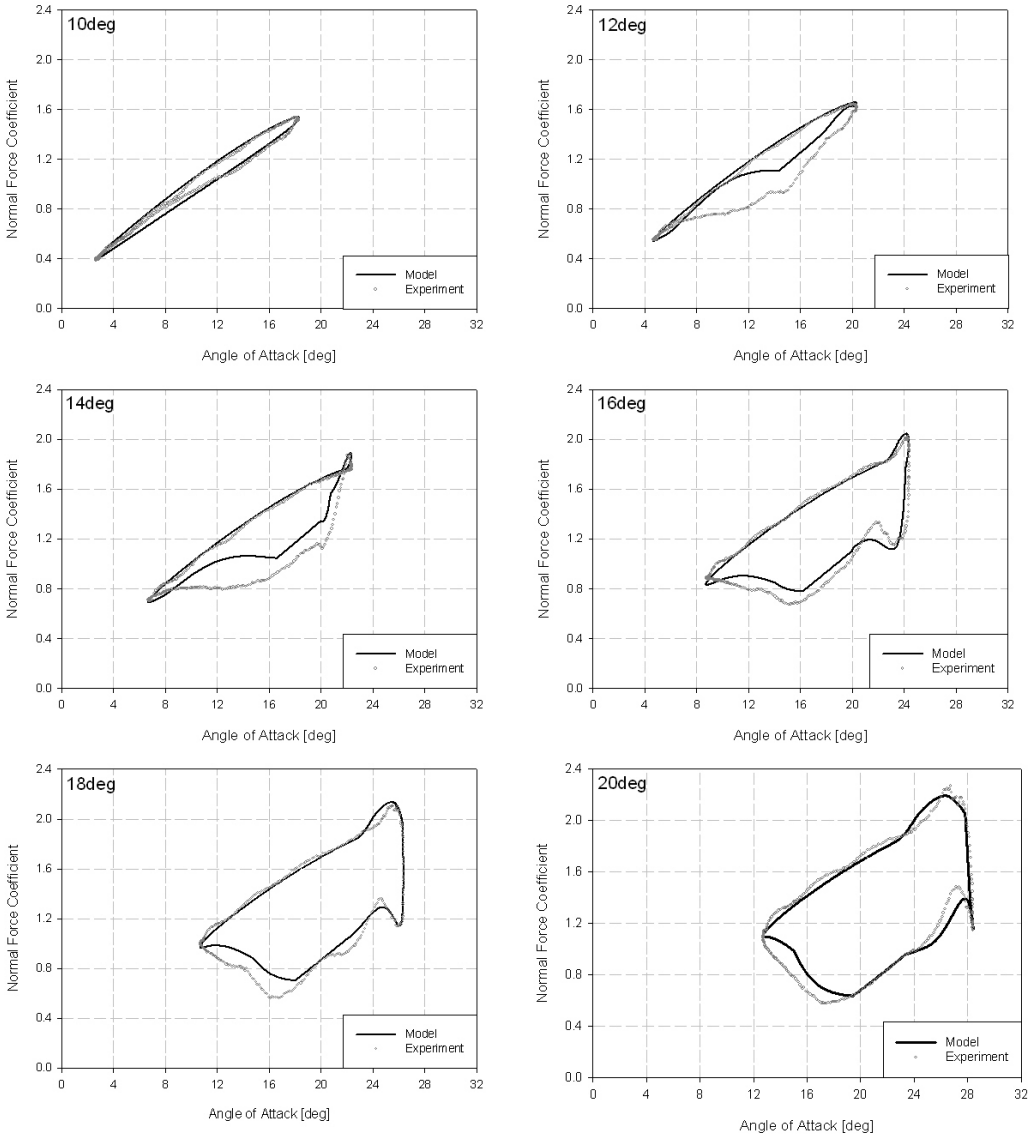

Figure 3.27: Normal force coefficient at various values of mean angle of attack, no AJVGs.

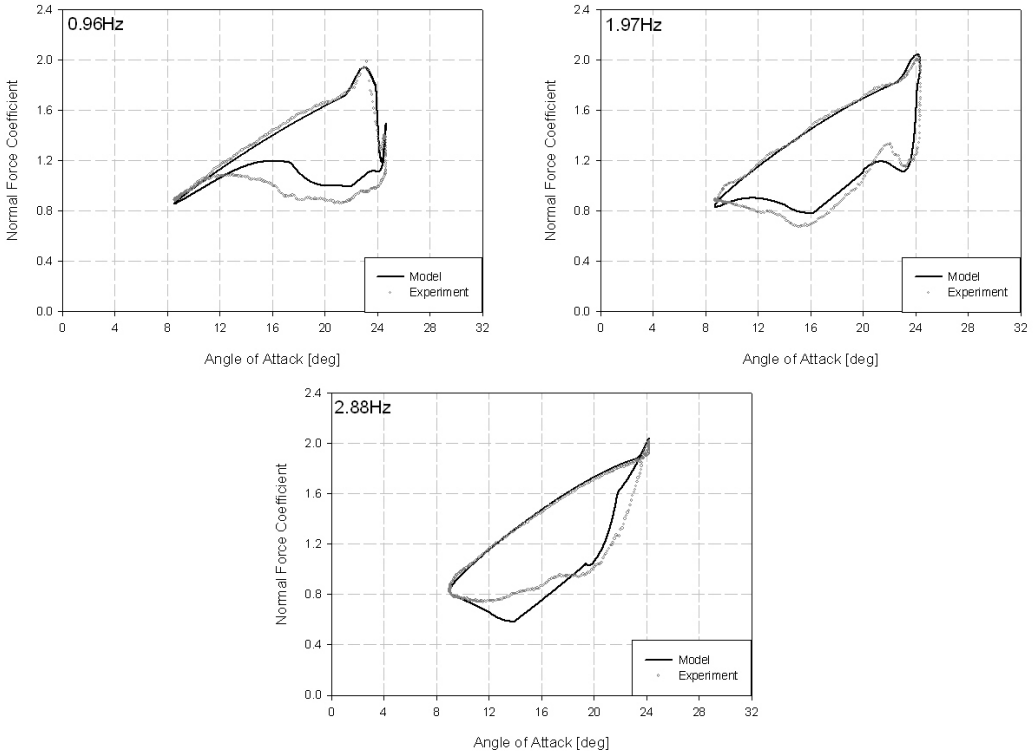

Figure 3.28: Normal force coefficient at various values of pitch frequency, no AJVGs.

Although the modifications presented so far were adequate for the normal force coefficient, further modification was required for the pitching moment and chord force coefficients. Prediction of the pitching moment coefficient during a ramp-up motion at four different pitch rates is shown in Figure 3.29. There are two main areas where the model decreases in correlation as the pitch rate increases. Firstly, the escalation of the nose-down pitching moment due to the first dynamic stall vortex occurs over a longer time period and secondly, the pitching moment divergence begins to occur before the critical angle of attack is reached. Together these effects result in a smoother, lengthier reduction in the pitching moment coefficient than the current method predicts. The author has therefore sought to address these deficiencies through two additional enhancements to the method.

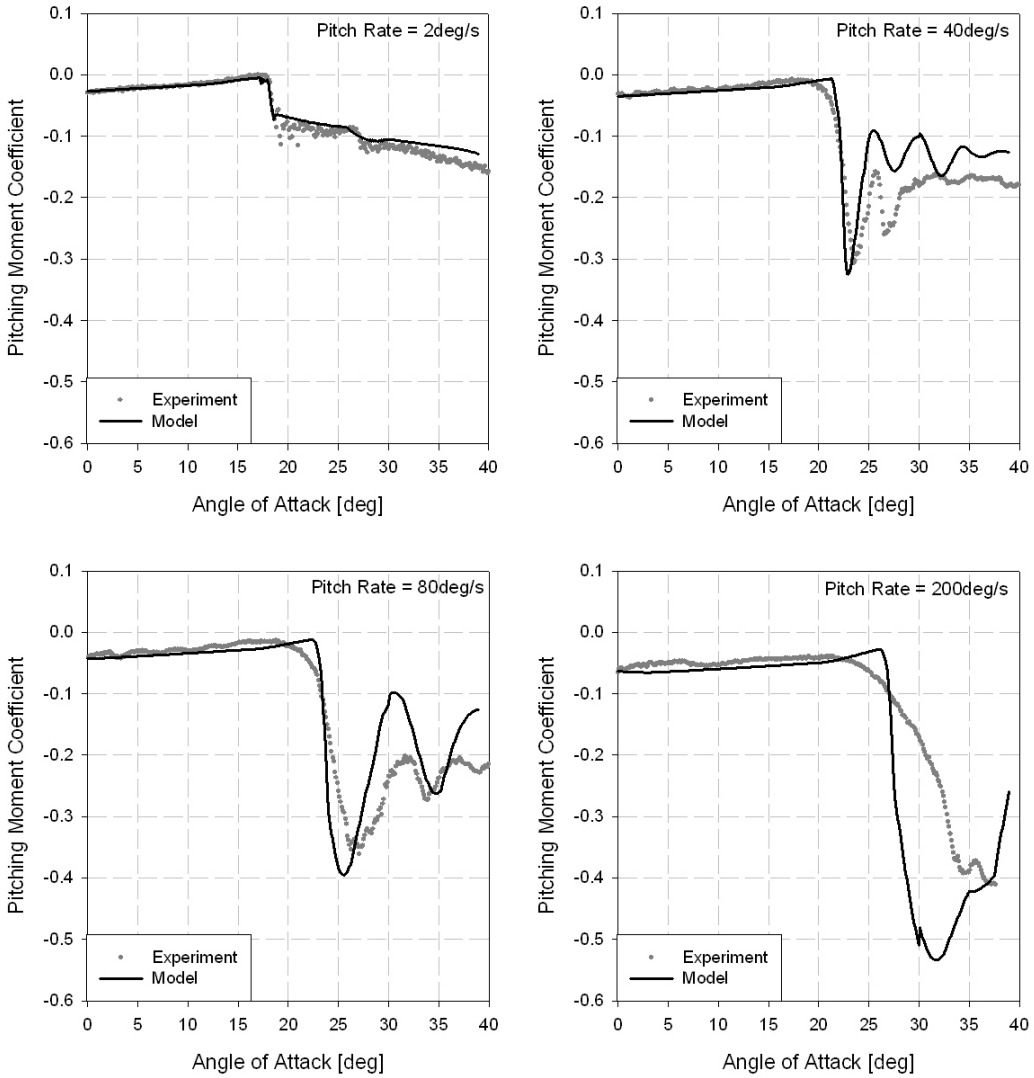

Figure 3.29: Initial modelling of pitching moment coefficient during ramp-up

Consider firstly the reduction of the pitching moment prior to the attainment of the critical angle of attack. Sheng et al (2006) suggest that one definition of the onset of dynamic stall is when the pitching moment has dropped by 0.05. This clearly implies that the centre of pressure has already started to move towards the rear of the aerofoil before the main stall effects occur, yet the unsteady method makes no attempt to model these physics.

The first suggested modification, therefore, is to include a pitch rate dependant addition to the pitching moment coefficient. It has been noted from the test data that the divergence of the pitching moment begins to occur close to where the instantaneous angle of attack (before pressure lag) reaches the critical angle and that, by definition, there has been a reduction of 0.05 by the time the pressure lagged angle of attack reaches the critical angle. Additionally, it has been noted that for dynamic pitching, the post-dynamic stall

vortex nose-down pitching moment coefficient is greater than in the static case but that the difference recedes during the convective phase of the reattachment. Therefore a simple addition to the pitching moment coefficient to account for this pre-stall divergence may be given by:

$$\begin{aligned} \Delta C_m &= -0.05\left(1-\cos\left(\frac{\pi}{2}\frac{s_m}{T_{m_1}}\right)\right) && 0 < s_m < T_{m_1} \\ \Delta C_m &= -0.05 && s_m \geq T_{m_1} \end{aligned} \qquad \textbf{3.28}$$

and:

$$\begin{aligned} \Delta C_m &= \Delta C_m \cos\left(\frac{\pi}{2}\frac{s_r}{T_r}\right) && 0 < s_r < T_r \\ \Delta C_m &= 0 && s_r \geq T_r . \end{aligned} \qquad \textbf{3.29}$$

The second deficiency noted was that the nose-down pitching moment takes longer to accumulate during the build-up phase of the dynamic stall vortex as pitch rate increases. The second modification takes account of this fact simply by the addition of a first order lag with time constant T_{m_2}. Generally the time constant is given a value close to zero but is altered to a preset value when $0 < \tau_v \leq T_v$. For correlation with the University of Glasgow test results a value of $T_{m_2} = 4$ was found to be reasonable.

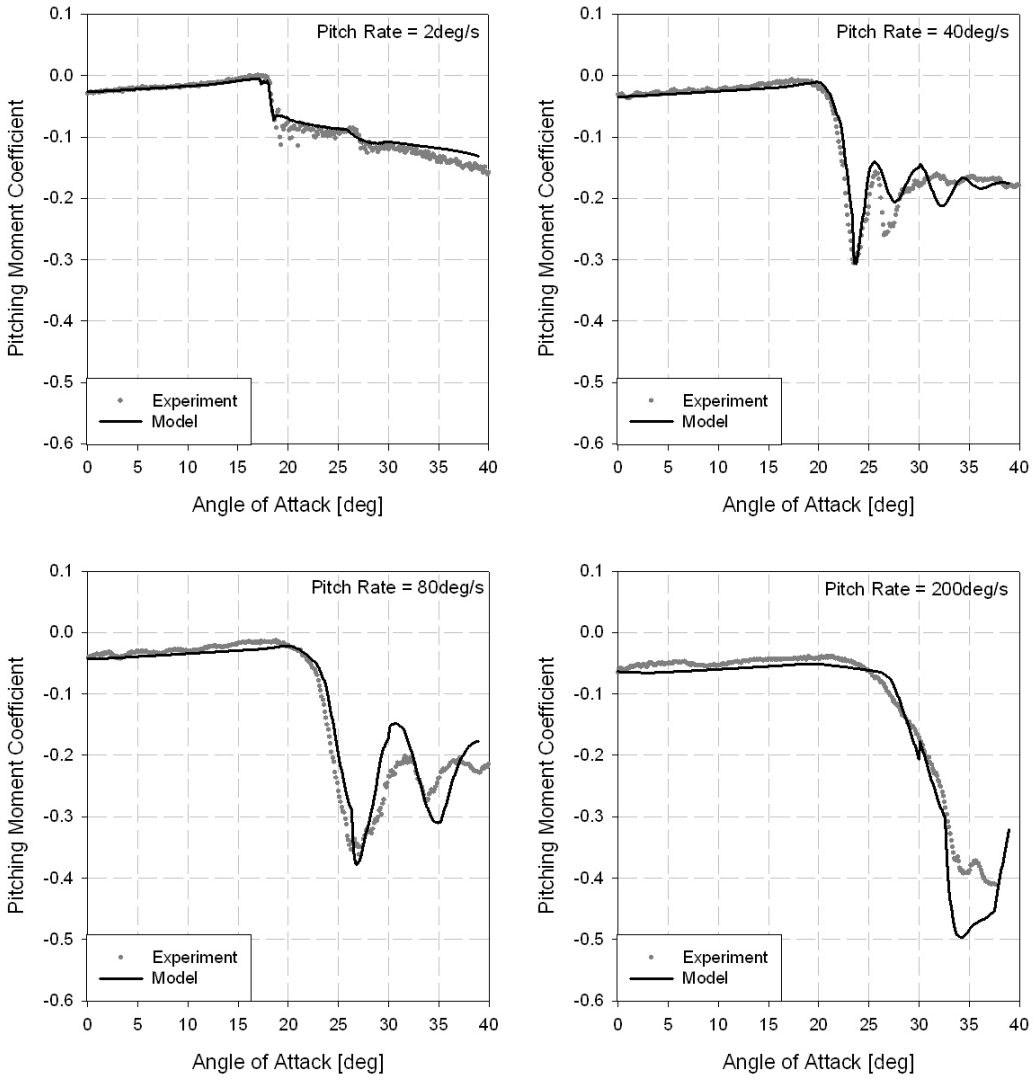

Figure 3.30: Improved modelling of pitching moment coefficient during ramp-up.

The modifications suggested above have been incorporated into the model and the new results for the ramp-up cases of Figure 3.29 are presented in Figure 3.30. There is a clear improvement in the correlation between the model and the test data due to the modifications, particularly in the highest pitch rate case. There is still however room for improvement in the modelling of the secondary and tertiary vortex effects and in the predicted magnitude due to the first vortex at the highest pitch rate.

The reconstruction of the pitching moment coefficient of the sinusoidal tests is presented for various values of mean angle of attack in Figure 3.31. The secondary increases in nose-down (negative) pitching moment due to the secondary vortex shedding is clearly under-predicted in all cases and, like the normal force coefficient plot, the magnitude of the effects in the light stall case at 12 degrees mean angle of attack is generally under-predicted. However, the entry into the dynamic stall is reproduced well for all values of

mean angles of attack. The effects due to the first stall vortex are generally well modelled, although the delay in the 20 degree case is clearly not long enough.

Figure 3.32 shows three different frequency cases with the mean angle of attack set at 16 degrees. In all cases the effects due to the first dynamic stall vortex are well modelled, however the variation of the reattachment with frequency is less well captured. In summary, there is clearly room for improvement in the reproduction of the pitching moment coefficient during dynamic pitching, however the correlation for the clean RAE9645 aerofoil presented above is considered to be sufficient for the current research.

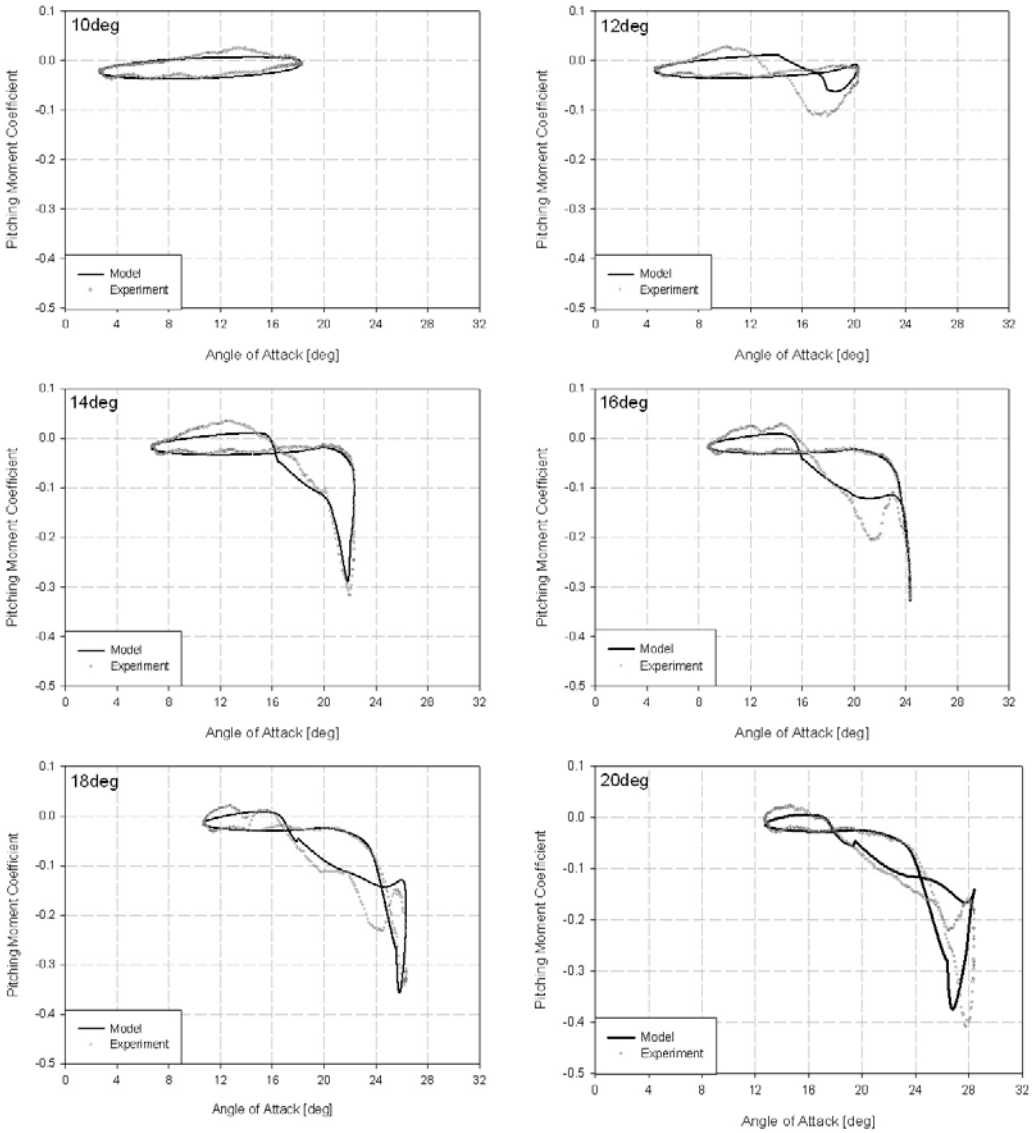

Figure 3.31: Pitching moment coefficient at various values of mean angle of attack, no AJVGs.

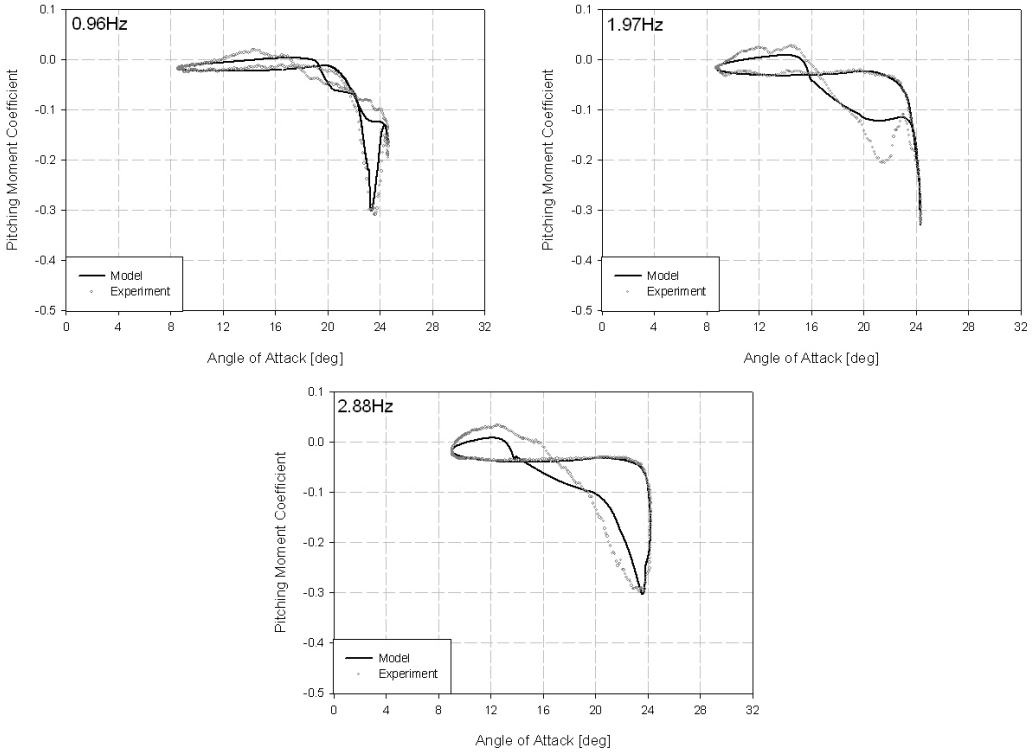

Figure 3.32: Pitching moment coefficient at various values of pitch frequency, no AJVGs.

Finally, consider the chord force coefficient model. Sheng et al (2007) base their model on an earlier version of the 3rd generation model and suggest a simple correction to the chord force coefficient model whereby $\sqrt{f}$ is replaced by $\sqrt{f}-0.2$ thus allowing for the negative chord force values noted from experiment. With the latest version and the new static coefficient model, such a simple correction is not possible and therefore a different approach is required. Firstly, it was noted that no correction was needed when the flow remains attached and therefore it was hypothesised that any correction should be proportional to $1-f'$. Additionally, the correction is required to increase with the pitch-rate whilst it was also noted from the ramp-up test results that there is some recovery in the chord force coefficient after an initial overshoot. Therefore, following the example of the method used for the dynamic stall vortex strength, the chord force correction was also made proportional to $f''-f'$. Together this gives an initial model of the form:

$$\Delta C_c = B_c\left(f''-f'\right)\left(1-f'\right) \qquad \textbf{3.30}$$

where B_c is a Mach dependent constant. This correction alone was found to be insufficient. In practice the additional reduction in the chord force is delayed until

dynamic stall onset from when it increases until the vortex reaches the trailing edge. Therefore the model becomes:

$$\begin{aligned} \Delta C_c &= 0 && s_v = 0 \\ \Delta C_c &= B_c\left(f'' - f'\right)\left(1 - f'\right)\sin\left(\frac{\pi}{2} \times \frac{s_v}{T_V + 0.5T_{VL}}\right) && 0 < s_v < T_V + 0.5T_{VL} \\ \Delta C_c &= B_c\left(f'' - f'\right)\left(1 - f'\right) && s_v \geq T_V + 0.5T_{VL}\,. \end{aligned} \qquad \textbf{3.31}$$

This correction is held constant during the convection stage of reattachment and is then allowed to dissipate during the boundary-layer reattachment phase. Finally, as for the pitching moment coefficient, an additional lag has been applied to the post-stall chord force coefficient. These corrections for the chord force coefficient have been incorporated into the model and Figure 3.33 presents the results for the ramp-up test cases of the University of Glasgow wind tunnel experiment. It is clear that the general correlation between model and experiment is good with the partial recovery of the chord force coefficient in the lower pitch-rate cases being captured. The peak value of the coefficient in the medium pitch-rate cases is however over-predicted and slightly delayed, although the error is considered to be acceptable.

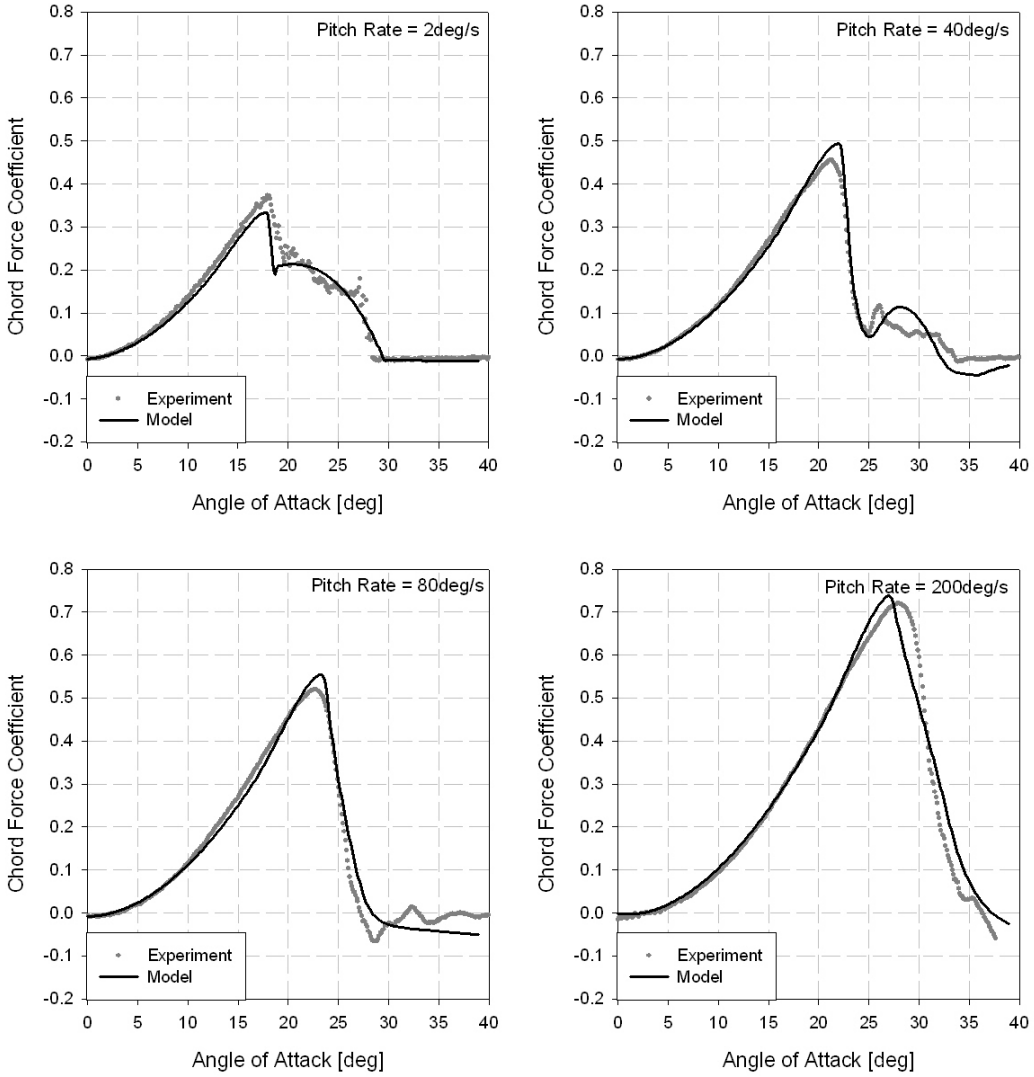

Figure 3.33: Modelling of chord force coefficient during ramp-up, no AJVGs.

Results for the reconstruction of the sinusoidal tests are presented for various values of mean angle of attack in Figure 3.34. There are clearly some aspects of the chord force coefficient which are poorly modelled. The reattachment in all cases happens too quickly and the effect of the light-stall at the mean angle of attack of 12 degrees is woefully under-predicted whilst the effects of stall at the highest mean angles of attack occur too soon. The modelling of the various frequency cases is shown in Figure 3.35. From these charts it is clear that the early re-attachment prediction gets worse at lower frequencies although for this value of mean angle of attack the effects of frequency on the chord force coefficient prediction are generally well captured. Overall, although there is clearly much room for improvement in the modelling it is a significant enhancement over the existing model. The modelling is also perceived to be adequate for the current purpose which aims to compare the effects of the clean RAE9645 aerofoil with those of the same aerofoil equipped with AJVGs.

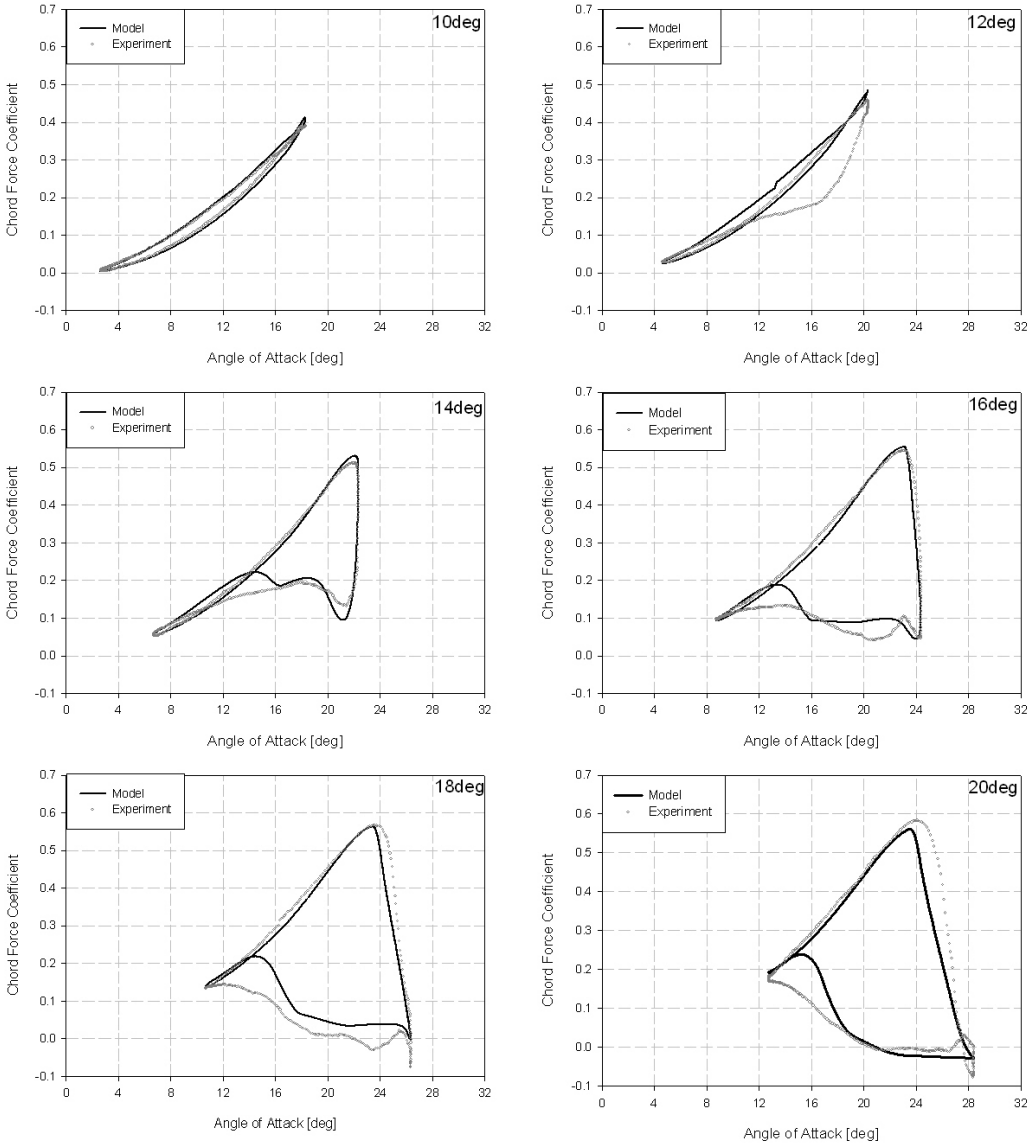

Figure 3.34: Chord force coefficient at various values of mean angle of attack, no AJVGs.

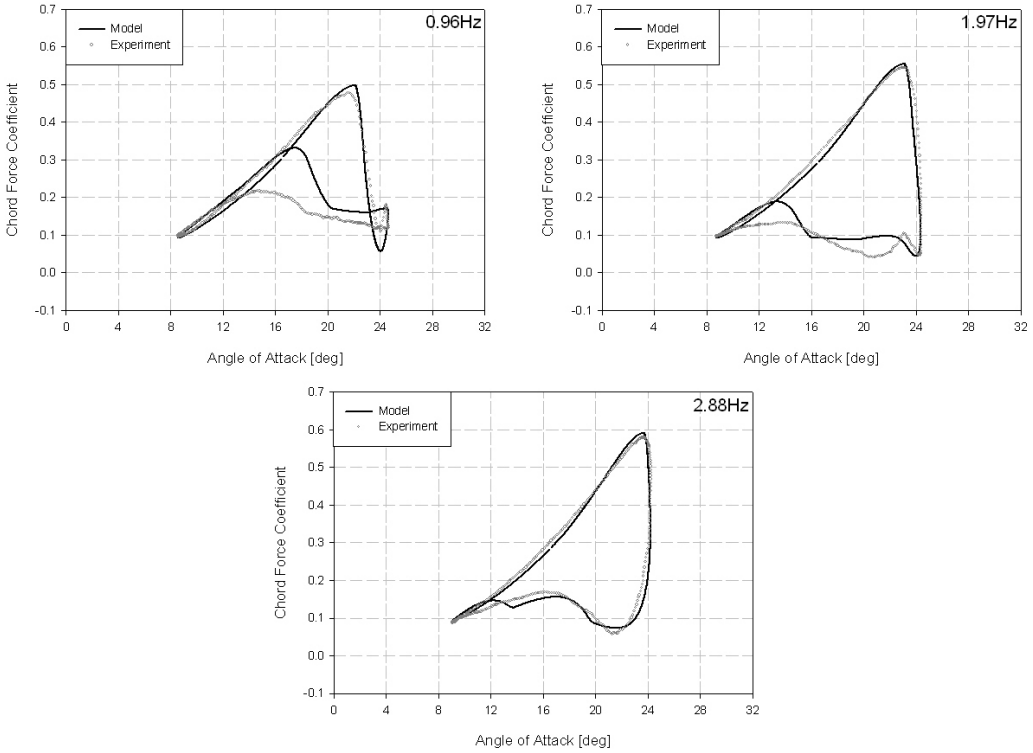

Figure 3.35: Chord force coefficient at various values of pitch frequency, no AJVGs.

3.3.3 Application to the Air Jet Vortex Generator Data

The dynamic model presented in the previous section was developed whilst considering the RAE 9645 aerofoil both with and without AJVGs operating. The same model can therefore be applied, for comparison, to the Air Jet Vortex Generator dynamic data simply by changing the Mach dependent coefficients. However one more addition to the model, not discussed in the previous section, is necessary.

In the static data modelling section it was shown that the trailing edge separation location exhibits hysteresis when the Air Jet Vortex Generators are in operation and therefore the separation location for an upward pitching aerofoil is different to that for a downward pitching aerofoil. However, the static tests were performed by bringing the aerofoil in small steps of angle of attack from either a fully attached or a fully separated condition. In the dynamic case, when the aerofoil reaches its maximum angle of attack, the flow is not necessarily fully separated and so a question arises - when the sign of pitch-rate changes prior to the flow being fully separated, which separation location variation should be used?

Presented in Figure 3.36 are the normal force plots for 3 mean angle of attack values. Included in the graphs are the prediction using the model with firstly the upward values of the separation location and secondly the downward values of the separation location.

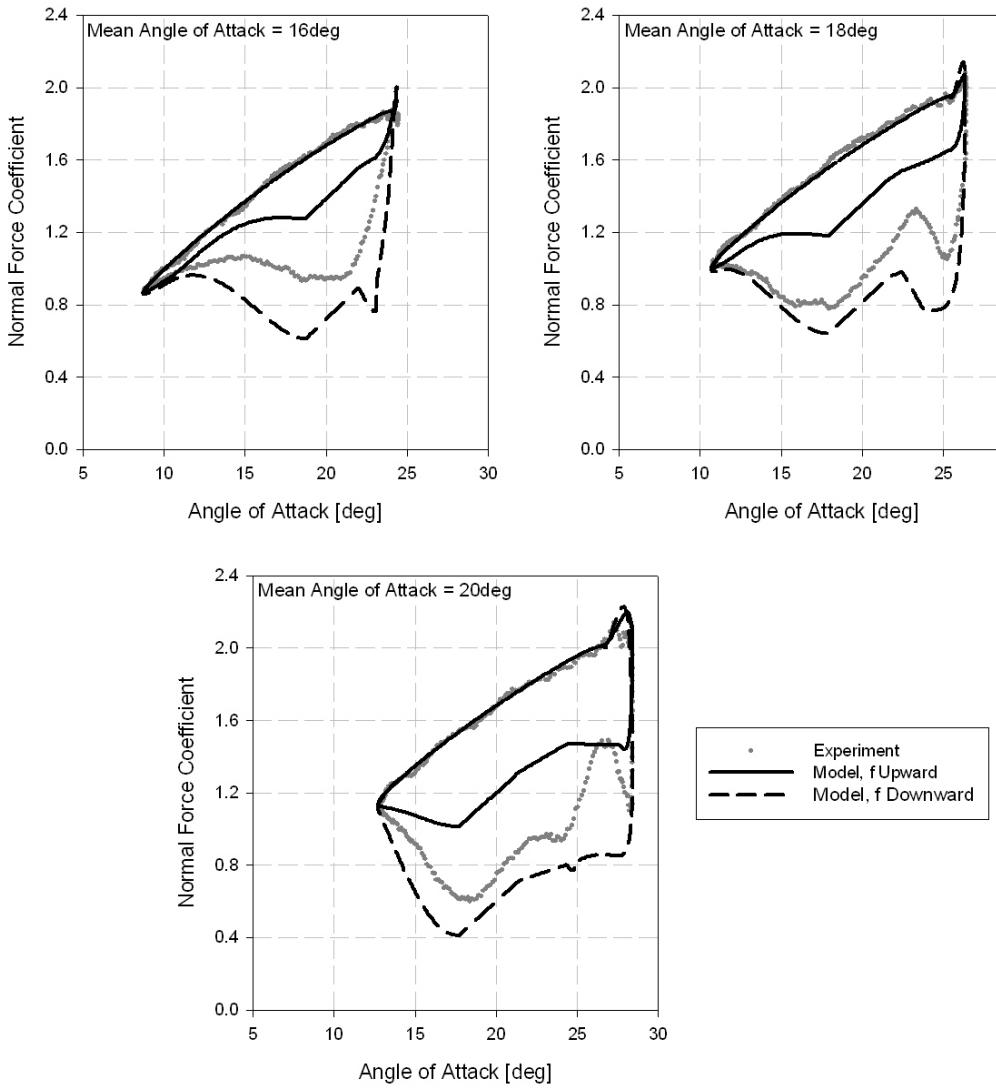

Figure 3.36: Effect on normal force coefficient due to static separation location hysteresis.

Clearly in each case the required value of the separation location must lie in between the two values. Notice that in the 20 degree angle of attack chart, the experimental data are closer to the model using the downward value than is the case in the 16 degree angle of attack chart. This therefore suggests a hypothesis that the separation location required by the model is an average of the two static variations but with the added complication of applying more weight to the downward variation if a larger amount of separation has occurred. This fits in with the static case where the aerofoil has been brought from an entirely separated state and so the downward variation is used. To model this, the upward separation location is used as the weighting between the upward and downward

separation locations such that if the separation location is at the leading edge the downward trend is used whilst if it is at the trailing edge the upward trend is used. The suggested model for the separation location variation for negative pitch rates is therefore:

$$f = f_u^{A_{fd}} f_u + \left(1 - f_u^{A_{fd}}\right) f_d \qquad \textbf{3.32}$$

where f_u and f_d are the upward and downward static variations respectively and A_{fd} is a constant. Additionally, to avoid a discontinuity when the pitch rate changes sign, the value for the separation location given by equation 3.32 is assumed to be attained after a non-dimensional time T_{fd} such that:

$$f = f_u\left(1 - \sin\left(\frac{\pi}{2}\frac{s_{fd}}{T_{fd}}\right)\right) + \left[f_u^{A_{fd}} f_u + \left(1 - f_u^{A_{fd}}\right) f_d\right]\sin\left(\frac{\pi}{2}\frac{s_{fd}}{T_{fd}}\right) \quad s_{fd} < T_{fd}$$
$$f = f_u^{A_{fd}} f_u + \left(1 - f_u^{A_{fd}}\right) f_d \quad s_{fd} \geq T_{fd}. \qquad \textbf{3.33}$$

The prediction, using the final model, of the normal force coefficient during dynamic pitching with Air Jet Vortex Generators is shown for various mean angles of attack in Figure 3.37 and for various frequencies in Figure 3.38.

The accuracy of the modelling appears to be comparable to that for the plain aerofoil with no AJVGs operating. The variation with frequency is not quite so well captured and the strength of the secondary vortex is significantly under-estimated, however, the characteristics of the primary stall vortex are well captured. Also note that with the AJVGs operating the flow is staying mostly attached up to and including the 14 degree mean angle of attack case. This represents the main advantage gained through the use of the AJVGs and is well captured by the model.

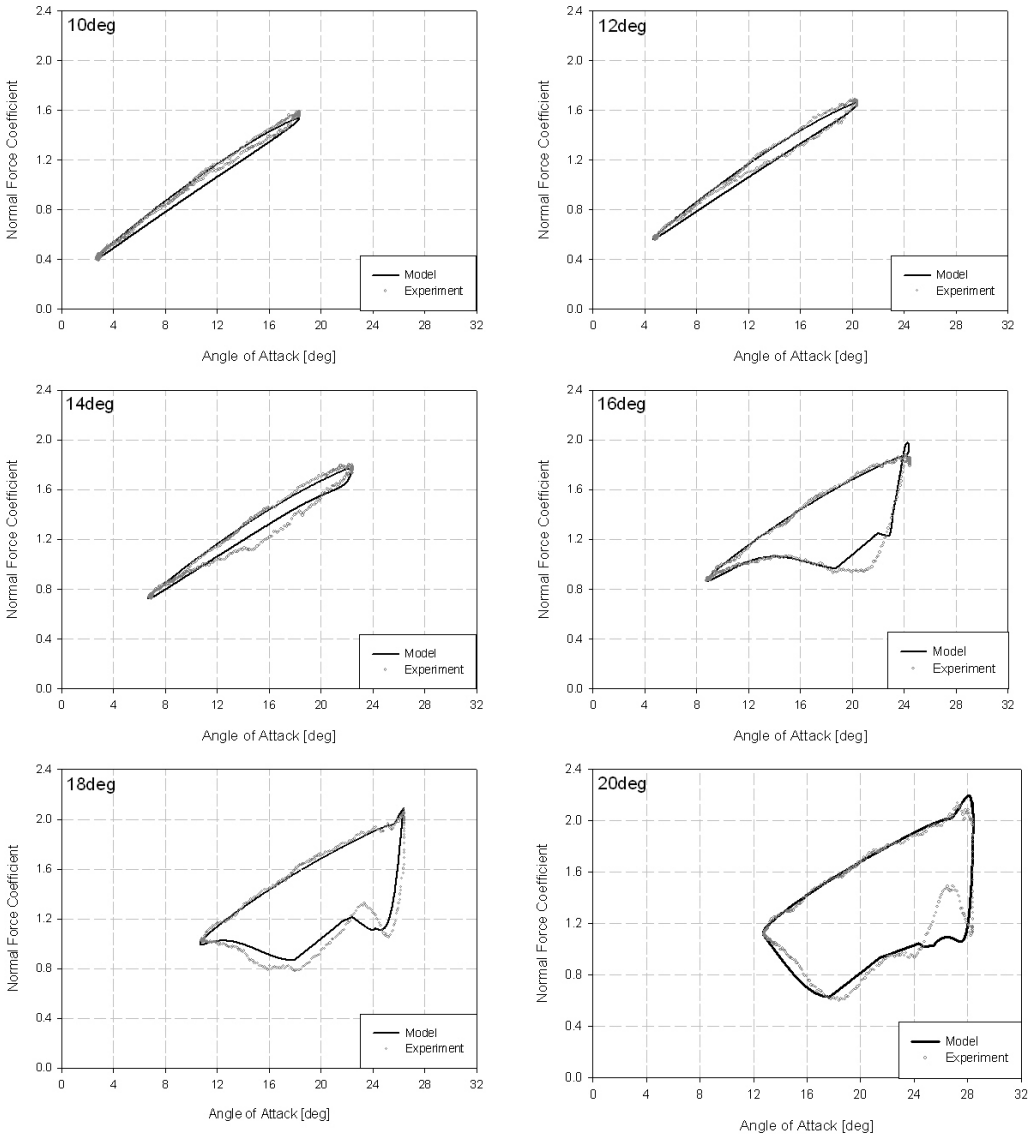

Figure 3.37: Normal force coefficient at various values of mean angle of attack, with AJVGs.

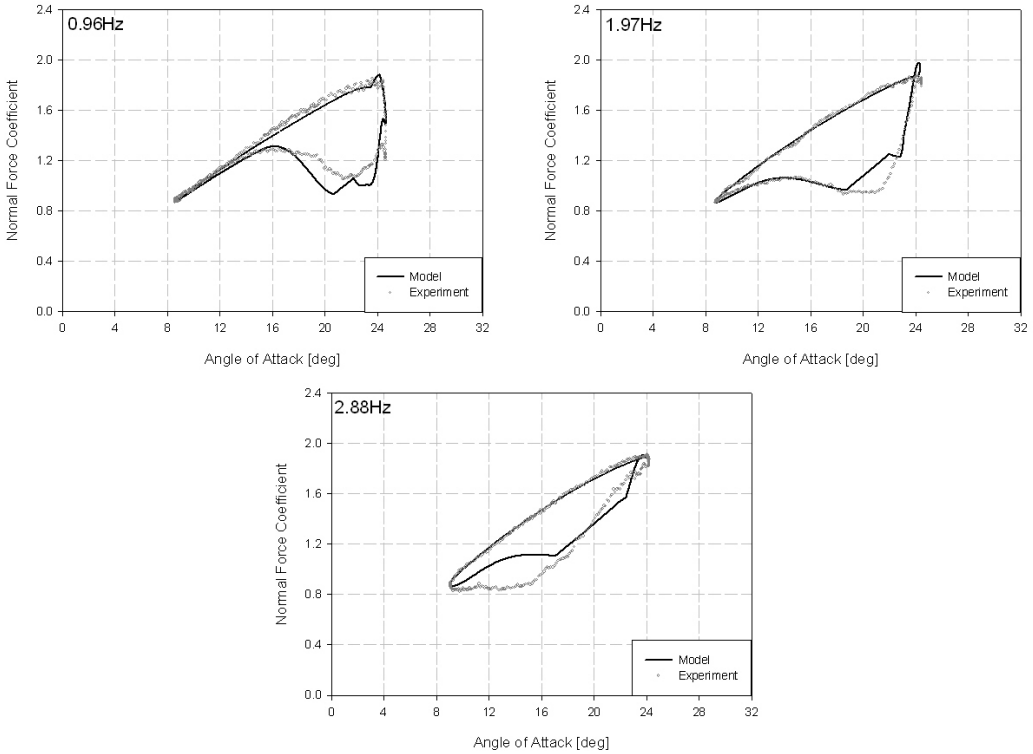

Figure 3.38: Normal force coefficient at various values of pitch frequency, with AJVGs.

The results for the pitching moment coefficient prediction for the AJVG-equipped aerofoil are shown in Figure 3.39 and Figure 3.40. The results are clearly not as good as those for the normal force coefficient. The delay in the increase in nose down pitching moment is captured but the magnitude of the moment due to the dynamic stall vortex in the light-stall cases is not well predicted and the secondary vortex of the deep stall cases is under-estimated. Both of these effects however are actually amplifications of errors in the normal force modelling. Note that in the 16 degree mean angle of attack case there is a clear prediction of the presence of a large dynamic stall vortex in both the normal force plot and the pitching moment plot and that both coefficients show an early reattachment in the 14 degree mean angle of attack case. In summary, the deep stall cases display good correlation for both the normal force and pitching moment coefficients with the exception of the secondary vortex while the light-stall cases over-predict the strength of the primary vortex and predict an early reattachment. These trends are also well illustrated in the plots at various frequencies.

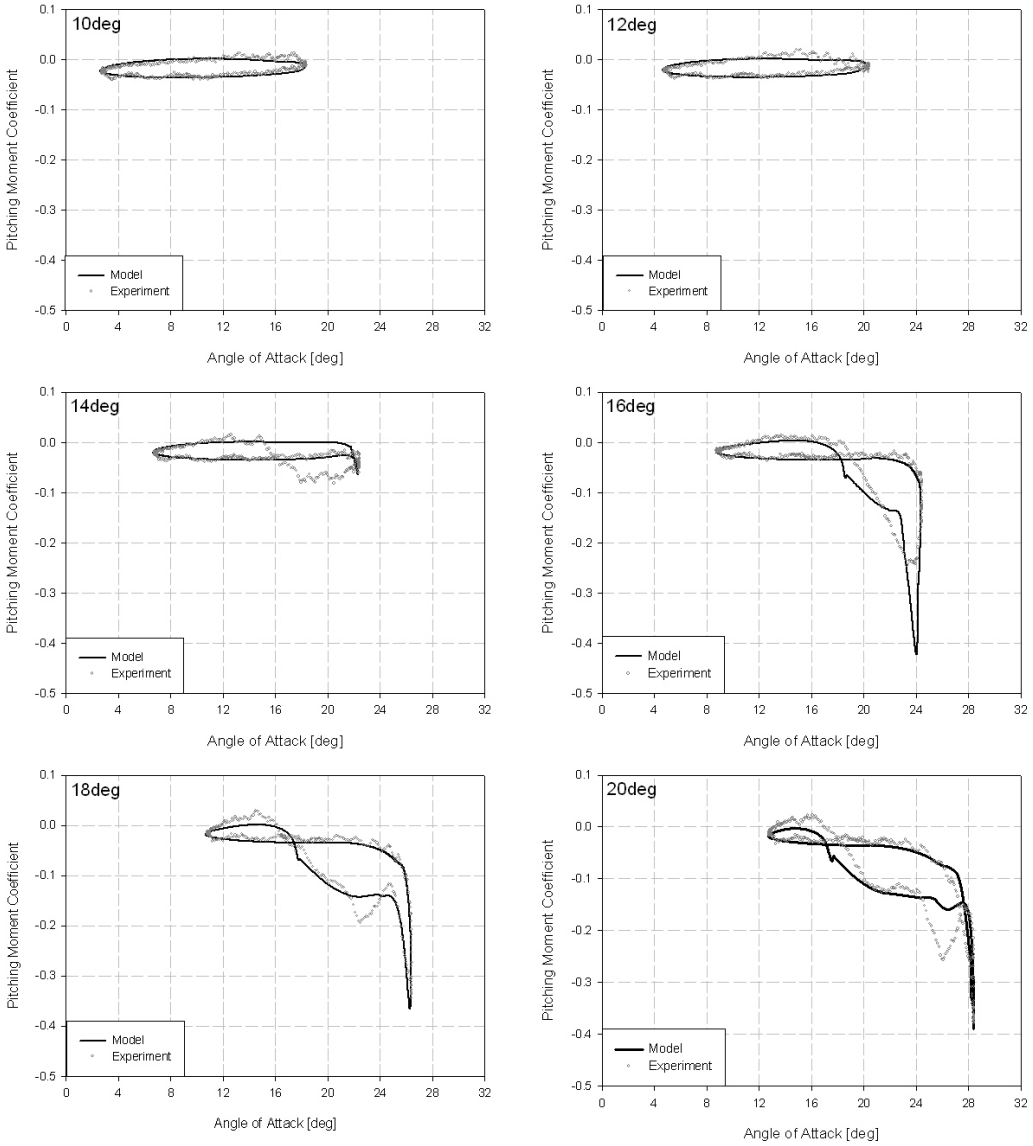

Figure 3.39: Pitching moment coefficient at various values of mean angle of attack, with AJVGs.

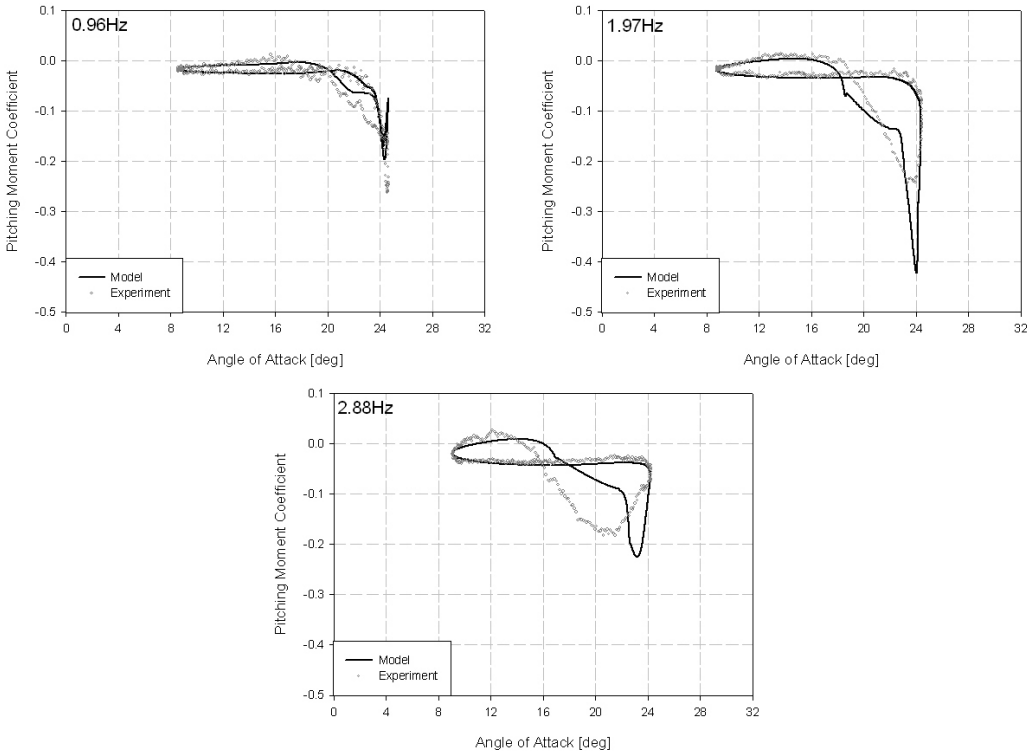

Figure 3.40: Pitching moment coefficient at various values of pitch frequency, with AJVGs.

Finally, the plots for the chord force coefficient are presented in Figure 3.41 and Figure 3.42. The general characteristics are reasonably captured; however as for the pitching moment prediction the reattachment is predicted to occur too soon, particularly in the light stall cases, this being particularly apparent in the lowest frequency case. Also the drop in the chord force coefficient is predicted to occur too late in the highest mean angle of attack case.

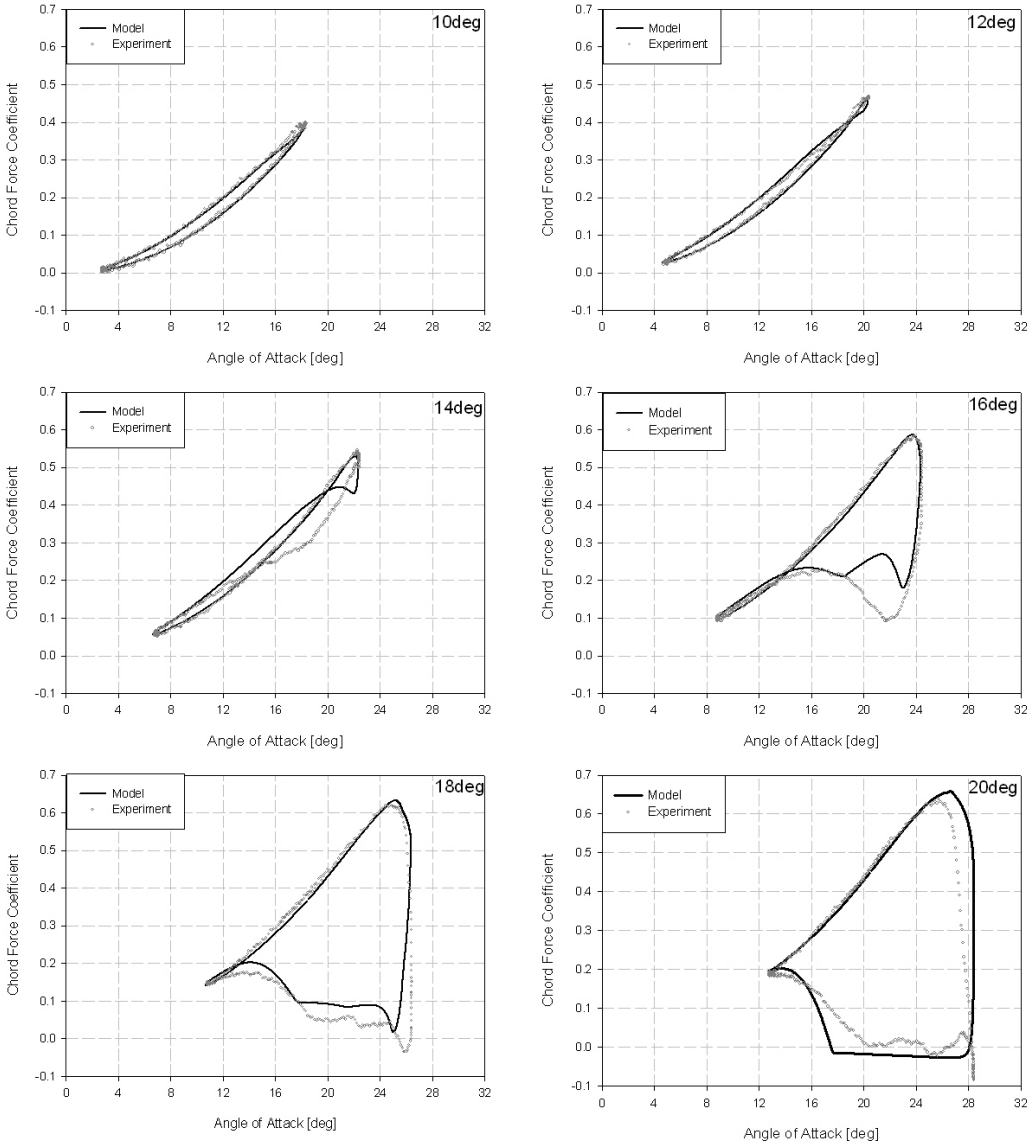

Figure 3.41: Chord force coefficient at various values of mean angle of attack, with AJVGs.

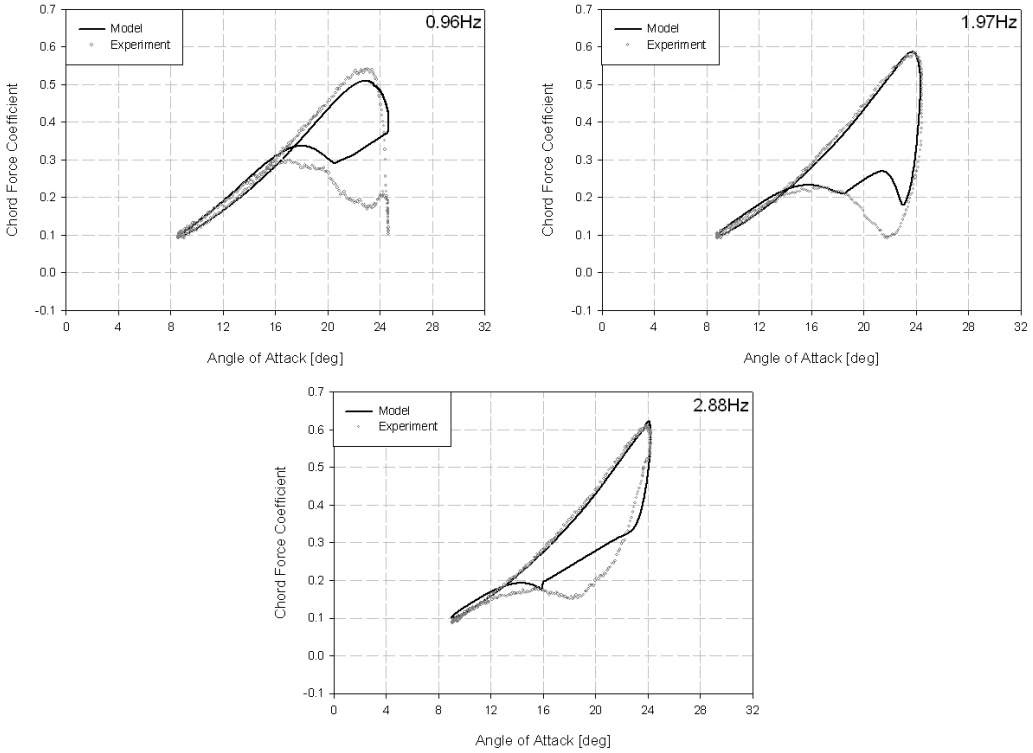

Figure 3.42: Chord force coefficient at various values of pitch frequency, with AJVGs.

Overall, the dynamic stall model with the suggested modifications provides a reasonable prediction of the behaviour over a range of frequencies and angles of attack for both the standard RAE 9645 aerofoil and for the aerofoil equipped with AJVGs. The correlation with the AJVG data is not as good as that for the clean aerofoil, however the main differences between the basic and AJVG equipped aerofoils are sufficiently captured. In conclusion, it is believed that the modifications suggested by the author have led to a model capable of adequately representing the effects due to AJVGs to enable a full rotor performance analysis.

3.4 Performance Enhancement of an Advanced Rotor

Having developed a model for the aerodynamic effects due to AJVGs, it may now be used within a rotor performance program to predict the advantages to be gained for the rotor as a whole. An advanced baseline rotor, based on the BERP III EH101 main rotor blade, is used for the evaluation. The use of an advanced platform ensures that a fair prediction of the advantages to be gained through active technologies is produced as the improvement over a low technology baseline could over-estimate the utility of a new technology. These performance predictions will then form the foundation upon which a discussion into the overall utility of AJVGs for helicopter rotors may be based. Before

the analysis is presented, a discussion on how the available data has been used is necessary as this highlights any limitations in the analysis which should be considered in the discussion which follows.

3.4.1 Application of the Data

It has been shown above that the unsteady aerodynamic coefficients due to AJVGs can be reasonably reproduced using the newly developed model. However, setting the input coefficients used by the model requires a range of experimental data. Unfortunately, data is only available for very low Mach numbers and so assumptions need to be made about higher Mach numbers in order to use the model within a rotor performance code, which will obviously encounter a wide range of Mach numbers over the rotor disc.

It has, however, been possible to set inputs for the clean aerofoils based on available data from the first generation model such that the new model has been made to behave like the first generation model (for example, recall that the newly proposed pre-stall variation has been based on the first generation model inputs). Whilst this does not utilise the increased fidelity of the new model, it avoided the need for a vast range of data and ensured that the baseline was in reasonable agreement with the previous predictions for the rotor. Using this method, the appropriate values for the coefficients were thus set for each of the aerofoils used in the baseline blade at Mach numbers ranging from 0.3 to 0.95 at intervals of 0.05 (as is standard for the 3rd generation model). An additional interpolation point for the low Mach number results was then added such that at Mach numbers of less than 0.1 the data presented above was used. For Mach numbers between 0.1 and 0.3 the aerofoil coefficients were interpolated between the new data and that based on the available 1st generation model data.

When AJVGs are to be used, the low Mach number coefficients are simply replaced by the AJVG data at the appropriate radial locations. In doing so, any 3-dimensional effects due to the AJVGs have been neglected. These effects should be greatest at the edges of the blown region, however as long as the blown region is of reasonable length the overall effects are expected to be small. In addition, the effects of any flow in the radial direction are not accounted for, however these effects should not be critical as the AJVGs are predominantly intended for use near stall on the retreating side of the disc where radial, or cross-flow, is reduced in comparison to the front and rear of the rotor disc. The investigation to be presented below employs the AJVGs along the entire section of blade which utilises the RAE 9645 aerofoil (as used in the University of Glasgow wind tunnel

experiments) i.e. from 68.5% radius to 84% radius. At the ends of the section the AJVG equipped aerofoil data is interpolated linearly to the baseline data for the adjacent, clean aerofoils.

The AJVGs were initially considered to be operating at Mach numbers below 0.1, above which the starting and stopping effects of the AJVGs are assumed to be captured through the interpolation to the uncontrolled aerofoil data. The use of the AJVGs below a given Mach number is reasonable as it has been suggested that they should only operate for a segment of blade azimuth on the retreating side so as to reduce operating requirements. Initial results, however, suggested that only operating the AJVGs below a Mach number of 0.1 is insufficient. At low thrust loadings, the advance ratio associated with stall gave a sufficiently low Mach number on the retreating side but the reduced severity of stall meant that the AJVGs did not make a significant difference. At higher thrust loadings, the maximum advance ratio before stall was insufficient for a reasonable portion of the blade to experience a Mach number below 0.1 for a sufficiently long period of time.

Clearly what is required is valid data with and without the AJVGs at higher Mach numbers but unfortunately, due to the limitations of the experiment, this is not available. Therefore, in order to give some idea of the usefulness of the AJVGs, the available low Mach number data was applied up to Mach numbers of 0.4 above which the data from the reproduced 1st generation results was used. For a fair comparison the clean aerofoil data from the experiment was also used up until a Mach number of 0.4.

The above discussion has highlighted the various assumptions made in applying the AJVG data to the rotor performance code. Clearly these assumptions will lead to inaccuracies, however they were considered to be necessary in order to obtain results from the data available at the present time. It is anticipated that the use of data at inappropriate Mach numbers should not affect the general trends too much as the incompressible data has only been extended up to a Mach number of 0.4. The predicted trends are therefore expected to be correct, although there will clearly be some doubt as to the precise magnitude of the benefits. It is therefore suggested that a similar investigation to that presented below should be carried out once data at higher Mach numbers becomes available.

Using the methodology thus outlined, the dissertation will now examine the change to the loads due to the AJVGs for an aircraft operating at firstly high, and then low, blade loading. (Note that the blade loading is defined as the thrust coefficient divided by the

solidity). The analysis provides insight into the overall effect due to the AJVGs and also gives confidence that the model is behaving correctly.

3.4.2 Analysis of a High Blade Loading Case

The following analysis will be performed for a flight case with a blade loading of 0.21 and an advance ratio of 0.29. This case has been found to lie on the stall boundary and is therefore ideal for investigating the effects due to AJVGs. Consider first the effects on the lift coefficient.

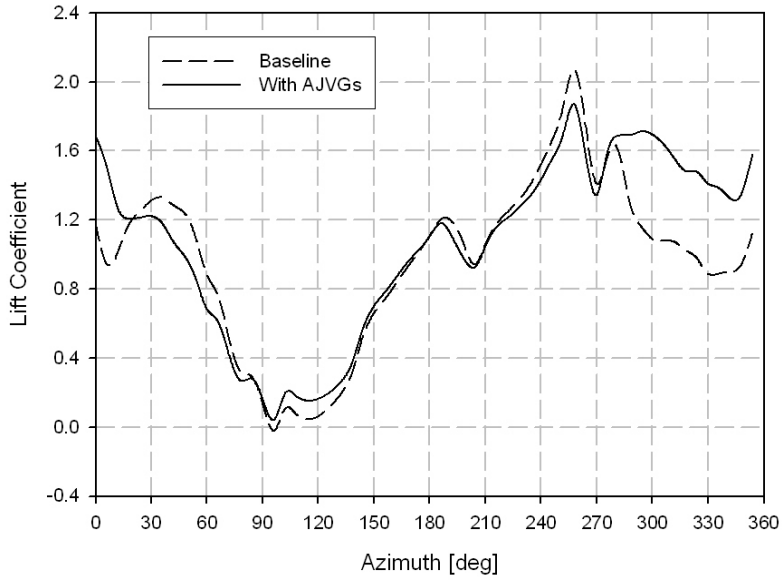

Figure 3.43: Azimuth Variation of Lift Coefficient, r=0.72R, C_T/s_r=0.21.

The azimuth variation of the lift coefficient at 72% radius, shown in Figure 3.43, reveals that the severity of the retreating blade stall is significantly reduced whilst the radial variation shown in Figure 3.44 also shows that the lift is indeed maintained all along the AJVG equipped section.

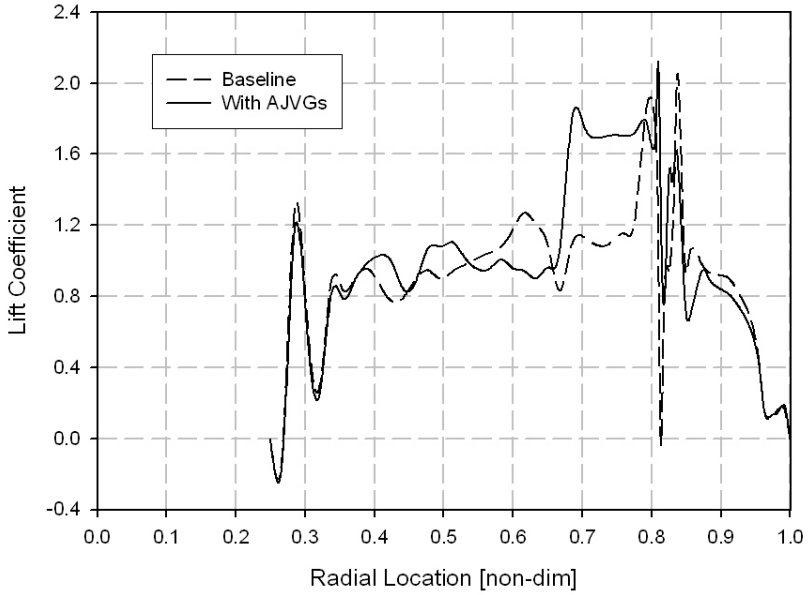

Figure 3.44: Radial Variation of Lift Coefficient, ψ=300 deg, C_T/s_r =0.21.

Figure 3.45 shows the lift force contours looking down onto the rotor disc (direction of flight up the page). The area highlighted in pink displays a substantial difference in the lift contours. As seen in the previous figures, the AJVGs have encouraged the flow to remain attached such that lift is sustained for longer over the high lift region of the blade.

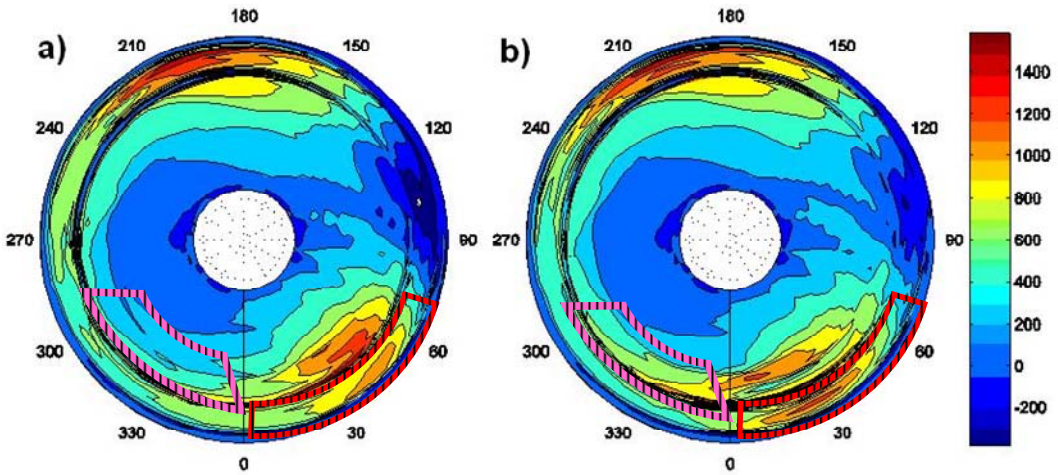

Figure 3.45: Lift Contours, a) no AJVGs b) with AJVGs, C_T/s_r =0.21.

Similar effects are in evidence for both the pitching moment and drag forces. Figure 3.46 shows the azimuth variation of both coefficients again at the 72% radius. The reduction in the stall severity due to the presence of the AJVGs has resulted in a much smaller divergence of the pitching moment and drag force coefficients on the retreating side.

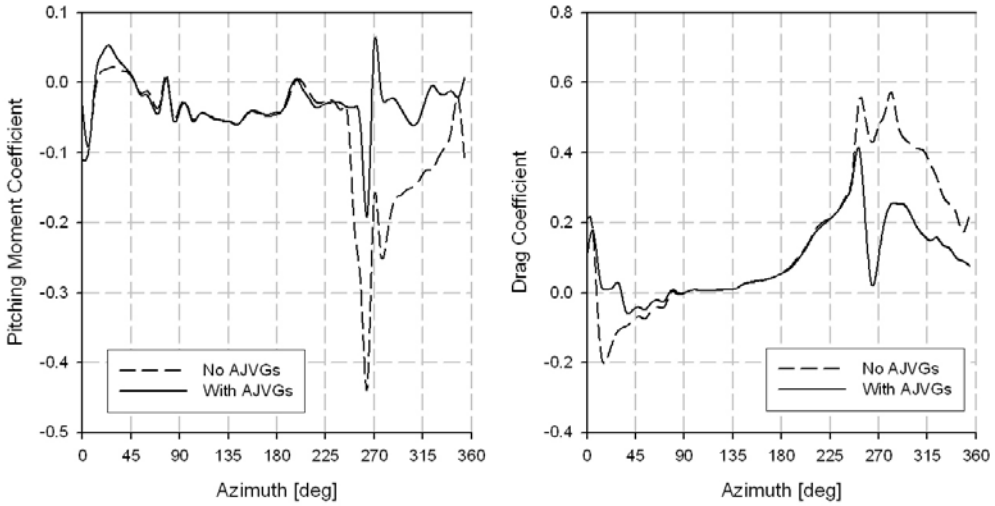

Figure 3.46: Azimuth variation of pitching moment (left) and drag force (right) coefficients, r=0.72R, C_T/s_r =0.21.

The contour plots for the pitching moment are shown in Figure 3.47. The difference with and without the AJVGs is even more obvious than for the lift force contours. The divergence of the pitching moment is clearly much reduced over the entire fourth quadrant of the azimuth for the whole portion of the blade equipped with the AJVGs.

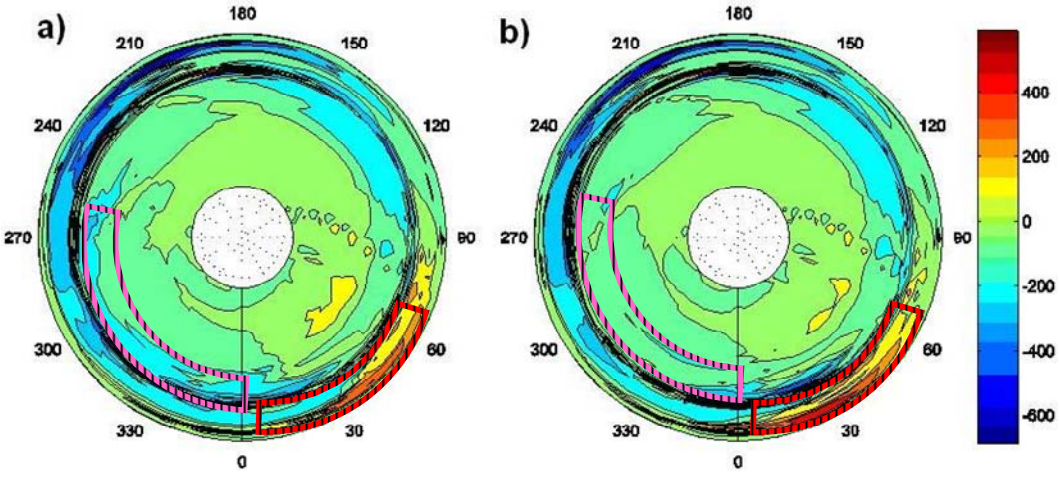

Figure 3.47: Pitching Moment Contours, a) no AJVGs b) with AJVGs, C_T/s_r =0.21.

Similarly, the contribution of the aerodynamic drag to the rotor torque is shown in Figure 3.48. The torque is plotted as opposed to the drag as the torque is more relevant in the integration for the total rotor power. The drag rise, and therefore the torque, in the fourth quadrant is much reduced suggesting that the rotor power will also be reduced.

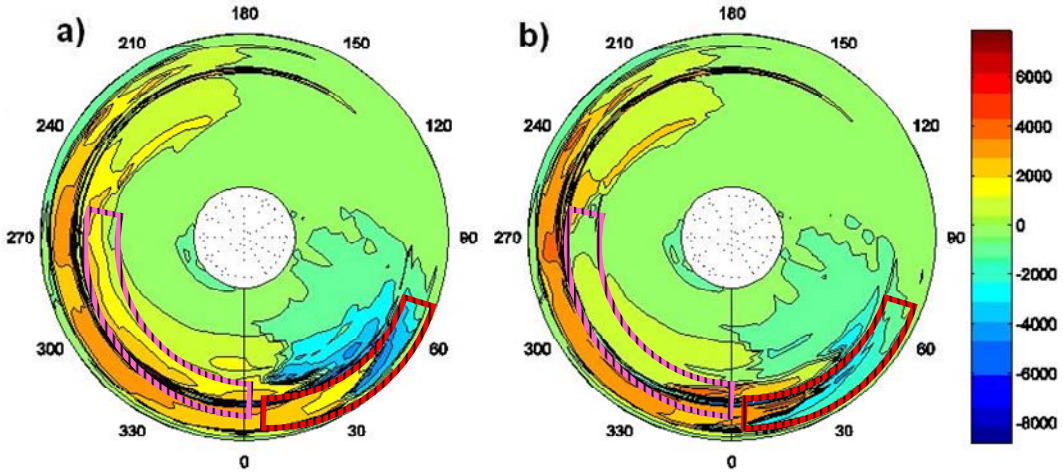

Figure 3.48: Torque Contours, a) no AJVGs b) with AJVGs, C_T/s_r =0.21.

So far, only the regions highlighted in pink on the contour plots have been discussed. Those highlighted in red, however, also show significant improvements in the lift, pitching moment and drag contours. These effects are due to small alterations in the rotor trim. The alleviation of the stall characteristics on the retreating blade mean that trim may be obtained with reduced values of both collective pitch and longitudinal cyclic pitch. This results in changes to the angle of attack contours as shown in Figure 3.49.

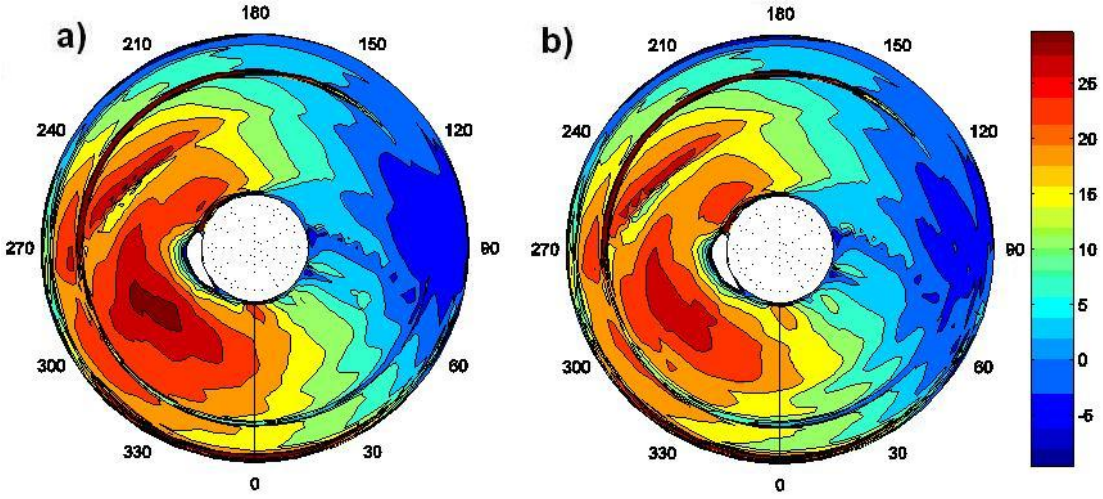

Figure 3.49: Angle of Attack Contours, a) no AJVGs b) with AJVGs, C_T/s_r =0.21.

The angle of attack is generally reduced on the retreating side while the area of negative pitch on the advancing side is also reduced. Importantly, the reduction in angle of attack at the rear of the disc means that the flow is able to reattach sooner as shown in Figure 3.50.

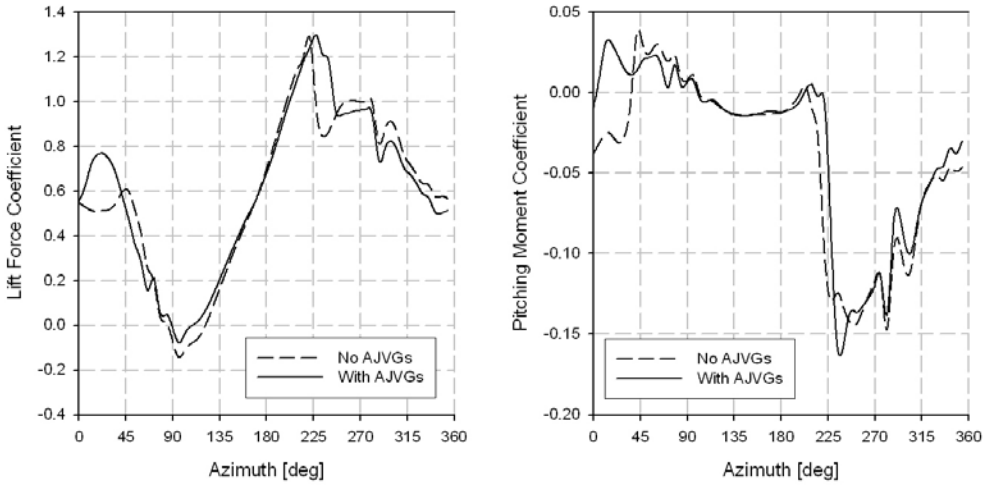

Figure 3.50: Azimuth variation of lift force (left) and pitching moment (right) coefficients, r=0.91R, C_T/s_r =0.21.

As suggested previously, the effects due to the reduction and delay of stall should be seen in the control load waveform due to the minimised pitching moment divergence leading to a reduction in the blade torsion response. The azimuth variation of the control loads is shown in Figure 3.51. Over the fourth quadrant of the rotor disc, the severity of the retreating blade stall has been reduced such that the pitching moment and drag force divergence are significantly lower. This culminates in a reduction in the negative control loads for much of the retreating half of the rotor azimuth.

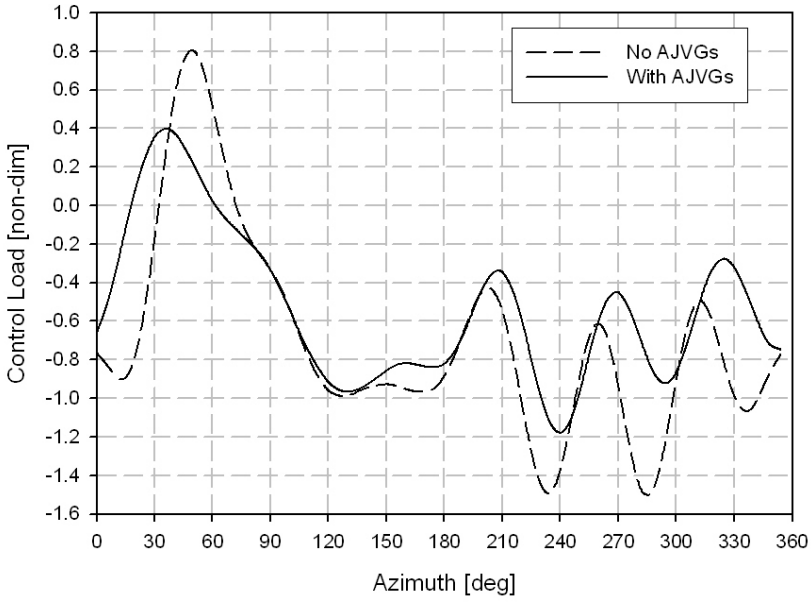

Figure 3.51: Pitch control loads with and without AJVGs, C_T/s_r =0.21.

In addition, the greater lift potential resulting from the operation of the AJVGs also means that the control angles required for trim are diminished. This, together with the influence of the AJVGs, means that the flow near the tip of the blade reattaches closer to

the rear of the rotor disc on the advancing side. Overall this gives a reduction in the maximum positive control load on the advancing side of the rotor. The two mechanisms together give a substantial reduction in the half peak-to-peak vibratory control load, thus suggesting that this parameter can indeed be used as an indicator for stall.

3.4.3 Analysis of a Low Blade Loading Case

At a lower blade loading, the stall characteristics of the rotor can be expected to be less influenced by the retreating blade. This section will therefore investigate the use of AJVGs in these conditions. Once again, an advance ratio close to the stall boundary is chosen, with the analysed condition being a blade loading of 0.17 and an advance ratio of 0.395.

The azimuth variation, at 70% radius, of the lift and pitching moment coefficients is shown in Figure 3.52. Whilst the AJVGs are clearly having a noticeable influence on the retreating blade stall, the magnitude of the effect is much reduced in comparison to the high blade loading case. The baseline magnitude of lift and pitching moment divergence due to the stall is smaller due to the lower blade loading and therefore the influence of the AJVGs on the overall rotor performance can be expected to be reduced.

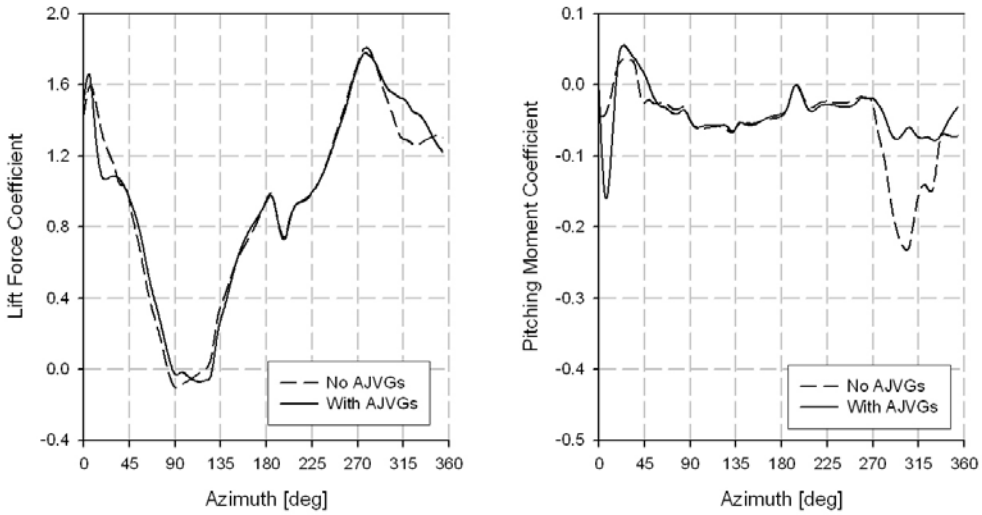

Figure 3.52: Azimuth Variation of Lift Force and Pitching Moment Coefficients, r=0.70R, C_T/s_r =0.17.

Plotting the pitching moment contours, as shown in Figure 3.53, reveals that the overall effect on the fourth quadrant is much less than observed for the high blade loading case. In addition, the AJVGs have had very little influence on the large region of negative pitching moment on the advancing side suggesting that the secondary mechanism of a change in trim is not occurring.

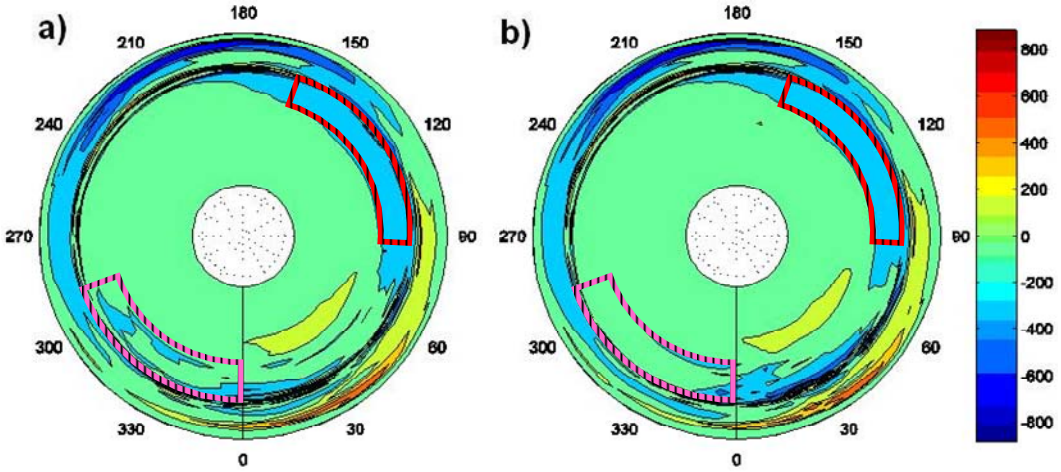

Figure 3.53: Pitching Moment Contours of Merlin, a) no AJVGs b) with AJVGs, C_T/s_r =0.17.

This is confirmed by comparing the control angles with and without AJVGs as shown in Figure 3.54. This means that a powerful mechanism identified in the higher blade loading result is not present in the lower blade loading case and therefore any associated performance enhancements will not occur.

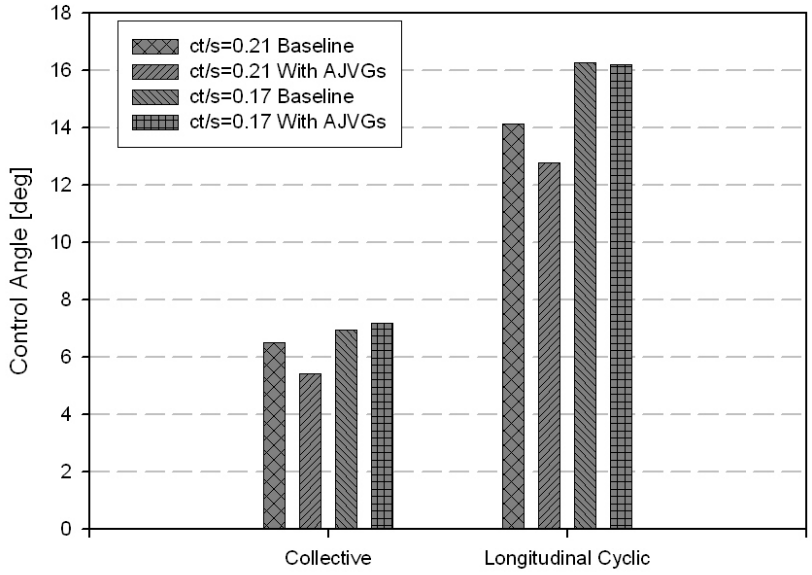

Figure 3.54: Control angles with and without AJVGs.

The overall effect on the control load waveform at low blade loading is presented in Figure 3.55. Clearly the AJVGs have had much less influence. Not only are the retreating side loads little affected, but also the lack of a change to the trim means that the large advancing side loads have not been influenced. The reduced influence of the AJVGs at this blade loading is therefore reflected in the control load trace and its peak-to-peak value.

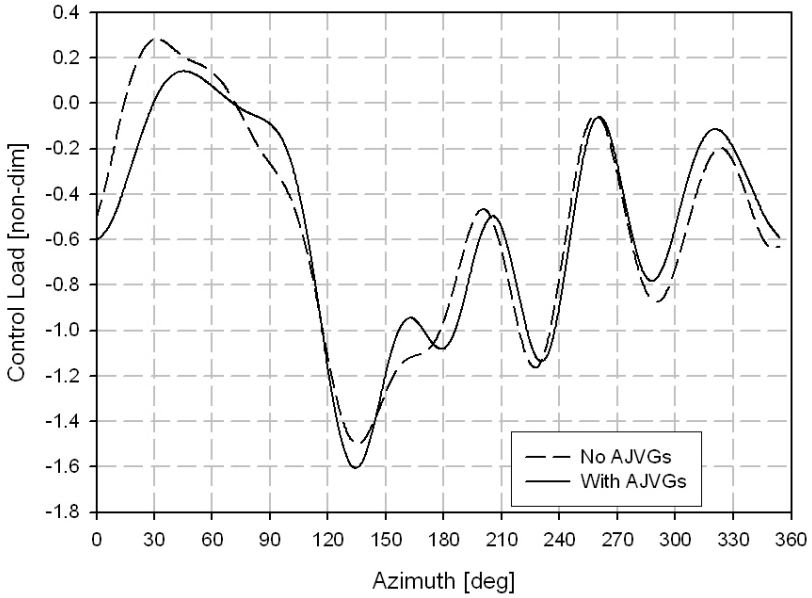

Figure 3.55: Merlin Pitch Control Loads, C_T/s_r =0.17.

The analysis in these two sections has revealed that, at higher blade loading, the AJVGs are having a significant influence on the retreating blade stall and, through interacting with the rotor trim, are also advantageously affecting the advancing blade loads. At lower blade loading, the influence of the AJVGs is much reduced as the retreating blade stall for the baseline blade is less severe. This reduced influence also means that the secondary mechanism of affecting the trim is also not present and therefore the overall effectiveness of the AJVGs is minimal. More cases will now be considered to better quantify the effect of AJVGs along the stall boundary.

3.4.4 Stall and Power Benefits due to Air Jet Vortex Generators

It has been previously suggested, Chan and Brocklehurst (2001), and confirmed by the analysis in the previous two sections that the vibratory control loads may be used as an indicator of blade stall. Plotted in Figure 3.56 are the vibratory control loads for a variety of advance ratios and blade loadings with and without the AJVGs.

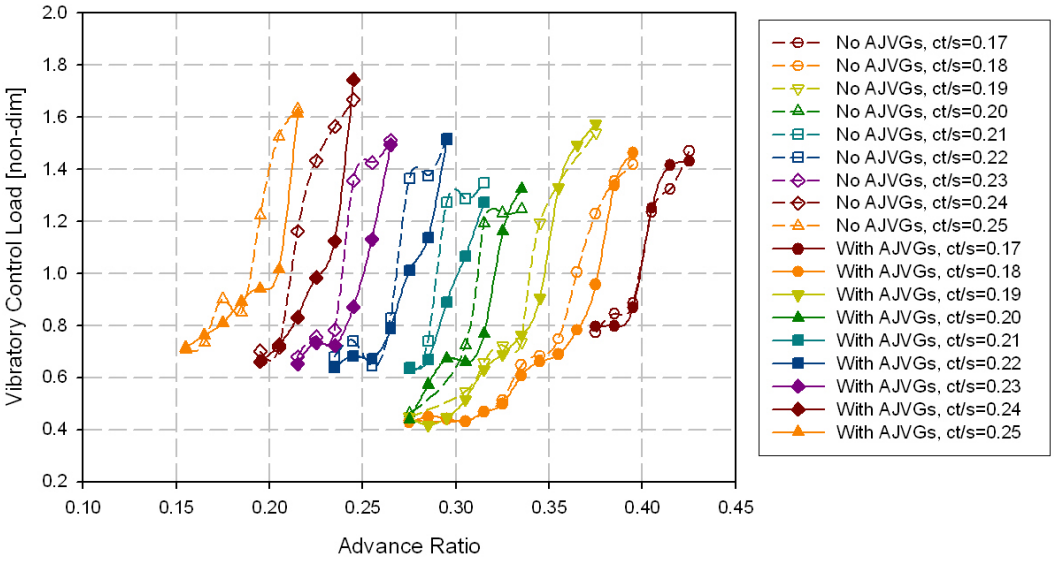

Figure 3.56: Vibratory control loads with and without AJVGs.

At each blade loading, the rise in the vibratory control loads is steadier with AJVGs than it is without AJVGs such that the attainment of a given value is delayed to a higher advance ratio. As may be expected from the analysis in the previous sections, the effectiveness reduces as the blade loading is decreased with almost no advantage at the lowest blade loading. Similar effects may be seen in the rotor power shown in Figure 3.57 with the delay in stall suggested by the reduced vibratory control loads clearly resulting in an equivalent delay in the power rise.

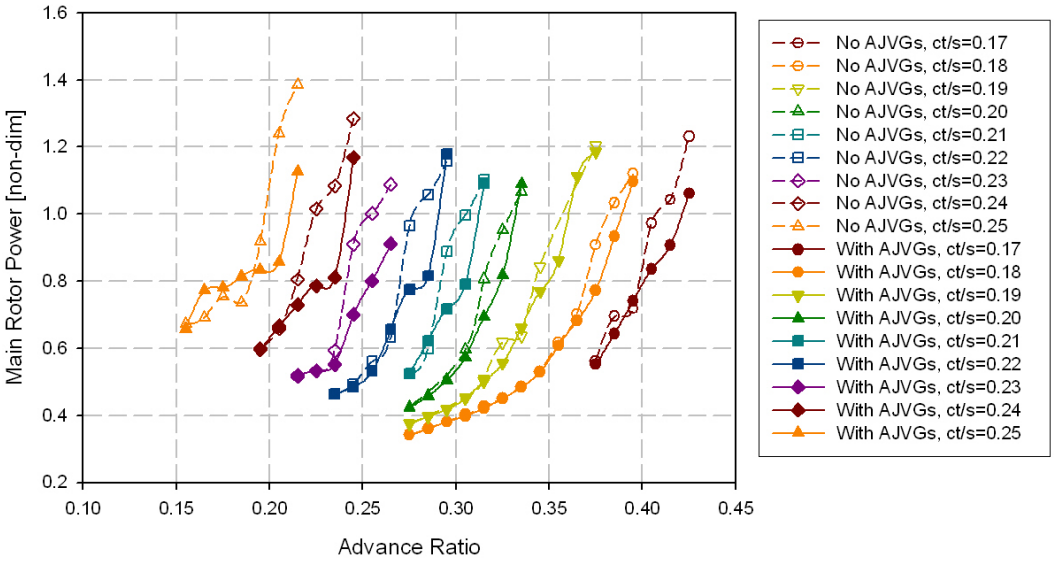

Figure 3.57: Main rotor power with and without AJVGs.

Chan and Brocklehurst (2001) suggested that the flight envelope may be approximated by the attainment of a constant value of vibratory control load. Figure 3.58 shows the

vibratory control load data for the non-blown aerofoil. At each thrust loading a steep rise in the vibratory control loads associated with the stall occurs when a non-dimensional value of around 1.0 is obtained (note that all the control load data presented herein has been normalised by the actual value at this point). This, therefore, defines the critical value above which blade stall is assumed to occur.

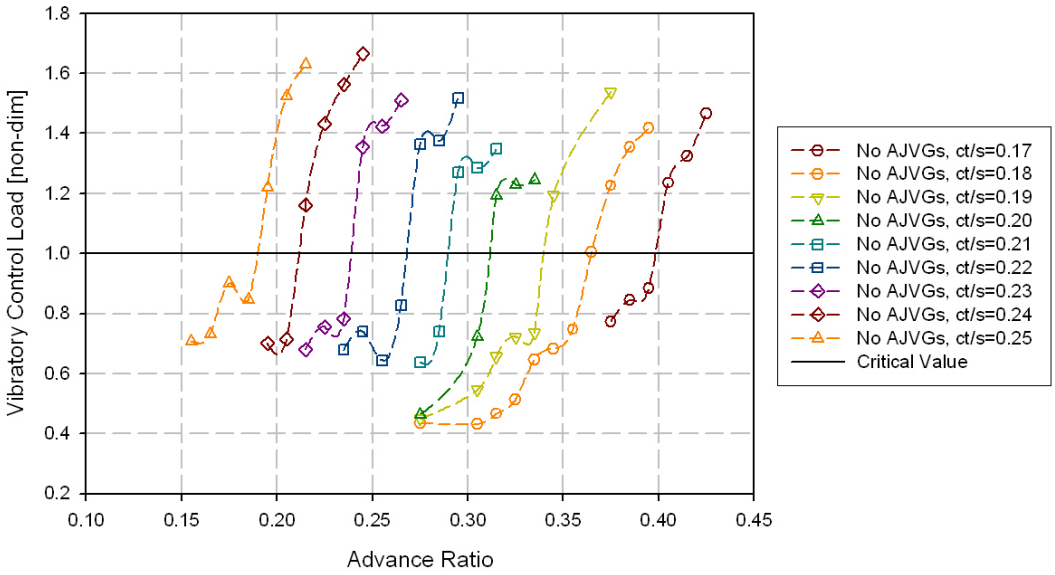

Figure 3.58: Definition of Critical Value of Vibratory Control Load.

From the data shown in Figure 3.56, the advance ratio at which stall occurs may be approximated through interpolation of the data for the critical value of vibratory control load. A simple linear interpolation may therefore be used, for both the blown and non-blown data sets, to define the stall boundaries as shown in Figure 3.59.

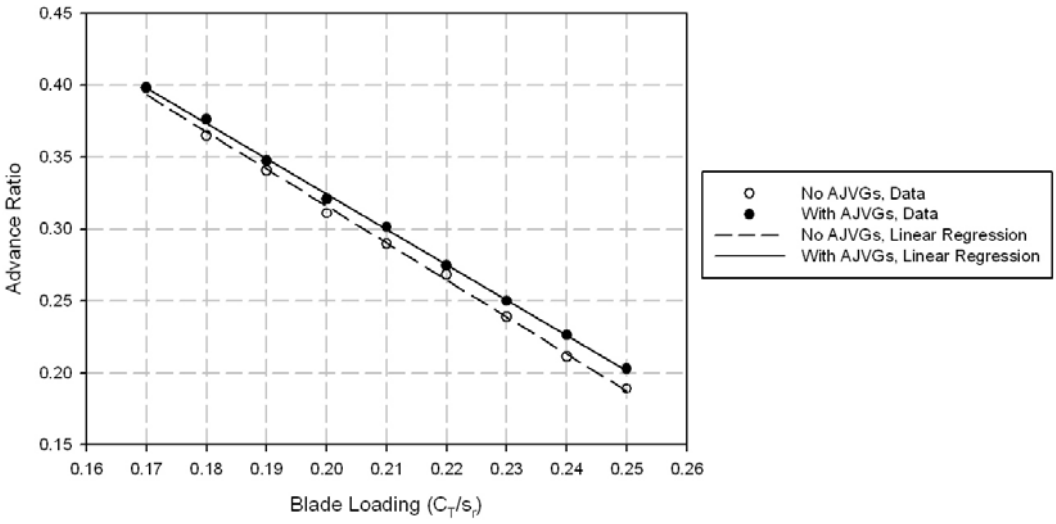

Figure 3.59: Envelope expansion using AJVGs.

The use of the AJVGs is giving a clear increase in the helicopter flight envelope. Although the increase at the lowest thrust loading case is hardly noticeable, at the highest thrust loading an increase equivalent to approximately 6 knots true air speed is obtained.

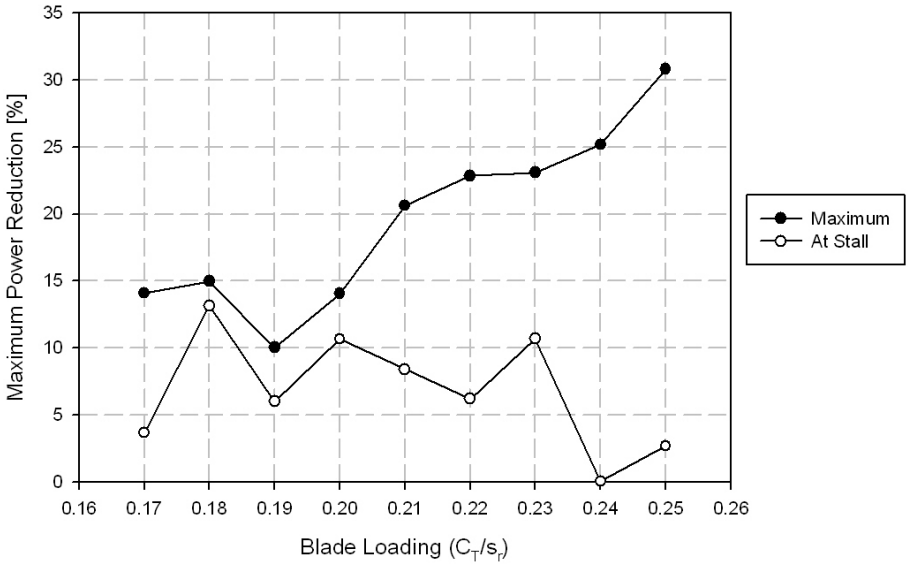

Figure 3.60: Maximum power reduction due to Air Jet Vortex Generators.

Figure 3.57 also suggests that significant power reductions are available using AJVGs and the maximum power reduction is plotted against blade loading in Figure 3.60. These figures, however, are extremely flattering as the baseline cases associated with these figures exhibit excessive stall characteristics such that in practice the rotor is unlikely to be operated for extended periods in these conditions due to excessive loads, adverse handling qualities and large (most likely unachievable) power requirements. If, however, the powers at the stall boundaries are compared, the reduction due to AJVGs is still of the order of 10 per cent, thus suggesting that operation close to the stall boundary is much more efficient if AJVGs are in use. It should be recalled, however, that the AJVGs have little influence over the aerodynamic coefficients away from stall such that they provide no power benefit at lower flight speeds. Therefore if the aircraft, with or without AJVGs, is to be operated only within the stall boundary then the sole advantages to be gained from the AJVGs is the delay of this boundary to higher speeds and the reduction in power in the small range of advance ratio just prior to stall. The overall effect of these advantages on some high speed flight profiles will therefore be considered in the following section.

3.4.5 Operational Benefits due to Air Jet Vortex Generators

The overall operational benefits due to AJVGs will be assessed using the mission analysis methods presented by Newman (1994). Newman (1994) uses actuator disc models for both the main and tail rotor powers and simplified fuel consumption rules to assess fuel flow rates and thus to analyse mission profiles. Newman's methods for the tail rotor (scaled to the size of the EH101) and fuel consumption have been used, but with the main rotor powers replaced by those presented in the previous section, thus accounting for the effects due to the stall of the main rotor and the advantage to be gained through the use of AJVGs. Full mission profiles will not be analysed here, but instead, as the main utility of the AJVGs is improving the performance close to the stall boundary, some high-speed 'dash' cases will be investigated.

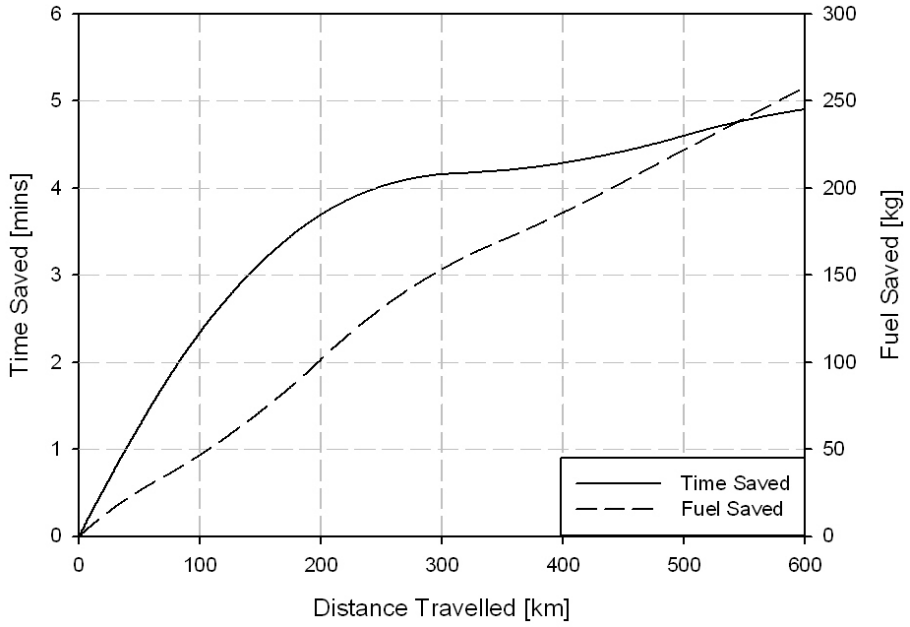

Figure 3.61: Savings in time and fuel due to a maximum speed dash with AJVGs.

Consider first a high-speed dash such that the aircraft is flying at the stall boundary. The mass of the aircraft at the start of the dash is assumed to be that equivalent to a blade loading of 0.25. As fuel is used, the aircraft weight and blade loading is reduced accordingly. The advance ratio throughout is then calculated according to the linear regression of the data shown in Figure 3.59 thus ensuring the aircraft is operating at the stall boundary. Using the obtained blade loading and advance ratio, the main rotor power is approximated by linearly interpolating the data presented in Figure 3.57 which is then used to approximate the tail rotor power, total aircraft power and fuel consumption according to the method presented by Newman (1994). The calculation is then stepped

through time to find the variation of aircraft mass, velocity and distance travelled. The time saved and fuel saved through the use of AJVGs is presented against the distance in Figure 3.61. Over 600km only 5 minutes are saved, however the saving in fuel of 250kg appears to be considerably more useful and the resulting extension in range and endurance for a given fuel consumption is shown in Figure 3.62.

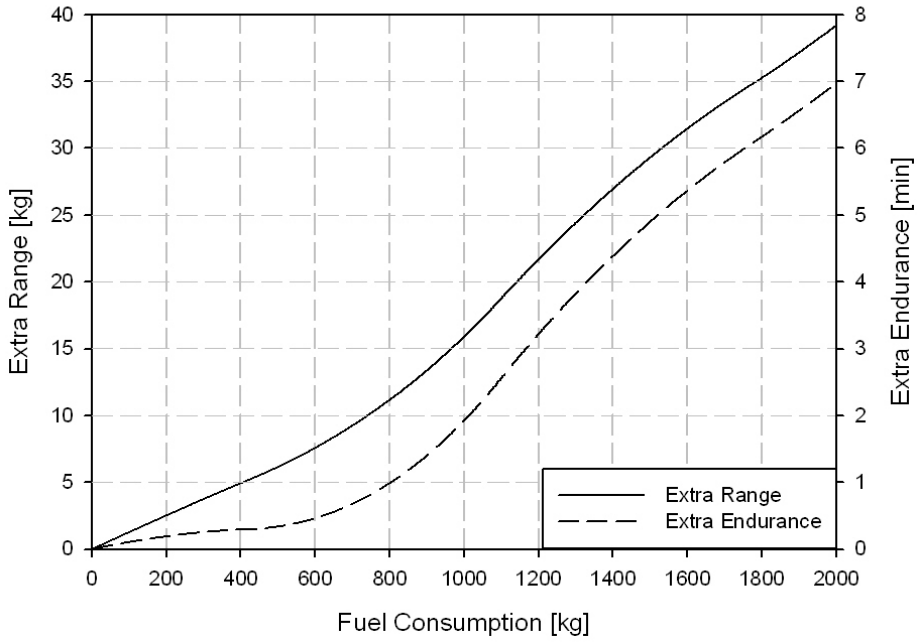

Figure 3.62: Range and endurance extension at maximum speed due to AJVGs.

A range extension of 40km could be useful, however it should be noted that this is not the absolute range of the aircraft, it is merely the range at maximum speed. In practice the maximum range would be obtained by flying at a reduced speed, further from the stall boundary where AJVGs are ineffective (this will be demonstrated below). Therefore, the only reason to sustain such high speed over prolonged periods of time would be to reduce the transit time. We therefore seek the reduction in transit time due to AJVGs over a given distance and for a maximum fuel load. For small distances, the aircraft can fly at the maximum speed defined by the stall boundary as the full fuel load will not be used. If longer distances are to be achieved, however, the flight speed must be reduced towards the optimum range speed such that the maximum fuel usage is not exceeded. By reducing speed, the benefit of the AJVGs will be lost and the saving in time will reduce towards zero.

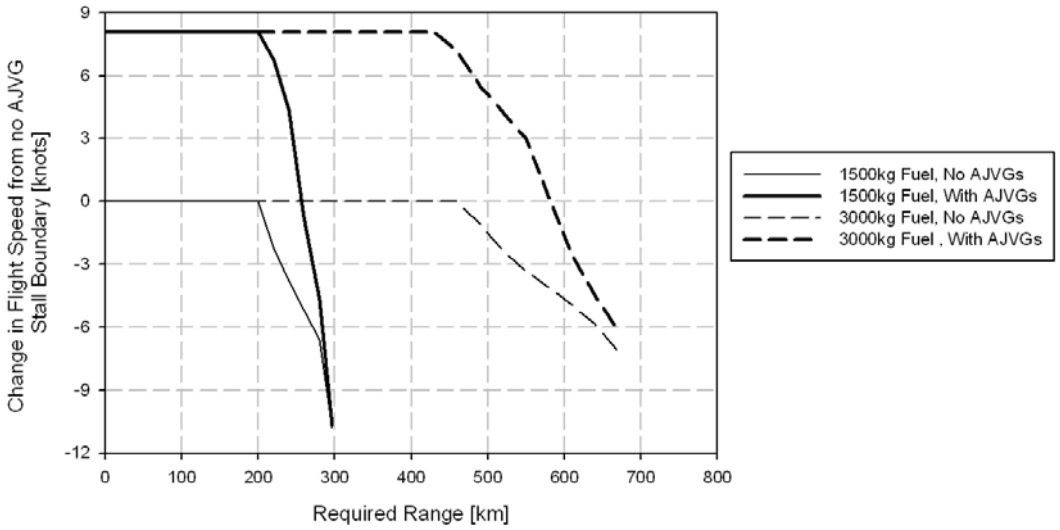

Figure 3.63: Reduction in flight speed to obtain required range for a given fuel mass.

The reduction in speed required to obtain a given range has been calculated for allowable fuel masses of 1500kg and 3000kg using the method discussed above. The results with and without AJVGs operating are shown in Figure 3.63. Note that for this purpose, the stall boundary with AJVGs was assumed to be at advance ratios 0.02 greater than that without AJVGs (independent of blade loading) and that the reduction in speed to increase the range was applied consistently across the blade loading range. Figure 3.63 shows that as the required range is increased, a reduction in speed is required in both the situations with and without AJVGs. This confirms that the optimum speed for maximum range is below the onset of stall. Furthermore, the with and without AJVG traces are converging on the plot yet the range is still increasing with further reductions in advance ratio, hence the optimum speed for range is below that at which the AJVGs become effective. This is an important result as it suggests that AJVGs cannot be used to increase the maximum range of the aircraft. Also, as the maximum endurance is obtained at the minimum power speed [see, for example, Newman (1994)], Figure 3.57 suggests that AJVGs have no influence on the endurance either.

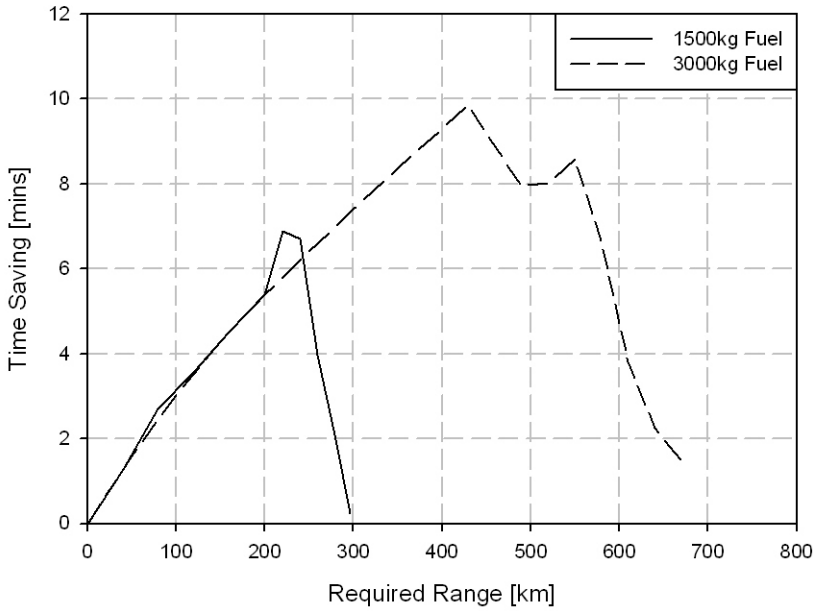

Figure 3.64: Time saving versus range due to AJVGs for two values of fuel mass.

The sole remaining advantage of AJVGs is therefore the increase in maximum speed. As suggested earlier, for a given fuel load, the speed advantage can only be realised over a limited range as flight speed must be reduced to obtain the maximum range. The time saved is therefore plotted against range for the two values of fuel mass in Figure 3.64. Clearly the maximum time saving increases with greater fuel load and for the large fuel load of 3000kg the time saving peaks at 10 minutes. However, this time saving is only realised over intermediate ranges and reduces rapidly as the maximum range is approached. Also, the time saving should be compared to the actual flight time of just over 2 hours. The reduction in transit time is therefore around 8-9%, indeed Figure 3.65 shows that this is fairly consistent over low-to-medium ranges before dropping off rapidly as larger ranges are required.

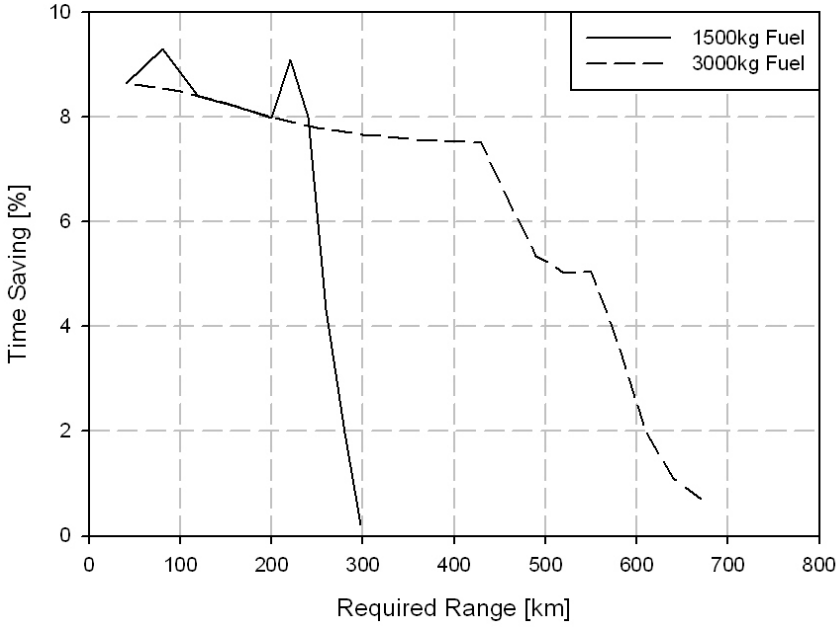

Figure 3.65: Percentage time saving versus range due to AJVGs for two values of fuel mass.

3.5 The Overall Utility of Air Jet Vortex Generators

In this chapter, an indicial aerodynamics model has been modified such that evidence could be gathered for an evaluation of the utility of Air Jet Vortex Generators for the performance enhancement of an advanced helicopter main rotor system. The method provided a prediction of the expansion of the flight envelope and the corresponding effects on the main rotor power. These power carpets were then used to investigate the overall impact on the operation of the aircraft.

As the AJVGs have little impact on the aerodynamic coefficients prior to stall they have little-to-no effect on the low-to-moderate speed performance characteristics of the helicopter. In particular, it has been demonstrated that AJVGs cannot improve the range or endurance of the aircraft. Through influencing the stall, however, the model suggests that the high-speed performance could be improved with a flight envelope expansion of the order of 6 knots being predicted. This improvement was most evident in conditions of high blade loading; however at lower blade loading the impact of the AJVGs was significantly reduced. Without influencing the low-speed performance, the only real operational advantage is to increase the maximum speed and to therefore reduce time taken for a given transit range. The model demonstrated that journey times could be reduced by around 8-9% for low-to-moderate distances but that the time saving rapidly

reduced for higher ranges which require a reduction in flight speed. The AJVGs are therefore only of use for an aircraft for which transit times are absolutely critical, even then the actual time savings are limited.

Against this advantage must be balanced by the cost of incorporating AJVGs into a rotor blade. The main components of the system are a high-pressure air supply, an array of high frequency valves, the jet orifices exhausting near the leading edge of the blade and the associated control hardware and software. Clearly one source of high-pressure air exists in the aircraft engines. These, however, are located in the fixed-frame and transporting this air supply to the valves in the blade would require a very complex system. Alternatively, a pump could be used to produce the supply in the rotating-frame, either at the hub or in the blade itself; however this will clearly lead to a substantial mass penalty. One suggestion [Krzysiak (2008)], has been to use a leading edge slot to supply the high-pressure air. The leading edge of the blade is, however, prone to erosion, with most blades incorporating leading edge erosion shields of high-strength ballistically tolerant materials such as titanium. If an air input duct is to be located on the leading edge then it will be subject to the same erosion and in a harsh desert environment will ingest significant amounts of sand and dust or, at the opposite end of the scale, could be prone to icing. The jet orifices themselves also need to be located near the leading edge. Although they would be located further back than an input duct, the same arguments can be applied with the operational reliability being questionable. In addition, as most rotor blades use a leading edge C- or D-spar as the main load-bearing component, the incorporation of orifices in this component could lead to stress-raisers which would complicate the structural design and manufacture of the blade. The flow control valves are best located close to the orifices to improve the controllability of the jet pulse and will therefore most likely also be located within the spar. If the valves are to be serviced or replaced then this would suggest that an access hatch in the main structural component becomes necessary thus further complicating the blade design and manufacture. Finally, the system will require a degree of computational hardware and software to control the valves, especially if the mass flow requirements are to be minimised. This control requirement is true of any on-blade active device and leads to further complexity, mass and cost. Overall the system will clearly lead to increased costs in manufacture, maintenance and logistics which should be considered against the operational benefits.

Figure 3.66: Tilt-Rotor aircraft provide higher speed and range whilst maintaining the ability to take off and land vertically. Top: The V-22 Osprey military tilt-rotor has seen operational deployment, photo courtesy of the United States Department of Defence. Bottom: The BA609 civil tilt-rotor is undergoing certification, photo courtesy of AgustaWestland.

The above discussion serves to introduce some of the complexity, reliability and cost issues which may be associated with the incorporation of an AJVG system. If the performance enhancement provided by the AJVGs is considered to be of paramount importance, however, then these problems are probably not insurmountable, albeit at considerably increased cost. Assuming that the benefit is worth the cost, then some consideration must also be given to the alternatives. As the only benefit provided by the AJVGs has been shown to be in the high-speed performance then they can be assumed to be only applicable to aircraft where high-speed performance is of great importance. In this sense they may be seen as an intermediate technology which goes towards bridging the gap between the conventional helicopter and the fixed-wing aircraft whilst maintaining the vertical flight capability. There are, however, alternative technologies both in service and in development. The Tilt-Rotor concept, Figure 3.66, has been demonstrated to provide flight speeds in excess of 300knots [Endres and Gething (2002)] and, in the form of the V-22 Osprey, is now proving itself in operational service. However, tilt-rotor technology to date has proven to require long development and certification times and may be considered to be a high-cost technology. As well as this,

in order to provide the high speeds, the hovering efficiency of the aircraft is reduced as the prop-rotors must be a compromise between the low-speed and high-speed flight regimes.

Figure 3.67: Recent technology demonstrator aircraft for higher-speed helicopters. Top: The Sikorsky X2 demonstrating the Advancing Blade Concept, photo courtesy of Sikorsky. Bottom: The Piasecki X-49A Speedhawk demonstrating the Vectored Thrust Ducted Propeller concept.

There have also recently been flight demonstrations of compound helicopters which demonstrate the Advancing Blade Concept (ABC) of Sikorsky and the Vectored Thrust Ducted Propeller (VTDP) concept of Piasecki; see Figure 3.67. Both of these concepts provide significant increases in the speed capability of the aircraft whilst maintaining a greater level of hovering efficiency using technologies which are hoped to provide reduced cost and complexity compared to the tilt-rotor. The ABC uses a coaxial rotor to eliminate retreating blade stall by achieving trim using the advancing blades of each rotor. As the retreating side of each rotor is unloaded, the speed of the rotors may be reduced by up to 20% to delay the onset of advancing blade stall whilst a pusher propeller at the tail is used to provide forward propulsion. The technology is not a new concept however it is hoped that previously encountered problems such as hub drag and vibration can be overcome using modern materials and control technology to achieve flight speeds of the order of 250knots [Vertiflite (2008)]. The VTDP maintains the single main rotor of the

helicopter and, at a stretch, could be considered for retrofit to existing aircraft. The traditional anti-torque tail rotor is replaced by a ducted propeller which is designed to provide anti-torque, yaw control and additional forward propulsion. This, together with a fixed wing offloads the main rotor by up to 50% thus delaying stall and allowing flight speeds of up to 230knots [Colucci (2007)].

All three concepts discussed clearly provide speed improvements which greatly exceed that predicted using AJVGs and also, unlike the AJVGs, significantly increase the maximum range of the aircraft. However, these concepts require considerable changes to the aircraft configuration and an advantage of the AJVGs might be that they could be retrofitted to an existing fleet using a replacement of the main rotor blades. Also, as the primary control of the aircraft is unchanged, the failure of the system would not be critical and therefore the retrofit might be achieved with a significantly lower level of testing and cost. The AJVGs might therefore be compared to other advanced concepts which might be considered for a retrofit. The technology which has shown the greatest level of promise in the literature is the Trailing Edge Flap (TEF), which will be considered in detail in the following chapter. If used in addition to the primary, blade root control system then this technology might also be considered for a retrofit. Like AJVGs, TEFs have also been predicted to provide a small enhancement to the high-speed performance of a conventional helicopter rotor [Chan and Brocklehurst (2001)]. Unlike the AJVGs, however, this technology has also been shown by flight test [Roth et al (2006)] to have the ability to actively control the dynamic response of the blade, thereby providing reductions in noise and vibration. There are therefore alternative technologies to AJVGs which could also be considered as a (comparatively) low cost retrofit solution and which are predicted to provide similar performance enhancements in addition to numerous other operational benefits.

In summary, the Air Jet Vortex Generators have been predicted to provide an enhancement to the high-speed performance of an advanced helicopter. This enhancement is however quite limited in its operational utility and will come only with considerable increase in cost, and maintenance requirements, particularly if required to operate in harsh environments. As well as this there are alternative technologies which can either provide far greater improvements in the high-speed and maximum range performance (albeit with considerable changes to the aircraft configuration) or can give similar levels of performance enhancement in addition to various other applications. It is therefore the opinion of the author that the cost of an AJVG system is unlikely ever to be

justified by the limited benefit and if it is then there are a range of alternatives which would be preferred due to either greater performance or additional applications.

Chapter 4 Trailing Edge Flaps and their Application to Blade Sailing

4.1 The Adaptability of Trailing Edge Flaps

We have seen from the literature that the application of active Trailing Edge Flaps (TEFs) to a helicopter rotor is far from being a new concept and that the TEF has been used for primary control, in place of the swashplate, on the operational Kaman H-2 Seasprite helicopter since the 1960s, [Endres and Gething (2002)]. More recently, however, TEFs have been prolific in the literature as the development of light-weight, high frequency actuators and modern control techniques has enabled their use for the higher harmonic, or secondary, control of rotor blades which is aimed predominantly at reducing vibration [Friedmann and Millott (1995), Jones and Newman (2006), Viswamurthy and Ganguli (2007)] and at the reduction of noise [Charles et al (1996), Patt et al (2006)]. Furthermore, the predicted vibration reduction capability has been proven in flight [Roth et al (2006)].

As a technology, therefore, TEFs are far more mature than the Air Jet Vortex Generators investigated in the previous chapter. Furthermore, whilst testing has already shown that the TEFs are capable of reducing both noise and vibration, numerical studies have also predicted an array of other uses such as performance improvement [Chan and Brocklehurst (2001), Almikus and Knutzen (2007)], fault interrogation [Stevens and Smith (2001)], blade load reduction [Kim et al (2003, 2006)], stability enhancement [Konstanzer (2005)] and the balancing of rotors with dissimilar blades [Roget and Chopra (2003, 2004, 2008)]. It is perhaps this adaptability to a wide range of uses which makes the active TEF such an attractive candidate for incorporation into an active blade.

A fine example of the adaptability of the TEFs to additional uses is provided by their application to the reduction of blade sailing. This novel concept was first presented by the author at the American Helicopter Society Annual Forum [Jones and Newman (2007)]. With this application, the incorporation of TEFs into a rotor blade would not only enable the proven noise and vibration reduction capabilities, but could also be used to substantially improve the operational effectiveness of the rotorcraft. The bulk of this chapter will therefore focus on the blade sailing application and builds on the results published by Jones and Newman (2007). The specially developed dynamics method along with some initial results will first be outlined before an investigation into a real operational case study is presented.

The chapter will conclude, however, with a discussion into the overall operational effectiveness and practicality of the active TEF system. Although the ability of the TEF to reduce vibration has been well proven in flight there are no immediate signs of an active rotor coming into service on a production helicopter. Possible reasons for this will be discussed which will lead on to the Active Trailing Edge (ATE) technology to be investigated in the next chapter.

4.2 Helicopter Blade Sailing

4.2.1 The Dynamic Interface

The operation of a helicopter from a sea-based platform, be it a Naval Frigate or an oil rig, presents many challenges over and above land-based operations which must be overcome if damage to the aircraft is to be prevented and, more importantly, to ensure safety to both air and ground crew. Such aspects of sea-based helicopter operation are discussed by Newman (2004). Before an aircraft can be routinely operated from a ship it must undergo a long and costly clearance process sometimes referred to as Dynamic Interface (DI) testing. A recent example of this, as shown in Figure 4.1 is the United Kingdom's qualification of the Apache helicopter for use on board its warships, Neville (2005).

Figure 4.1: The Apache helicopter, seen here operating from HMS Ocean has recently been cleared for shipborne operations by the United Kingdom Ministry of Defence, photo courtesy of the UK Ministry of Defence.

Although model and full-scale testing is vital, as discussed from a Dutch viewpoint by Fang and Booij (2006), simulation has steadily taken on an increasingly important role

not only in the DI testing process but also in the evaluation of the potential of new technologies being developed to enhance operations at sea, Ferrier et al (2007). Such simulations must incorporate dynamics models for both the ship and helicopter, including modelling the effect due to the sea-state on the ship motion. A simplified example of some of the complex coupling involved in such simulation is shown in Figure 4.2.

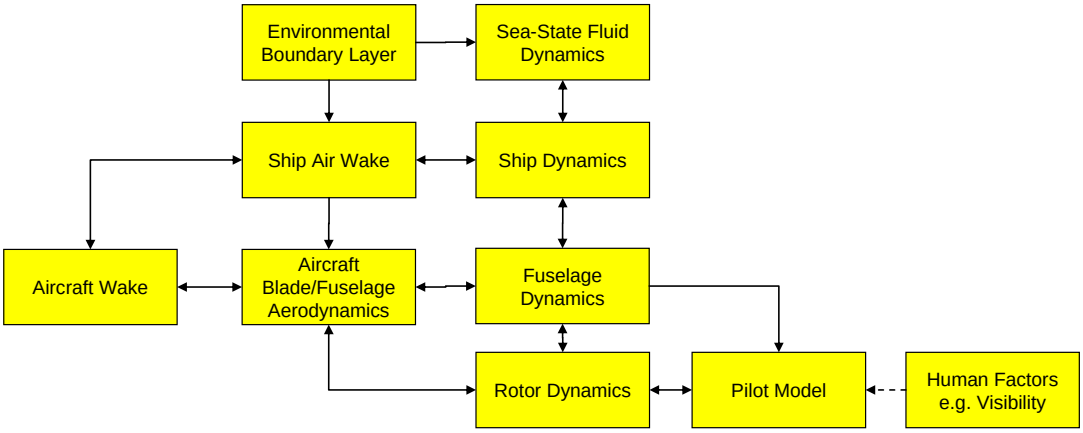

Figure 4.2: Block-diagram illustrating some of the complex coupling involved in Dynamic Interface modelling.

A typical example of a DI simulation method is reported by He et al (2002) and Kang et al (2003) who describe the use of FLIGHTLAB with two options for the airwake modelling. The first option uses time-accurate airwake data from CFD which can influence the rotor wake (upon which it is superimposed) but cannot in turn be influenced by the rotor wake. Alternatively a coupled mean flow solution for the ship and the rotor wakes can be calculated using a panel method for the ship with turbulence data superimposed onto the solution from the CFD results. More recently, Bridges et al (2007) have presented a truly coupled solution which suggested that the one-way coupling method was conservative in terms of its pilot workload prediction.

4.2.2 The Blade Sailing Problem

Dynamic interface testing and simulation is then clearly a huge topic however the point of interest here is much more specific. As part of the DI testing process, any limitations to the operating environment within which the rotor can be engaged and disengaged must be investigated. In high-wind conditions, such as those found on the deck of a ship or oil-rig, the rotor start-up (engagement) or shut-down (disengagement) operations can lead to the occurrence of blade sailing. In these conditions, the aerodynamic loading of the blades still exists while the centrifugal stiffening does not. This may result in large blade deflections or, for blades of greater stiffness, a significant increase in blade loads.

Large deflections do not only make operations hazardous, they can also significantly restrict the operational envelope of the aircraft. For an articulated rotor, the larger deflections will result in blade droop stop and anti-flap stop impacts. When the rotor is up to speed these stops are retracted as the centrifugal and aerodynamic stiffening of the blade provides sufficient stability to restrict the flapping motion of the blade. However, as the rotor slows, the stops are automatically extended to restrict the articulation range of the rotor, indeed when the rotor is at rest it is the droop stop which prevents the blades from dropping to the ground under the influence of gravity. Impacts with these stops can however exert large loads on both the blade and the stop itself. In more extreme conditions, blades of relatively low stiffness can undergo deflections large enough to result in the blade impacting the aircraft fuselage, such occurrences being referred to as boom-strikes or, in the case of tandem rotor helicopters, tunnel-strikes. Stiffer blades can be expected to exhibit smaller deflections however this is at the expense of larger blade loads.

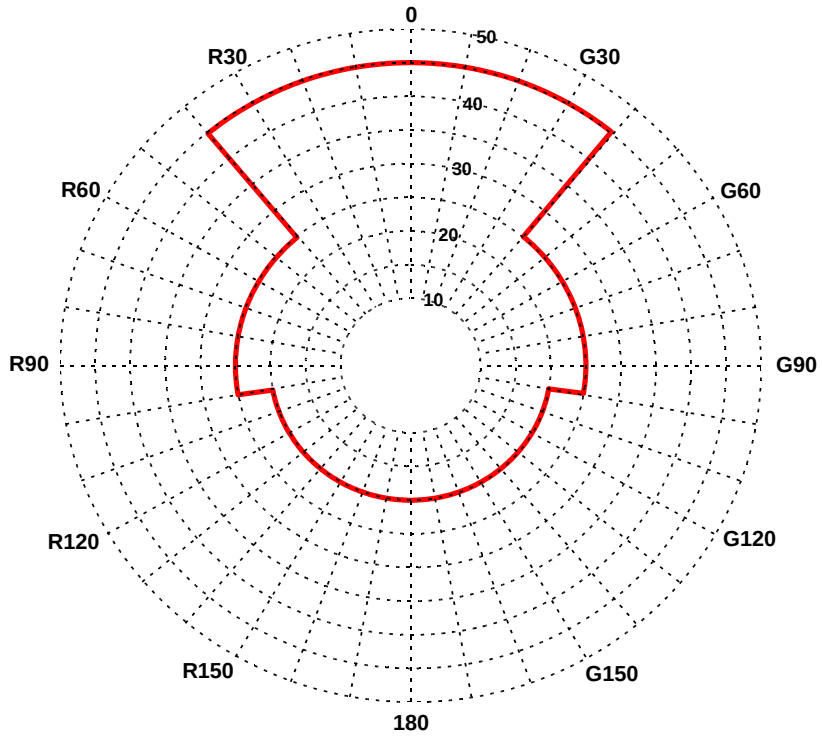

Figure 4.3: Example SHOL diagram depicting the limit of safe wind speed and direction combinations, wind speed typically in knots.

In summary, the blade sailing phenomenon is a limiting condition which must be considered in the design of a helicopter rotor system. To ensure that the design limit loads are never exceeded and to avoid any fuselage impacts, during the Dynamic Interface testing and simulation process, an envelope known as a Ship/Helicopter Operational Limit (SHOL) is defined for rotor engagement and disengagement in terms of

wind speed and direction, outside of which the operation is considered to be unsafe, see Figure 4.3. This envelope can in turn restrict the overall SHOL, which takes account of all operational aspects, and can severely limit the operational effectiveness of the aircraft.

4.2.3 The Passive Reduction of Blade Sailing

Several passive methods for reducing blade sailing have been investigated. Geyer et al (1998) considered the effects of altering existing parameters which would require little or no modification of the rotor system; however none of the suggested methods were particularly successful. The application of constant cyclic or collective pitch was found to be detrimental to the maximum tip deflection and alteration of the droop stop angle was not considered to be feasible for blade sailing reduction, particularly as too large a change would prevent it from extending at all. Geyer et al (1998) also considered the use of a rotational flap damper located at the flapping hinge. This damper had little effect with the current flap stop angles, however if the flap stop angle is increased allowing more potential energy into the blade then maximum downward tip deflections may be reduced if a damper four times the strength of the lead-lag damper is used. This is a very large amount of damping however and would result in a significant mass penalty and would transmit large loads into the rotor head.

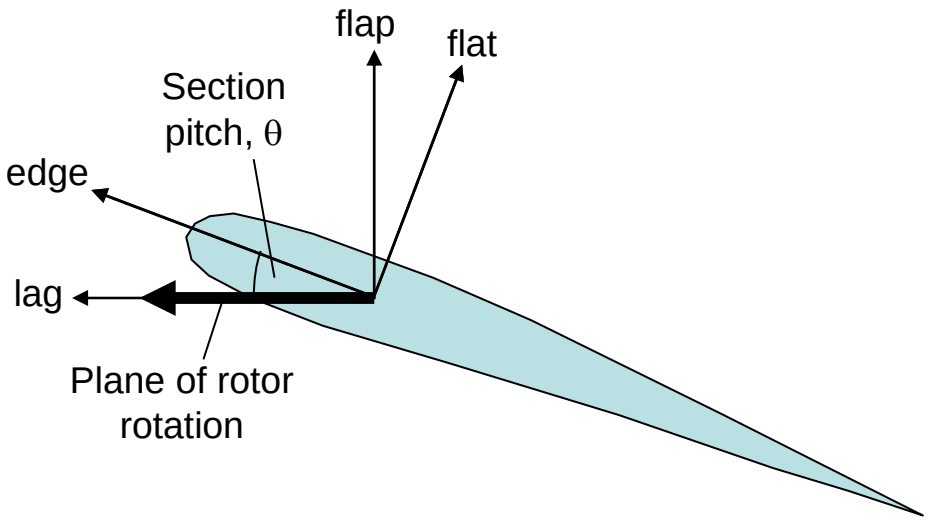

Figure 4.4: Definition of flat-edge and flap-lag coordinate systems.

Keller and Smith (1999b) discussed increasing the collective pitch over the rotor speed range at which the maximum downward tip deflections are encountered. The idea of such an increase was to stiffen the blade in the flapwise direction by increasing the pitch along the blade, thereby putting a component of the larger edgewise stiffness in the direction of interest, see Figure 4.4. The downward deflections could occasionally be reduced

however the resulting increase in lift forcing gave increases in the upward tip deflections and in the blade bending moments.

In his PhD dissertation, Keller (2001) continued the investigation into the use of a flap damper by considering a greater range of inflow cases. It was confirmed that the damper would need to provide around 4 times the damping of a typical lag damper to have the desired effect. Even then it is necessary to raise the anti-flap stop to allow sufficient energy into the blade which meant that the upward tip deflections were often increased. As well as this, many of the maximum downward tip deflections were found to occur before the blade has lifted from the droop stop and in these cases the damper is still inactive and is therefore entirely ineffective.

Both the flap damper and the raised collective pitch methods attempt to reduce the response of the blades without affecting the cause of the problem. Keller (2001) however also considered a method designed to reduce the problem at source by deploying spoilers on the blade to reduce the lift forcing, see Figure 4.5. Spoilers covering only the outer 15 per cent of the blade span were found to be optimal and could successfully reduce both upward and downward tip deflections.

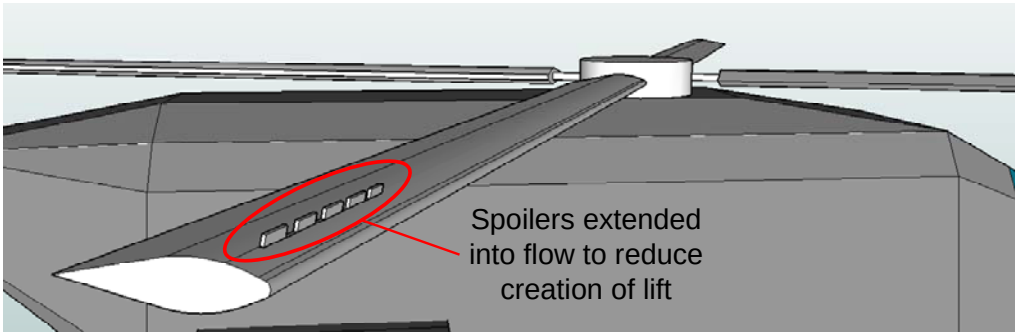

Figure 4.5: On-blade spoilers were suggested for the reduction of blade sailing by Keller (2001).

A concern raised was that the spoilers could increase the required torque during engagement however it was found that the torque produced by the spoilers was small in comparison to that produced when the blade impacts a lead or lag stop. This method then appears to be the most successful method suggested by the researchers at the Pennsylvania State University. Spoilers and their associated actuation mechanism would however come with cost, weight and maintenance penalties yet would have no other use than during engagement/disengagement operations. Their location near the leading edge of the blade could also prove challenging to the structural design as most rotor blades use a leading edge D-spar or C-spar as the main load bearing component.

4.2.4 The Active Control of Blade Sailing

Keller et al (2001, 2003) first considered using active control of blade sailing for a gimballed rotor. The idea was to use existing swashplate actuators and on-blade feedback to minimise the maximum gimbal angle experienced during engagement/disengagement operations. The control method used the system equations of motion plus an approximation of the forcing. With a full knowledge of the flow field within which the rotor was operating, the maximum gimbal response could be reduced by greater than 50 per cent; however errors in the measured wind speed and direction were shown to reduce the effectiveness of the control. The research showed the promise of active methods for the reduction of blade sailing; however the dependence of the control philosophy on knowledge of the incident wind could prove troublesome in the highly unsteady flow fields experienced over typical flight decks. The system would be dependent upon feedback from anemometers which would have to reliably predict the wind direction regardless of the location on the flight deck.

The research presented in this dissertation was the first application of on-blade active control to be applied to helicopter rotor blade sailing and was introduced by Jones and Newman (2007). The method uses active trailing edge flaps with feedback of the blade tip velocity. As trailing edge flaps are being considered for many purposes their application to the blade sailing problem could be achieved simply with the addition of an on-blade accelerometer with no other modifications required. The use of the velocity feedback also means that no knowledge of the inflow is required. Further research into this promising approach to the blade sailing problem will be presented below.

It should be mentioned that following the publication by Jones and Newman (2007), other authors have considered other means of actively controlling blade sailing. Researchers at Carleton University have been developing prediction methods capable of investigating the feasibility of using active blade twist for blade sailing reduction. Much of the effort to date has focussed on developing the models capable of predicting the dynamic characteristics of a blade incorporating active elements and Wall et al (2008) discuss an experiment designed to validate the methods. Kouli et al (2008) then present some initial results using the models with some basic continuous twist inputs. The initial results suggest that the blade twist can indeed have an appreciable effect on the downward tip deflection thus encouraging continued investigation into using the technology for the active control of blade sailing.

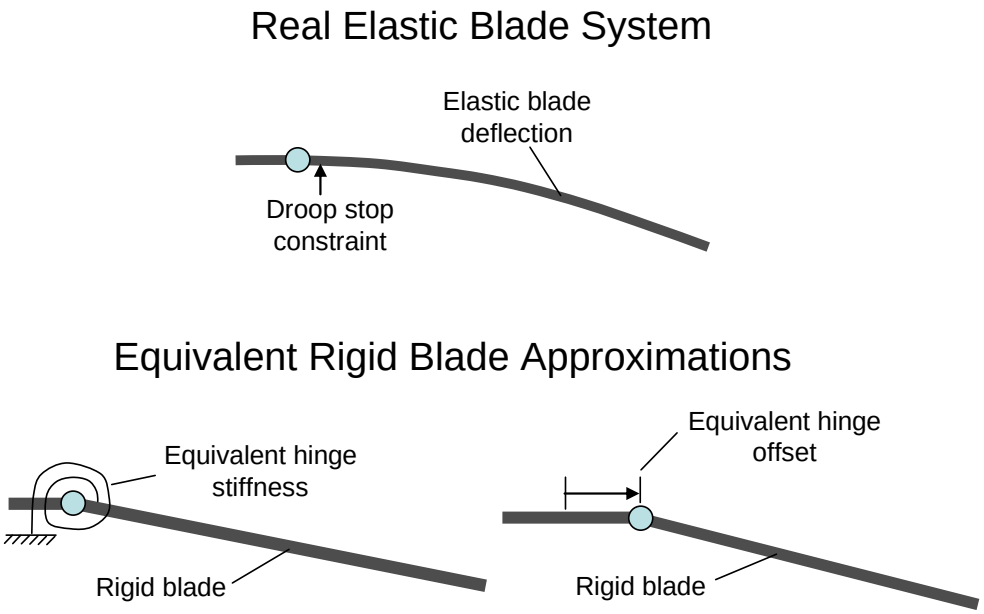

Figure 4.6: Equivalent rigid blade approximations of elastic blade deflection on a droop stop.

Ramos et al (2009) then considered using individual blade control activated at the blade root. To simplify development of the feedback control, the blade response was approximated using a single flapping mode degree-of-freedom whereby the effects due to the droop and anti-flap stops are modelled using a non-linear modal stiffness. When the blade is not in contact with the stop, the mode natural frequency takes its normal value, however when contact with a stop occurs the frequency is increased such that the elastic deflection of the blade on the stop is approximated by an equivalent rigid blade mode with an applied hinge stiffness, as shown in Figure 4.6. The model of the elastic response of a blade on a stop is therefore equivalent to modelling a semi-rigid rotor blade using an equivalent flapping hinge offset, see for example Newman (1994). Using this 'flapping oscillator' approximation and further linearising the model, the input of pitch control based on the feedback of the blade flapping and flapping rate, is shown to be equivalent to increasing the system stiffness and damping respectively. In practice the feedback applied is dominated by the flapping velocity terms with increased stiffness being applied where extra authority is available. The control methodology is then basically similar to that used by Jones and Newman (2007) and demonstrated substantial reductions in tip deflections. Piccirillo et al (2009) apply the same dynamic model as Ramos et al (2009) to investigate the use of Shape Memory Alloys (SMAs) and Magnetorheological Dampers (MRDs) for the reduction of blade sailing. These are not active control devices but apply additions to the stiffness and damping terms of the equation of motion directly and resulted in similar levels of tip deflection reduction to the active blade root control

method. Unlike the active methods however, it is unlikely that these passive devices could have any other useful purpose.

In summary, the most effective devices for the reduction of blade sailing appear to be those which tackle the problem at source through aerodynamic interaction. Furthermore, due to mass and cost considerations it is unlikely that a complex device would be incorporated into a blade design unless it can be applied to more than just the blade sailing problem. The application to blade sailing of the higher harmonic control devices, currently being considered by industry for a number of purposes, would therefore appear to be an ideal solution. The author first presented research into the application of TEFs to the blade sailing problem [Jones and Newman (2007)] and this was followed by a succession of papers [Kouli et al (2008), Ramos et al (2009), Piccirillo et al (2009)] investigating the use of a variety of devices. Further research into the use of TEFs for the reduction of blade sailing will be presented in the following sections, including their application to a real operational case study.

4.3 The Modelling of Blade Sailing

4.3.1 Background

The development of models for blade sailing was led by Newman (1990, 1992, 1995a, 1995b, 1999) at the University of Southampton. The behaviour of the rotor blades during rotor engagement and disengagement is influenced by more than just the rigid body motion of the blades however normal modal methods, as typically used in rotor performance programs, are based upon an assumption of constant rotor speed as the modes become inapplicable for any large rotor speed variations. To overcome this problem Newman uses a single (flapwise) degree of freedom modal method which includes a correction term to account for the variations in rotor speed. The variation of the rotor speed was prescribed using observations from test, the aerodynamic inflow was based on data and observations from wind-tunnel and full-scale tests, Hurst and Newman (1985), and the lift coefficients were calculated using the quasi-steady assumption with trailing edge stall corrections similar to those used in the third generation model. Droop stop and anti-flap stop modelling was accomplished using linear springs with a large spring rate and appropriate contact logic, Newman (1992). Newman (1995a) showed a reasonable agreement with model-scale tests and predicted the possibility of boom strikes and blade fatigue for the Westland Sea King and Westland Lynx aircraft respectively.

The CH-46 Sea Knight helicopter, Figure 4.7, has been in service with the United States Navy and Marine Corp for several decades and during that time has suffered over 100 tunnel-strikes of varying severity from dented fuselage panels to a severing of the synchronisation shaft, Geyer et al (1998). For this reason the CH-46 aircraft has been the subject of many engagement/disengagement tests however the large number of possible cases and the associated expense led to the funding of analytical investigations to be carried out by the U.S. Naval Air Warfare Centre and the Pennsylvania State University. The method used was first reported by Geyer et al (1996, 1998). Unlike Newman (1995), the blade dynamics were integrated through time using a Finite Element discretisation which included a coupled torsion degree of freedom. The droop stop and anti-flap stop were modelled using conditional rotational springs and a flap damper could be modelled using a similar method. Like Newman (1995), blade element theory was used for the calculation of the aerodynamic loads however an option to use an unsteady aerodynamics model using the indicial method was included. The authors concluded, however, that the effects due to the unsteady model were only significant at the highest of wind speeds with spacially varying gusts and that the torsion degree of freedom was only necessary for blades of very high amounts of flap-torsion coupling. This then supports the simplifying assumptions made by Newman (1995).

Figure 4.7: The CH-46 Sea Knight helicopter. Note the blade flexibility evident in the rear rotor and the tandem rotor layout with the transmission 'tunnel' between the rotor pylons. Photographed by the author at the USS Midway Aircraft Carrier Museum, 2009.

Keller and Smith (1999a) discuss the validation against experiment of the blade dynamics model used in the analysis discussed by Geyer et al (1998). The prediction of flapping angle, blade tip deflection and blade strains just outboard of the flap stop are compared to a model-scale experiment in which a blade is 'dropped' onto its droop stop. The full finite-element integration method is compared to integration in modal space. Two modal methods are used; the first is similar to Newman and uses a single set of modes with a hinged-free boundary condition, the second switches between the hinged-free modes and a set of fixed-free modes depending upon the droop stop/blade contact situation. All three methods are found to correlate well with the experiment, however, the modal methods are more efficient, particularly the switching method which requires fewer modes as they are more representative of the root condition. The inclusion of the small amount of structural damping found in test had little effect on the tip deflection but was found to significantly affect the high frequency content of the blade strains. It should be noted however that the zero-damping assumption results in a conservative result. Keller and Smith (1999b) also investigated differences in predicted blade sailing due to the use of a flow field predicted using CFD and that prescribed using a basic linear gust model. The quantitative results were found to be quite different thus highlighting how the phenomenon can be quite specific to the flow field within which the aircraft is residing.

A different approach to the problem by Bottasso and Bauchau (2001) uses multibody modelling, a finite element based technique. This technique uses existing elements in multibody dynamics analyses thus neglecting the need for the derivation of new equations of motion and validation for specific cases. This enables a high degree of flexibility in the analysis of new rotor systems and the addition of different components such as the pitch control mechanism. It is also claimed that the technique is better able to capture higher frequency effects of stop contacts than a finite mode representation; however the results of Keller and Smith (1999a) suggest that the modal method is perfectly adequate. The use of the technique has been validated against the work by Geyer et al (1998) and against experimental values of static deflections and modal frequencies obtained for the H-46 helicopter.

More recently, Kang et al (2004) have applied an adaptation of their FLIGHTLAB based Dynamic Interface model [Kang (2003)] to the prediction of blade sailing. Elements have been added to model the anti-flap stops and droop stops and blade flexibility is modelled using a modal method which is coupled in the flap and lag degrees of freedom. The rotor inflow is interpolated from an *a priori* calculated CFD solution for the ship airwake along

with a Peters and He (1995) wake model. Ship motion is calculated using a ship motion program with the motion of the helicopter fuselage on its landing gear also included.

4.3.2 Stimulus for a New Model

Some initial work on the investigation into the mitigation of blade sailing using a trailing edge flap was conducted using the dynamics method developed by Newman (1995). It was desirable however to investigate the effects on more modern rotor blade designs such as the EH101. Such designs tend to have increased rigidity in the flapwise direction and therefore although they can be expected to yield smaller deflections in blade sailing conditions, this is done at the expense of increased loads in both the blades and the rotor hub. Blade sailing is therefore still considered as a possible limiting condition for rotor operations and continued investigation is still of great importance.

The EH101 main rotor blade does not have a traditional set of anti-flap and droop stops. Instead, a pin-type system is used, as represented by the schematic shown in Figure 4.8. During normal rotor operation the pin is disengaged and the flap hinge is as a normal articulated rotor hinge. Once the rotor has slowed below a given speed however, a pin at the root of the rotor blade engages into the rotor head. This restrains the blade and essentially changes the root boundary condition of the blade from pinned to fixed such that the fundamental flap mode changes from being a pinned-free to a built-in-free mode.

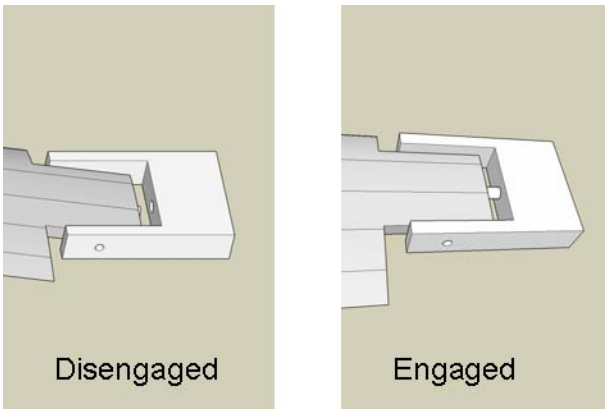

Figure 4.8: Schematic representing a pin-type anti-flap/droop stop in disengaged and engaged positions.

For a true representation of this system therefore, the root boundary condition must be changed during the rotor engage/disengage operation and therefore if a modal method is used then two sets of modes would be required with the appropriate one being used, dependent upon the root pin situation. Such switching methodologies have been employed elsewhere [Keller and Smith (1999a)] and the use of this method would be

possible within Newman's (1995) program however this would require some considerable modification.

However, with the desire to correctly model the root-pin boundary condition, work initially commenced on a program to calculate consistent sets of (single-degree-of-freedom) modes for a blade with a variety of root boundary conditions with the intention of providing input to a modal switching blade sailing procedure. During the development of this program however it was realised that it would be possible to integrate the governing equations, through time, to provide a new dynamic method for the calculation of the blade sailing phenomenon. This new program could then be compared to the modal approach of Newman for existing cases but would also be immediately capable of modelling the pin-type flap stops without further modification and so could be used for the investigation into using TEFs for the mitigation of blade sailing on the EH101 helicopter. Also, by solving the problem directly from the blade mass and stiffness properties the effects due to changes in the blade configuration could be directly assessed without the requirement for a separate modal calculation routine.

The following sections therefore cover the development of the dynamics method. The analysis was developed using the same single degree-of-freedom formulation as Newman (1995) so that the methods could be directly compared, however it should be noted that it could be more readily adapted to more advanced dynamic formulations as, unlike the Newman (1995) method, the centrifugal stiffening terms need not be explicitly extracted.

4.3.3 Flapwise Deflection of a Rotating Beam

Figure 4.9 displays the forces and moments acting on an element of a non-uniform, rotating rotor blade.

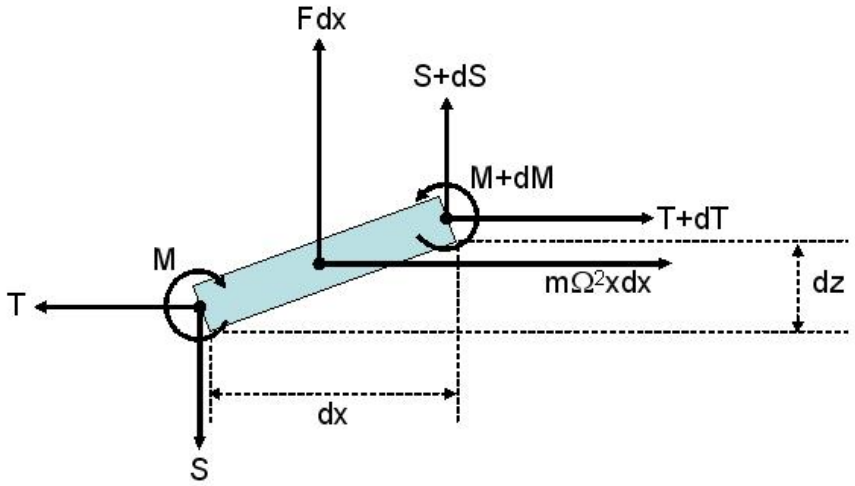

Figure 4.9: Calculation of Displacement for a Blade Element

Resolving the forces vertically and horizontally and taking anticlockwise moments about the left-hand end of the element yields:

$$\begin{aligned} S + dS + Fdx - S &= 0 \\ T + dT + m\Omega^2 r dx - T &= 0 \\ M + dM + \left(S + dS\right)\cdot dx + Fdx \cdot \frac{dx}{2} - \left(T + dT\right)\cdot dz - M &= 0\,. \end{aligned} \qquad \textbf{4.1}$$

Taking $dx \to 0$ and performing the integration for the blade tension results, after simplification, in:

$$\begin{aligned} \frac{dS}{dx} &= -F \\ T &= \Omega^2 \int_r^R m\eta d\eta \\ \frac{dM}{dx} + S - T\frac{dz}{dx} &= 0\,. \end{aligned} \qquad \textbf{4.2}$$

This set currently has more unknowns than equations and so the set of equations is completed using the beam equation:

$$\frac{d^2M}{dx^2} = \left[EIz''\right]''\,. \qquad \textbf{4.3}$$

If the deflection derivative is included as an unknown then a system of four first order differential equations may be formed into a matrix equation:

$$\begin{Bmatrix} M \\ S \\ z \\ z' \end{Bmatrix}' = \begin{bmatrix} 0 & -1 & 0 & T \\ 0 & 0 & 0 & 0 \\ 0 & 0 & 0 & 1 \\ 1/EI & 0 & 0 & 0 \end{bmatrix} \begin{Bmatrix} M \\ S \\ z \\ z' \end{Bmatrix} + \begin{Bmatrix} 0 \\ -F \\ 0 \\ 0 \end{Bmatrix}. \quad \textbf{4.4}$$

4.3.4 Solution of the Blade Equations of Motion

The matrix equation of motion for a blade element, i, derived above may be written as:

$$d_i' = M_i d_i + c_i \quad \textbf{4.5}$$

where d is the state vector and c is a forcing vector. The state vector at radial station i+1 may then be approximated from the state vector at radial station i using:

$$d_{i+1} = M_i d_i \Delta x_i + c_i \Delta x_i + d_i \quad \textbf{4.6}$$

where Δx_i is the radial distance between station i+1 and station i.

Consider the first 4 radial stations of a blade. Using equation 4.6, the state vector at station 2 may be written in terms of that at station 1 as:

$$\begin{aligned} d_2 &= M_1 d_1 \Delta x_1 + c_1 \Delta x_1 + d_1 \\ d_2 &= \left[M_1 \Delta x_1 + I\right] d_1 + \Delta x_1 I c_1 \\ d_2 &= N_2 d_1 + H_{1,2} c_1 \end{aligned} \quad \textbf{4.7}$$

where I is the identity matrix of size 4 and N_2 and $H_{1,2}$ are square matrices of size 4. Similarly the state vector at position 3 may be written in terms of that at position 1 as:

$$\begin{aligned} d_3 &= M_2 d_2 \Delta x_2 + c_2 \Delta x_2 + d_2 \\ d_3 &= M_2 N_2 d_1 \Delta x_2 + M_2 H_{1,2} c_1 \Delta x_2 + c_2 \Delta x_2 + N_2 d_1 + H_{1,2} c_1 \\ d_3 &= \left[M_2 N_2 \Delta x_2 + N_2\right] d_1 + \left[M_2 H_{1,2} \Delta x_2 + H_{1,2}\right] c_1 + \Delta x_2 I c_2 \\ d_3 &= N_3 d_1 + H_{1,3} c_1 + H_{2,3} c_2 \end{aligned} \quad \textbf{4.8}$$

and finally the vector at location 4 may be written:

$$\begin{aligned} d_4 &= M_3 d_3 \Delta x_3 + c_3 \Delta x_3 + d_3 \\ d_4 &= M_3 N_3 d_1 \Delta x_3 + M_3 H_{1,3} c_1 \Delta x_3 + M_3 H_{2,3} c_2 \Delta x_3 + c_3 \Delta x_3 + N_3 d_1 + H_{1,3} c_1 + H_{2,3} c_2 \end{aligned} \quad \textbf{4.9}$$

$$d_4 = \left[M_3 N_3 \Delta x_3 + N_3\right] d_1 + \left[M_3 H_{1,3} \Delta x_3 + H_{1,3}\right] c_1 + \left[M_3 H_{2,3} \Delta x_3 + H_{2,3}\right] c_2 + \Delta x_3 I c_3$$
$$d_4 = N_4 d_1 + H_{1,4} c_1 + H_{2,4} c_2 + H_{3,4} c_3 .$$

Considering the examples shown above, the matrix, N, at any radial station, i, may be calculated using the recursive formula:

$$\begin{aligned} N_1 &= I \\ N_{i+1} &= M_i N_i \Delta x_i + N_i \end{aligned} \qquad \textbf{4.10}$$

and the matrices $H_{k,i}$ are given by:

$$\begin{aligned} &\left(k > i-1\right) \Rightarrow H_{k,i} = 0 \\ &\left(k = i-1\right) \Rightarrow H_{k,i} = \Delta x_{i-1} I \\ &\left(k < i-1\right) \Rightarrow H_{k,i} = M_{i-1} H_{k,i-1} \Delta x_{i-1} + H_{k,i-1} . \end{aligned} \qquad \textbf{4.11}$$

The state vector at radial station i may therefore be expressed in terms of the state vector at radial position 1 as:

$$d_i = N_i d_1 + \sum_{k=1}^{i-1} H_{k,i} c_k \qquad \textbf{4.12}$$

and if the blade root is at radial position 1 then the state vector at the tip may be expressed in terms of that at the root by:

$$d_{tip} = N_{tip} d_{root} + \sum_{k=root}^{tip-1} H_{k,tip} c_k \; . \qquad \textbf{4.13}$$

The solution of equation 4.13 is possible once boundary conditions are applied. For the single, flapwise, degree of freedom case considered here, the blade shear and bending moment at the tip must be equal to zero whilst the displacement and displacement slope must be calculated. The root conditions however are dependent upon the type of blade being considered. For a hingeless or 'built-in' type root such as that found on the Lynx helicopter, the displacement and displacement slope are known (note that built-in coning, or ‘precone’, may be applied through a non-zero value of the displacement slope) whilst the blade shear and bending moment must be calculated. For an articulated rotor head, with flapping hinges, such as that of the Sea King, the displacement and the bending moment are equal to zero whilst the displacement slope and the shear must be calculated.

Consider the flapwise deflection of a hingeless rotor as an example. After application of the boundary conditions and summation of the forcing terms, equation 4.13 may be written as:

$$\begin{Bmatrix} 0 \\ 0 \\ z_{tip} \\ z'_{tip} \end{Bmatrix} = \begin{bmatrix} N_{tip}^{11} & N_{tip}^{12} & N_{tip}^{13} & N_{tip}^{14} \\ N_{tip}^{21} & N_{tip}^{22} & N_{tip}^{23} & N_{tip}^{24} \\ N_{tip}^{31} & N_{tip}^{32} & N_{tip}^{33} & N_{tip}^{34} \\ N_{tip}^{41} & N_{tip}^{42} & N_{tip}^{43} & N_{tip}^{44} \end{bmatrix} \begin{Bmatrix} M_{root} \\ S_{root} \\ 0 \\ \beta_0 \end{Bmatrix} + \{C\} \qquad \textbf{4.14}$$

where β_0 is the known slope due to the built-in coning angle and C is the sum of the forcing terms:

$$\{C\} = \sum_{k=root}^{tip-1} \begin{bmatrix} H_{k,tip}^{11} & H_{k,tip}^{12} & H_{k,tip}^{13} & H_{k,tip}^{14} \\ H_{k,tip}^{21} & H_{k,tip}^{22} & H_{k,tip}^{23} & H_{k,tip}^{24} \\ H_{k,tip}^{31} & H_{k,tip}^{32} & H_{k,tip}^{33} & H_{k,tip}^{34} \\ H_{k,tip}^{41} & H_{k,tip}^{42} & H_{k,tip}^{43} & H_{k,tip}^{44} \end{bmatrix} \{c_k\}. \qquad \textbf{4.15}$$

To obtain a solution using standard methods, any unknowns are required to be in the same vector. Any known values at the root (such as the built-in coning) are firstly added to the forcing vector. Next, columns of the matrix, N, which relate to root values stipulated in the boundary conditions are set to zero. Finally the unknowns on the left-hand side of the equation are moved over to the right-hand side utilising the columns of the matrix which were vacated due to the root conditions. The final matrix equation, which may be solved using standard techniques, is therefore:

$$\begin{Bmatrix} 0 \\ 0 \\ 0 \\ 0 \end{Bmatrix} = \begin{bmatrix} N_{tip}^{11} & N_{tip}^{12} & 0 & 0 \\ N_{tip}^{21} & N_{tip}^{22} & 0 & 0 \\ N_{tip}^{31} & N_{tip}^{32} & -1 & 0 \\ N_{tip}^{41} & N_{tip}^{42} & 0 & -1 \end{bmatrix} \begin{Bmatrix} M_{root} \\ S_{root} \\ z_{tip} \\ z'_{tip} \end{Bmatrix} + \{C\} + \beta_0 \begin{Bmatrix} N_{tip}^{14} \\ N_{tip}^{24} \\ N_{tip}^{34} \\ N_{tip}^{44} \end{Bmatrix}. \qquad \textbf{4.16}$$

Note that the procedure outlined above may be implemented for an arbitrary set of boundary conditions using appropriate logic.

4.3.5 Estimation of the Inertia Terms

The forcing consists of the aerodynamic forcing, the force due to gravity and the inertia forces thus:

$$F_i = L_i - m_i g - m_i \ddot{z}_i \qquad \textbf{4.17}$$

where g is the gravitational acceleration. The acceleration term, $\ddot{z}_i$, may be estimated using a method similar to that for a spatial discretisation next to a boundary in computational fluid dynamics. One method of deriving the approximation is through a

set of Taylor series expansions. The displacements at the previous time steps, z_{i-1} and z_{i-2}, are given by:

$$z_{i-1} = z_i + \left(\frac{dz}{dt}\right)_i (-\Delta t) + \left(\frac{d^2z}{dt^2}\right)_i \frac{(-\Delta t)^2}{2} + \left(\frac{d^3z}{dt^3}\right)_i \frac{(-\Delta t)^3}{6} + \ldots \quad \textbf{4.18}$$

$$z_{i-2} = z_i + \left(\frac{dz}{dt}\right)_i (-2\Delta t) + \left(\frac{d^2z}{dt^2}\right)_i \frac{(-2\Delta t)^2}{2} + \left(\frac{d^3z}{dt^3}\right)_i \frac{(-2\Delta t)^3}{6} + \ldots. \quad \textbf{4.19}$$

Multiplying equation 4.18 by 2 and subtracting equation 4.19 leads to:

$$2z_{i-1} - z_{i-2} = z_i - (\Delta t)^2 \left(\frac{d^2z}{dt^2}\right)_i + (\Delta t)^3 \left(\frac{d^3z}{dt^3}\right)_i + \ldots \quad \textbf{4.20}$$

which upon rearrangement gives:

$$\left(\frac{d^2z}{dt^2}\right)_i = \frac{z_i - 2z_{i-1} + z_{i-2}}{(\Delta t)^2} + O(\Delta t) + \ldots. \quad \textbf{4.21}$$

The estimation for the acceleration therefore involves the displacement at the current time step and so terms must be added to the solution matrix as well as the forcing vector. Equation 4.4 therefore becomes:

$$\begin{Bmatrix} M \\ S \\ z \\ z' \end{Bmatrix}' = \begin{bmatrix} 0 & -1 & 0 & T \\ 0 & 0 & \frac{m}{(\Delta t)^2} & 0 \\ 0 & 0 & 0 & 1 \\ 1/EI & 0 & 0 & 0 \end{bmatrix} \begin{Bmatrix} M \\ S \\ z \\ z' \end{Bmatrix} + \begin{Bmatrix} 0 \\ -L + mg + m\left(\frac{z_{j-2} - 2z_{j-1}}{(\Delta t)^2}\right) \\ 0 \\ 0 \end{Bmatrix}. \quad \textbf{4.22}$$

Equation 4.21 also reveals that the acceleration approximation is first-order accurate. In practice this means that for a typical sinusoidal motion, the acceleration will lag by approximately 1 time step. As the aerodynamic forcing inflow geometry due to blade deformation must also lag by this amount this error is considered to be reasonable.

4.3.6 Traditional Anti-Flap and Droop Stops

Anti-Flap and Droop stops constrain the blade to minimum and maximum deflections at particular radial locations and these constraints must therefore be enforced through the application of a point force at the stop location. In the current method, the value of the force to be applied is to be explicitly calculated at each time step using the displacement at the stop as an additional boundary condition. An additional radial element of small

size is added at the droop stop location and the force is applied to this element. Applying the boundary conditions for an articulated blade to equation 4.13 gives:

$$\begin{Bmatrix} 0 \\ 0 \\ z_{tip} \\ z'_{tip} \end{Bmatrix} = \begin{bmatrix} N_{tip}^{11} & N_{tip}^{12} & N_{tip}^{13} & N_{tip}^{14} \\ N_{tip}^{21} & N_{tip}^{22} & N_{tip}^{23} & N_{tip}^{24} \\ N_{tip}^{31} & N_{tip}^{32} & N_{tip}^{33} & N_{tip}^{34} \\ N_{tip}^{41} & N_{tip}^{42} & N_{tip}^{43} & N_{tip}^{44} \end{bmatrix} \begin{Bmatrix} 0 \\ S_{root} \\ 0 \\ z'_{root} \end{Bmatrix} + \{C\}. \quad \textbf{4.23}$$

If a force is applied at the stop location then an addition must be made to the forcing vector C such that equation 4.23 becomes:

$$\begin{Bmatrix} 0 \\ 0 \\ z_{tip} \\ z'_{tip} \end{Bmatrix} = \begin{bmatrix} N_{tip}^{11} & N_{tip}^{12} & N_{tip}^{13} & N_{tip}^{14} \\ N_{tip}^{21} & N_{tip}^{22} & N_{tip}^{23} & N_{tip}^{24} \\ N_{tip}^{31} & N_{tip}^{32} & N_{tip}^{33} & N_{tip}^{34} \\ N_{tip}^{41} & N_{tip}^{42} & N_{tip}^{43} & N_{tip}^{44} \end{bmatrix} \begin{Bmatrix} 0 \\ S_{root} \\ 0 \\ z'_{root} \end{Bmatrix} + \{C\} + P_{stop} \begin{Bmatrix} H^{12} \\ H^{22} \\ H^{32} \\ H^{42} \end{Bmatrix}_{stop,tip} \quad \textbf{4.24}$$

where P_{stop} is the force applied by the stop. The state vector at a flap/droop stop location is given by:

$$d_{stop} = N_{stop} d_{root} + \sum_{k=root}^{stop-1} H_{k,stop} c_k \quad \textbf{4.25}$$

and the displacement of the blade at the stop is:

$$z_{stop} = \begin{bmatrix} N_{stop}^{31} & N_{stop}^{32} & N_{stop}^{33} & N_{stop}^{34} \end{bmatrix} \begin{Bmatrix} M_{root} \\ S_{root} \\ z_{root} \\ z'_{root} \end{Bmatrix} + C_{stop} \quad \textbf{4.26}$$

where C_{stop} is given by:

$$C_{stop} = \sum_{k=root}^{stop-1} \begin{bmatrix} H_{k,stop}^{31} & H_{k,stop}^{32} & H_{k,stop}^{33} & H_{k,stop}^{34} \end{bmatrix} \{c_k\}. \quad \textbf{4.27}$$

Forming equations 4.24 and 4.26 into a single matrix equation yields:

$$\begin{Bmatrix} 0 \\ 0 \\ z_{tip} \\ z'_{tip} \\ z_{stop} \end{Bmatrix} = \begin{bmatrix} N_{tip}^{11} & N_{tip}^{12} & N_{tip}^{13} & N_{tip}^{14} & H_{stop,tip} \\ N_{tip}^{21} & N_{tip}^{22} & N_{tip}^{23} & N_{tip}^{24} & H_{stop,tip} \\ N_{tip}^{31} & N_{tip}^{32} & N_{tip}^{33} & N_{tip}^{34} & H_{stop,tip} \\ N_{tip}^{41} & N_{tip}^{42} & N_{tip}^{43} & N_{tip}^{44} & H_{stop,tip} \\ N_{stop}^{31} & N_{stop}^{32} & N_{stop}^{33} & N_{stop}^{34} & 0 \end{bmatrix} \begin{Bmatrix} 0 \\ S_{root} \\ 0 \\ z'_{root} \\ P_{stop} \end{Bmatrix} + \begin{Bmatrix} C^1 \\ C^2 \\ C^3 \\ C^4 \\ C_{stop} \end{Bmatrix} \quad \textbf{4.28}$$

and the final matrix equation to be solved is:

$$-\begin{Bmatrix} C^1 \\ C^2 \\ C^3 \\ C^4 \\ C_{stop} - z_{stop} \end{Bmatrix} = \begin{bmatrix} 0 & N_{tip}^{12} & 0 & N_{tip}^{14} & H_{stop,tip} \\ 0 & N_{tip}^{22} & 0 & N_{tip}^{24} & H_{stop,tip} \\ -1 & N_{tip}^{32} & 0 & N_{tip}^{34} & H_{stop,tip} \\ 0 & N_{tip}^{42} & -1 & N_{tip}^{44} & H_{stop,tip} \\ 0 & N_{stop}^{32} & 0 & N_{stop}^{34} & 0 \end{bmatrix} \begin{Bmatrix} z_{tip} \\ S_{root} \\ z'_{tip} \\ z'_{root} \\ P_{stop} \end{Bmatrix}. \quad \textbf{4.29}$$

When the blade is in contact with a stop then equation 4.29 must be solved, when a contact is avoided row 5 and column 5 may be omitted and the solution obtained as before.

4.3.7 Pin-Type Anti-Flap/Droop Stop

The ability of the program to accept an arbitrary set of boundary conditions means that these conditions may be easily changed at any time. This fact greatly simplifies the modelling of a pin-type anti-flap/droop stop. When the pin is not engaged, the boundary conditions are set to those appropriate for an articulated blade and when it is engaged the boundary conditions are altered to those for a built-in root.

4.3.8 Calculation of the Aerodynamic Forces

In order to calculate the aerodynamic forces acting on the blades, the inflow to each blade segment, i.e. the angle of attack and Mach number, needs to be calculated. This is accomplished in the program using a series of coordinate transformations which are provided in the Appendix. Given the inflow conditions, the new dynamics method calculates the resulting sectional lift coefficient using the same aerodynamic model as Newman (1995). The model is a simple quasi-steady derivation which uses the same trailing edge stall equations as the 3rd generation model. Given the simplicity of the model for the basic aerofoil, the trailing edge flaps have been modelled using a simple correction to the zero-lift angle, according to thin aerofoil theory [see, for example, Chan and Brocklehurst (2001)]. However, the assumption that the lift coefficient varies linearly with flap deflection had to be reviewed.

During rotor engagement and disengagement the rotor speed is clearly reduced well below the normal operating value. This means that the dynamic head encountered by the blades is significantly reduced and therefore the flap deflections required to influence any blade sailing can be expected to be reasonably large such that the assumption of a constant value for the flap effectiveness is no longer valid. ESDU (1994) provides data for the variation in 2-dimensional flap effectiveness, η_{2D}, with the absolute value of the flap deflection angle. The data can be accurately represented using a third degree polynomial such that:

$$\eta_{2D} = A_\eta \left(\delta + \varphi\right)^3 + B_\eta \left(\delta + \varphi\right)^2 + C_\eta \left(\delta + \varphi\right) + D_\eta \qquad \textbf{4.30}$$

where A_η, B_η, C_η and D_η are constants and φ is a trailing edge geometry parameter [see ESDU (1994)].

As well as the 2-dimensional flap effects, the flap effectiveness is also limited due to its finite aspect ratio. An approximation for these effects, as used by Kim et al (2004), is given as:

$$\eta_{3D} = \frac{AR_f}{\left(AR_f + 2\left(AR_f + 4\right)/\left(AR_f + 2\right)\right)} \qquad \textbf{4.31}$$

where the flap aspect ratio is given by:

$$AR_f = \frac{L_f}{c_f} \qquad \textbf{4.32}$$

where L_f is the flap length and c_f is the flap chord. The overall change in the zero lift forcing due to the flap deflection is therefore:

$$\Delta\varepsilon_0 = \eta_{3D}\eta_{2D}\left[1 + \frac{\left(\sin\psi_h - \psi_h\right)}{\pi}\right]\delta\,. \qquad \textbf{4.33}$$

Where the term in brackets is the effect due to the flap according to thin aerofoil theory (see the following chapter for a derivation) and ψ_h is the hinge location in the circular chordwise coordinate system. The normal force coefficient, including the effects due to the flap is then given by:

$$C_n = C_{l_\alpha} \sin\left(\alpha + \Delta\varepsilon_0\right) \tfrac{1}{4}\left(1 + \sqrt{f}\right)^2 \qquad \textbf{4.34}$$

where f is the trailing edge separation location given by the equations of the form used in the 3rd generation model.

4.3.9 Validation of the New Dynamics Method

Figure 4.10 presents a comparison of the tip deflection prediction using Newman's (1995) method (model 1) and the new method (model 2) for a Lynx engagement operation. The general form of the plots is in good agreement and both models capture the 'spike' that occurs soon after rotor run-up is commenced. The new model predicts a larger spike than the old model but predicts a slightly smaller peak-to-peak displacement once normal operating rotor speed is achieved.

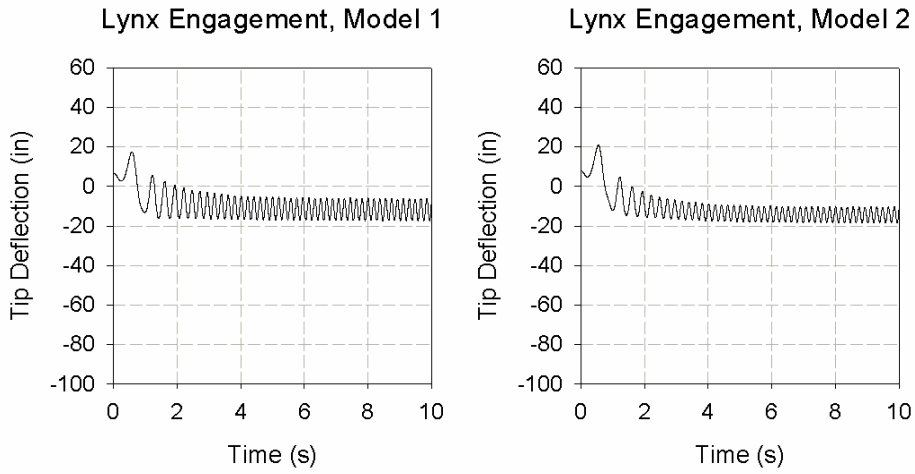

Figure 4.10: Tip deflection prediction for a Lynx rotor engagement using Newman's (1995) method (model 1) and the new method (model 2).

Figure 4.11 presents similar plots for a Lynx disengagement operation. Once again the plots are generally similar and both models predict a spike at around 24 seconds. The magnitude of this spike again differs slightly between the models however the most notable difference between the two plots is the prediction by the old model of a small oscillation when the rotor is at rest. The tip deflection reaches a steady amplitude oscillation according to model 1 as opposed to the steady state predicted by model 2. This difference is considered to be numerical and could be eliminated by the application of a small level of damping which would in reality be present in the structure of the blades.

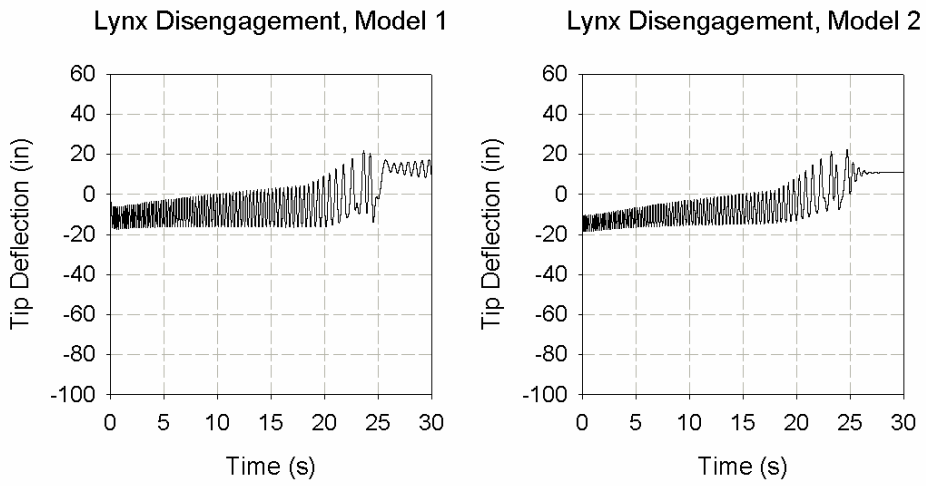

Figure 4.11: Tip deflection prediction for a Lynx rotor disengagement using Newman's (1995) method (model 1) and the new method (model 2).

Figure 4.12 displays a comparison of the two models for the Sea King engagement operation. The plots are conceptually very similar and the initial spikes, soon after run-up is commenced, are of similar magnitude and appear to be in even better agreement than for the Lynx plots.

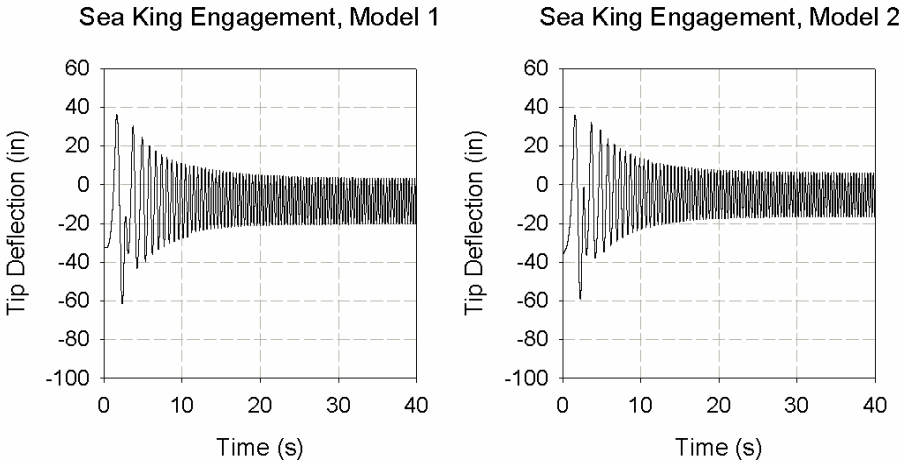

Figure 4.12: Tip deflection prediction for a Sea King rotor engagement using Newman's (1995) method (model 1) and the new method (model 2).

The plots for the Sea King disengagement are shown in Figure 4.13. The maximum and minimum spikes are well captured by both models however the old model once again predicts a large oscillation of the blade at rest which is not predicted using the new model.

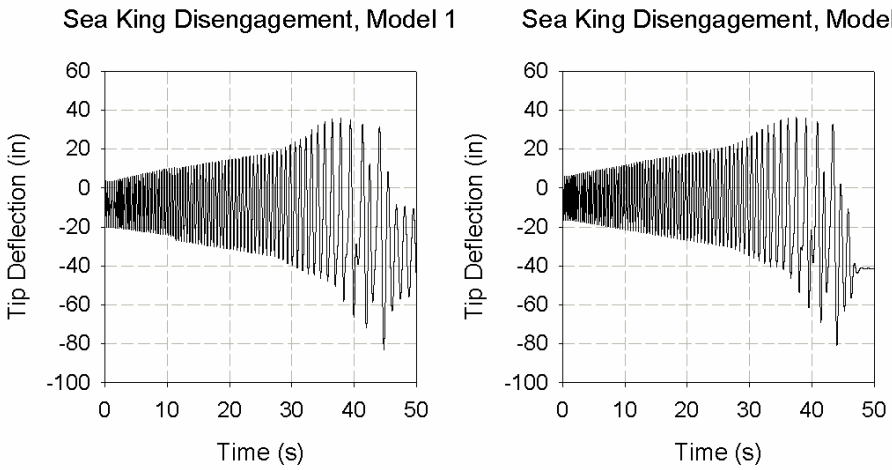

Figure 4.13: Tip deflection prediction for a Sea King rotor disengagement using Newman's (1995) method (model 1) and the new method (model 2).

Figure 4.14 compares the minimum and maximum values of the tip deflection taken from the previous plots. These values are in good agreement with the possible exception of the Lynx engagement.

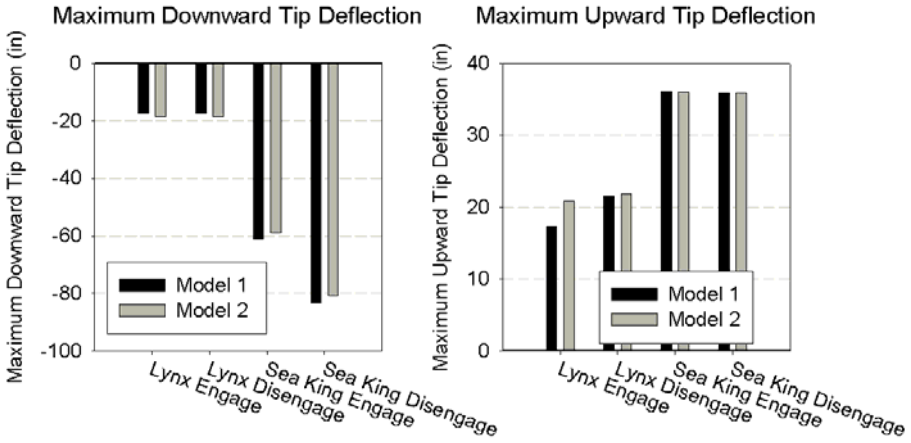

Figure 4.14: Maximum and minimum tip deflection predicted using Newman's (1995) method (model 1) and the new method (model 2).

Overall the two models compare well. The Sea King results are generally better correlated than the Lynx results and the plots for the engagement operation are qualitatively closer than those for the disengage operation. In particular there is a large discrepancy between the models in the prediction of the blade dynamics once the rotor speed approaches zero. This is attributed to the fact that neither model incorporates structural damping. Therefore as the rotor reduces towards zero the aerodynamic damping becomes small and the stability of the solution becomes dependent upon the numerical method. It is suggested that the application of a small amount of structural damping to each model would alleviate these discrepancies. These effects however are

not of importance for the investigations which follow as the main effects of blade sailing appear to occur well before the discrepancies begin.

4.4 Application of the Trailing Edge Flap to Blade Sailing

This section presents the philosophy developed for the reduction of blade sailing using Trailing Edge Flaps. Much of this research was performed using Newman's (1995) method which was adapted to incorporate the aerodynamic effects due to Trailing Edge Flaps and focussed on predictions for the Lynx and Sea King aircraft. A summary of the results and conclusions from this work will be presented here but for further information the reader should refer to Jones and Newman (2007). This section will therefore mostly present results obtained using the new method and will consider the operational implications of using a Trailing Edge Flap for the reduction of blade sailing of a stiffer rotor blade which is more representative of those installed on more modern aircraft such as the EH101.

4.4.1 Summary of Results using the Old Method

To demonstrate the philosophy a simplified wind model originally suggested by Newman (1995) and hard-coded into the software was used. This model consists of a constant horizontal velocity traversing the deck with a superimposed vertical velocity which varies linearly across the rotor disk (Figure 4.15). Throughout this investigation the horizontal velocity was kept constant at 50 knots. Unless otherwise stated, the maximum/minimum values of the vertical wind velocity (at the lateral extents of the rotor disc) are +/-15 knots.

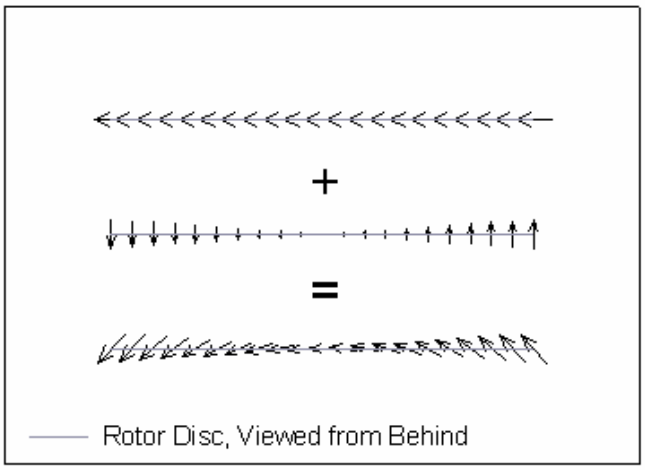

Figure 4.15: Schematic of the simplified wind model.

During initial research into the Sea King aircraft, operation of the TEF in relation to the blade tip displacement, velocity and acceleration was investigated. From these results it was found that considerable reductions in the blade tip excursions could be achieved by deflecting the TEF in opposition to the blade tip deflection velocity (i.e. if the blade tip is moving upwards then the flap deflection should be negative and vice versa, see Figure 4.16).

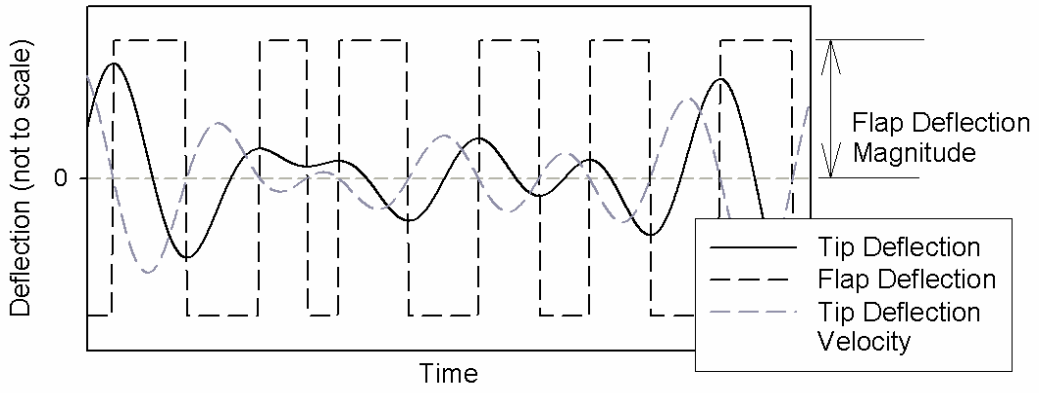

Figure 4.16: Schematic of flap deflection scheduling.

Using this deflection philosophy a parametric study of TEF parameters was performed for both the Lynx and Sea King aircraft. The TEF chord was held constant at 15% but the spanwise geometry was investigated through trialling lengths of 10%, 15% and 20% radius and locations varying from 45% to 95% in 10% intervals. For each TEF geometry, the effect due to the magnitude of the TEF deflection was investigated with deflections from 0 to 50 degrees being trialled in 5 degree intervals. In addition, as the main effects due to blade sailing occur at lower rotor speed the effect of only operating the TEF up to a set maximum rotor speed was also investigated. This rotor speed is referred to by the author as the 'flap omega' and defines the rotor speed at which TEF deflections commence for a rotor disengagement or the rotor speed at which the deflections are stopped for a rotor engagement. 'Flap omega' values from 4% to 100% normal operating speed were used and in all cases the flap deflections were stopped for rotor speeds below 2% of the operating rotor speed. In each case the maximum and minimum tip deflections were recorded for analysis.

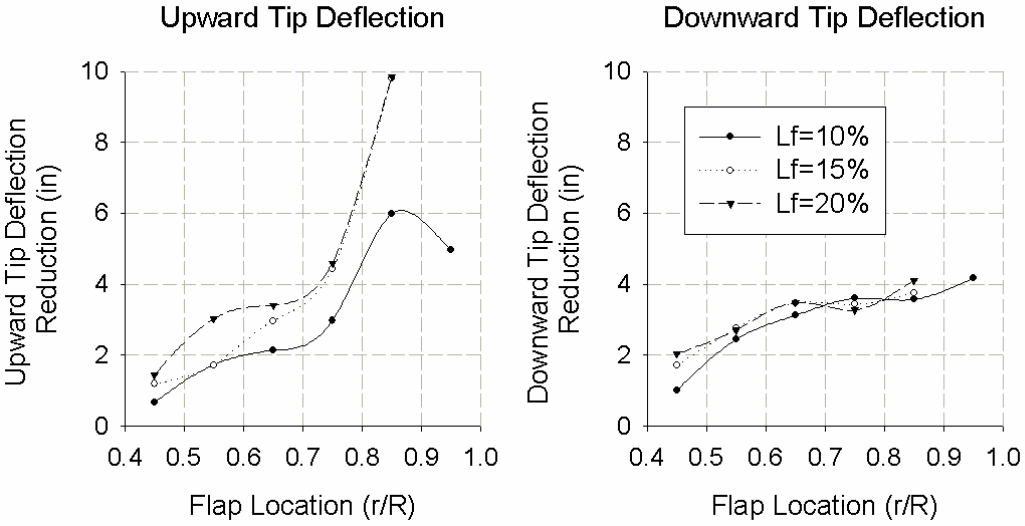

Figure 4.17: Optimum tip deflection reduction for the various flap geometries during Lynx engagement.

As an example of the effects due to TEF size and location, the optimum reductions for each flap location and length are plotted for the Lynx engagement operation in Figure 4.17. The maximum reductions in blade excursions are observed when using a larger flap farther outboard, which is to be expected due to the greater dynamic head giving an increase in flap effectiveness. The flap of 20% span located at 85% radius was found to be optimum for all cases and the remaining results will be for the optimum flap geometry unless otherwise stated.

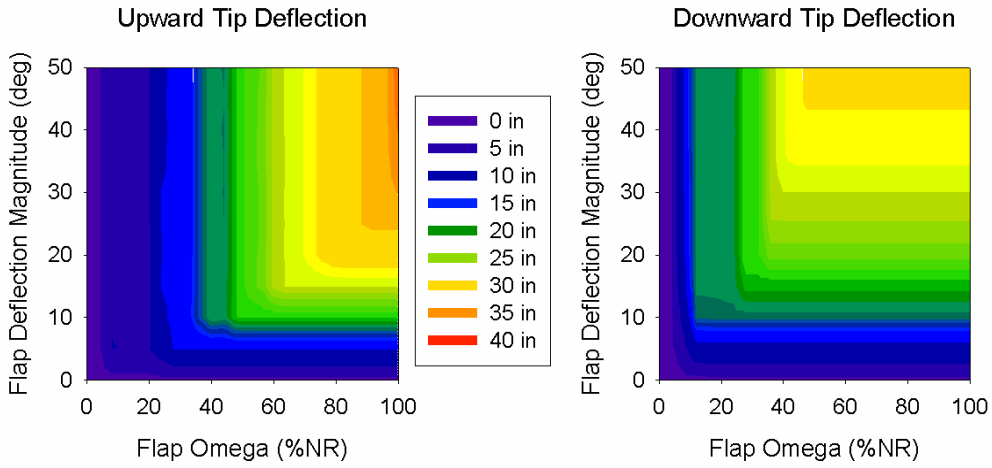

Figure 4.18: Maximum and minimum tip deflection during Sea King engagement.

An example of the effect on tip deflections due to the TEF deflection magnitude and the 'flap omega' is presented for a Sea King engagement in Figure 4.18. Clearly the maximum possible deflection should be used for the maximum reduction in tip deflections. The blade tip excursions are obviously much more pronounced for the

articulated, flexible blade of the Sea King than they are for the Lynx and even at full rotor speed the blade deflections are relatively large. For this reason Figure 4.18 suggests that greater deflection reductions are achieved if the flap is utilized up to 100%NR. However, significant reductions in both the upward and downward tip deflections are still possible with a flap operated only at lower rotor speeds.

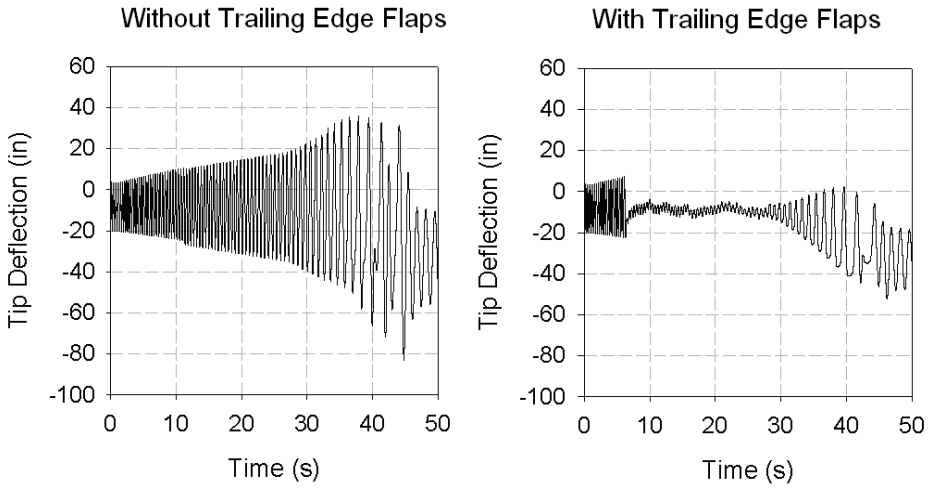

Figure 4.19: Tip deflection plots for a Sea King disengagement with and without TEF operation. TEF is 20% span located at 85% rotor radius and using +/-50deg deflection up to 80% normal operating rotor speed.

The tip traces plotted in Figure 4.19 display a Sea King disengagement with and without a TEF deflection of +/-50 degrees using the optimum TEF geometry and a flap omega of 80%NR. Even with the 50 deg deflection, further reductions would still be possible if a greater controlling force were available i.e. the flap has become saturated from around 30 seconds into the trace. It is also clear from this plot that the flap could be used only at lower rotor speeds if a larger, though not excessive, tip deflection is tolerated at the higher rotor speeds.

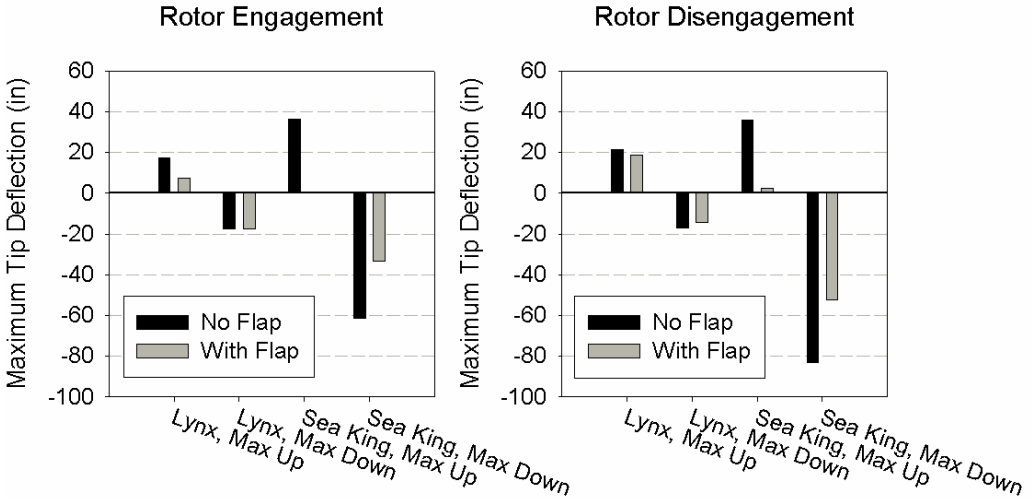

Figure 4.20: Maximum tip deflection with and without flap actuation, Newman's (1995) method.

A summary of the maximum upward and downward tip deflections for both Lynx and Sea King aircraft is presented in Figure 4.20. The no flap cases are shown alongside cases for the optimum flap operating to 100%NR with a deflection magnitude of 50 degrees. Clearly the reductions in the Lynx blade excursions are small; a result which is unsurprising given that the stiff, hingeless rotor of this aircraft would be expected to be less susceptible to blade sailing. The deflections of the Sea King rotor in contrast have been greatly reduced. The downward deflections during both rotor engagement and disengagement have been reduced by almost 30 inches and the flap appears to be equally effective during both operations.

The main conclusion to be made from the initial investigation using the old dynamics method was that a TEF operating in opposition to the blade tip velocity could considerably reduce the tip excursions of a Sea King rotor blade under blade sailing conditions. The results are maximised using as large as possible a TEF located near the tip of the blade to maximise the dynamic head and therefore the forcing capability. The effectiveness was generally improved with increasing deflection capability; however it was found that it is only necessary to deflect the flap once the rotor has slowed to significantly less than 50% of its normal operating speed.

4.4.2 Further Investigation using the New Method

A similar investigation using the new dynamics method confirmed that the flap of 20% span located at 85% radius is the optimum. All results in this section are therefore for this optimum flap geometry and in order to encapsulate all possible gains, results for a deflection magnitude of 50 degrees and a flap omega of 100%NR are shown. Figure 4.21 shows the maximum and minimum deflections for both the Lynx and Sea King. A comparison of Figure 4.20 and Figure 4.21 suggests that both dynamics methods are predicting similar reductions in blade sailing using the trailing edge flap providing confidence in proceeding with further investigations using the new method.

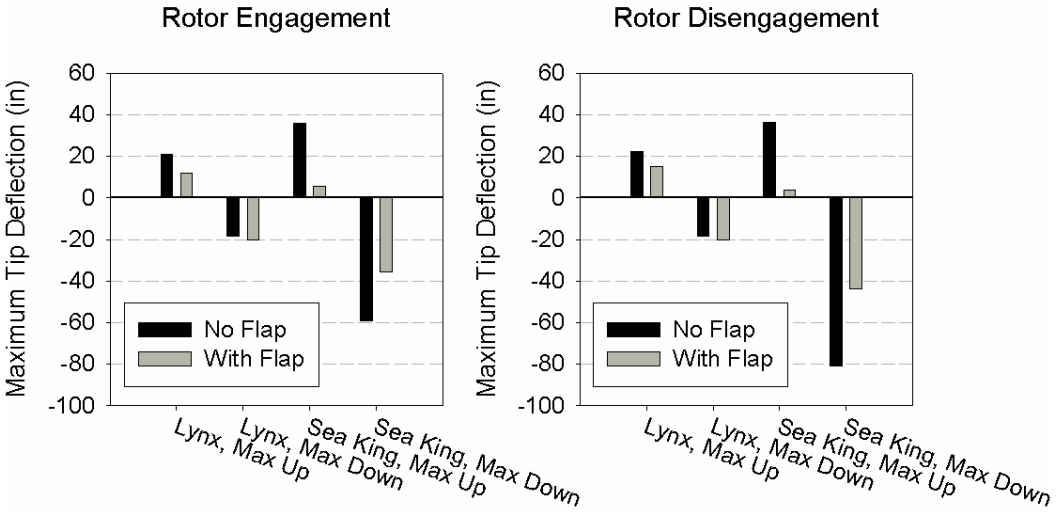

Figure 4.21: Maximum tip deflection with and without flap actuation, new method.

The new program enables an arbitrary blade to be more easily analyzed without the need for an external modal calculation and is also capable of modelling the pin-type anti-flap/droop stop. The Sea King data was therefore modified by increasing the mass and stiffness distributions to obtain a stiffer blade which is more representative of modern blades such as the BERP III on the EH101. The effect of the linear wind distribution described in the previous section on the engagement and disengagement operation of this blade was investigated using both the traditional and pin-type flap stops. The minimum tip deflections and the maximum absolute bending moment for each blade with no flap actuation are presented in Figure 4.22.

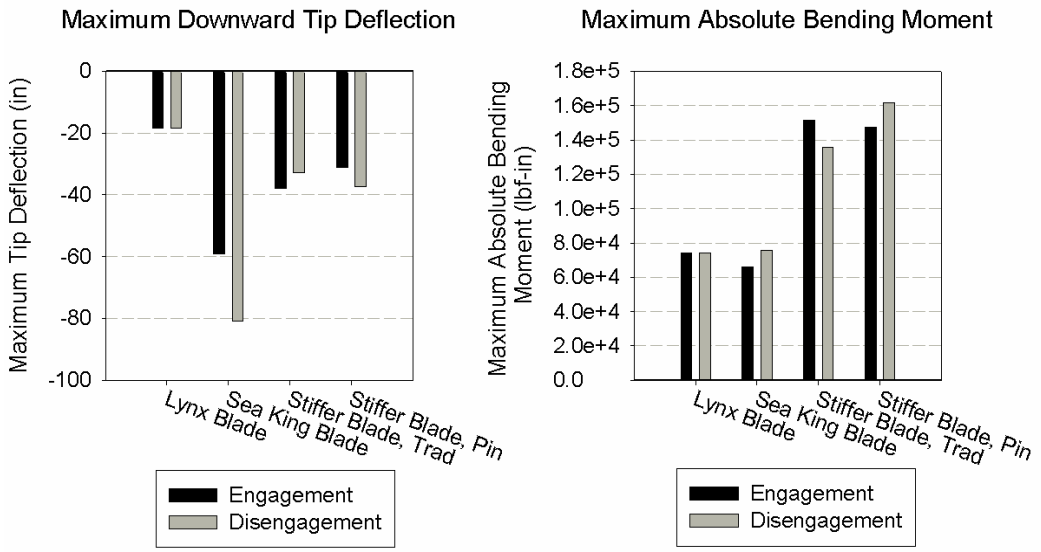

Figure 4.22: Tip deflections and bending moments for various blades.

As is to be expected, the tip deflection of the stiffer blade is much smaller than that for the Sea King and the maximum bending moment has increased correspondingly. The

difference between the stop types is relatively small, with the pin-type being advantageous during rotor engagement but disadvantageous during rotor disengagement, however the presence of these differences suggest it is important to correctly model the boundary condition of the pin-type stop. The tip traces for both stop types during rotor disengagement are shown in Figure 4.23. The tip displacements are generally similar although there are some clear qualitative differences around 35 seconds.

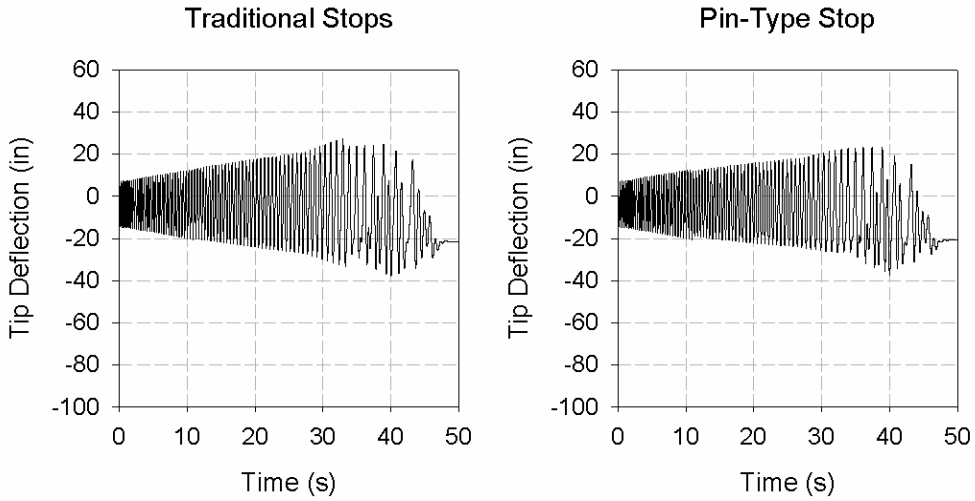

Figure 4.23: Comparison of tip traces for the stiffer blade with different stops.

The maximum downward blade deflections and the maximum absolute blade bending moments are presented for the stiffer blade with and without flap actuation in Figure 4.24. Firstly it is interesting to note that the use of the pin-type stop has resulted in a significant increase (of the order of 15%) in the maximum bending moment during the disengagement operation in comparison to the traditional flap stop. This again highlights the importance of correctly modelling this root boundary condition.

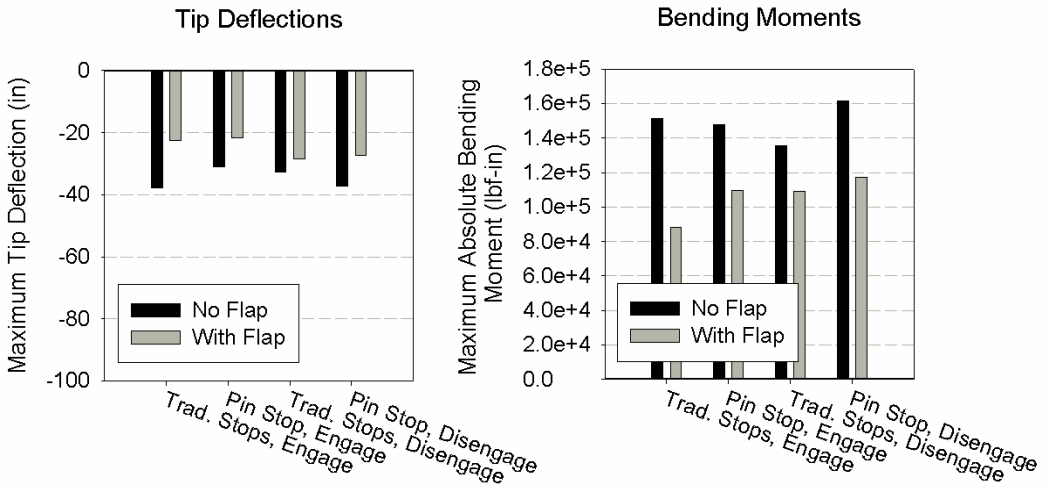

Figure 4.24: Effect of TEF on stiffer blade deflections and bending moments.

The TEF has less of an effect on the stiffer blade deflections than it did for the Sea King. For this blade however the blade excursions are of less importance than the associated bending moments. The blade loads are significantly reduced when using either of the stop types although for this blade the flap appears to be more effective during rotor engagement than during rotor disengagement.

The predicted reductions in both tip deflections and bending moments of the stiffer blade can have significant operational implications. Blade sailing can lead to a reduction of the Ship Helicopter Operating Limits (SHOL) if a wind velocity producing a limit load or deflection during blade sailing represents the lowest limit for safe rotor operation. The use of the TEF using the methodology developed above may significantly delay the occurrence of blade sailing to wind conditions of greater severity and thus expand the operational envelope of the shipborne helicopter.

Consider then the effect of varying the vertical wind velocity component of the simplified wind model. Figure 4.25 shows the variation of maximum and minimum tip deflections for the stiffer rotor with traditional-type flap stops. Results are shown without the TEF and with the TEF of optimal geometry being actuated at a deflection magnitude of 50 degrees and a flap omega of 100%NR.

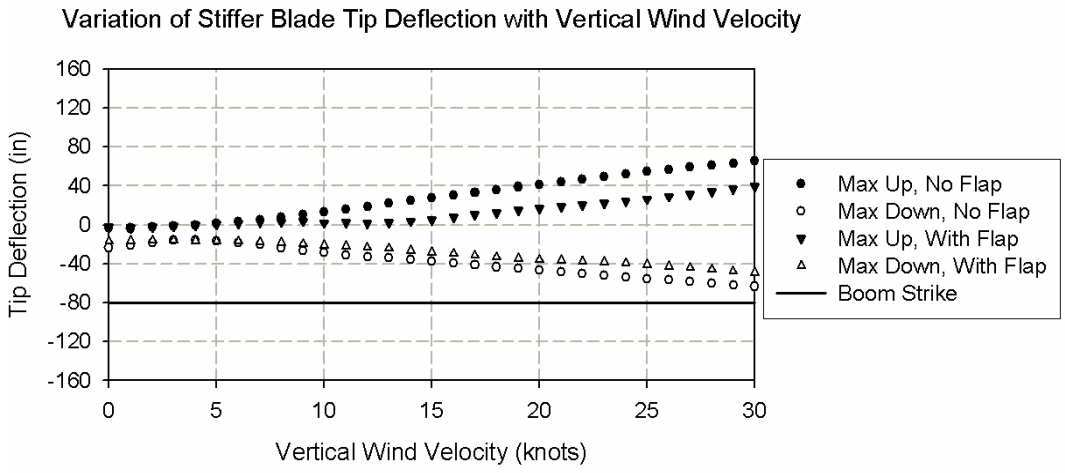

Figure 4.25: Variation of stiffer blade tip deflection with vertical wind velocity during rotor disengagement with and without TEF control.

Although the TEF reduces the tip deflections throughout the wind velocity range, it is clear that the baseline case does not encounter a boom strike throughout the range tested (the 'boom strike' line represents the tip deflection required for a boom strike on the Sea King helicopter). Although the blade deflection itself might not be such a critical issue for this relatively stiff rotor blade, a SHOL limit might be defined by the blade structural

loads. Figure 4.26 therefore displays the available reduction in maximum and minimum bending moments during disengagement of the stiffer rotor with traditional-type stops.

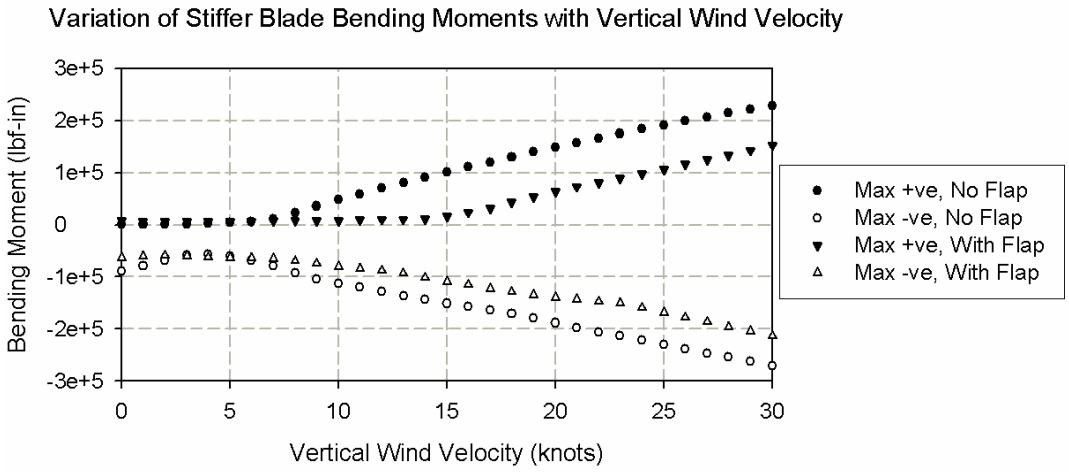

Figure 4.26: Variation of stiffer blade bending moment with vertical wind velocity during rotor disengagement with and without TEF control.

Clearly the trailing edge flap is capable of large reductions in blade bending moments during rotor disengagement and this is shown throughout the vertical wind speed range. This reduction considerably increases the wind speed required to attain a given bending moment. Suppose, for example, that the blade is structurally limited to bending moments of +/-150000 lbf-in. The negative bending moment limit is reached first either with or without the TEF. Without the TEF the limit is reached at a vertical wind velocity of 15knots. With the actuation of the TEF the attainment of the limit is delayed to a wind speed of around 22.5knots. The maximum allowable wind speed for the disengagement operation is therefore increased by around 50%. If disengagement represents the overall SHOL limit then the operational boundary could be significantly increased.

4.5 Application to a Real Operational Case Study

The concept of using a TEF for the reduction of blade sailing has been developed using an idealised gust model to represent hypothetical conditions on the deck of a ship. In this section the concept will be applied to a real case study using more realistic wind conditions and a true measure of an operational limitation.

The centrisep (Figure 4.27 and Figure 4.28) is an air filter attached above the cockpit of many Sea King helicopters to ensure that the flow entering the engines is free of sand and other such particles and has been successfully used for over a decade. Recently however, there have been a few occurrences of the rotor blade coming into contact with the centrisep. The resulting damage to both the centrisep and the blade has only been noticed

during the pre-flight check for the following flight. The exact circumstances and timing (i.e. during landing, taxiing or engagement/disengagement) at which the blade strikes are occurring is therefore unknown.

Figure 4.27: Image of a Sea King Helicopter with centrisep

An investigation was conducted using the new dynamics method to determine whether it is likely that a rotor blade could come into contact with the centrisep during a rotor engagement or disengagement operation in normal operating conditions. Specifically, normal operating conditions means the consideration of wind speeds up to 45 knots gusting up to 70 knots and ground sloping up to angles of 9 degrees.

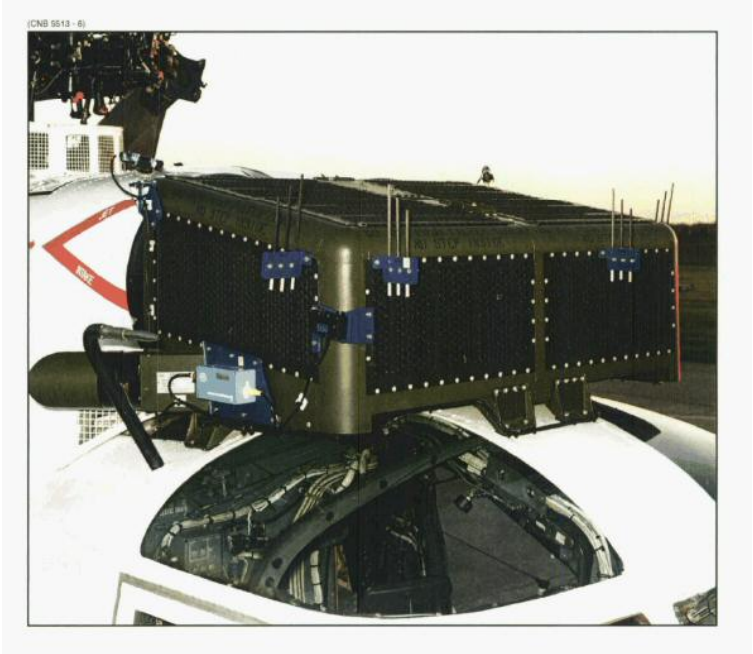

Figure 4.28: Close Up Image of the centrisep

This section presents the results of this investigation before considering the impact that the use of a trailing edge flap might have on this real-world blade sailing issue.

4.5.1 Flow over Terrain

For the purpose of this investigation it was required to define the variation of the environmental boundary layer as it passes over a given set of terrain such that the global velocity field, within which the aircraft resides, may be prescribed for input into the blade sailing program. Following some research into the topic some empirical formulas for the variation of the flow speed were found in reports from the Engineering Sciences Data Unit (ESDU). Report number ESDU (1993) provides calculation methods for 'speed up' factors over a set of topographical features which may be superimposed to form an arbitrary landscape and ESDU (2000) and ESDU (1985) provide methods for including the effects of gusty and turbulent conditions.

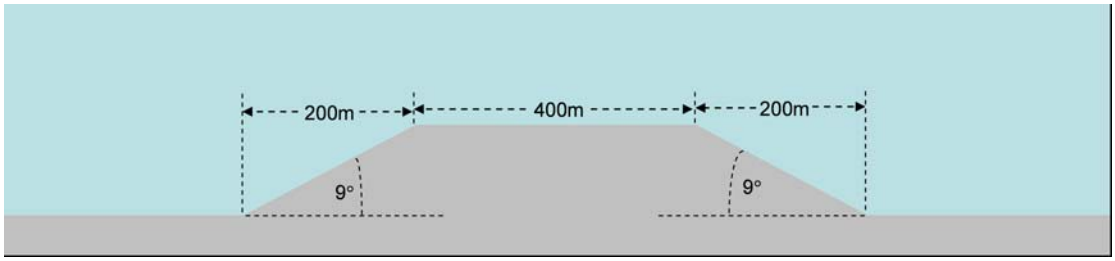

Figure 4.29: Geometry of the Ramp Terrain

The investigation required the modelling of sloping ground on airport aprons however it was desirable that a single terrain shape could be designed such that a variety of slope cases could be obtained from a single data set. The geometry decided upon is shown in Figure 4.29. The up and down ramps allow for the calculation of cases on windward and leeward slopes. The long slopes also allow cases to be run either close to, or away from, a gradient change.

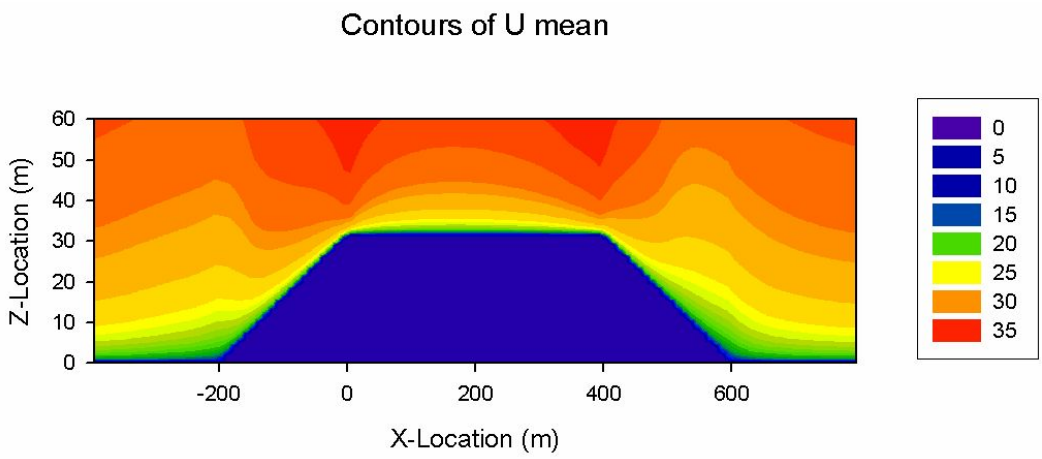

Figure 4.30: Contours of Mean Horizontal Velocity

For this terrain, the equations from the ESDU reports were used to calculate the horizontal velocity as shown in Figure 4.30. The vertical velocity values were then calculated using continuity such that a full 2-dimensional velocity field could be defined for use by the blade sailing program.

4.5.2 Results for Various Locations and Orientations

To investigate the effects due to sloping ground on the engagement and disengagement operations of the Sea King helicopter main rotor, simulations have been run at various locations on the terrain defined in the previous section. At the various locations the effect of the helicopter orientation was also considered by running cases with wind coming from various directions with respect to the fuselage. The various locations and orientations tested are shown in Figure 4.31.

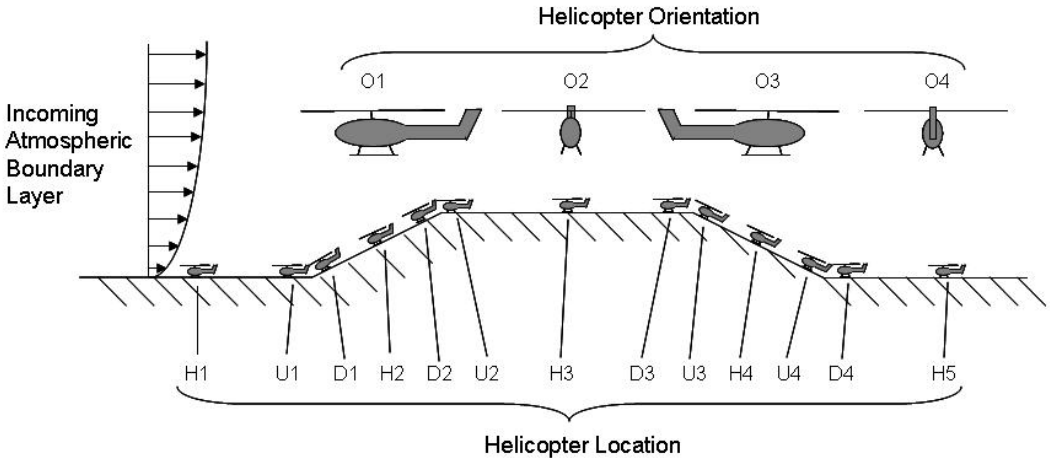

Figure 4.31: Numerical Test Locations and Orientations

The numbering of the various locations may seem arbitrary at first. However when the flow presented in Figure 4.30 is considered it may be deduced that at some locations the

rotor experiences an upwash; whilst at others it experiences a downwash or is predominantly horizontal. Locations H1-5 are the predominantly horizontal cases and locations U1-4 and D1-4 are the upwash and downwash cases respectively. The various locations have been numbered in this manner as blade sailing has been found in the past to be heavily influenced by flow through the rotor disc, Newman (1995).

The azimuth at which the primary blade is located on commencement of the rotor engagement/disengagement operation was found to have an influence on the magnitude of the separation distance between the blade and the centrisep. Therefore, for each location and orientation, the starting azimuth of the primary blade was varied from 0 to 66 degrees in increments of 6 degrees (note that starting azimuths greater than or equal to 72 degrees are equivalent to those less than 72 degrees for the 5-bladed rotor). For the figures presented below, the minimum value of each of the starting azimuth cases is plotted such that each plot is in effect a worst case scenario in terms of operation commencement.

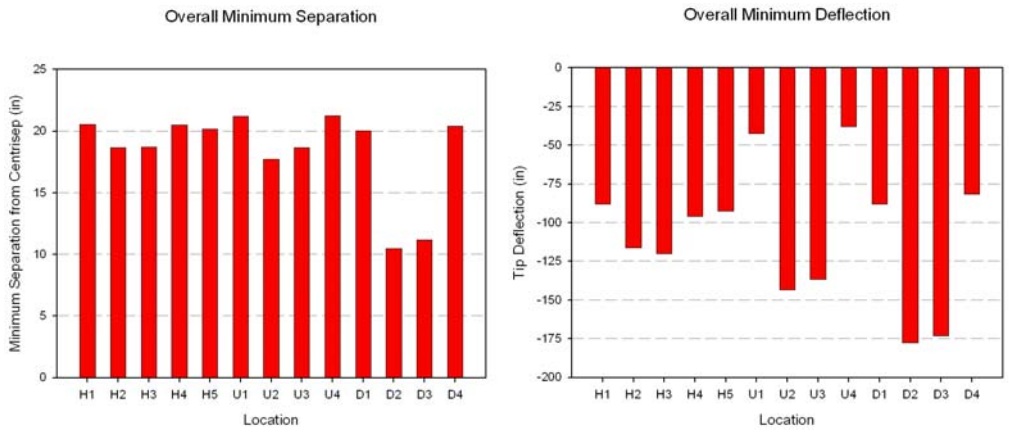

Figure 4.32: Overall Minimum Clearance and Tip Deflection during Disengagement

In order to provide an immediate visualisation of the worst locations on the standard terrain, the separation distance from the centrisep and the minimum tip deflections were minimised over both the starting azimuth and the fuselage orientation and plotted for each location in Figure 4.32 and Figure 4.33, which represent disengagement and engagement respectively. The minimum tip deflection plots are included to provide a guide as to which cases are generating the most blade sailing generally, whilst the separation from the centrisep is more specific to the blade strike problem being considered here.

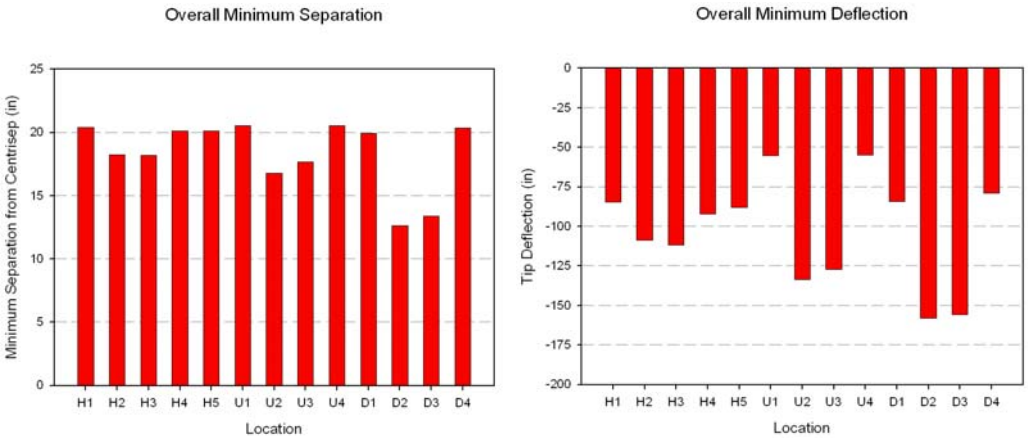

Figure 4.33: Overall Minimum Clearance and Tip Deflection during Engagement

It is immediately apparent that the worst cases in terms of both blade sailing and centrisep separation are with the fuselage located at D2, D3, U2 and U3. Note that all of these cases are with the fuselage located close to the top of a ramp such that the rotor is experiencing a flow which is convex in nature and is hence applying an equivalent positive coning to the rotor disc. Note also that in cases U2 and D3 the ground is flat and therefore it is the flow being generated by the ramp and not the fuselage tilt itself that is affecting the results. Comparing Figure 4.32 to Figure 4.33 it appears that although the trends in terms of location are similar, the blade sailing is generally worse during disengagement than during engagement. The results also show that the centrisep separation distance is smaller during disengagement which suggests that a blade strike is more likely during rotor disengagement than engagement.

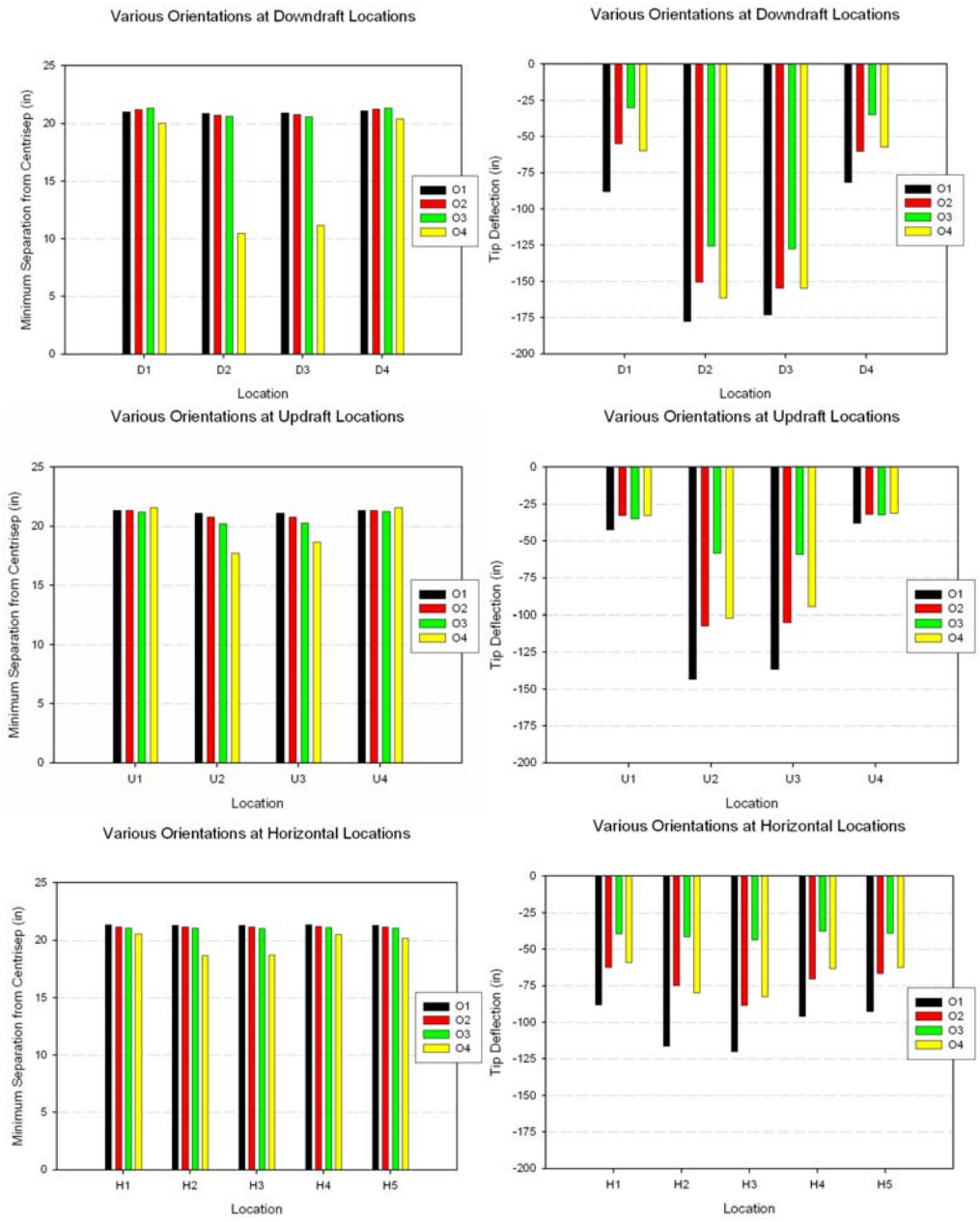

Figure 4.34: Minimum Clearance and Tip Deflections at Various Orientations - Disengagement

Figure 4.34 considers the effects due to the fuselage orientation on the disengagement operation. The downward tip deflection is generally greater for the downflow cases than for the horizontal and upflow cases. With flow going down through the rotor disc, the blades experience a more negative angle of attack and they are forced downward resulting in the increase of the downward tip deflection. Also there is clearly a general trend suggesting that orientations O2 and O4 are generally similar whilst case O1 gives an increase in the downward tip deflection and case O3 gives a reduction in the downward tip deflection. This effect is believed to be due to the shaft tilt of the Sea King helicopter. Cases O2 and O4 are with the helicopter experiencing a crosswind. In these cases the

shaft tilt results in the disc being tilted in a direction perpendicular to the predominant flow and therefore has little influence on the amount or direction of flow going through the rotor disc. In case O1 the shaft tilt causes the rotor disc to be tilted toward the flow and therefore an increase in the amount of flow going down through the rotor disc can be expected. Case O3 is opposite to case O1 and with more upward flow through the disc, any downward forcing of the blades is reduced. Therefore the results suggest that a helicopter with forward shaft tilt can be expected to experience greater downward tip deflections during engagement and disengagement when the helicopter is in a headwind.

The centrisep clearance shows entirely different trends. There is little effect due to location unless the helicopter is at orientation O4, i.e. with the wind from port. At this orientation, the blade deflection at the radius of the centrisep is at a minimum when it is above the location of the centrisep. At the other orientations the deflection of the blade may well be greater, as the tip deflection plots suggest, however this deflection occurs when the blade is at an azimuth which is away from the centrisep and therefore the minimum separation distance is not affected. The dominant effect of the fuselage orientation is therefore in dictating the azimuth at which the blade deflection is a minimum and therefore, even though blade deflections may be greater in a headwind due to the shaft tilt, the blades are likely to pass closer to the centrisep when the wind is coming from the port side. Note also that the cases which cause the blade to move close to the centrisep are D2 and D3. In these cases the mean flow is such that the rotor experiences a downflow on the starboard side of the disc thus forcing the blade downward as it moves toward the nose.

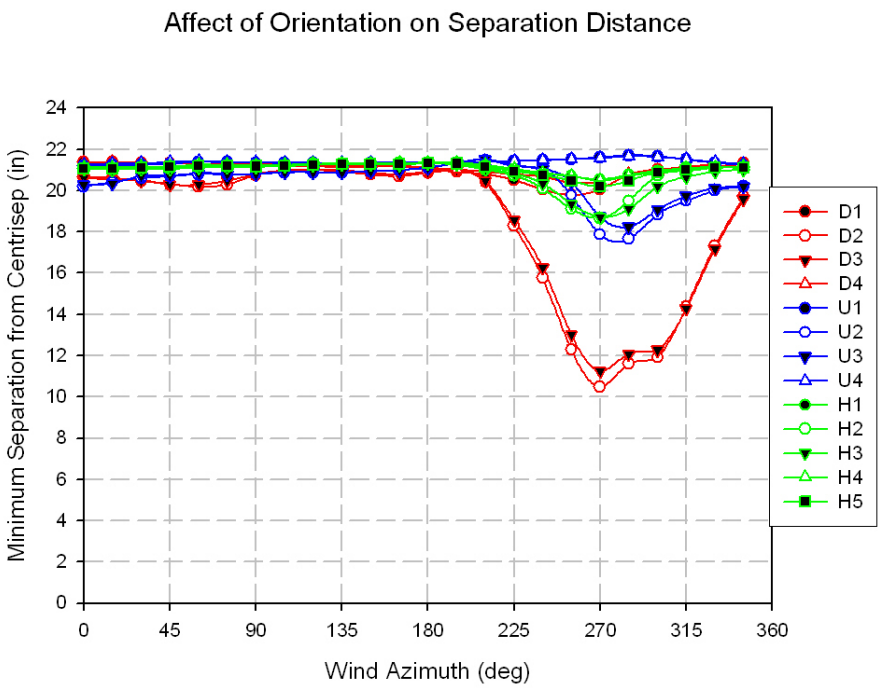

Figure 4.35: Effect of orientation on centrisep clearance

So far only orientations every 90 degrees have been considered however it is possible that the worst cases are at orientations between these values. Therefore the orientation of the fuselage is now altered such that the wind comes from any given azimuth such that a wind azimuth of 0 degrees is equivalent to orientation O3 and a wind azimuth of 270 degrees is equivalent to orientation O4. The result of this study is shown in Figure 4.35 which confirms that the minimum centrisep clearance occurs when the wind is coming from, or just forward of, 270 degrees.

The worst case is therefore with the helicopter at location D2 with orientation O4. In this case the helicopter is at the top of a windward facing slope with the starboard wheel up the slope and the wind coming from the port side. Also note however that case D3 also provides a large reduction in clearance. This suggests that the most critical cases are when the aircraft is located just upstream of a convex change in the terrain.

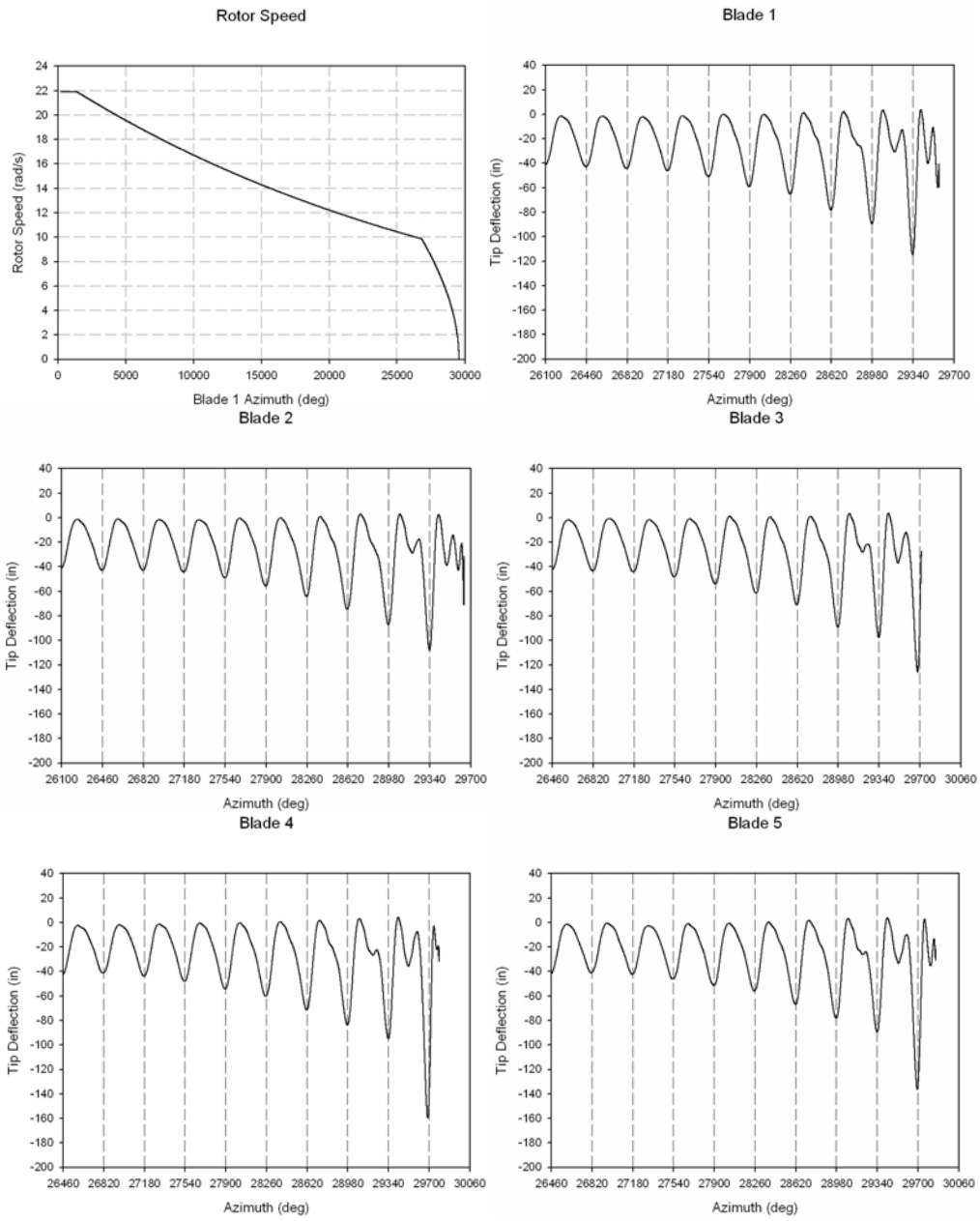

Figure 4.36: Tip Plots against Azimuth for the Worst Case

For further insight, Figure 4.36 presents plots of the tip deflection against the cumulative azimuth for the worst case. The gridlines in the plots are all at azimuths equivalent to 180 degrees, i.e. when the blade is directly over the nose of the helicopter. It is immediately clear that the rotor inflow is forcing the blades into a predominantly 1/rev response. In the worst case shown here, the flow is from port with a large downward component over much of the rotor disc. This causes an effective disc tilt towards the nose of the aircraft, thus reducing the clearance between the blades and the centrisep.

4.5.3 Experimental Support for Observations

An experimental investigation was designed and performed by Dr S. Newman to support the results found in the numerical study described above. Briefly, the experiment consisted of a single-bladed model rotor mounted on a leeward facing ramp in a wind tunnel (see Figure 4.37 through Figure 4.39).

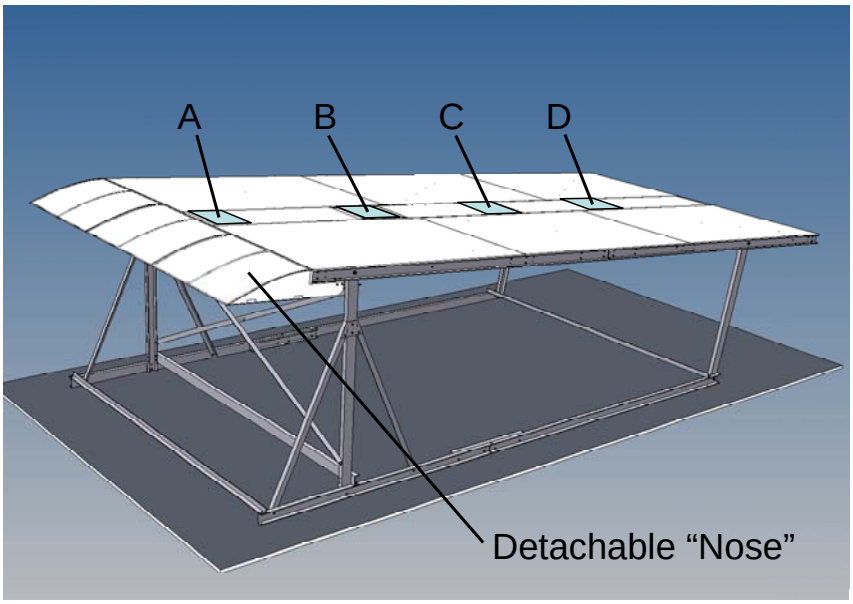

Figure 4.37: 3-Dimensional drawing of the ramp showing the four rotor positions and detachable "nose". Image courtesy of Dr S. Newman.

The ramp could be tilted at a variety of discrete angles by using different length vertical supports at the rear end of the ramp, although it should be noted that all results presented here are for an angle of 10 degrees. The rotor could be moved up and down the slope to provide the four positions labelled A to D in Figure 4.37. Here results from positions A and B will be used as these are approximately equivalent to positions U3 and H4 respectively in the numerical study. The model rotor also incorporated a shaft tilt of approximately 2 degrees and the model could be rotated on the ramp in steps of 90 degrees such that orientations equivalent to O1-4 in Figure 4.31 could be studied.

Figure 4.38: Image of the rotor model mounted at position A on the ramp in the wind tunnel. Note that the flow direction is towards the observer such that the ramp provides a leeward-facing slope. Image courtesy of Dr S. Newman.

The original set up incorporated a 'nose' to the ramp which effectively turned the flow onto the ramp such that it remained attached and was therefore similar in nature to the terrain flow in the numerical investigation. Part way through the experiment the 'nose' was removed to promote flow separation from the leading edge of the ramp such that a large re-circulating region was in existence over the ramp. Although less representative of the current case study, this configuration was observed to promote larger amounts of blade sailing and is perhaps more representative of the sea-borne scenarios which are more typically associated with the phenomenon.

Figure 4.39: Close-up image of the single-blade teetering rotor model mounted at position B on the ramp. Image courtesy of Dr S. Newman.

The intention of the experiment was to support the qualitative conclusions of the numerical study in terms of trends and worst case positions and orientations. It was never intended that the experiment could be used to quantitatively validate the model. One reason for this is that the numerical method was not developed to be able to predict the behaviour of teetering rotors and some modification to the program would be required to do this. Secondly, a major feature of the numerical model is the aeroelastic formulation and this could not possibly be verified using the current model rotor which would be best approximated as a rigid blade. Finally, it is unlikely that the experimental set-up would be able to provide sufficient aerodynamic data to make a quantitative comparison viable as such a comparison would require a detailed knowledge of the flow field to be input to the numerical method. The following discussion therefore focuses on the qualitative results and their similarity to those predicted using the numerical method.

Figure 4.40 presents the flapping angle against time for four different cases. All four cases are with the shaft tilted toward the top of the slope and therefore an increase in the flow going down through the rotor can be expected in all cases. The top two charts are with the 'nose' attached and are thus in attached flow whilst the bottom two charts are for separated flow with the 'nose' removed.

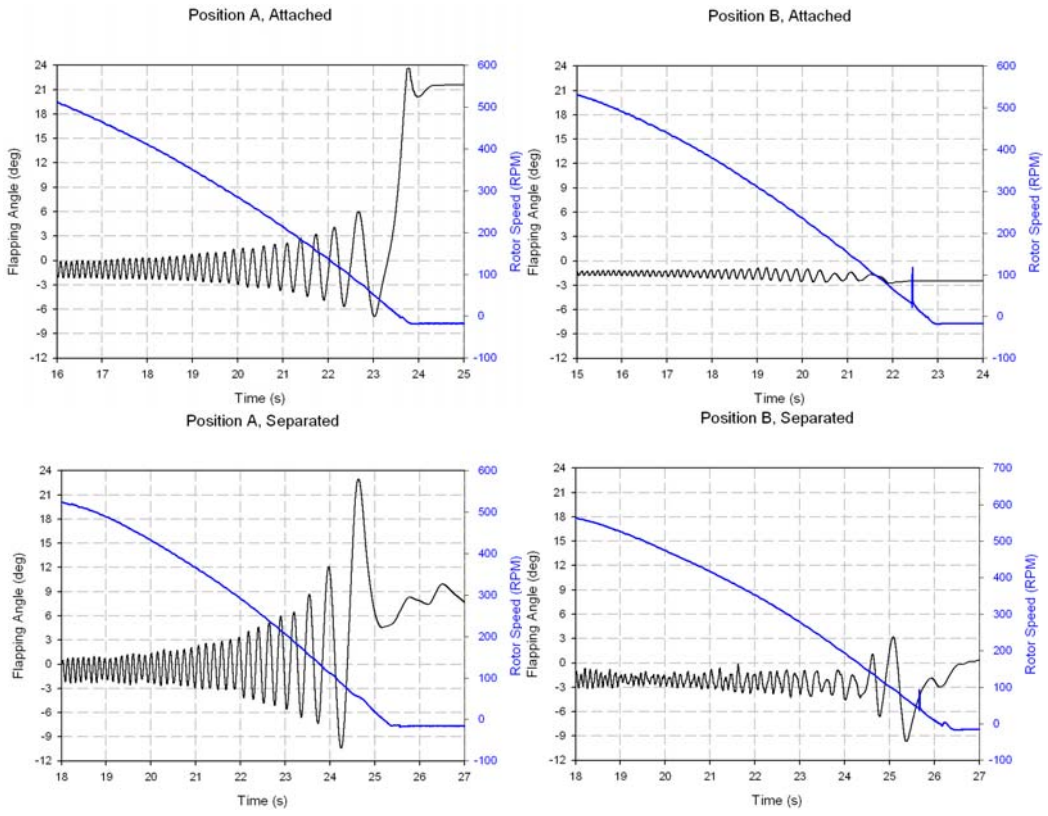

Figure 4.40: Experimental Flapping Angles at Various Locations

Firstly consider position A which is at the top of the ramp. For attached flow, the forward part of the rotor disc can be expected to experience a greater flow up through the disc in comparison to that at the rear of the disc where the flow is expected to have turned down the ramp. This case is therefore approximately equivalent to U3. For separated flow, a large amount of the flow can be expected to be travelling up through the rotor disc, this case therefore emphasises the effects of upwash on a decelerating rotor.

Position B is located further down the ramp. In the attached flow case, the oncoming wind is approximately parallel with the ramp surface and the flow can be expected to be almost horizontal across the rotor disc (neglecting the effect of the shaft tilt) such that this case is approximately equivalent to H4. For separated flow, this position is almost fully immersed in the separated region and therefore the dominant flow over the rotor disc is harder to predict.

From the flapping angles of Figure 4.40, it is immediately clear that there is more blade sailing apparent at location A than at location B. As well as this the separated flow cases appear to contain greater deflections than the attached flow cases. In order to quantify these observations, the flapping deflections during rotor deceleration between rotor speeds of 500 and 0 rpm were analysed. In each case the mean, minimum and maximum flapping angle were obtained as shown in Figure 4.41. These values must be taken as only approximately representative however as they may be affected greatly by the rotor finishing azimuth.

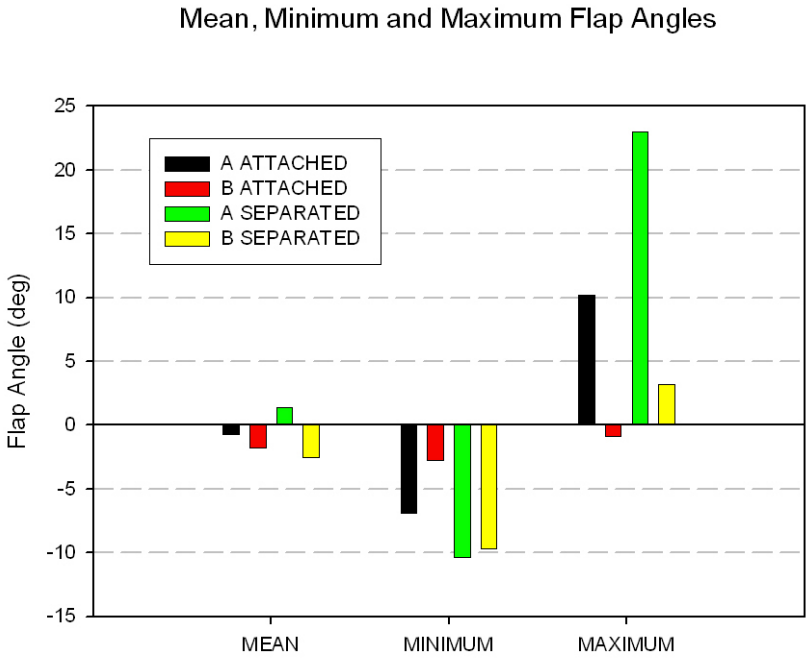

Figure 4.41: Minimum Flapping Angles for Various Locations

The mean value is included to provide an approximation of the general flow over the rotor disc. The generally negative values are possibly in part due to the orientation of the shaft tilt. The larger mean values at position A relate to the upflow present at the top of the slope, with the upflow being particularly large in the separated case. The separated case at position B displays a more negative value than the attached flow case; it is therefore possible that the rotor at this location is experiencing some downflow due to a recirculating flow pattern.

From the minimum and maximum values note firstly that the attached flow case at position B exhibits little to no blade sailing. This provides some evidence to support the hypothesis that it is the presence of an axial flow which drives the blade sailing. Also the fact that this case is showing considerably less blade sailing than the attached flow case at position A supports the numerical result shown in Figure 4.32 where cases at location H4 exhibit smaller tip deflections than those at location U3.

The large amount of upflow for the separated case at position A resulted in a large amount of blade sailing. Although the flow through the rotor disc at position B is expected to be less, resulting in less blade sailing, it exhibits a similar value for the minimum tip deflection. It is possible that this is due to the hypothesis that the rotor is immersed in a predominantly downward flow field at this location. This therefore supports the results of the numerical investigation where larger downward tip deflections resulted from cases where flow was passing down through the rotor than where flow was

passing up through the rotor. Also note that a reduction in centrisep clearance is expected to result from a downward deflection of the blade and therefore, for a similar amount of blade sailing, it is the downflow cases rather than the upflow cases which result in the most reduced clearance as shown in the numerical study.

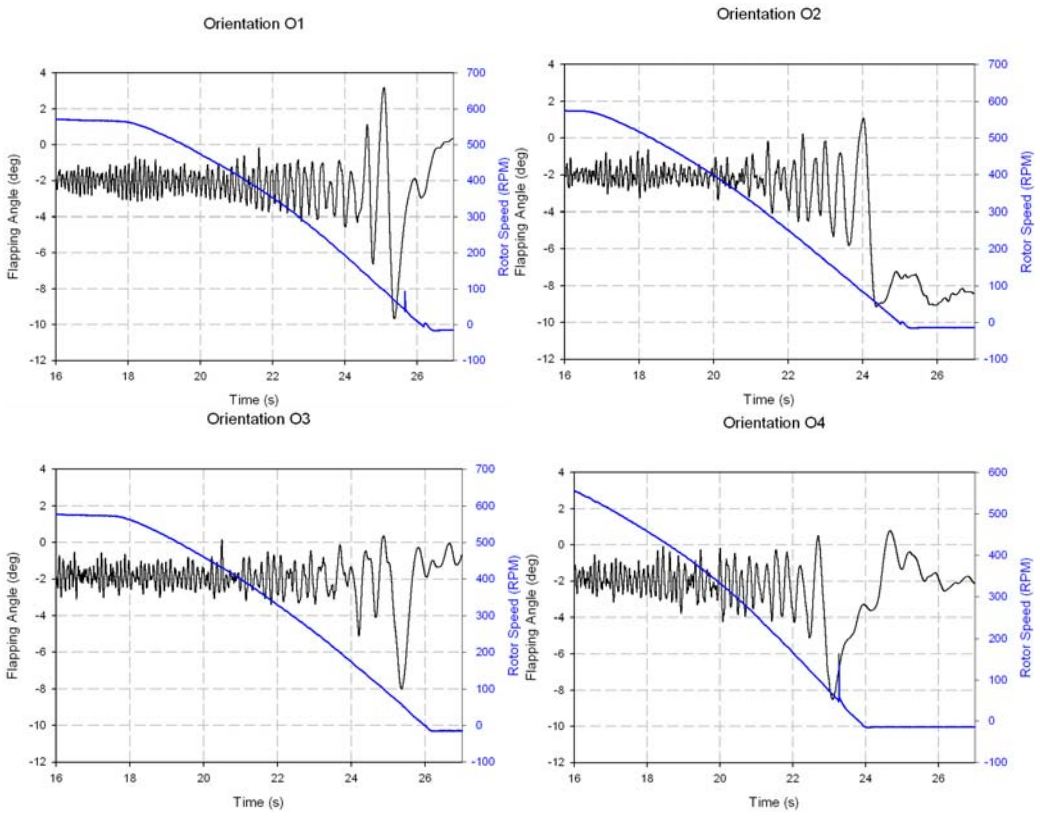

Figure 4.42: Experimental Flapping Angles at Four Orientations

The influence of the shaft tilt on blade deflections is also supported by the experiment. Figure 4.42 displays plots of blade flapping angle against time for the four orientations O1-4 (see Figure 4.31) at position B in the separated flow case.

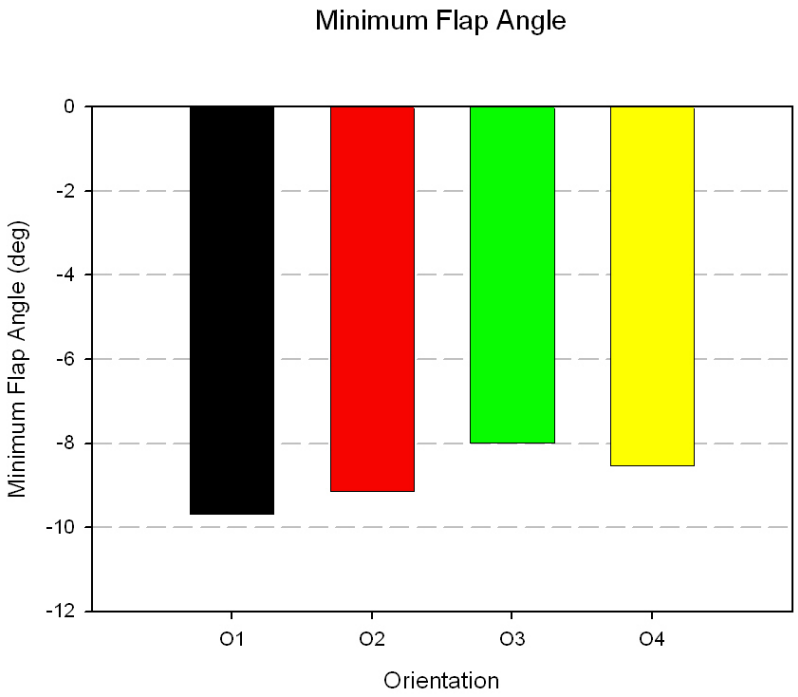

Figure 4.43: Minimum Flapping Angles for Various Orientations

It is immediately apparent that the maximum downward flap angle during deceleration for orientation O3 (shaft tilted downstream, see Figure 4.31) is much less than that for orientation O1 (shaft tilted upstream, see Figure 4.31). The minimum flapping angle is plotted in Figure 4.43 from which it may be seen that there is clear agreement with the results from the numerical investigation with the hypothesised effect of the shaft tilt on the flow passing through the rotor disc being demonstrated.

4.5.4 Mitigation using Trailing Edge Flaps

The use of trailing edge flaps to mitigate the effects due to blade sailing has already been demonstrated in section 4.4. Consider then the use of a flap of the optimum configuration of 20% span located at 85% radius to reduce the proximity of the blade to the centrisep in the worst case as analysed in the previous section. To ensure that the maximum effect may be observed the flap omega will be held at 100% however the flap deflection magnitude will be varied between 0 and 50 degrees.

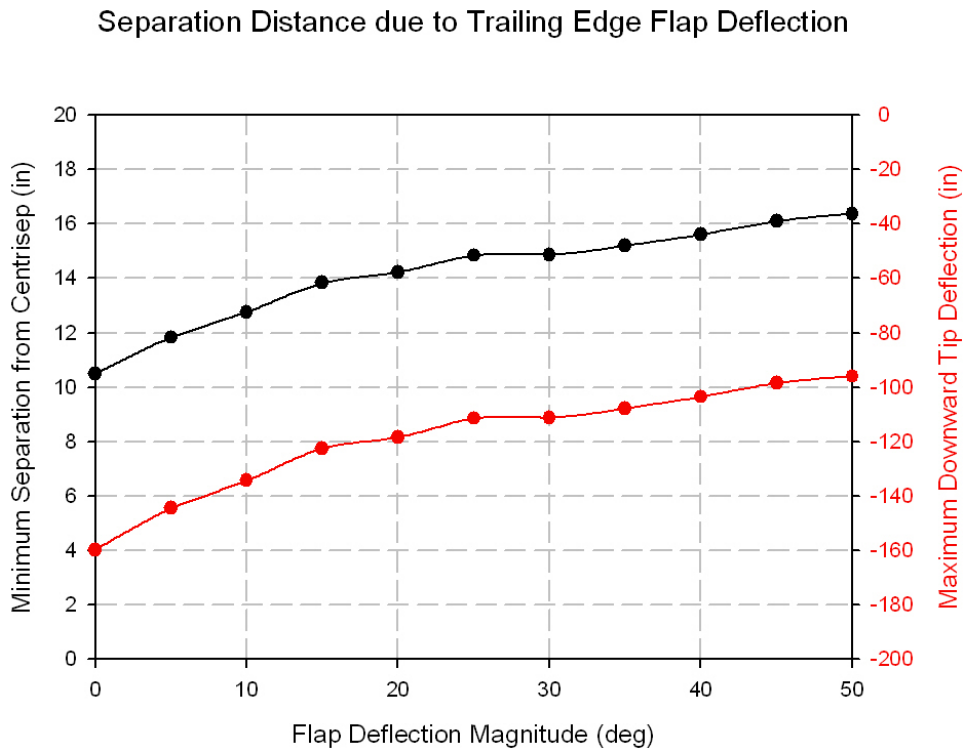

Figure 4.44: Centrisep clearance due to trailing edge flap deflection magnitude.

Figure 4.44 plots, for blade number 4, the minimum separation distance and the maximum downward tip deflection against the flap deflection magnitude for the worst case (location D2, orientation O4). The flap is clearly having an advantageous effect with the separation distance being increased by 6 inches when the full 50 degrees of deflection is used. The chart however does highlight the requirement for large deflections. For a deflection of 5 degrees, which is more typical of current actuation systems, the benefit is much smaller, although a decrease in tip deflection of around 1.5ft is still possible. Clearly such a difference might still prevent the occurrence of damage to the rotor and fuselage.

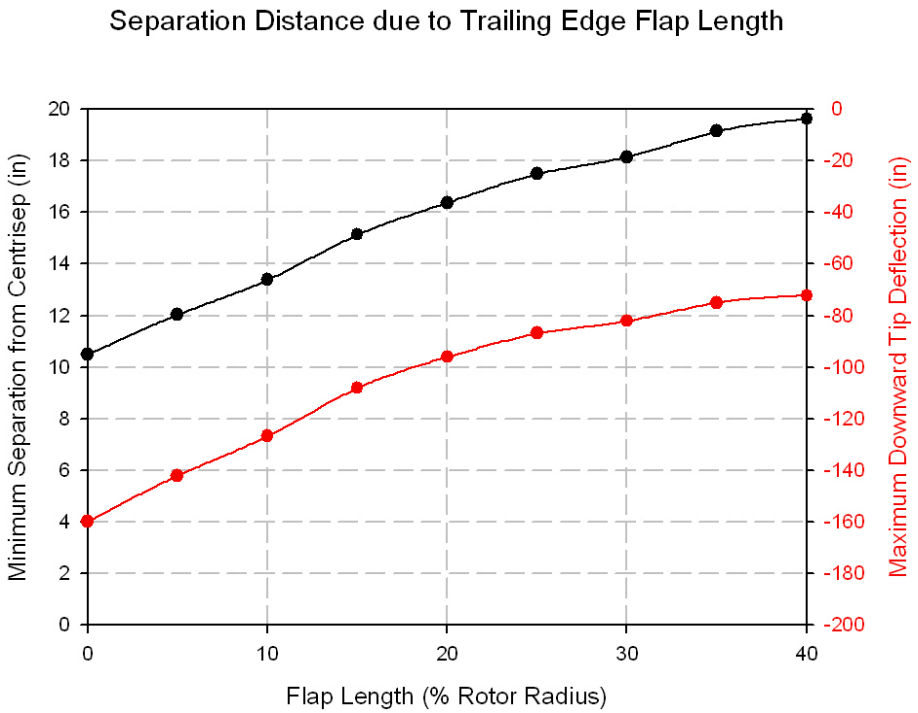

Figure 4.45: Centrisep clearance due to trailing edge flap length.

Note, however, that even with 50 degrees deflection the downward tip deflection is still significant. Consider then extending the length of the flap further inboard. Figure 4.45 shows the variation of the centrisep clearance and tip deflection with the flap length. The outer extent of the flap has been held constant at 95% radius with the inner extent varied to give the various flap lengths shown. With a flap of 40% radius the minimum clearance from the centrisep is close to 20 inches which is approximately the value during normal rotor disengagement in zero wind. In other words, it takes a flap of approximately 40% blade radius with a deflection capability of +/-50 degrees to totally resolve the centrisep issue.

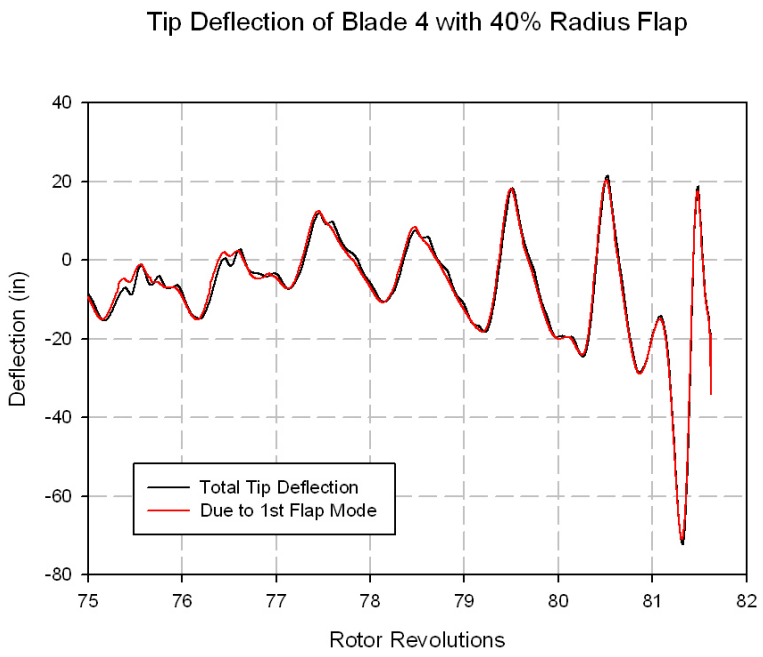

Figure 4.46: Tip deflection of blade 4 with 40% flap operating with 50 degrees deflection.

The downward tip deflection is also of significance and the tip deflection plot shown in Figure 4.46 reveals that this deflection occurs in the final rotation of the rotor. In order to investigate the reason behind this large deflection a brief modal analysis has been conducted. Appropriate modes were used depending on the anti-flap/droop stop condition such that if the blade was in contact with the droop stop then a built in boundary condition was applied at the stop. This assumes that there is zero curvature between the blade root and the stop which given the small distance between them is a reasonable approximation.

Due to the orthogonality of the modes, the response and forcing of each mode may be obtained from the full solution (as given by the new dynamics method) by multiplying the total values by the appropriate mode shape and then integrating along the radial coordinate of the blade. Figure 4.46 contains a plot of the tip deflection due to the first mode alone and reveals that the large deflection of the final cycle is almost entirely due to this mode. The origin of this large deflection may therefore be investigated through the breakdown of the forcing of this mode.

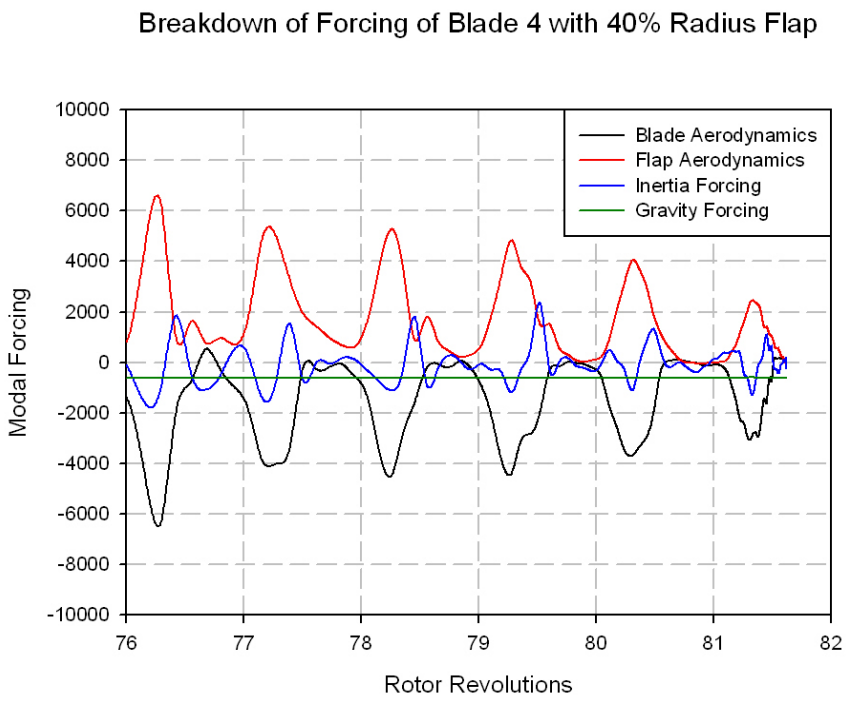

Figure 4.47: Breakdown of forcing of 1st flapping mode during blade sailing with 40% flap.

In Figure 4.47 the modal forcing has been decomposed into the aerodynamic, inertia and gravitational modal forcing components with the aerodynamic modal forcing being further split into flap dependent and flap independent constituents. The control philosophy for the flap deflection is clearly working well as the flap independent aerodynamic forcing is being reasonably well cancelled by the flap dependent component. In the final cycle however the residual inertia component becomes significant and cannot be adequately countered by the flap due to the small dynamic head of the slow turning rotor. With the absence of the centrifugal stiffening the residual inertia in the blade is sufficient to lead to the relatively large peak in the tip deflection observed in the final cycle.

4.5.5 Summary of the Case Study

The application of Trailing Edge Flaps to a real operational case study has confirmed that they may be used to significantly increase the separation between the rotor blades and the fuselage of a Sea King helicopter. In particular, it has been predicted that a reduction in the clearance between the rotor blade and the centrisep may occur during rotor engagement and disengagement operations when the prevailing wind is coming from the port side and a significant component of the wind is going down through the rotor disc. This case study therefore builds on the research published by Jones and Newman (2007)

by applying the concept to a realistic situation for which the qualitative behaviour has been verified through wind tunnel testing.

The operation of the trailing edge flaps was found to increase the minimum clearance of the blade from the centrisep through the general reduction of the blade sailing phenomenon. The deflection of the blade was however found to be dominated by its inertia in the final rotation of the rotor during disengagement. At this stage of the operation the aerodynamic forcing available from the TEF becomes small as the dynamic head is significantly reduced as the rotor slows. For this reason, large flaps with a very large deflection range would be required to completely control the blade response; however the deflection of smaller TEFs through a narrower range is still predicted to be advantageous to a lesser degree. Therefore if TEFs are to be installed on a rotor for any purpose then serious consideration should be given to their use during the engagement and disengagement operations as any reduction in the deflection and loads of the blades could be worthwhile.

4.6 Operational Implications for the Trailing Edge Flap

The study presented in the previous section has served to highlight one of the key advantages of actively controlled devices and the active Trailing Edge Flap in particular, namely, their inherent adaptability. The study has shown that the TEF need not only be used for the control of the blade's higher harmonic response, but that its inherent adaptability means that it should also be considered for uses which can significantly enhance the operational effectiveness of the rotorcraft. This adaptability is supported by the literature from which we have seen that a wide number of applications have been suggested.

The ability of the TEF to be applied to a wide range of functions stems from the fact that the deflection schedule can be tailored to any given purpose. In the case of vibration reduction, the deflection schedule would be calculated through the minimisation of a cost function made up of data supplied by accelerometers located in the fuselage. For the blade sailing application it was suggested that the flaps would simply be deflected in opposition to the blade tip deflection velocity which could be provided by an accelerometer located at the blade tip. The main hardware which constitutes the TEF system is therefore unchanged whilst the various applications can be provided for with the addition of the appropriate feedback sensors and the corresponding software. For example, Patt et al (2006) suggested that the function of the TEFs could be altered

between vibration and noise reduction, depending upon the requirement at a given flight condition, simply through the use of a toggle switch in the cockpit. Similarly, the emphasis of the control at high speed could switch from one of vibration reduction to performance enhancement and loads reduction and a method for achieving this automatically, based on a feedback of the control loads is presented for the Active Trailing Edge in the next chapter.

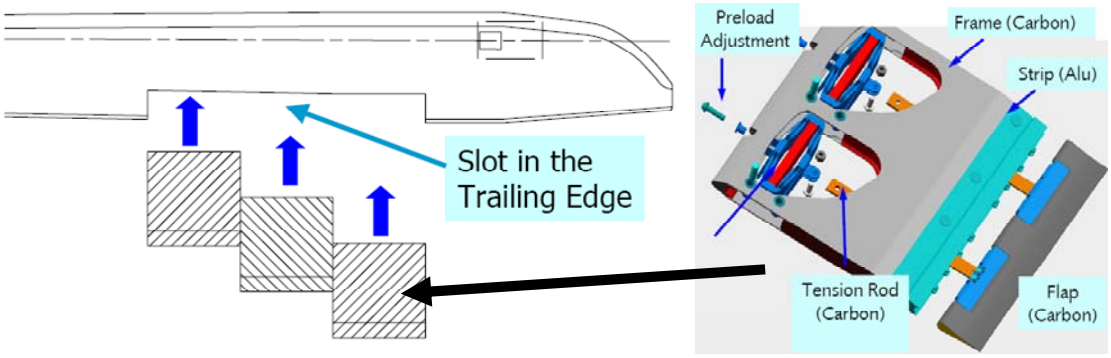

Figure 4.48: Schematic of the modular construction of the ECD Trailing Edge Flaps, images reproduced from Roth et al (2006).

Another key advantage of the TEF is the simple fact that it is, as the name suggests, a trailing edge device. This important fact means that the TEF structure and mechanism need not interfere with the main load paths of the blade. Indeed as a servo-flap, the TEF may be mounted altogether separately and behind the main blade structure as done by Kaman on its Seasprite helicopter. This configuration, however, comes with inherent drag penalties and the more recent designs have preferred the integral TEF configuration. Nevertheless such designs may still be achieved without interrupting the main load bearing structure of the rotor blade which is almost always provided by a leading edge C- or D-spar. This fact means that the challenges of structural design and maintenance of a TEF-equipped blade can be expected to be significantly lower than one equipped with leading-edge (for example nose-droop) or distributed (such as active twist) devices. It is interesting to note, for example, that the TEF-equipped blade flight tested by Eurocopter Deutschland (ECD) is based on the prototype EC145 blade [Dieterich et al (2006)] and that a completely new bespoke design was not required. Furthermore, as the EC145 has a leading edge C-spar the TEFs and their associated actuation mechanism could simply be slotted into the rear of the blade as standalone modules (Figure 4.48), a capability which is clearly useful in the maintenance of the TEF mechanisms.

Despite these advantages, the technology has not yet come into service on a production aircraft. Clearly, the TEFs can only be marketed on a cost-benefit basis against

alternative technologies. Whilst the benefits of the active TEF have been well demonstrated by a vast amount of numerical analysis and confirmed by both model- and full-scale tests, the costs can be expected to be high due to the requirement for high-performance actuators, powerful computing and flight-worthy software. This high cost will clearly count against the technology in comparison to other systems. Consider, for example, the most widely studied applications for TEFs, i.e. vibration and noise reduction. For vibration reduction, the TEFs are competing against a wide range of fuselage-based active and passive solutions. Passive devices (such as the Lynx head absorber) are generally cheap and relatively low maintenance but can be heavy and will have poor off-design performance. Active solutions such as the Active Control of Structural Response (ACSR) system on the EH101 will be closer to the TEFs in terms of both cost and benefit and have the clear advantage of proven reliability. For noise reduction, manufacturers are still pursuing passive rotor technology (such as the Blue Edge technology of ECD, Gotzhein (2010)), and variable speed rotors (such as that demonstrated on the Hummingbird demonstrator, Colucci (2008)), both of which should come with lower maintenance requirements than an active TEF system.

There are therefore existing technologies already covering a wide range of the cost-benefit trade-off and which have well proven reliability. We have seen in this chapter that the active TEF, with its multi-function capability could feasibly meet multiple requirements and thus replace more than one system whilst also having the ability to be applied to numerous other applications such as fatigue load minimisation and envelope expansion which could bring reductions in operating costs. But in order to do this the reliability of the system must be extremely high and the maintenance costs reduced to an absolute minimum such that it can compete on a cost-benefit basis against the wide range of existing and proven technologies.

The Active Trailing Edge (ATE) technology is very similar to the TEF but aims to overcome some of its disadvantages. The elimination of such shortcomings, particularly in reliability, could prove to make the difference in a close comparison of technologies and therefore the ATE will be the focus of the following chapter.

Chapter 5 The Active Trailing Edge

5.1 Characteristics of the Active Trailing Edge

We have seen from the previous chapter that the active Trailing Edge Flap (TEF) can be applied to a wide range of applications. The use of discrete hinges to attach the flap to the main blade structure enables actuation requirements to be minimised due to the negligible stiffness associated with the hinges; however this design results in a couple of deficiencies in the TEF concept. Firstly, the inevitable gap between the main blade and the TEF provides a source of drag which is not present on a clean, single-element aerofoil. Secondly, the exposure of the hinges and other parts of the actuation mechanism, such as a push rod, to the external environment could lead to a reduction in reliability and increased maintenance requirements when operating in harsh environments.

In order to avoid such issues, instead of using discrete flaps, it would be desirable to morph the blade structure itself such that a smooth aerodynamic profile is maintained whilst no aspects of the actuation system are exposed to the environment. One method of achieving this is to actively control the twist of the entire blade and such "Active Twist" rotors have been demonstrated in model-scale experiments, Bernhard and Wong (2005). Twisting the entire blade, however, requires the active material to be embedded within the main structure of the blade and the advantage of TEFs being located behind the main load path is lost. Furthermore, whilst active blade twist enables the servo-effect of the TEFs to be reproduced, the capability to provide a more localised lift forcing is lost (the benefits of such forcing will be shown later in this chapter). It should also be noted that Friedmann and Millott (1995) have shown that pitching the whole blade at the root is less efficient than using TEFs as, unlike the latter, it does not use the aerodynamics to its advantage and this same argument should apply to active twist.

An alternative method is to morph only the trailing edge and such concepts are referred to as the Active Trailing Edge (ATE). One such design for an ATE proposed by Ahci and Pfaller (2008), and reproduced in Figure 5.1, consists of a piezoelectric bender surrounded by a filler material providing the aerodynamic profile for the trailing edge. Clearly, unlike the TEF, none of the actuation mechanism is exposed to the environment and the smooth aerodynamic profile promises a reduction in drag. Unlike the active twist concept, however, the main advantages of the TEF are maintained as the ATE need not interfere with the main load path, enables a localised lift forcing capability and uses the aerodynamics to its advantage. However, the ATE is clearly required to morph its

surrounding structure (unlike the TEF which uses discrete hinges) and the direct use of the piezoelectric material means that there is no possibility of incorporating an amplification mechanism. Therefore the deflection capability of an ATE can be expected to be less than that achieved by a discrete flap.

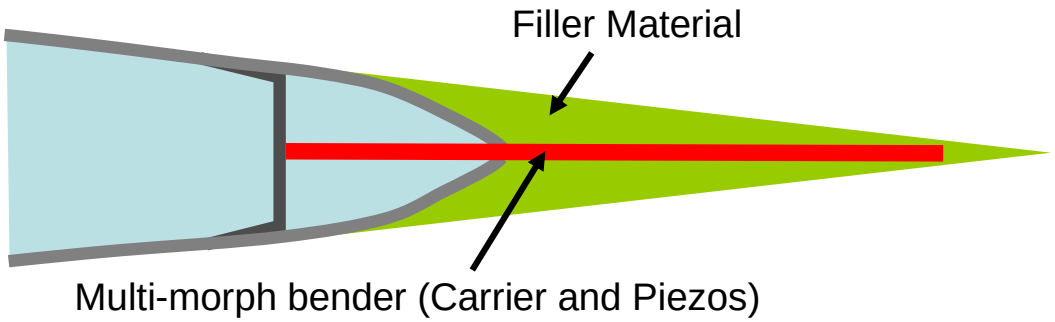

Figure 5.1: Proposed design for an Active Trailing Edge. Based on Ahci and Pfaller (2008).

Due to the lack of a discrete hinge, the morphing of the trailing edge provides a smooth variation in the external profile not given by the TEF which means that the effect on the airloads is somewhat different. As the overall deflection can be expected to be less it is important that the differences in the airloads are captured in order to properly evaluate the effectiveness of the ATE. This chapter will therefore first present the development of a new model for the ATE which incorporates the effects due to aerofoil morphing. The new model is then used in an investigation into the effectiveness of an ATE of limited deflection capability for the primary purpose of vibration reduction before the overall utility of the ATE, including its application to performance enhancement, is discussed.

5.2 Modelling the Airloads due to an Active Trailing Edge

The literature has revealed some recent research into active devices using coupled CFD-CSD techniques, but these papers only present a very limited number of results due to the large computational cost associated with such methods. Here a more efficient method is sought such that the effectiveness of the ATEs can be investigated through incorporation of the method into a rotor performance program; indeed most of the numerical research into TEFs has used such reduced-order aerodynamic models. Consider a summary of the dominant contributors to the subject as shown in Table 5.1.

Institute (Lead)	Example	Rotor Model	Flap Model
Boeing	Straub and Charles (1999)	CAMRAD II	Hariharan and Leishman
ECD	Dieterich et al (2006)	CAMRAD II	Thin Aerofoil Theory
University of	Milgram and Chopra	UMARC	Hariharan and Leishman

Maryland	(1998a), Shen and Chopra (2004)		for plain flaps, Theodorsen for balanced flaps.
Sikorsky	Chaudhry et al (2009)	RCAS	Thin Aerofoil Theory/ Look-up tables
University of Michigan	Myrtle and Friedmann (2001)	In-house	RFA
Pennsylvania State University	Kim et al (2004)	In-house	Hariharan and Leishman
DLR	Leconte et al (2001)	S4	Semi-Empirical Unsteady Model
ONERA	Leconte et al (2001)	ROTOR	Look-up tables
ATIC	Kobiki et al (1999)	In-house	Theodorsen
University of Stuttgart	Konstanzer (2005)	CAMRAD II	Hariharan and Leishman
Indian Institute of Science	Viswamurthy and Ganguli (2006)	In-house	Hariharan and Leishman

Table 5.1: Commonly used modelling methods for trailing edge flap aerodynamics.

Much use has clearly been made of the CAMRAD II and UMARC rotor codes. These programs both include a compressible, unsteady indicial aerodynamics model for the trailing edge flaps developed by Hariharan and Leishman (1996). Most of the in-house rotor programs have also incorporated this model and it must therefore be considered to be the standard model of choice. Further detail into the derivation of this model will become clear below, however it should be noted that both compressibility and unsteady effects are accounted for.

The model does however have one clear limitation, highlighted by Shen and Chopra (2004), in that it is only valid for a plain flap. Shen and Chopra (2004) however used an aerodynamically balanced flap design to reduce actuator loads and therefore the compressible model of Hariharan and Leishman (1996) had to be neglected for a quasi-steady version of Theodorsen's incompressible theory which by definition will clearly not properly model the effects due to compressibility or unsteady forcing.

There are other methods which have been used which could be adapted for flaps of types other than the plain flap. Many of the methods use look-up tables to replace the thin-aerofoil approximations, indeed such tables can be used to correct the asymptotic quasi-steady values of the circulatory load in the Hariharan and Leishman model; however these methods cannot be expected to correctly account for the unsteady effects due to more arbitrary deflection shapes such as those due to aerodynamically balanced flaps or ATEs. A different methodology is the Rational Function Approximation (RFA) which has been used in the past for fixed-wing stability but has been adapted for the modelling of trailing edge flaps by Myrtle and Friedmann (2001). This model uses a least squares

method to fit a transfer function to tabulated oscillatory response data. The inverse Laplace transform is then used to convert the transfer function into a time domain state-space model which may be easily coupled with a rotor dynamic formulation for efficient time integration. Clearly, the model is dependent upon the oscillatory data to which the transfer function is fitted with Myrtle and Friedmann (2001) using the doublet-lattice method to provide attached flow oscillatory data. Liu et al (2008b) compared the RFA aerodynamic model with results obtained using CFD for an unsteady case with varying angle of attack, flap deflection and Mach number. Non-linear effects at the highest Mach numbers were poorly predicted, however the approach was found to give a reasonable agreement under most rotorcraft conditions. The method could then be used to provide an RFA for any available set of data which could be very useful when CFD and/or wind tunnel data is available. In the early design stages however when parameters such as flap chord, flap overhang, or the deflection shape of an active trailing edge must be optimised, the oscillatory data would need to be obtained for each case and a separate RFA derived. Clearly such a method would not be as efficient as a model which can account for these changes simply by changing an input parameter.

A more general derivation is therefore required to capture the effects due to an arbitrary deflection shape without the need for a vast array of input data. The general approach will not only allow for ATEs but can also be reduced to the plain flap and could be used to model aerodynamically balanced flaps, thus providing much greater flexibility than the Hariharan and Leishman (1996) model. As will be seen below, the method will be closely coupled to the existing Third Generation aerodynamic model by modifying the contribution to the integrated boundary condition such that maximum use of the existing structure is made in order to improve efficiency. The use of this structure also ensures that the unsteady, compressible capability of the model is maintained such that, when a plain flap is being modelled, the method provides approximately the same level of fidelity as the Hariharan and Leishman (1996) model.

5.2.1 Circulatory Load Calculation

Recall from Chapter 2 that the boundary condition at an aerofoil camber line, as given by thin aerofoil theory, may be written as:

$$\frac{\left(w_i(x)+w_w(x)\right)}{V}=\frac{dY}{dx}. \qquad \textbf{5.1}$$

In the existing Third Generation aerodynamic model, the camber of the aerofoil, given by the right-hand-side of equation 5.1, is assumed to be equal to zero; however the circulatory effects due to the deflection of either a TEF or ATE may be modelled by applying a non-zero variation of the camber line. In addition, quasi-steady effects may also be captured by including the apparent velocities which arise from camber line deflection rates, see Figure 5.2.

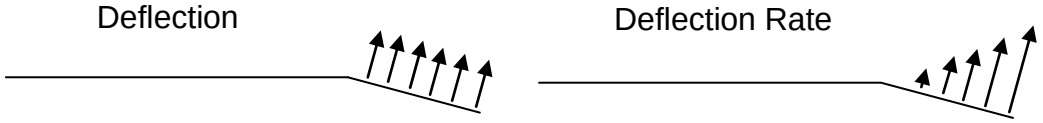

Figure 5.2: Apparent inflow velocities from flap deflection and deflection rate.

From equation 5.1 therefore, the change in the induced velocity distribution due to changes in camber becomes:

$$\Delta\left(\frac{w_i(x)}{V}\right)=\Delta\left(\frac{dY}{dx}-\frac{w_w(x)}{V}\right)=\Delta f_c(x). \qquad \textbf{5.2}$$

Following the derivation given in Chapter 2, the changes to the lift and pitching moment coefficients given by the change in boundary condition are then given by:

$$\begin{aligned}\Delta C_l &= C_{l_\alpha}\Delta\varepsilon_0\\ \Delta C_m &= \Delta\mu_0-\frac{\pi}{2}\Delta\varepsilon_0\end{aligned} \qquad \textbf{5.3}$$

where:

$$\begin{aligned}\Delta\varepsilon_0 &= -\frac{1}{\pi}\int_0^\pi \Delta f_c(1-\cos\psi)\,d\psi\\ \Delta\mu_0 &= -\frac{1}{2}\int_0^\pi \Delta f_c(1-\cos 2\psi)\,d\psi\,.\end{aligned} \qquad \textbf{5.4}$$

For a plain TEF hinged at x_h (or ψ_h in the alternative coordinate system), the change in the induced velocity distribution is given by the sum of effects due to the change in camber line, which is a non-zero constant from the hinge to the trailing edge, and the change in apparent velocity due to the deflection rate, which varies linearly from the hinge. Thus:

$$\begin{aligned}\Delta f_c(x) &= 0 && x<x_h\\ \Delta f_c(x) &= -\delta-\dot\delta(x-x_h)/V=-\left(\delta+\dot\delta\frac{c}{2V}(\cos\psi_h-\cos\psi)\right) && x>x_h\end{aligned} \qquad \textbf{5.5}$$

where δ is the flap deflection angle in radians (positive trailing edge down) and a dot denotes a time derivative. Therefore equations 5.4 become:

$$\Delta\varepsilon_0 = \frac{1}{\pi}\int_{\psi_h}^{\pi}\left(\delta + \dot{\delta}\frac{c}{2V}\left(\cos\psi_h - \cos\psi\right)\right)\left(1-\cos\psi\right)d\psi$$
$$\Delta\mu_0 = \frac{1}{2}\int_{\psi_h}^{\pi}\left(\delta + \dot{\delta}\frac{c}{2V}\left(\cos\psi_h - \cos\psi\right)\right)\left(1-\cos 2\psi\right)d\psi\ . \qquad \textbf{5.6}$$

The additions to the circulatory components of the normal force and pitching moment due to the flap deflection are found by performing the integrations of equations 5.6 and substituting into equations 5.3. The results obtained are the final values for the circulatory response which may be corrected for compressibility using the Prandtl-Glauert factor to obtain those used by Hariharan and Leishman (1996).

Now consider the case of an arbitrary change in the camber-line. The integrations may be performed, as for the 3rd generation model, using the mid-point rule. In order to properly capture camber-line geometry, such as that given by a flapped aerofoil, the 10 segments used in the Third Generation model are insufficient as changes in gradient may only occur between segments. For example a flap hinge may only be exactly modelled when located at 2, 10, 21, 35, 50, 65, 79, 90 and 98 per cent chord and therefore a 15% flap would be approximated by either a 10% or 21% flap which is clearly inadequate for an investigation into flap size requirements. For this reason, the effects of the camber-line are modelled using 100 segments and equations 5.4 are therefore approximated by:

$$\Delta\varepsilon_0 = -\frac{1}{\pi}\sum_{j=1}^{100}\Delta f_{c_j}\left(1-\cos\psi_j\right)\frac{\pi}{100} = -0.01\sum_{j=1}^{100}\Delta f_{c_j}\left(1-\cos\psi_j\right)$$
$$\Delta\mu_0 = -\frac{1}{2}\sum_{j=1}^{100}\Delta f_{c_j}\left(1-\cos 2\psi_j\right)\frac{\pi}{100} = -0.005\pi\sum_{j=1}^{100}\Delta f_{c_j}\left(1-\cos 2\psi_j\right). \qquad \textbf{5.7}$$

Note that, with the use of the smaller segments, ψ is assumed to be constant over each segment and is taken to be the value at the centre of the segment such that:

$$\psi_j = \tfrac{\pi}{200}\left(2j-1\right). \qquad \textbf{5.8}$$

The change in the final value of the circulatory lift and pitching moment due to the changes in camber are therefore given by substitution of equations 5.7 into equations 5.3 which, after simplification, gives:

$$\begin{aligned}\Delta C_l &= -C_{l_\alpha}\, 0.01 \sum_{j=1}^{100} \Delta f_{c_j} \left(1-\cos\psi_j\right) \\ \Delta C_m &= \frac{\pi}{4\beta}\, 0.02 \sum_{j=1}^{100} \Delta f_{c_j} \left(\cos 2\psi_j - \cos\psi_j\right).\end{aligned} \qquad \textbf{5.9}$$

Note that, as for the basic aerofoil, a compressibility factor has been applied to the pitching moment coefficient. Equations 5.9 therefore contain the change in forcing for the asymptotic values of the circulatory loads which are added to those for the basic aerofoil and multiplied by the same circulatory indicial response function to account for the unsteady effects of the shed wake, as explained in Chapter 2. However, as discussed by Hariharan and Leishman (1996), to approximate additional effects, primarily those of viscosity due to the thickening boundary layer near the trailing edge, factors must be applied to these circulatory loads based on experimental evidence. For the current research, these factors will be set based on a steady-state correlation which will be presented below.

5.2.2 Non-Circulatory Load Calculation

Recall from an earlier chapter that the initial impulsive pressure distribution in response to a step change in inflow is given by:

$$\Delta C_p\left(\psi, s=0\right) = \left(\frac{4}{M}\right)\Delta\mu_w\left(\psi\right). \qquad \textbf{5.10}$$

Also recall that, in the Third Generation model, this loading is factored by the shape of the equivalent incompressible pressure distribution which, along with an exponential decay, is used to approximate the dissipation of the non-circulatory load in response to an indicial change in angle of attack as:

$$\Delta C_p\left(\psi, s\right) = -\left(\frac{4}{M}\right)\sin\psi \exp\left(\frac{-s}{T_I}\right)\Delta\alpha\,. \qquad \textbf{5.11}$$

The non-circulatory loads due to the Active Trailing Edge can therefore be modelled using the reverse flow theorems whereby the change in the local, chordwise distributed, inflow due to the deflection and deflection rate of the ATE is added to that due to the

external flow and integrated with the known pressure distribution for the response due to angle of attack as described in Chapter 2. This can therefore be used along with the assumed exponential decay for the non-circulatory indicial response to obtain the total contribution of the non-circulatory loads to the unsteady aerodynamic coefficients.

For example, the instantaneous value of the non-circulatory component of the lift coefficient due to the ATE is given by:

$$\Delta C_l\left(s=0\right)=\frac{4}{M}\int_0^1 -\Delta f_c \sin\psi\, dx=\frac{4}{M}\left(\sum_{j=1}^{100} -\Delta f_c \times 0.005\pi \sin^2\psi_j\right). \qquad \textbf{5.12}$$

Similarly the initial value of the pitching moment due to the change in camber-line is given by:

$$\Delta C_m\left(s=0\right)=-\frac{4}{M}\left(\sum_{j=1}^{100} -\Delta f_c \times \frac{0.125\pi}{100}\left(\sin\psi_j-\sin 2\psi_j\right)\sin\psi_j\right). \qquad \textbf{5.13}$$

These non-circulatory loads are then integrated through time using the same indicial response (decay) function as for the basic aerofoil using the recurrence solution method. It should be noted at this stage that due to the applied weighting, the instantaneous value of the non-circulatory loading is substantially under-predicted due to the low value of weighting near the trailing edge. Therefore for extremely high frequencies the results for a plain flap may not be as accurate as those predicted using the Hariharan and Leishman (1996) model however the results presented in section 5.4 show that the approach is sufficiently accurate for normal actuation frequencies and the flexibility provided by the approach is considered by the author to be of more use than a small improvement in accuracy at frequencies which are not generally considered.

5.2.3 Calculation of the Unsteady Drag Force

Hariharan and Leishman (1996) give the unsteady drag force for a flapped aerofoil as:

$$C_d = C_n \sin\theta + C_f \delta - C_c \cos\theta + C_{d0} \qquad \textbf{5.14}$$

where C_f is the flap force coefficient, which is defined as the lift integrated only over the flap portion of the aerofoil. This is slightly different to the equation for the basic aerofoil due to the addition of the flap force term, which must be included to correctly resolve the force over the flap. For the variable camber being considered here, as the deflection

angle is not necessarily constant along the camber-line, the resolution must be carried out within the chordwise integration such that the $C_f\delta$ term is replaced by a resolved force coefficient which will be denoted by $C_{f\delta}$ to give the drag coefficient as:

$$C_d = C_n \sin\theta + C_{f\delta} - C_c \cos\theta + C_{d0} . \qquad \textbf{5.15}$$

Recall from Chapter 2 that according to Joukowsky's theorem, the circulatory lift force per element dx is given by:

$$dL = \rho U \gamma(x) dx . \qquad \textbf{5.16}$$

Using the form of the vorticity distribution introduced by Glauert (1947), the coefficient of force, integrated over the portion of the aerofoil to which the camber change is applied (referred to here as the flap force coefficient) is given by:

$$C_f = 2\int_{\psi_h}^{\pi} \left(A_0 \cot\frac{\psi}{2} + \sum_1^{\infty} A_n \sin n\psi \right) \sin\psi \, d\psi . \qquad \textbf{5.17}$$

From this result, the resolved force coefficient, as required for the drag model, may be written as:

$$C_{f\delta} = -2\int_{\psi_h}^{\pi} \left(A_0 \cot\frac{\psi}{2} + \sum_1^{\infty} A_n \sin n\psi \right) \frac{dY}{dx} \sin\psi \, d\psi . \qquad \textbf{5.18}$$

Furthermore, if the appropriate moment arm is added to the flap force integral then a hinge moment coefficient (positive trailing edge down) may be derived as:

$$C_h = \int_{\psi_h}^{\pi} \left(A_0 \cot\frac{\psi}{2} + \sum_1^{\infty} A_n \sin n\psi \right) (\cos\psi - \cos\psi_h) \sin\psi \, d\psi . \qquad \textbf{5.19}$$

The coefficients A_n are calculated numerically as for the basic aerofoil but including the Δf_c due to the deflection and deflection rate of the ATE. Unfortunately, for the partial aerofoil integration, the series remains infinite but may be truncated to provide a reasonable approximation. In practice the author has found that the contribution from only the first 5 terms provides sufficient accuracy, as shown in Figure 5.3 for a plain flap example.

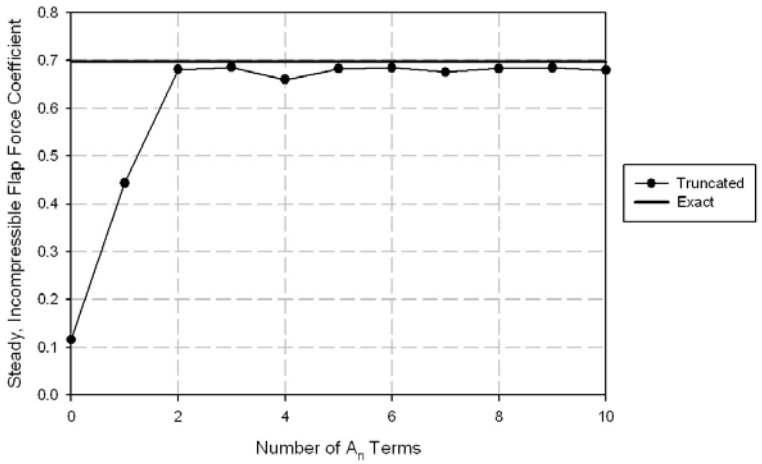

Figure 5.3: Effect due to number of A_n terms on the flap force integral for the deflection of a 25% chord plain flap.

The impulsive forces and moments over the ATE portion of the aerofoil are calculated as for the lift and pitching moment coefficients except with the integral taken only over the relevant chord section and with the appropriate resolution or moment arm applied. Note that the reverse flow theorems are only valid for the coefficients obtained from the full chordwise integration and therefore this partial integration is only really valid for angle of attack perturbations. For arbitrary perturbations such as an ATE deflection the result is only strictly valid at the instant the perturbation is applied and therefore the application of the normal force weighting may not be justified. This simplification, however, has been used to maintain the generality of the model and the response of the coefficients at normal deflection frequencies is found to be reasonably predicted using this assumption, indeed any error introduced is negligible in comparison to those due to inaccuracies in the circulatory component, see section 5.4.

All that remains then is the calculation of the chord force which, as suggested by Hariharan and Leishman (1996), is given by:

$$C_C = C_{L_\alpha} A_0^2 \,. \qquad \textbf{5.20}$$

For an aerofoil with changing camber, A_0 consists of the sum of the effective angle of attack due to the basic aerofoil added to an increment due to the camber change such that:

$$A_0 = \alpha_E + A_{0F_E} \qquad \textbf{5.21}$$

where A_{0F_E} is the pressure lagged value (i.e. the circulatory indicial function is applied) of A_{0F} where:

$$A_{0F} = -\tfrac{1}{\pi}\int_0^{\pi} \Delta f_c \, d\psi = \sum_{j=1}^{100} -\Delta f_c \, 0.01 . \qquad \textbf{5.22}$$

As for the lift and moment coefficients, an effectiveness factor must be applied to A_{0F} for the best representation to be obtained.

5.3 Deflection Shapes for the Active Trailing Edge

Before a validation of the model is presented, the reader will first be directed to consider the deflection shapes which might arise due to an Active Trailing Edge. The model presented in the previous section has clearly been derived to be capable of representing an arbitrary camber-line deflection shape; however of most interest here is the shape which best represents an ATE, although for comparison purposes it is also desirable to maintain the plain flap modelling capability. In this section, a simple distribution shape is suggested which is capable of modelling both plain flaps and typical ATE deflection shapes through the variation of a single parameter, thus simplifying the implementation of these shapes.

5.3.1 Variation of Camber using Power Distribution

A deflection shape given by a power distribution is suggested such that the variation in camber along the chord is given by: $x > x_h$

$$\begin{aligned} \Delta Y &= 0 && x < x_h \\ \Delta Y &= -\delta(t)(c - x_h)\left(\frac{x - x_h}{c - x_h}\right)^F && x > x_h . \end{aligned} \qquad \textbf{5.23}$$

The selection of this distribution will be justified below. The addition to the induced velocity around the aerofoil is therefore given by:

$$\Delta f_c(x) = \Delta\left(\frac{dY}{dx} - \frac{w_w(x)}{V}\right) = -\delta F\left(\frac{x - x_h}{c - x_h}\right)^{F-1} - \frac{\dot{\delta}(t)}{V}(c - x_h)\left(\frac{x - x_h}{c - x_h}\right)^F . \qquad \textbf{5.24}$$

The deflection shapes given by the power distribution are shown for various values of F in Figure 5.4. Note that when F equals 1, equation 5.23 gives the equation for a plain hinged trailing edge flap. In this case the model is approximately equivalent to that published by Hariharan and Leishman (1996). Indeed the circulatory components of the

models only differ in the constants used in the indicial response function (as the new model uses those already incorporated into the Third Generation model).

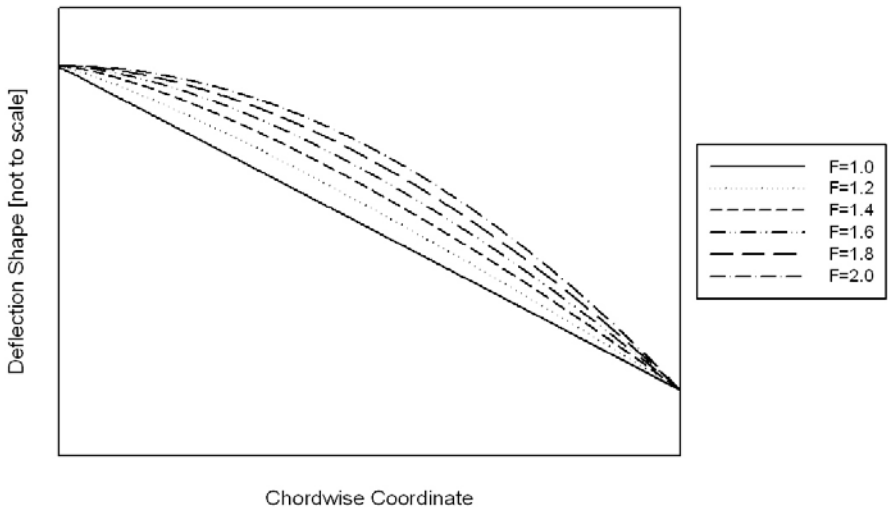

Figure 5.4: Effect on Trailing Edge Shape due to Shape Parameter, F.

For values of F greater than 1, the second derivative of the camber change becomes continuous across the effective hinge giving a smoother camber-line which is more representative of the hingeless ATEs currently being considered in industry, as will be shown in the following section.

5.3.2 Deflection Shape for Constant Strain

One method for deflecting the trailing edge is the piezo-bender, Ahci and Pfaller (2008). As shown in Figure 5.5, piezo-ceramic actuators are located above and below a central flexible beam which is cantilevered from a rigid part of the blade such as the rear of the main spar. A voltage is applied across the actuators such that they expand out of phase with each other causing the beam to bend and thus deflecting the trailing edge of the aerofoil.

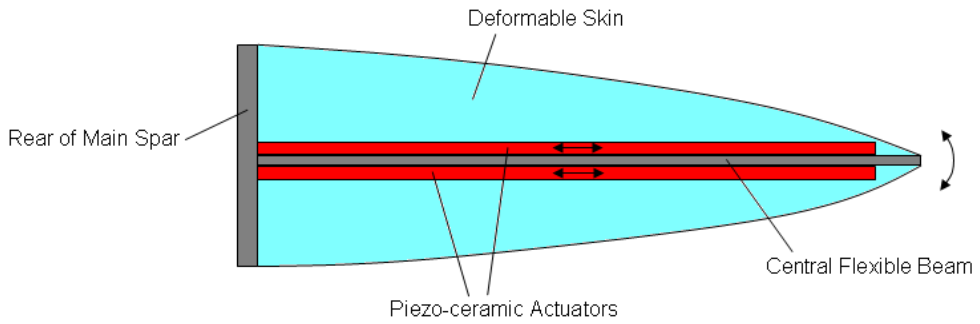

Figure 5.5: Schematic of a Piezo-Bender Trailing Edge Actuator.

On the application of the voltage, the actuators expand with a constant strain along their length. This fact may be used to estimate the deflection shape which can be expected from such a device.

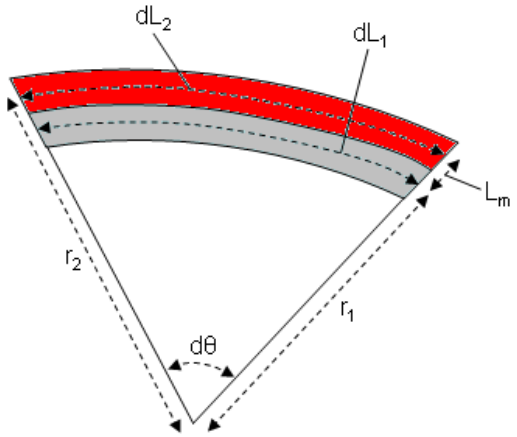

Figure 5.6: Geometry for the Calculation of the Deflection Shape of a Constant Strain Actuator.

Consider an infinitesimal segment of the flexible beam after deformation as shown in Figure 5.6. The length of the beam segment is dL_1 and is assumed to be unchanged with the deflection whilst the extended length of the actuator segment is dL_2. Prior to deformation, the actuator length must equal the beam length such that the pre-deformed length of the actuator segment is dL_1. The strain, which is assumed to be constant along the entire actuator, is therefore given by:

$$\varepsilon_{actuator} = \frac{dL_2 - dL_1}{dL_1}. \qquad \textbf{5.25}$$

From the geometry of Figure 5.6, therefore, the actuator strain is given by:

$$\varepsilon_{actuator} = \frac{dL_2 - dL_1}{dL_1} = \frac{r_2 d\theta - r_1 d\theta}{r_1 d\theta} = \frac{r_2 - r_1}{r_1} \Rightarrow \varepsilon_{actuator} = \frac{l_m}{r_1}. \qquad \textbf{5.26}$$

In other words the actuator strain is given by the distance of the actuator from the beam divided by the radius of curvature of the beam. Therefore for an actuator of constant strain located an invariant distance from the beam centreline, the deflection shape must have a constant radius of curvature.

Consider a trailing edge deflection using the power distribution of the previous section with a shape parameter of 2.0. The first derivative of the deflection shape is:

$$\frac{dY}{dX} = -\delta(t) F \left(\frac{x - x_h}{c - x_h} \right)^{F-1} = -2\delta(t) \left(\frac{x - x_h}{c - x_h} \right) \quad \textbf{5.27}$$

and the second derivative is:

$$\frac{d^2Y}{dX^2} = -\delta(t)(F-1) F \left(\frac{1}{c - x_h} \right) \left(\frac{x - x_h}{c - x_h} \right)^{F-2} = -\frac{2\delta(t)}{c - x_h}. \quad \textbf{5.28}$$

The radius of curvature is given by [James (1996)]:

$$r_1 = \frac{\left[1 + \left(dY/dX\right)^2\right]^{\frac{3}{2}}}{\left|d^2Y/dX^2\right|} = \frac{\left[1 + 4\delta^2(t)\left(x - x_h/c - x_h\right)^2\right]^{\frac{3}{2}}}{\left|-2\delta(t)/(c - x_h)\right|}. \quad \textbf{5.29}$$

For small flap deflections the first derivative term becomes negligible and the radius of curvature is approximately constant with a value given by:

$$r_1 \approx \frac{c - x_h}{2\delta(t)}. \quad \textbf{5.30}$$

The power distribution of deflection with a shape parameter of 2.0 is therefore appropriate for a constant strain piezo-bender actuation device. Furthermore, from equations 5.26 and 5.30 the deflection is related to the strain by:

$$\delta(t) \approx \frac{(c - x_h)\varepsilon_{actuator}}{2l_m}. \quad \textbf{5.31}$$

The strain capability of the piezo actuators is generally known and therefore the maximum deflection is dependent upon the thickness of the bender and the length (chord) over which the actuators are mounted. Assuming there is a limit on the minimum value of l_m, larger equivalent flap deflections will be obtained for larger chords. This technology is perhaps then better suited to larger chord flaps and blades.

Interdigitised Electrode (IDE) actuators available from MIDE exhibit a strain capability of +/-374με. These actuators are 0.38mm thick and therefore to attain 4 degrees of deflection of a 15% chord flap located on the constant chord portion of the EH101 main

rotor blade, the central bending material would have to be a maximum of 0.35mm thick. This emphasises the difficulties associated with the use of such technology and the limited deflections which may be obtained. It is therefore vital that the effects due to such small deflections are accurately predicted and the difference in deflection shape could prove to be very important.

5.4 Validation of the Active Trailing Edge Model

In this section the new model will first be correlated using the plain flap configuration before consideration is given to the Active Trailing Edge prediction.

5.4.1 Representation of a Plain Flap

An additional advantage of representing the indicial responses using exponential functions is that the method of Laplace transforms may be used to explicitly calculate their representation of the response to a sinusoidal forcing which may then be compared to experimental data. Such data is presented by Hariharan and Leishman (1996) for a 25% chord plain flap and this data will be used to evaluate the capability of the current method.

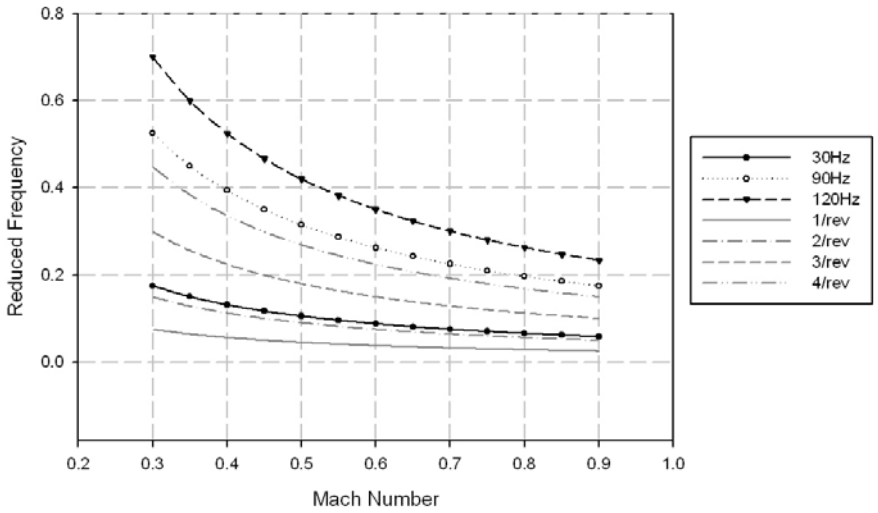

Figure 5.7: Reduced frequency of validation data compared to typical values for the EH101 main rotor.

Firstly, however, consideration should be given to the range of important reduced frequencies as presented in Figure 5.7. The test data is available for a range of Mach numbers at frequencies of 0Hz, 30Hz, 90Hz and 120Hz. For each frequency, as the Mach number varies whilst the chord stays constant, the reduced frequency changes. Similarly the effect due to Mach number on the reduced frequency for the EH101 main rotor has

been plotted for various deflection frequencies at harmonics of the rotor rotation frequency. Figure 5.7 therefore shows that the important deflection frequencies of 4-6/rev (the importance of these frequencies will be explained below) lie between the 30Hz and 90Hz test cases. Consider also the maximum Mach number as shown in Figure 5.8. Due to the presence of the BERP tip on the EH101, in the present study the ATEs will not be used outboard of 0.8% radius (see below). Even for advance ratios up to 0.4 the Mach number does not exceed 0.75 at this location and this should be considered when viewing the following validation.

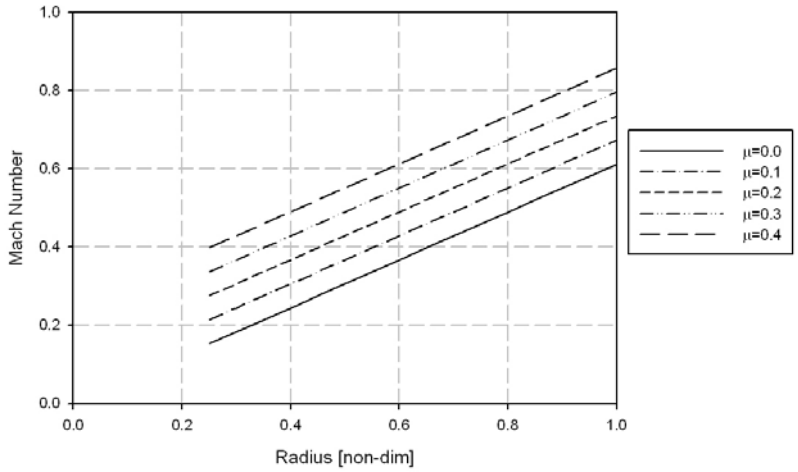

Figure 5.8: Approximation of maximum (advancing blade) Mach number variation with radial location and advance ratio for the EH101 main rotor.

The correlation between the current model and the experimental data for the normal force coefficient is shown in Figure 5.9. In the steady state (0Hz), the variation with Mach number is reasonably well captured. Note that in practice this steady variation with Mach number could be corrected using lookup tables; however the prediction using only the Prandtl-Glauert correction is reasonable. The effect of the frequency at 30Hz is also well correlated with the test data; however the effect on the higher 90Hz and 120Hz frequencies is over-predicted. This is a feature which can also be observed in the Hariharan and Leishman (1996) model, particularly at low Mach number and is entirely due to the circulatory component. This would suggest that the circulatory indicial response has been optimised for the lower frequencies which dominate the blade pitching and the result here might be improved by using a modified function for the higher frequencies associated with a flap/ATE. However, as the frequencies of interest for the current research lie below the 90Hz test case the model is deemed to be sufficiently accurate for purpose.

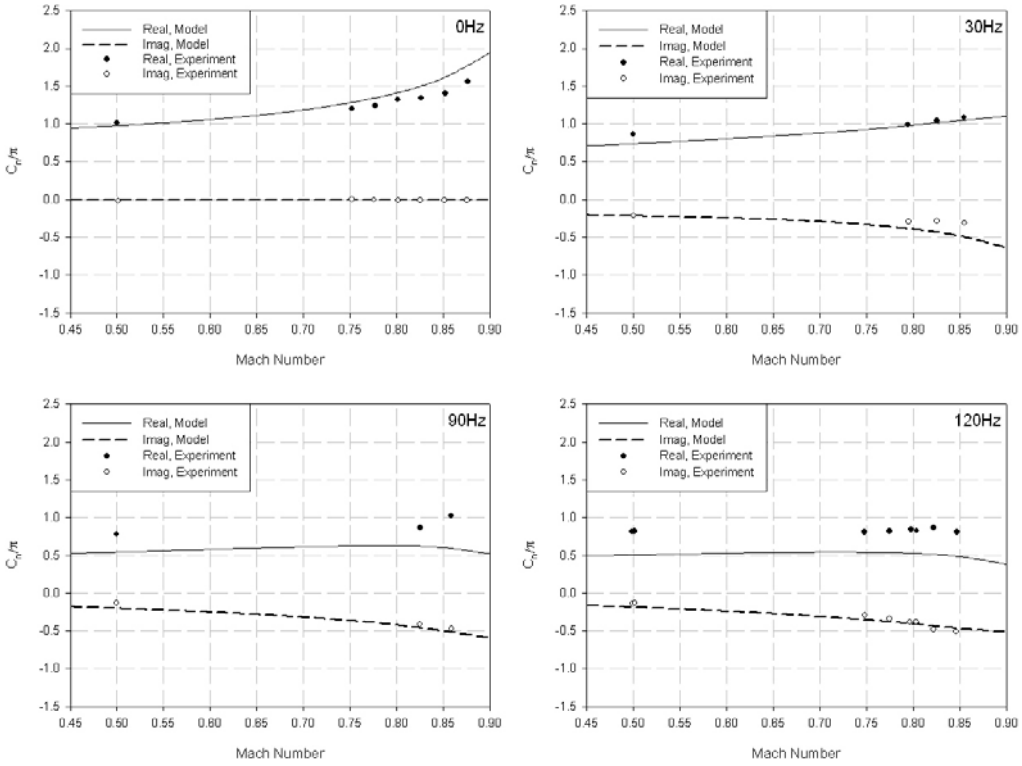

Figure 5.9: Normal force prediction for a plain flap operating with a sinusoidal deflection at a variety of frequencies and Mach numbers. Markers show experimental data from Hariharan and Leishman (1996), lines are the prediction using the current model.

The plot of the pitching moments, shown in Figure 5.10, reveal that the effect on frequency is much less pronounced than for the normal force coefficient and this is reflected by the model. The effect of Mach number on the steady result is reasonably predicted but again the higher frequency results could be improved by modification of the circulatory response function (a feature also observed in the predictions of Hariharan and Leishman (1996)). However, as for the normal force coefficient, the prediction up to the frequencies of interest is considered to be adequate.

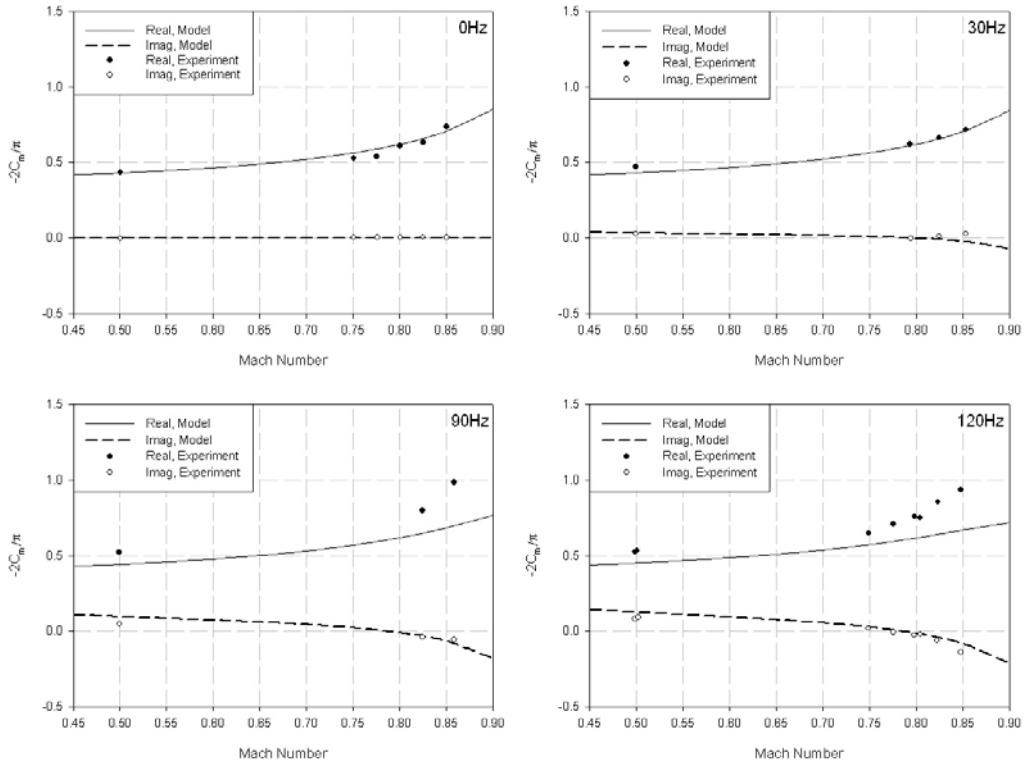

Figure 5.10: Pitching moment prediction for a plain flap operating with a sinusoidal deflection at a variety of frequencies and Mach numbers. Markers are experimental data from Hariharan and Leishman (1996), lines are the prediction using the current model.

Finally, the hinge moment coefficient is plotted in Figure 5.11. The steady-state variation with Mach number is not as well correlated as for the other coefficients and the correlation of the real component actually improves with actuation frequency. The prediction of the Imaginary response at low Mach number is less well predicted and this is in common with Hariharan and Leishman (1996) who put this down to the influence of viscous effects at the trailing edge having a larger effect on the hinge moment. Overall though the correlation is considered to be good enough to provide confidence that the closely related flap force coefficient is also reasonably predicted for use in the drag coefficient.

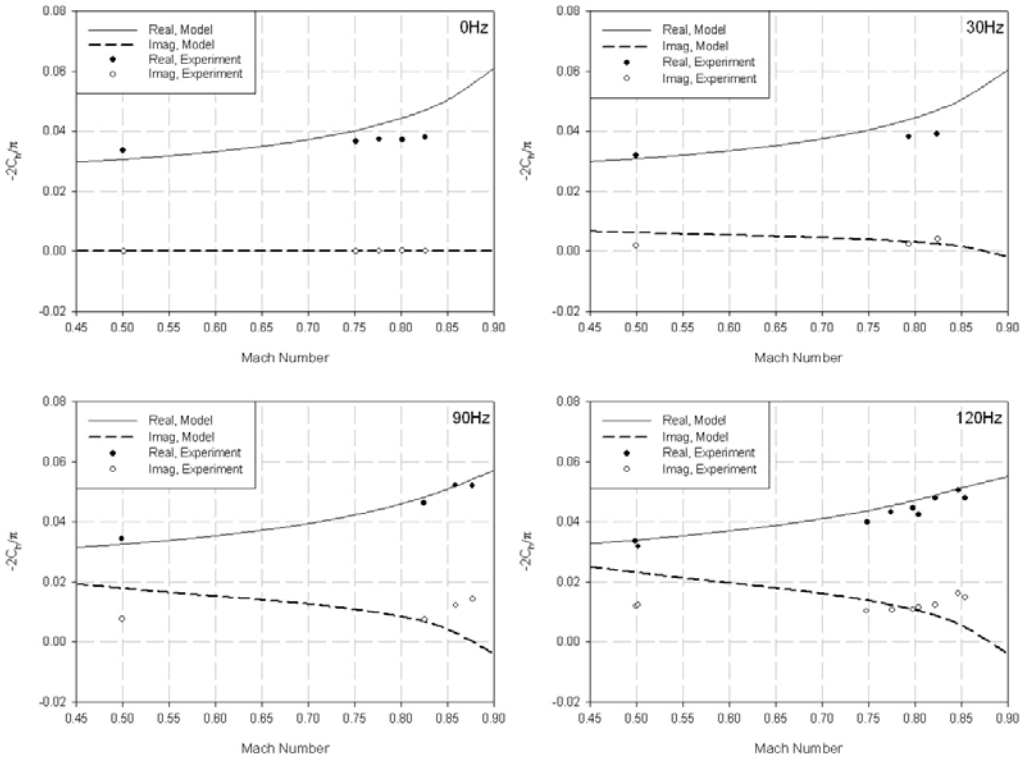

Figure 5.11: Hinge moment prediction for a plain flap operating with a sinusoidal deflection at a variety of frequencies and Mach numbers. Markers are experimental data from Hariharan and Leishman (1996), lines are the prediction using the current model.

Hariharan and Leishman (1996) also present the hysteresis loops for two of the cases with the first at the moderate 30Hz frequency and the second at the highest 120Hz frequency. The latter is of particular interest as results are shown for a Mach number of 0.748 which is around the highest value required for the current research. The plots of lift and pitching moment coefficient are reproduced in Figure 5.12 and Figure 5.13 respectively with the prediction given by the newly adapted Third Generation model (using a shape parameter value of 1) included for comparison.

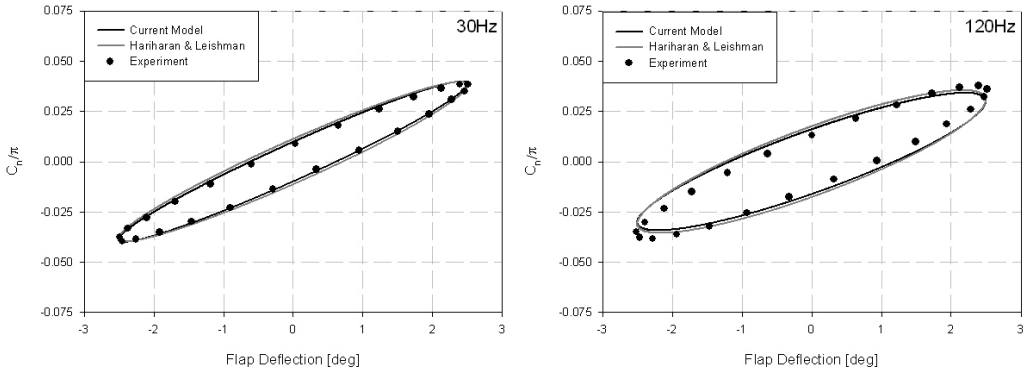

Figure 5.12: Normal force coefficient prediction for a plain flap operating at 30Hz, Mach = 0.5 (left) and 120Hz, Mach = 0.748 (right).

From both figures it is clear that, as expected, the new model is providing very similar predictions for the plain flap to the Hariharan and Leishman (1996) model.

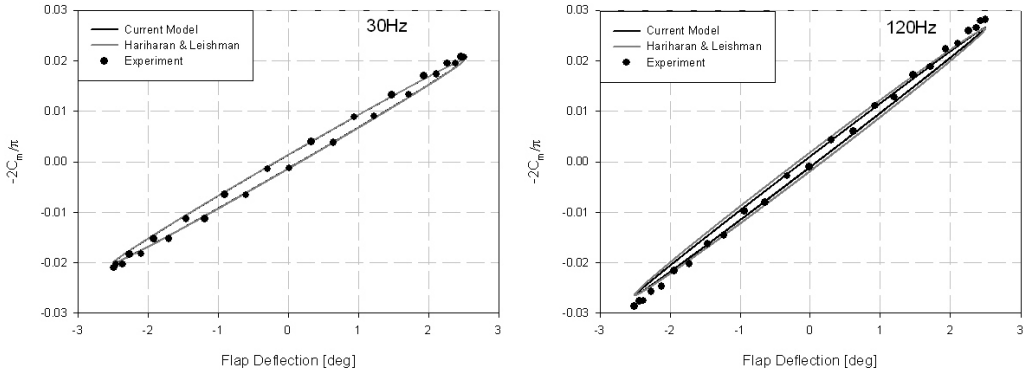

Figure 5.13: Pitching moment coefficient prediction for a plain flap operating at 30Hz, Mach = 0.5 (left) and 120Hz, Mach = 0.748 (right).

The aerodynamic hinge moment coefficients for the two cases are presented in Figure 5.14. Considering the accepted difficulty in predicting hinge moments, due to the domination of viscous effects, the prediction by both models is reasonable. Unfortunately no data for drag force coefficients is presented by Hariharan and Leishman (1996) so cannot be considered here; however a validation in the steady-state will be presented in the following section.

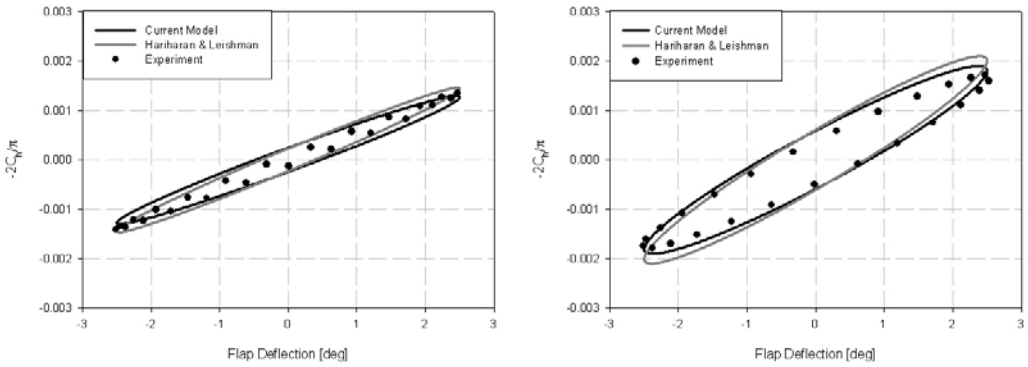

Figure 5.14: Hinge moment coefficient prediction for a plain flap operating at 30Hz, Mach = 0.5 (left) and 120Hz, Mach = 0.748 (right).

Overall, the newly developed Active Trailing Edge model has been shown to be generally comparable to the existing model of Hariharan and Leishman (1996) when modelling a plain flap up to the moderate frequencies and Mach numbers of interest. Comparisons to the experimental data have given confidence in the derivation of the model such that it may be extended to consider the effects of more arbitrary changes in camber.

5.4.2 Varying the Camber Shape Parameter

Various camber shapes were previously defined as shown in Figure 5.4. A brief validation of the effect due to the shape parameter has been performed for the steady-state case. For this validation, the new model is compared to coefficients obtained using the XFOIL program, Drela (2001). XFOIL is a coupled panel-method and boundary layer code which is quick and easy to run and accepts the input of user-defined aerofoil shapes. The author therefore produced aerofoil coordinates for each deflection shape, based on a NACA 0012 aerofoil, as demonstrated for deflection shapes of F=1 and F=2 in Figure 5.15. As shown, the deflection of the camber line was assumed to follow the prescribed shape whilst the aerofoil coordinates were assumed to be attached perpendicular to the camber line.

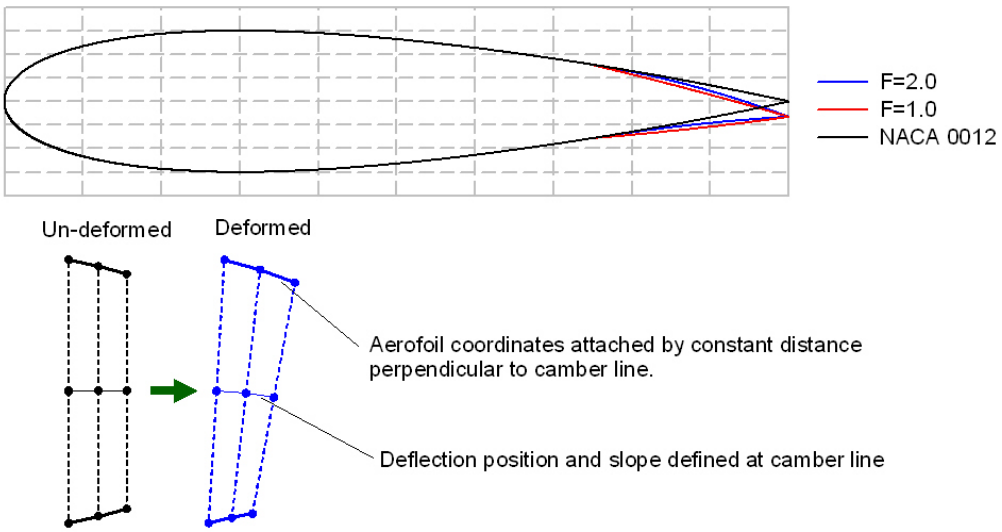

Figure 5.15: Coordinate deformation for an aerofoil of finite thickness using a deflection defined at the camber line.

Using the methodology outlined, XFOIL simulations were performed for the NACA0012 aerofoil at zero angle of attack for the inviscid case and at a Reynolds number of 3.0×10^6. Results were obtained for various values of shape parameter, each with a deflection of 1 degree (note from the definition of the power distribution that the angular deflection defines the motion of the straight line connecting the equivalent hinge location and the trailing edge). The change to the lift and pitching moment coefficients were then compared to those predicted using the new model as shown in Figure 5.16 and Figure 5.17.

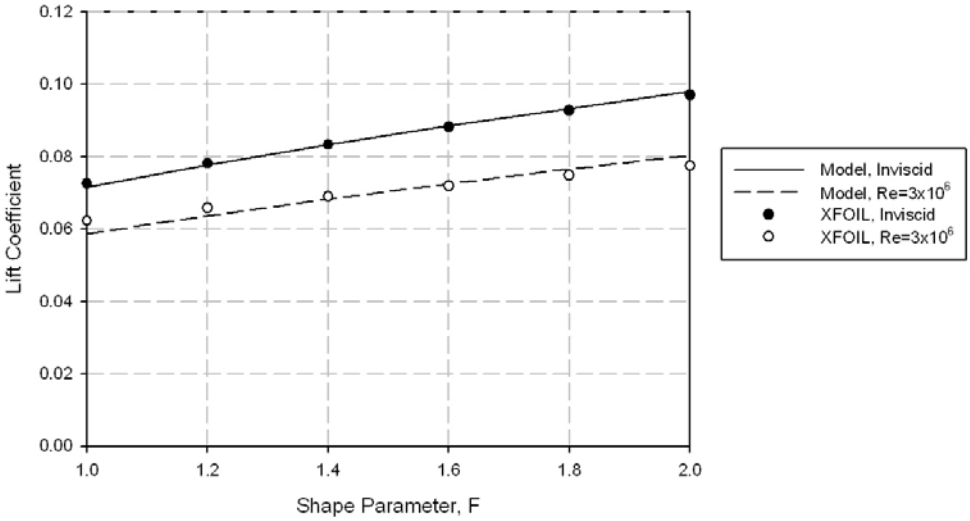

Figure 5.16: Validation of the new model with XFOIL for steady lift coefficient due to varying shape factor.

Note that, as suggested by Hariharan and Leishman (1996), the application of factors to account for viscous effects is required. Such factors are used to pre-multiply the circulatory component of each coefficient and are included in the newly derived method. In the current validation, however, these factors were not varied with shape factor such that the variation observed is purely due to the modelling. Clearly the variation of the coefficients with shape factor in the inviscid case is well captured by the new methodology, whilst the viscous effects are causing the effect of the shape parameter to be slightly reduced. The model is still however deemed to be sufficiently accurate to capture the main effects during an investigation into various deflection shapes without the need to produce separate values of effectiveness multipliers for every shape to be considered (which could be a time-consuming process).

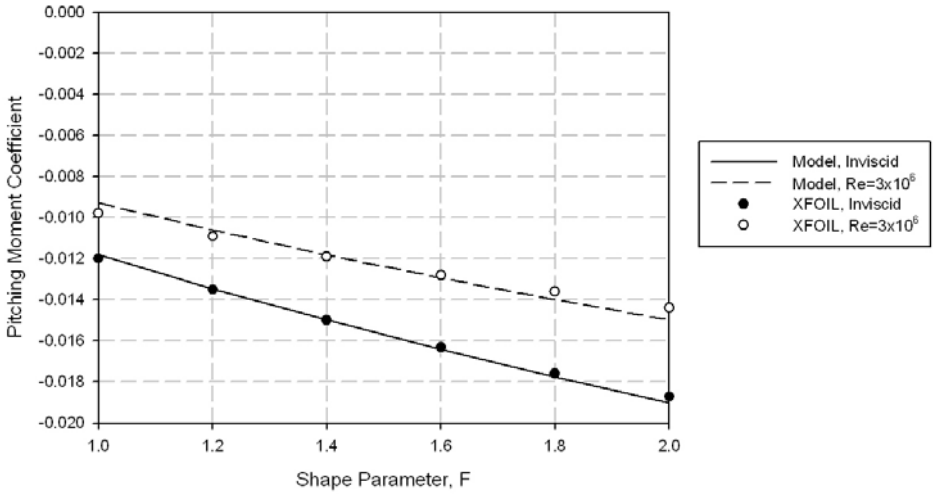

Figure 5.17: Validation of the new model with XFOIL for steady pitching moment coefficient due to varying shape factor.

Results have also been obtained for the drag coefficient. As for the lift and pitching moment coefficients, the flap effectiveness parameter for the chord force has been held constant such that any change is due purely to the modelling. The drag coefficient at a variety of ATE deflections and angles of attack is shown in Figure 5.18 and Figure 5.19 for shape parameters of 1 and 2 respectively.

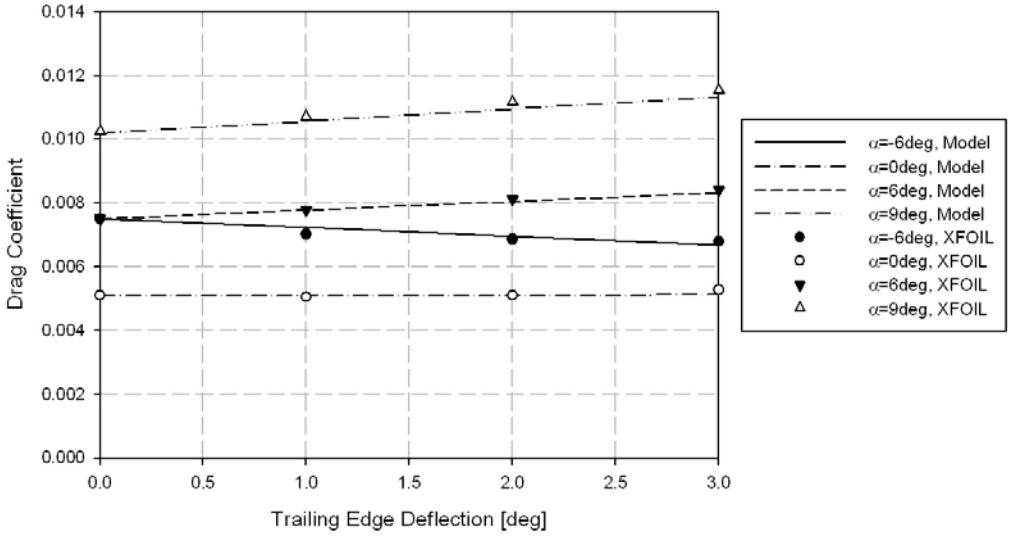

Figure 5.18: Validation of the new model with XFOIL for steady drag coefficient with a shape parameter of 1 for various ATE deflections and angles of attack.

The correlation could be improved slightly by adjusting the chord force effectiveness parameter for each deflection shape, however even with holding it constant the correlation is reasonable. Note also that there is very little difference between the drag coefficients for the shape parameters of 1 and 2, suggesting that the latter is more efficient in terms of the lift-to-drag ratio.

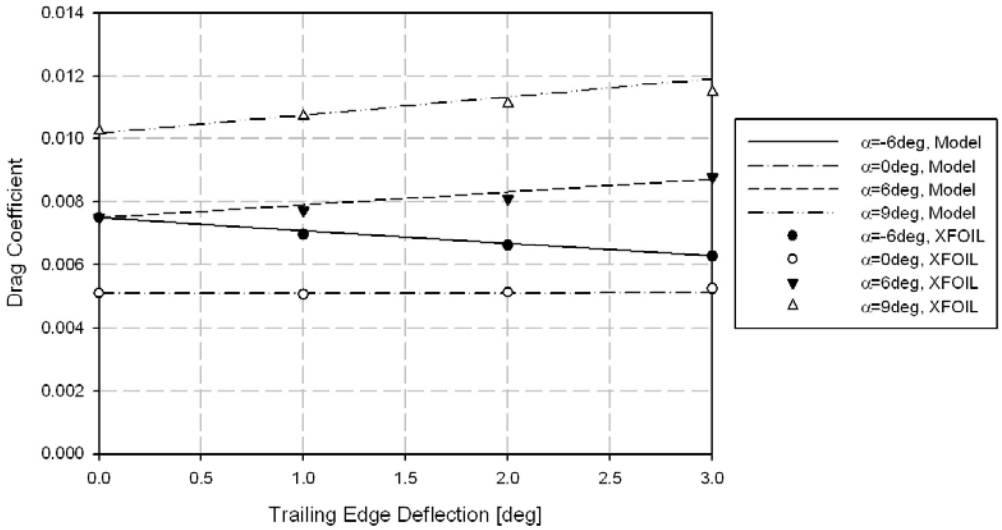

Figure 5.19: Validation of the new model with XFOIL for steady drag coefficient with a shape parameter of 2 for various ATE deflections and angles of attack.

An example of how the lift and pitching moment coefficients vary with the shape parameter in an unsteady case is shown in Figure 5.20 and Figure 5.21, clearly such results should be correlated against experimental data as and when it becomes available.

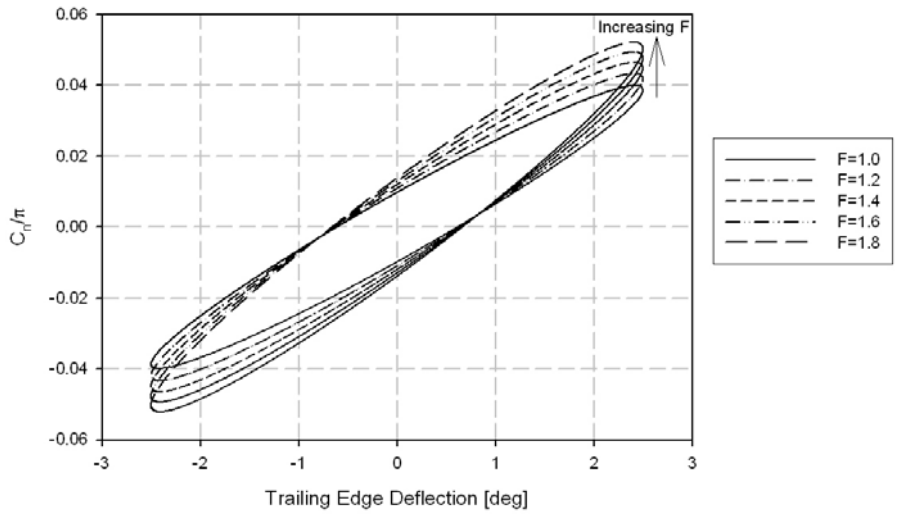

Figure 5.20: Effect due to shape parameter on normal force coefficient for unsteady trailing edge deflections at 30Hz, Mach = 0.5.

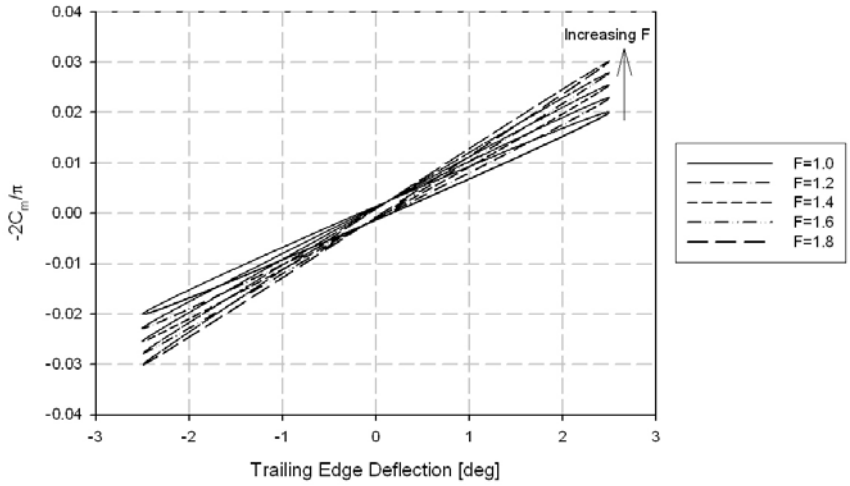

Figure 5.21: Effect due to shape parameter on pitching moment coefficient for unsteady trailing edge deflections at 30Hz, Mach = 0.5.

It is clear from the steady-state results, and from the model prediction for the unsteady coefficients, that by increasing the shape parameter and delaying the deflection further towards the trailing edge, the increments in the normal force and pitching moment coefficients are increased. This suggests that for a given actuation requirement the deflection of the trailing edge may be decreased. Figure 5.22 shows the variation, with shape factor, of the trailing edge deflection required to produce the same lift increment as 1 degree of deflection of a plain flap. For example, a trailing edge with a shape parameter of 2.0 requires approximately 74% of the deflection of a plain flap (shape parameter 1.0) to give an equivalent change in lift coefficient.

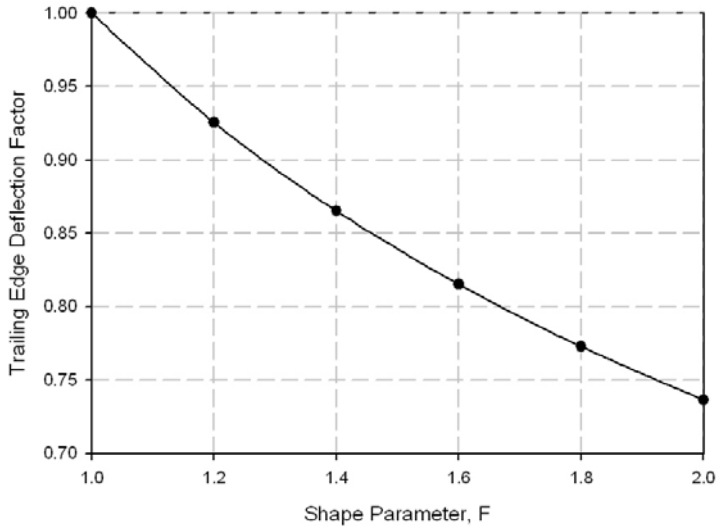

Figure 5.22: Effect due to Trailing Edge Shape Parameter on Deflection Factor.

This is an important result; indeed the reader should recall from the earlier discussion how the deflection of an ATE may be limited compared to a hinged Trailing Edge Flap.

The increase in lift available per degree of deflection could therefore be critical in the evaluation of such technologies, and the current model has been shown to be capable of predicting such effects.

5.5 Enhancement of an Advanced Rotor using Active Trailing Edges

The literature review presented in an earlier chapter revealed a number of analytical investigations into the application of trailing edge flaps to vibration reduction using a range of rotor performance codes. The author carried out one such investigation using the Hariharan and Leishman (1996) model implemented inside the r150 rotor performance program. The Westland Lynx was used as the example aircraft and the results were presented by the author at the European Rotorcraft Forum (ERF), Jones and Newman (2006). The investigation provided an insight into the physical mechanisms which enable the reductions in vibration. In particular it was demonstrated that TEFs could be used on a blade which is stiff in torsion (as is the case for the BERP III rotor blade) provided that the flaps are advantageously positioned in terms of the nodes of the lower frequency modes which may be manipulated to reduce the vibration. The direct manipulation of the modes of interest through lift modal forcing means that a different physical mechanism is being used to that demonstrated in flight by Eurocopter Deutschland (ECD) [Dieterich et. al. (2006)], which relies on the servo-effect on a soft-in-torsion blade.

The main focus of this chapter, however, is to demonstrate the application of the newly emerging technology of Active Trailing Edges. As for the Air Jet Vortex Generators, the example rotor will again be the BERP III equipped EH101, such that the results are a fair indication on the improvement to be made on current technology. The lessons learned from the previous investigation by Jones and Newman (2006) will therefore be used to ensure that the ATEs are adequately positioned for the reduction of vibration of the relatively stiff-in-torsion rotor blade. Note that the BERP III rotor blade has a 1st torsion mode frequency greater than 7/rev, compared to a frequency of less than 4/rev for the ADASYS, TEF-equipped, rotor flight tested by ECD [Dieterich et. al. (2006)].

However, the application of ATEs will not only be investigated in terms of vibration. One of the recurring themes of this dissertation is that the TEF and ATE technologies are particularly attractive due to their multi-purpose capability. Chan and Brocklehurst (2001) predicted that significant increases to the flight envelope were possible using the TEF. However, no consideration was given to vibration and the investigation focussed

primarily on retreating blade stall in flight conditions requiring a very high blade loading. The current investigation will therefore use a modified version of the previously developed vibration optimisation algorithm [Jones and Newman (2006)] to consider the simultaneous reduction of vibration and control loads. In high-speed flight, the pitching moments experienced on the advancing side can cause a considerable rise in control loads which can limit the flight envelope. Keeping such control loads within design constraints can have a significant impact on the blade design by limiting the use of aerofoil camber, which improves retreating side behaviour, and built-in blade twist, which improves the hover performance. It will therefore be demonstrated here that, even with a more limited deflection capability, the ATEs may be used to reduce both vibration and the advancing blade control loads. This will provide a clear example which suggests that future ATE equipped blades could reduce the current design compromise between dynamic and aerodynamic considerations such that use may be made of increased amounts of both camber and blade twist and to thus improve the overall performance of the helicopter. Finally, note that the investigation will be performed with a modest deflection capability such that the effects due to the deflection shape, as captured using the new model, become much more critical.

The following section will present the optimisation algorithm used for the multi-objective application of ATEs, following which the placement of the ATEs will be briefly discussed before results are presented.

5.5.1 Optimisation Algorithm

The optimisation algorithm being used for the scheduling of the flap deflection is based on a control method for higher harmonic control (HHC) as described by Johnson (1982). A global helicopter model is defined as:

$$z = z_0 + T\theta \tag{5.32}$$

where z is a vector containing the real and imaginary components of the harmonics of the loads to be reduced, z_0 is the corresponding uncontrolled response, θ is a vector of the various harmonics of flap deflection and T is a transfer matrix. If only vibration is being considered then z consists of the N/rev fixed-frame hub loads (N being the number of rotor blades). Note that only the N/rev loads are used as in a steady flight condition, the periodic response of the rotor blades means that only harmonics at integer multiples of the number of blades are transmitted to the fuselage (with all other harmonics cancelling during the summation over the blades), see, for example, Newman (1994). If

performance enhancement is to be considered through control load minimisation then harmonics of this parameter must also be included in z. The model therefore assumes that the response of the vibratory hub and control loads to input ATE deflection harmonics is linear. This approximation has been found to be reasonable in steady-state forward flight conditions, with reasonable results being demonstrated for the Trailing Edge Flap by a number of authors [see, for example, Kim et al (2004), Jones and Newman (2006)].

In order to estimate the transfer matrix, an off-line identification is performed whereby a series of 'trial' control vectors are input and the vibratory hub load response recorded. The transfer matrix is then estimated using Least-Squares fitting which results in [see Johnson (1982)]:

$$T = Z_{Trial}\theta_{Trial}\left(\theta_{Trial}^{T}\theta_{Trial}\right)^{-1} \quad \textbf{5.33}$$

where θ_{Trial} is a matrix containing the trial input vectors and Z_{Trial} is a matrix composed of the corresponding response vectors.

With the linearised model thus identified, a cost function must now be defined for the optimisation. The cost function consists of the weighted sum of squares of the hub and control loads added to a similar weighted summation of the input control harmonics, thus:

$$J = z^{T}W_{z}z + \theta^{T}W_{\theta}\theta \quad \textbf{5.34}$$

where W_z and W_θ are weighting matrices. The z weighting matrix allows for the relative importance of the various hub and control loads to be adjusted whilst the control weighting matrix enables the allowable deflection to be constrained (as described in more detail below).

Substituting equation 1.1 into equation 5.34 and setting $\partial J/\partial\theta_j = 0$ for each component, j, of θ gives a set of equations which may be solved [see Johnson (1982) for further details] to give the optimum control vector, θ_{opt}, as:

$$\theta_{opt} = -\left(T^{T}W_{z}T + W_{\theta}\right)^{-1}T^{T}W_{z}z_{0}\,. \quad \textbf{5.35}$$

The optimised control input may then be used to obtain the corresponding optimum hub and control loads.

All that remains is to set the weighting matrices. Firstly, consider the z-vector weighting matrix, W_z. In order to analyse the vibration reduction capability of the ATEs, a vibration index consisting of a single value for each flight case is desirable. It is possible to model the vibration at specific points in the fuselage using rigid, or elastic, body transfer functions which relate the calculated hub loads to accelerations at the given locations in the fuselage. Such transfer functions are derived from experiment and/or finite element modelling of the fuselage based on shake test or finite element data. The use of such transfer functions therefore considers the response of the fuselage structure as much as the vibratory rotor loads. Here, however, in order to investigate the effectiveness of the active system, we seek the ability to reduce all the fixed-frame vibratory loads produced by the rotor, thus demonstrating that the system can be effective regardless of the nature of the fuselage response and the relative importance of the individual hub loads. Therefore a transfer function has been used which assumes that each of the hub loads contributes equally to the vibration prior to applying the control. The vibration index is therefore given by:

$$V = \sqrt{W_{F_x} F_x^{\,2} + W_{F_y} F_y^{\,2} + W_{F_z} F_z^{\,2} + W_{M_x} M_x^{\,2} + W_{M_y} M_y^{\,2} + W_{M_z} M_z^{\,2}} \qquad \textbf{5.36}$$

where F_i and M_i are the magnitudes of the fixed-frame N/rev hub forces and moment and the W factors are their corresponding weightings. During an investigation into the application of TEFs to the Lynx helicopter [Jones and Newman (2006)] it was found that greater reductions in the hub shears and rolling- and pitching- moments are possible if the vibratory torque is excluded from the optimisation. Consultations with staff at Westland Helicopters Limited revealed that the vibratory torque is usually omitted from their vibration index as it can give misleading results due to its complicated interaction with the rotor shaft and gearbox dynamics. Therefore the weighting on the vibratory torque has been set to zero for the current investigation. To ensure that the remaining hub loads were given equal importance, their weighting values were set such that each hub load gives an equal contribution to the vibration index when averaged over the speed range tested.

In order to optimise for the simultaneous reduction of the control loads, harmonics of this parameter must also be included in the z-vector and weighted accordingly. In order to change the weighting from hub loads to control loads, the control loads are given a weighting of W_C, which is varied between 0 and 1, whilst the hub load weightings are further multiplied by 1- W_C. In conditions, away from stall, where the vibratory control

loads are relatively low, zero control load weighting is required such that the ATEs may concentrate on vibration reduction. As the stall boundary is approached, the vibratory control load begins to rise and the weighting must be increased. This behaviour has been achieved by setting the control weighting as:

$$\begin{aligned} W_C &= \exp\left[k_C \left(CL_{vib_0} - CL_{vib_{ref}} \right) \right] && \left(CL_{vib_0} < CL_{vib_{ref}} \right) \\ W_C &= 1 && \left(CL_{vib_0} \geq CL_{vib_{ref}} \right) \end{aligned} \qquad \textbf{5.37}$$

where CL_{vib_0} is the vibratory control load with zero flap input and $CL_{vib_{ref}}$ is a reference value at which full weighting is put on the control loads. The factor k_C controls how swiftly the change to control load optimisation occurs. In practice a value of:

$$k_C = 10 / CL_{vib_{ref}} \qquad \textbf{5.38}$$

has been found to be reasonable. In the current work only the first harmonic of control loads is included in the optimisation and therefore the weighting matrix is set as:

$$W_z = (1-\beta) \begin{bmatrix} (1-W_C)W_{F_x} & 0 & 0 & \cdots & 0 & 0 & 0 \\ 0 & (1-W_C)W_{F_x} & 0 & \cdots & 0 & 0 & 0 \\ 0 & 0 & (1-W_C)W_{F_y} & \cdots & 0 & 0 & 0 \\ \vdots & \vdots & \vdots & \ddots & \vdots & \vdots & \vdots \\ 0 & 0 & 0 & \cdots & (1-W_C)W_{M_z} & 0 & 0 \\ 0 & 0 & 0 & \cdots & 0 & W_C & 0 \\ 0 & 0 & 0 & \cdots & 0 & 0 & W_C \end{bmatrix} \qquad \textbf{5.39}$$

Where the factor, (1-β), will be described below.

Finally, the control vector weighting matrix, W_θ, must be calculated in order to constrain the input to a prescribed maximum value. Using the method originally suggested by Cribbs and Friedmann (2001), W_θ is given the form:

$$W_\theta = \beta I \qquad \textbf{5.40}$$

where I is the identity matrix and β is a scalar which varies between 0 and 1. Recall that the hub load weighting matrix is also pre-multiplied by (1-β) and, therefore, when $\beta=0$ the input vector is unconstrained whilst when $\beta=1$ the input vector alone is being minimised and the optimum input, according to equation 5.35, will be zero. For

intermediate values of β the focus of the cost function will shift from the hub load vector to the control vector, thus allowing the control input to be constrained. In order to prescribe this constraint, the value of β is calculated in an iterative process in order to minimise the expression:

$$\left(\delta_{\max,opt} - \delta_{\max}\right)^2. \qquad \textbf{5.41}$$

The quantity, $\delta_{max,opt}$ is the maximum scheduled flap deflection as calculated for the optimum input vector given by equation 5.35 for the current value of β and δ_{max} is the prescribed maximum allowable deflection. Thus the input control schedule is constrained to the prescribed maximum.

5.5.2 Design Parameters for the Active Trailing Edges

This section discusses the choice of the design parameters for the Active Trailing Edges used in the current research. The parameters include the number, size, location and allowable deflection for the ATEs.

In a previous investigation into the use of TEFs on the Lynx aircraft, Jones and Newman (2006), it was found that it is best to use multiple flaps, each operating at multiple harmonics in order to achieve the greatest possible vibration reduction and therefore for this investigation it was decided to use three flaps each operating at multiple harmonics of the rotor rotation frequency. For a helicopter rotor in a steady-state condition where the rotor forcing and response is periodic with the rotor rotation, it can be shown [see, for example, Newman (1994)] that, due to the way the harmonics of load are summed over the blades, only vibration at rotor harmonics which are integer multiples of the number of blades, N, is transmitted to the fuselage. For example, as the EH101 being studied here has a 5-bladed main rotor, in the steady-state, only vibration at 0/rev, 5/rev, 10/rev, etc… will be felt in the fuselage. Clearly 0/rev is the steady-state which should correspond to the required trim and following this the N/rev frequency is the most important as the magnitude of the response drops off rapidly with frequency. The control of vibration in helicopters therefore focuses on the N/rev response in the fuselage.

Furthermore, if the loads of a single blade in the rotating-frame of reference are considered then it can also be shown [see, for example, Newman (1994)] that the N/rev vertical bounce and yaw moment in the fuselage-, or fixed-, frame of reference will be due to the corresponding N/rev loads in the rotating-frame. Likewise, it can be shown that the rolling- and pitching-moments in the fixed-frame are due to the rotating-frame

flapping and torsion moments at (N-1)/rev and (N+1)/rev and that the longitudinal and lateral shears in the fixed-frame will be due to the rotating-frame radial and lag shears at (N-1)/rev and (N+1)/rev. Therefore, to influence the fixed-frame vibration at N/rev, as the flaps are located on the blade in the rotating-frame, they should be deflected at harmonics of N-1/rev, N/rev and N+1/rev, or 4, 5 and 6/rev for the 5-bladed main rotor of the EH101 helicopter being considered here. In this study, as the vibratory control loads are also to be minimised, the input frequencies of 1 and 2/rev are also included.

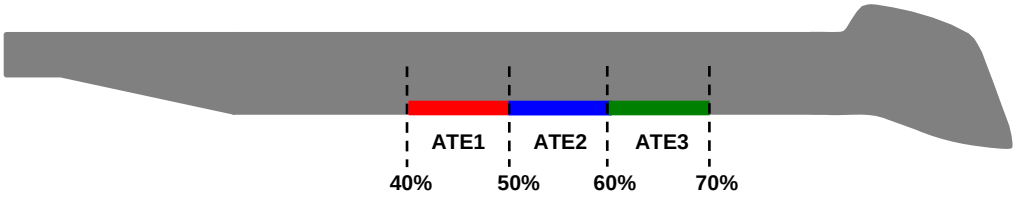

Figure 5.23: Active Trailing Edge locations used in the current research.

The three ATEs have been positioned so that they can influence both vibration and stall with each being of 10% span and located between 40-70% of the rotor radius, as shown in the sketch in Figure 5.23. Although this may not be optimum for vibration reduction (for example, Jones and Newman (2006) found that a TEF located near the tip was very effective), locating them further inboard enables them to influence the control loads without applying overly large structural torques to the blade. In terms of vibration reduction, as the ATE produces changes predominantly out-of-plane (i.e. the drag forcing is small compared to the lift forcing) their optimum location can be expected to be dependent upon the flapwise deflection shape of the modes. In addition, as the natural frequencies of the 2nd flap mode (2.5-3/rev), 2nd lag mode (4.5-5/rev) and 3rd flap mode (5.5-6/rev) are closest to the frequencies of interest, forcing these modes is likely to have the greatest effect on the 5/rev fixed-frame vibration (this will be justified through analysis of the results later in this chapter).

The flapwise deflection shapes of these three modes are shown in Figure 5.24. With the suggested ATE locations, the two outer-most ATEs spanning from 50-70% rotor radius can provide lift forcing to all three modes of interest. The inner-most ATE region is less ideal for forcing the 3rd flap mode but is still able to influence the two lower frequency modes. Overall, the ATE locations are considered to be a reasonable compromise between the vibration reduction and control load requirements.

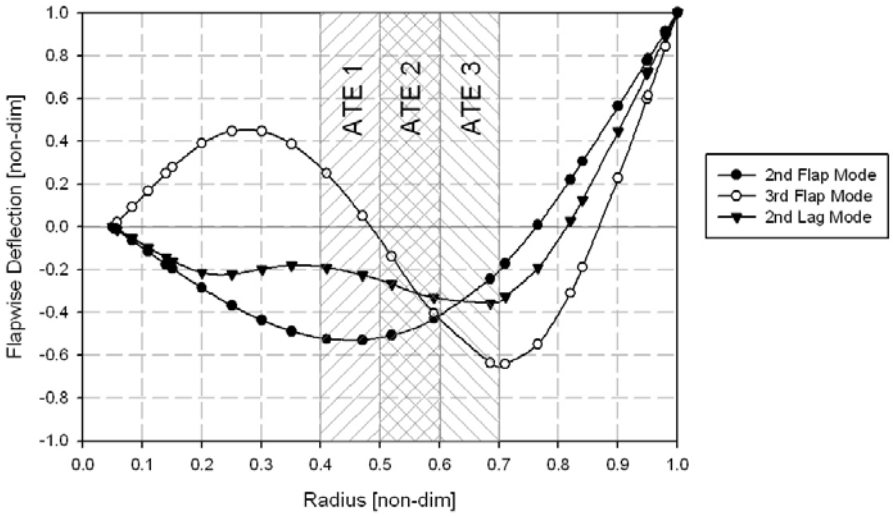

Figure 5.24: Active Trailing Edge locations with respect to the flapwise deflection of the 2nd flap and lag modes and the 3rd flap mode of the BERP III blade of the EH101.

Finally, a maximum deflection capability for the ATEs must be set for the analysis. Whirl tower testing of ECDs ADASYS rotor demonstrated a half peak-to-peak TEF deflection capability of 6 degrees [Dieterich et. al. (2006)]. It will be assumed that the BERP III rotor under consideration will require a similar level of forcing to obtain the required vibration reduction. Therefore, if an ATE of quadratic deflection shape is to achieve a similar lift increment then thin aerofoil theory suggests that a half peak-to-peak deflection of 4.42 degrees is required. This has therefore been imposed as the deflection constraint throughout the following study.

5.5.3 Vibration Reduction Results

The vibration reduction capability of the ATEs will first be presented. These results have been calculated with only the weighted hub loads included in the optimisation, i.e. the control weighting, W_C, has been fixed to zero. Figure 5.25 presents the resulting vibration index, with and without the ATEs operating, for a range of advance ratios at a blade loading of 0.17. Clearly the ATEs are predicted to provide a significant improvement, showing reductions in excess of 75% over most of the speed range. The effectiveness, however, decreases at the higher speeds, when the onset of stall occurs.

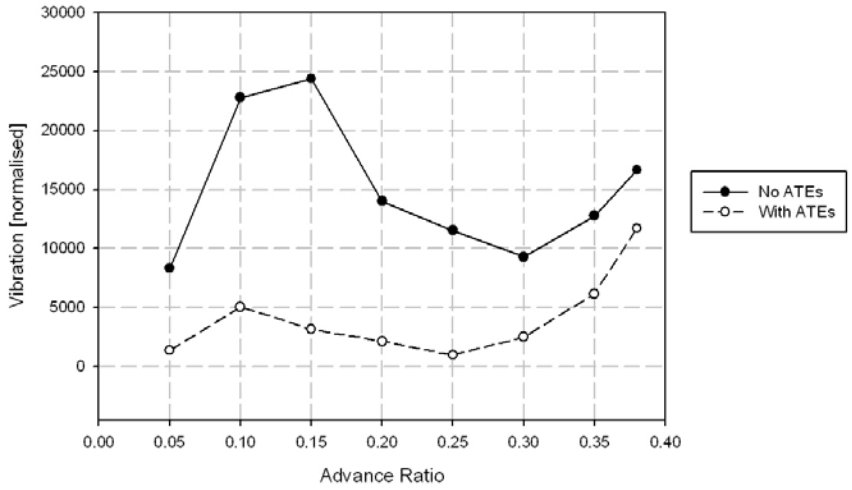

Figure 5.25: Vibration Reduction due to ATE Vibration Control, C_T/σ=0.17.

The effect on vibratory control loads due to the optimisation for vibration reduction is shown in Figure 5.26 from which it may be seen that the optimisation for vibration reduction has generally caused the vibratory control loads to increase which could have a considerable impact on the fatigue life of the control system. It should also be noted that if the actuation of the ATEs is causing the vibratory control loads to increase it could also be causing other responses in the rotating-frame to increase which could have a significant effect on the blade structural loads and its corresponding fatigue life.

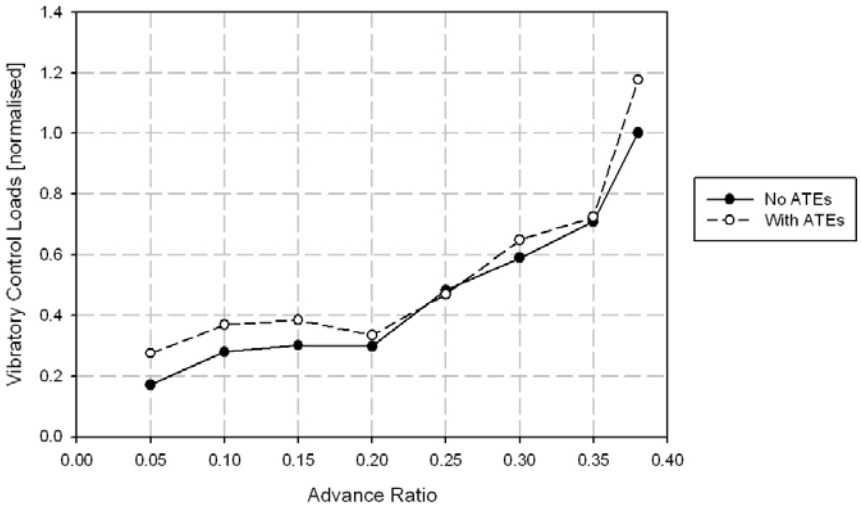

Figure 5.26: Vibratory control loads due to vibration optimisation using Active Trailing Edges, C_T/σ =0.17.

Overall, the reduction of vibration using the ATEs is successful, especially considering the limitation imposed on the deflection capability. At the highest advance ratios, however, the effectiveness is reduced and it is in these flight conditions where the

optimisation should become more concerned with the control of effects associated with the onset of stall, such as the minimisation of the vibratory control loads.

5.5.4 Analysis of Vibration Reduction Mechanisms

Before moving on to the consideration of minimising the vibratory control loads, some insight into the physical mechanisms used by the ATEs to reduce the vibration will be given. Much of the literature regarding the reduction of vibration using TEFs considers blades which are relatively soft in torsion. This is not true of the BERP III main rotor blade being considered in this case which is relatively stiff in torsion, with a natural frequency greater than 7/rev. The mechanisms for the reduction in vibration can therefore be expected to differ from the torsion dominated responses seen in much of the literature. This section therefore contains an investigation into the mechanisms used by the ATEs and serves to justify some of the statements made in the earlier section regarding the choice of location for the ATEs.

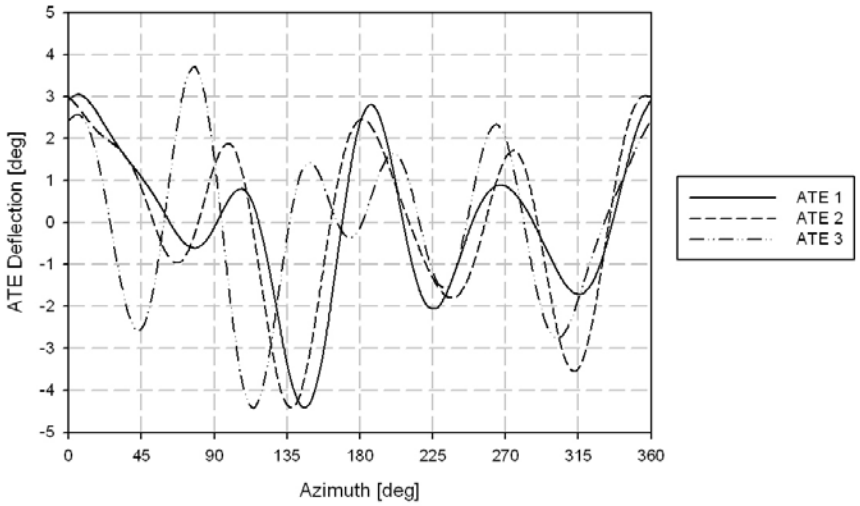

Figure 5.27: Active Trailing Edge deflection schedules for vibration reduction at an advance ratio of 0.15, C_T/σ =0.17.

Firstly, consider the deflection schedule applied to each ATE as shown in Figure 5.27. The deflections applied to each ATE are clearly different, particularly for the most outboard ATE. The use of different schedules by the optimiser would clearly suggest that this is advantageous and justifies the use of a number of smaller ATEs as opposed to one large region.

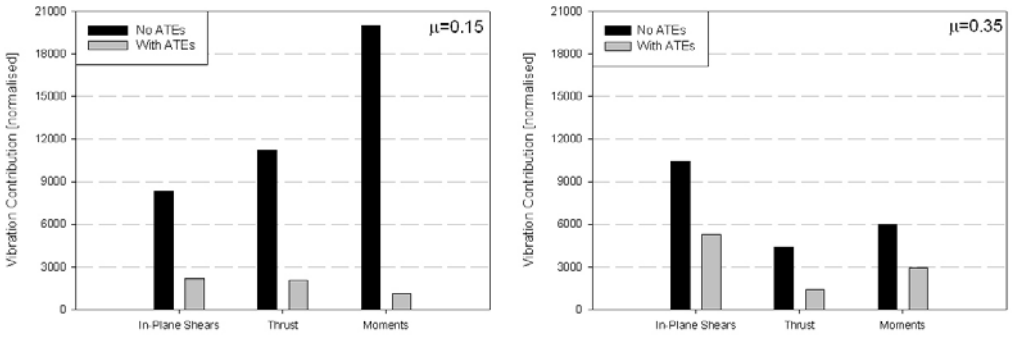

Figure 5.28: Contribution of Hub Loads to Vibration Index.

Now consider which hub loads contribute to the vibration, as shown in Figure 5.28. At low speed, the vibration is predominantly due to the out-of-plane hub loads, i.e. the thrust and the rolling and pitching moments, whereas at high speed the out-of-plane loads are much reduced so that the in-plane, longitudinal and lateral, shears are more significant. The reduction of the vibratory thrust is successful at both low and high speeds but the control of the in-plane shears and the out-of-plane moments is reduced at high speed.

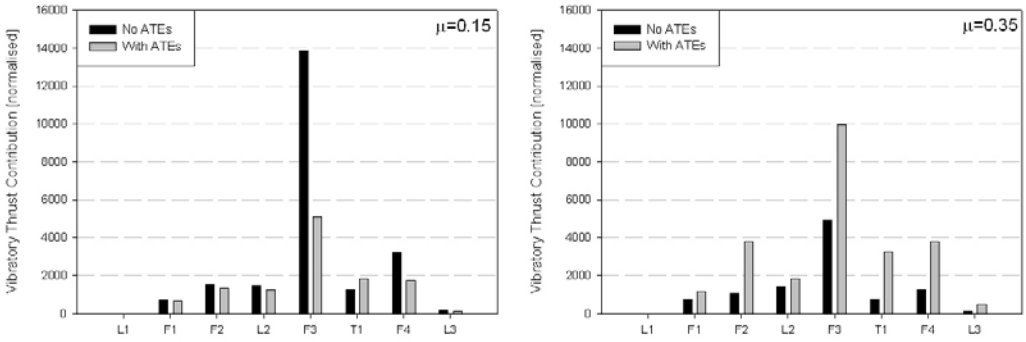

Figure 5.29: Magnitudes of Modal Contributions to Vibratory Thrust.

Consider now the reduction of the out-of-plane loads, taking the vibratory thrust as an example. Figure 5.29 shows that at low speed, the benchmark case is dominated by the magnitude of the 3rd flap mode and the active control devices have considerably reduced this component. At high speed however, all the modal contributions of the benchmark case are of a level more comparable to the controlled loads at low speed and there is therefore no one dominant modal component for the control to focus on. Instead, many of the modal contributions are increased by the active control, suggesting that the mechanism for reduction is based on phasing.

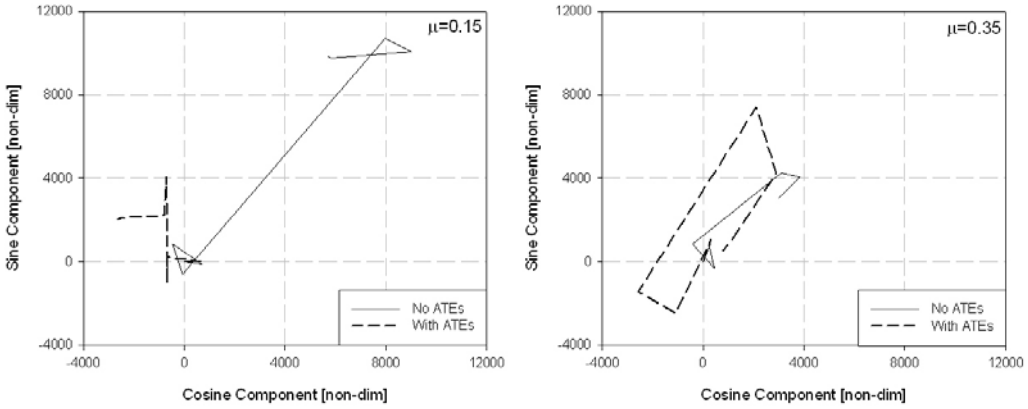

Figure 5.30: Argand Diagrams of Modal Contributions to Vibratory Thrust.

To confirm this hypothesis, Figure 5.30 presents Argand diagrams of the modal contributions to the vibratory thrust. At low speed the reduction in the 3rd flap component is clear to see whereas at the higher speed the cancellation of the various components is in evidence. It is therefore suggested that if the vibration is due to a large component from one or more modes then the active system will reduce that component, however if all modal components are relatively small then the optimiser may work more efficiently by phasing those contributions. It is in this situation, where many of the modal responses are increased, that the impact on blade and control loads may be undesirable. However, common to both flight speeds is the fact that the vibratory thrust has been reduced primarily through an interaction with the flapping modes, in particular the 3rd flap mode, which justifies the positioning of the ATEs with respect to the nodes of this mode.

The mechanism for the reduction of the in-plane shears is less intuitively apparent and the complexity of such a mechanism will be demonstrated here. Take the advance ratio case of 0.15 as an example for which Figure 5.28 shows that the in-plane shears are successfully reduced. The 5/rev fixed-frame in-plane shears are composed of the rotating-frame in-plane loads, i.e. the radial and lag shears, at 4/rev and 6/rev. The magnitudes of these shears are shown in Figure 5.31 which clearly reveals that all the contributing rotating-frame loads are significantly reduced. The reduction of the largest load, i.e. the 6/rev lag shear, will be analysed further.

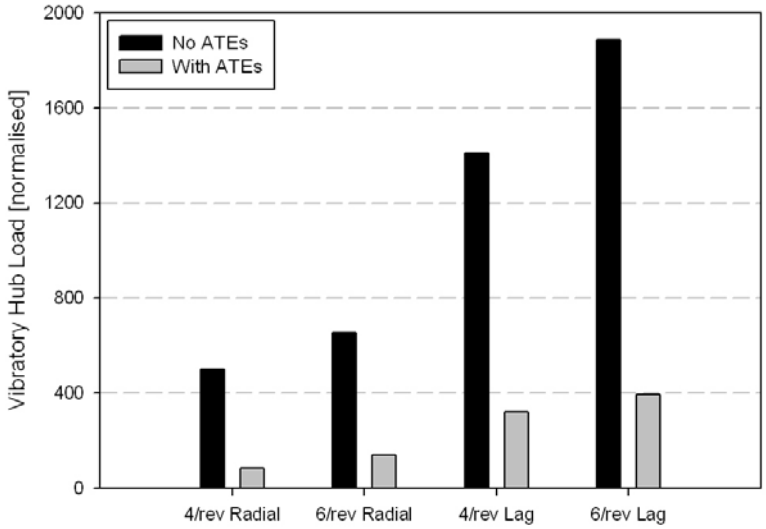

Figure 5.31: Magnitudes of rotating-frame hub shears with and without ATEs, μ=0.15.

The actuation of the trailing edge causes forcing predominantly in terms of lift and pitching moment with the drag effects being much less significant. However, the in-plane shears, particularly the lag shears, can be expected to be predominantly influenced by the lag modes. This is confirmed for the example here in Figure 5.32, which reveals that the 6/rev lag shear has flap and torsion mode contributions which are almost insignificant compared to the lag modes. Note that the contribution labelled as "higher" in this plot represents additional load due to the lag damper which, being a discrete load, cannot be adequately represented with only the low order modes and therefore a correction for the higher order modes is added. [Here it is only necessary to appreciate that this contribution is due to the lag damper, for further information on how it is calculated refer to Hansford (1986).] The reduction due to the ATEs is therefore predominantly due to the 2nd lag mode and the damper force with a smaller contribution due to the 3rd lag mode. So how does the trailing edge actuation affect the response of the lag modes to achieve this result?

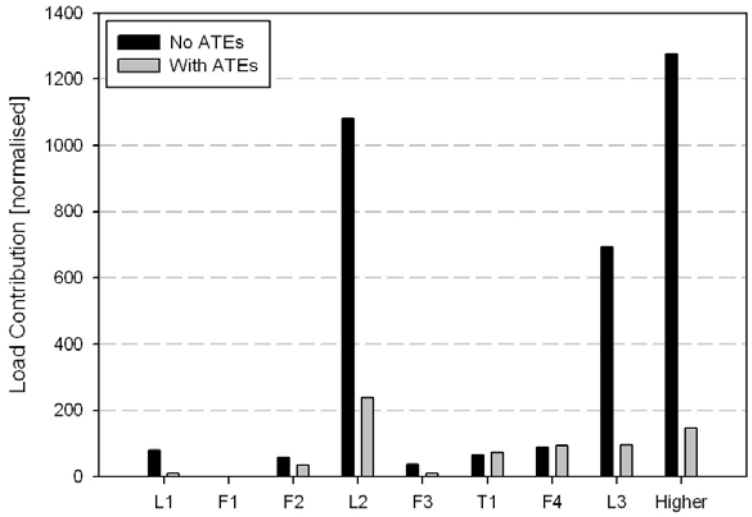

Figure 5.32: Magnitudes of modal contributions to 6/rev lag shear, μ=0.15.

To answer this, the 6/rev sources of modal forcing of the 2nd lag mode, with and without the ATEs will be considered. The magnitudes of the main sources of forcing are displayed in Figure 5.33. It is quite clear that the dominant sources are the lift forcing and the lag damper forcing, with the sizeable lift contribution being due to the level of flap-lag coupling present in the BERP III blade. Also clear is that the ATEs have successfully reduced the contribution of both of these sources of forcing, particularly that due to the lag damper.

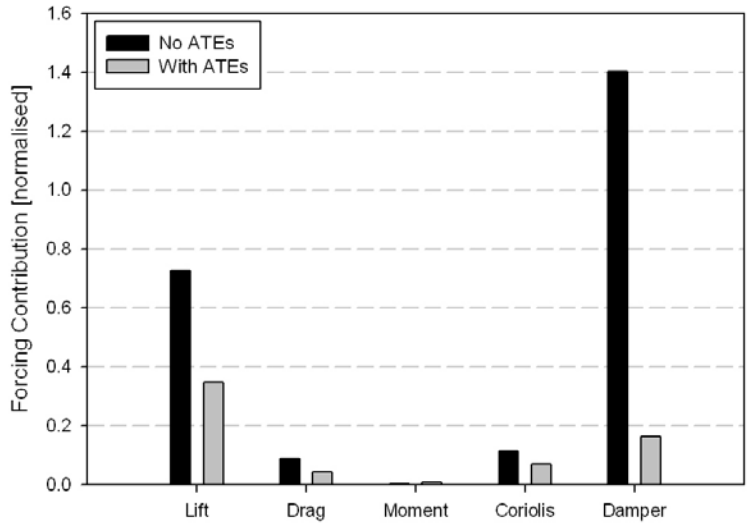

Figure 5.33: Major Contributions to the modal forcing of the 2nd Lag Mode at 6/rev.

Continuing further, the source of the large damper load at 6/rev should be investigated. This load is directly related to the 6/rev component of the damper rod velocity which may in turn be decomposed into the modal contributions. These contributions are displayed

for the current example in Figure 5.34, which reveals that the lag damper velocity is dominated by the 2nd lag mode.

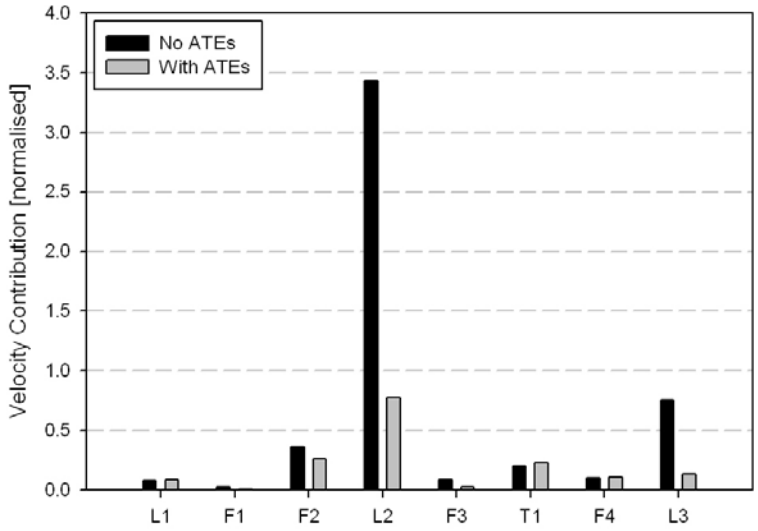

Figure 5.34: Magnitudes of modal contributions to 6/rev lag damper velocity, μ=0.15.

The response of the 2nd lag mode at 6/rev is then highly coupled with the lag damper response. Furthermore, it was shown that the 6/rev lag shear, which gives a large contribution to the fixed-frame in-plane hub loads, is dominated by the second lag mode and the effect of the lag damper force on the higher modes. The reduction of the 6/rev radial shear is therefore due to a reduction of the coupled 2nd lag mode-lag damper contributions. The ATEs cannot directly influence the lag damper force but they were shown to influence the 2nd lag mode through direct lift modal forcing. Therefore, consideration of the flapwise deflection shape of the 2nd lag mode in the location of the ATEs is justified by its influence over the in-plane shears.

In summary, the analysis presented in this section suggests that both the out-of-plane and in-plane loads may be influenced by the predominantly out-of-plane aerodynamic forcing of the flap and lag modes nearest to the frequency of interest. Because of this the location of the ATEs with regard to the flapwise deflection shapes of the 2nd flap and lag modes and the 3rd flap mode is justified.

5.5.5 Reduction of Vibratory Control Loads

So far it has been shown that, with careful placement, the ATEs are capable of considerable reductions in the vibratory hub loads of a stiff-in-torsion blade using modest deflections. The effect on the control loads was, however, disregarded and the results, as

shown in Figure 5.26, displayed an increase in the vibratory control loads across the speed range. The concentration of the optimisation on using lift modal forcing to configure the modal responses for reduction of the hub loads has neglected the influence of the corresponding pitching moment on the control loads, which have, as a result, been increased. As discussed earlier, this could result in reduced fatigue life of major components of the control system. In addition, the fact that the vibratory control loads have been increased also raises the possibility that the harmonics of rotating-frame blade loads not contributing significantly to the fixed-frame vibration may also have been increased. This could also, therefore, be detrimental to the fatigue life of the blade itself.

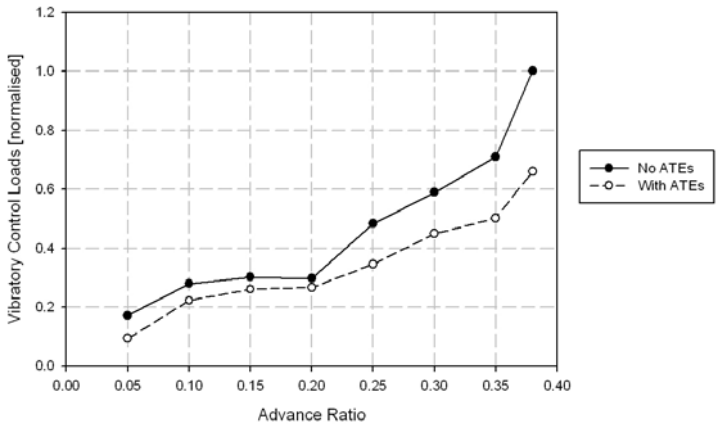

Figure 5.35: Vibratory control Load reduction using Active Trailing Edges, C_T/s_r=0.17.

An investigation into the reduction of the control loads will therefore now be presented. The optimiser has first been used to put full weighting onto the vibratory control loads throughout the speed range, i.e. WC=1, whilst the effect on hub vibration is neglected. The resulting vibratory control loads are plotted in Figure 5.35. The reduction can be observed over the whole advance ratio range, but is particularly apparent at high speed.

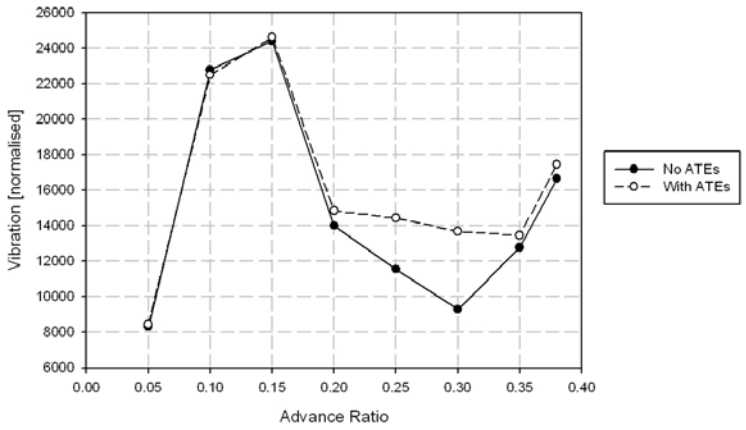

Figure 5.36: Effect on vibration due to control load reduction, C_T/s_r =0.17.

The effect on vibration due to the reduction of the control loads is shown in Figure 5.36. Throughout the advance ratio range the ATEs are having an adverse effect on the vibration. At the lower advance ratios, however, the reduction in vibratory control loads is not required as the levels are significantly lower than those found at high speed. Clearly then the ATEs should continue to be used for vibration reduction up until some critical value of vibratory control loads is obtained, following which the algorithm should automatically change to vibratory control load reduction.

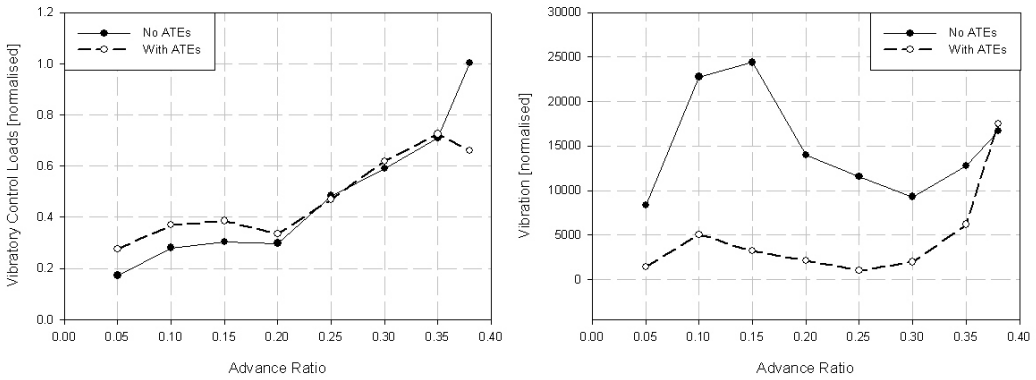

Figure 5.37: Vibratory control load (left) and hub vibration (right) using Active Trailing Edges with mixed control load and vibration optimisation, C_T/s_r =0.17.

This objective is obtained by using the weighting calculation suggested in equation 5.37. The vibratory control loads and hub vibration resulting from using this method are shown in Figure 5.37. Up to an advance ratio of around 0.35 the ATEs are being used to minimise the vibration at a small cost to the vibratory control loads. Once the critical value of vibratory control load is reached the emphasis switches to the control loads, which are successfully reduced at a small cost in vibration.

5.5.6 Analysis of Control Load Reduction Mechanisms

This section presents an analysis into how the ATE reduces the vibratory control loads, as was demonstrated in the previous section. A single flight case, at the highest advance ratio of 0.38, will be considered with the benchmark case being compared to that using the ATEs optimised with the weighting fully on the vibratory control loads.

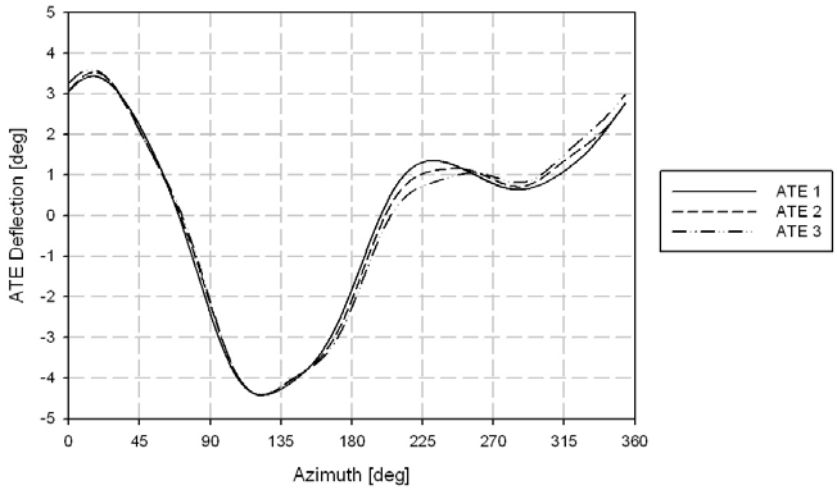

Figure 5.38: Active Trailing Edge deflection schedule for vibratory control load reduction at an advance ratio of 0.38, C_T/s_r =0.17.

The azimuth variation of the optimum ATE deflection schedule for vibratory control load reduction is shown in Figure 5.38. Note firstly that the algorithm has successfully limited the deflection to the maximum of 4.42 degrees and that this maximum allowed deflection is being used. Unlike for vibration reduction, the traces for all three ATE regions are very similar such that they are effectively acting like a single large ATE region, this would perhaps justify locating the ATEs at adjacent radial locations. The main feature that should be noted of the schedule itself is the large upward deflection of all three ATEs on the advancing side; the effect of this will become clear below.

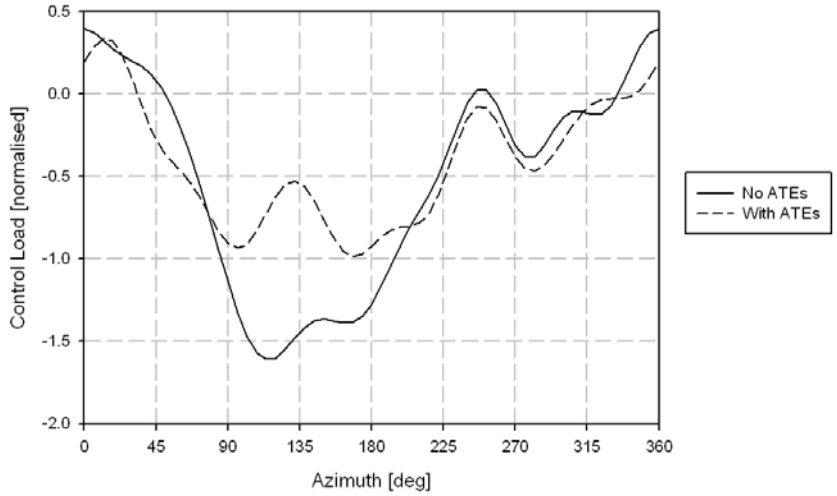

Figure 5.39: Azimuth variation of control load at an advance ratio of 0.38, C_T/s_r=0.17.

The resulting variation of the control load around the azimuth is shown against the baseline case in Figure 5.39. For this lightly loaded, high speed, case the control load is large on the advancing side as the advancing blade limit is approached (as opposed to a

higher thrust loading case which would be dominated by retreating blade stall). It is also clear that the upward deflection of the ATEs on the advancing side has resulted in a considerable reduction of the control load.

The radial distribution of the aerodynamic pitching moment at an azimuth of 102 degrees is shown in Figure 5.40 (note that the pitching moment coefficient has been multiplied by the square of the Mach number to represent the effects due to the changing dynamic head). For the baseline blade, the pitching moment outboard of approximately 0.68 is largely negative whilst inboard regions display a positive pitching moment. This is due to the aerodynamic design of the BERP III blade which uses a high lift, cambered, aerofoil to provide improved performance over the radial segment with the largest lift contribution, whilst further inboard an aerofoil designed for a nose-up moment (referred to as a reflex section) is used to balance the pitching moment created by the high-lift section [see Harrison et. al (2008)].

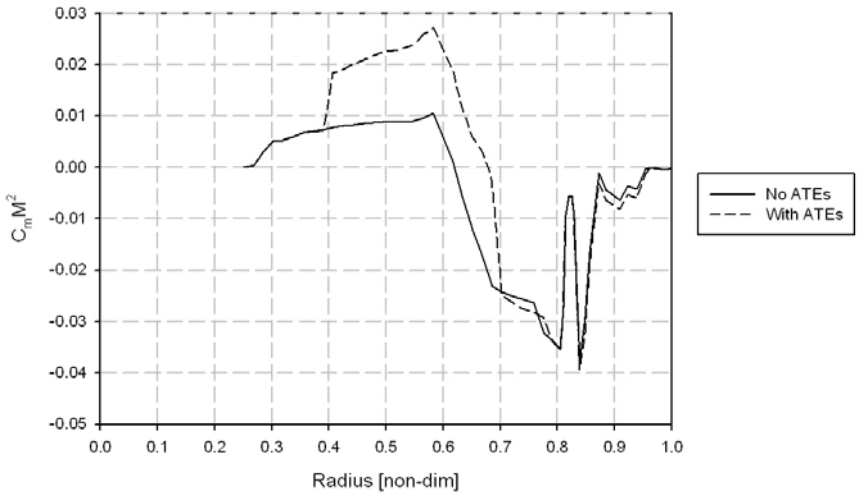

Figure 5.40: Aerodynamic pitching moment at 102degrees azimuth for an advance ratio of 0.38, C_T/s_r =0.17.

Figure 5.40 reveals that the upward deflection of the ATEs on the advancing side has complemented the function of the reflex section by further countering the large nose-down pitching moments creating by the high-lift section at the high Mach numbers on the advancing side, thus reducing the magnitude of the control load experienced. Clearly the design of the reflex section in the BERP III blade was required to be a compromise between the pitching moments on the advancing side and the lift performance on the retreating side. Using the ATEs to perform this function means that less of a compromise is required as the camber may be optimised according to azimuth and flight condition. This will be investigated further in the following section.

5.5.7 Optimal use of ATE for Performance and Vibration

Rather than using the ATEs to reduce the control loads, as was shown in the preceding section, the existing (and therefore acceptable) maximum control loads could be maintained at high speed by using the ATE to return the aerofoil profile to the passive design whilst a constant offset neutral position could be used at lower flight speeds, where control loads are less of a concern. Such an offset effectively means that the datum aerofoil has greater camber and an improved lift-drag ratio, as shown in Figure 5.41. The vibration reduction capability of the ATEs is largely unaffected over most of the flight envelope as they may still be deflected at higher harmonics about this mean offset using the same peak-to-peak deflection as before. When high dash speeds are required the ATE can return the aerofoil to a low pitching moment configuration on the advancing side to keep the control loads within constraints whilst the presence of the offset also means that the maximum downward deflection of the ATEs is increased. The performance advantage to be gained from an increased downward deflection capability will be briefly investigated here in terms of both hover performance and retreating blade stall delay.

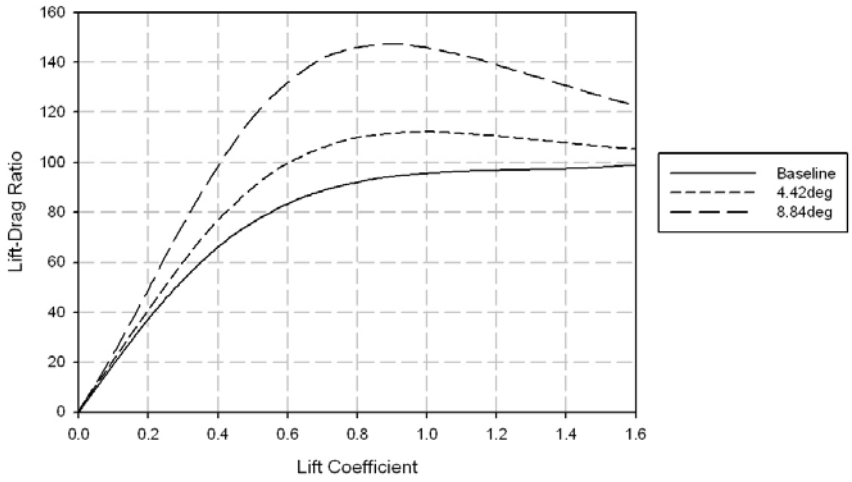

Figure 5.41: Improvement of lift-drag ratio with ATE deflection.

Consider first the effect on hover performance due to downward deflections of the ATEs. If the ATEs are located sufficiently far inboard then their deflection can increase the lift over the inboard section of the blade to more evenly distribute the lift and thus reduce the induced power factor. The effectiveness of using Trailing Edge Flaps for this purpose has been studied in detail using CFD by Gagliardi and Barakos (2009); however a simplified theory will be used here to demonstrate the main effects. Annulus theory [see, for example, Newman (1994)] may be used to approximate the effect on induced power due to constant ATE deflections in hover. Adapting the derivation provided in chapter 3 of

Newman (1994), by including a simple linear addition to the lift coefficient due to the ATE, results in a quadratic relation for the radial distribution of the induced velocity coefficient which may be solved using the quadratic formula to give:

$$\lambda_i(\bar{x}) = -\frac{1}{16}s_r C_{l_\alpha} + \frac{1}{2}\sqrt{\left(\frac{s_r C_{l_\alpha}}{8}\right)^2 + \frac{s_r \bar{x}}{2}\left(C_{l_\alpha}\theta + C_{l_\delta}\delta\right)}. \qquad \textbf{5.42}$$

where $\bar{x}$ is the non-dimensional radial location, s_r is the rotor solidity, C_{l_α} is the lift slope due to angle of attack and C_{l_δ} is the assumed linear change in lift coefficient per radian of ATE deflection, δ. Using this distribution of induced velocity, the thrust and induced power may be found [see Newman (1994)] such that the induced power coefficient can be interpolated for a given thrust value. Using this approach, the deflection of the ATEs has been optimised to minimise the induced power for a given thrust coefficient. This has been performed for a range of linear twist values as shown in Figure 5.42. In this study each ATE has been constrained to use deflections only between 0 and 8.84 degrees such that the total deflection range is the same as that assumed for the vibration reduction study presented above.

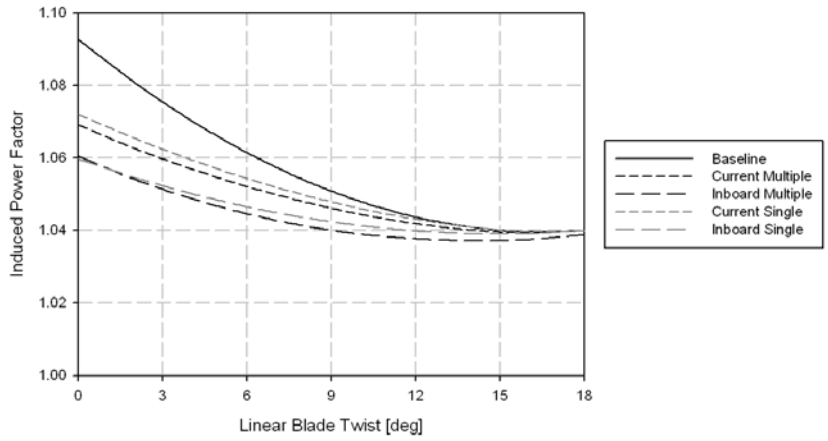

Figure 5.42: Reduction of induced power coefficient due to deflection of ATEs in hover. Results presented for ATEs located as for vibration reduction (40-70% rotor radius, short dash) and 10% further inboard (30-60% rotor radius, long dash). Grey lines are for single ATE, black lines are for 3 independently deflected ATEs.

The results for two ATE distributions are plotted. The results labelled 'Current Multiple' use the distribution from the previous vibration reduction investigation whilst the 'Inboard Multiple' plot represents a distribution where the ATE from 60-70% rotor radius has been replaced with an inboard ATE from 30-40% rotor radius. The lines labelled 'single' use the same total extents but the same deflection is given to all three ATEs.

Although the methodology is clearly very simple, the effectiveness of the ATE deflection is of a similar order to that predicted by Gagliardi and Barakos (2009) who suggested that a blade of 7 degrees twist could be made to behave like blades of 10 and 13 degrees of twist using plain and slotted flaps respectively. Although the inboard ATEs are clearly most effective, those further out still provide a worthwhile benefit which may be improved by optimising the deflection of each ATE independently. Clearly then this suggests that the inclusion of the offset in the ATE deflection range provides sufficient downward deflection capability to enable some improvement in the hover performance of a moderately twisted blade, even if the ATE locations are optimised for vibration reduction. This improvement in hover efficiency could remove the necessity for very high twist which may otherwise provide a significant challenge in the dynamic design of the rotor blades, as was the case for the BERP IV blade where increased twist resulted in the design goal being set to simply maintain the vibration performance of the existing BERP III blade [Harrison et al (2008)].

Consider now the effect of an increased downward deflection at the high speed, high blade loading portion of the flight envelope where the rotor reaches the retreating blade stall boundary. The stall delaying effectiveness of a Trailing Edge Flap using a 1/rev input superimposed onto an offset deflection has been investigated using a rotor performance program by Chan and Brocklehurst (2001). In this case the downward deflection of the ATE provides additional lift which, to maintain trim, must be neutralised by a reduction in angle of attack of the blades. This angle of attack reduction will be provided by a combination of the servo-effect (i.e. the blade twisting due to the pitching moment exerted by the ATE) and changes in the control angles. The relative magnitude of these contributions is dependent upon the torsion stiffness of the blade but in either case the reduction in angle of attack means that the attainment of the blade stall angle is postponed with corresponding delays in the stall induced rise in power and control loads. The approximate magnitude of the effect can again be investigated using a simple blade element approach.

In chapter 5 of Newman (1994) the thrust coefficient is derived from blade element theory as:

$$C_T = \frac{s_r C_{l_\alpha}}{2}\left[\theta_0\left(\frac{2}{3}+\mu_x^2\right)-\mu_x B_1-\mu_{zD}\right]. \qquad \textbf{5.43}$$

In this formula, μ_x is the velocity in the plane of the rotor disc and μ_{zD} is the velocity through the rotor disc (including the downwash), both non-dimensional with respect to the rotor tip speed. Once again it will be assumed that the lift coefficient varies linearly with ATE deflection, but in addition to the constant deflection, a sinusoidal component will also be included such that the total ATE deflection is given by:

$$\delta = \delta_0 - \delta_1 \sin\psi \,. \qquad \textbf{5.44}$$

If an ATE region has a length, L_f and has its centre located at x_c (both non-dimensional with respect to the rotor radius), then using the derivation and assumptions of Newman (1994), the thrust coefficient becomes:

$$C_T = \frac{s_r C_{l_\alpha}}{2}\left[\theta_0\left(\frac{2}{3}+\mu_x^2\right)-\mu_x B_1-\mu_{zD}\right]+\frac{L_f s_r C_{l_\delta}}{2}\left[\delta_0\left(\frac{2}{3}\left(3x_c^2+\tfrac{1}{4}L_f^2\right)+\mu_x^2\right)-2x_c\mu_x\delta_1\right]. \qquad \textbf{5.45}$$

Note that if a full span ATE (L_f=1 and x_c=0.5) with $C_{l_\delta} = C_{l_\alpha}$ is assumed then δ_0 and δ_1 become equivalent to θ_0 and B_1 as is to be expected. Now, if trim is to be maintained then the change in thrust coefficient due to the deflection of the ATE must be zero and therefore the change in θ_0 and B_1 may be written as a function of δ_0 and δ_1:

$$\Delta\theta_0\left(\frac{2}{3}+\mu_x^2\right)-\mu_x\Delta B_1 = -L_f\frac{C_{l_\delta}}{C_{l_\alpha}}\left[\delta_0\left(\frac{2}{3}\left(3x_c^2+\tfrac{1}{4}L_f^2\right)+\mu_x^2\right)-2x_c\mu_x\delta_1\right]. \qquad \textbf{5.46}$$

The same process may also be followed for the mean rolling moment. Following Newman's (1994) derivation and including the ATE lift term results in:

$$\frac{2}{3}\mu_x\Delta\theta_0-\frac{1}{4}\left(1+\frac{3}{2}\mu_x^2\right)\Delta B_1 = -L_f\frac{C_{l_\delta}}{C_{l_\alpha}}\left[\delta_0\frac{2}{3}\mu_x\left(3x_c^2+\tfrac{1}{4}L_f^2\right)-\delta_1\frac{x_c}{2}\left(2x_c^2+\tfrac{1}{2}L_f^2+\tfrac{3}{2}\mu_x^2\right)\right]. \qquad \textbf{5.47}$$

We therefore have two equations involving the two unknowns, $\Delta\theta_0$ and ΔB_1. Solving for these unknowns gives:

$$\Delta\theta_0 = -L_f\frac{C_{l_\delta}}{C_{l_\alpha}}\left[\frac{\delta_0\left(G_0-\mu_x^2\left(\frac{1}{2}\left(5G_0-3\right)-\frac{9}{4}\mu_x^2\right)\right)+\delta_1 3\mu_x x_c\left(G_1-1\right)}{1-\mu_x^2\left(1-\frac{9}{4}\mu_x^2\right)}\right] \qquad \textbf{5.48}$$

$$\Delta B_1 = -L_f \frac{C_{l_\delta}}{C_{l_\alpha}} \left[\frac{\delta_0 4\mu_x^3 (1-G_0) + \delta_1 2x_c \left(G_1 - \mu_x^2 \left(\frac{1}{2}(5-3G_1) - \frac{9}{4}\mu_x^2 \right) \right)}{1-\mu_x^2 \left(1-\frac{9}{4}\mu_x^2\right)} \right]$$

where common geometric parameters have been substituted as:

$$\begin{aligned} G_0 &= 3x_c^2 + \tfrac{1}{4}L_f^2 \\ G_1 &= 2x_c^2 + \tfrac{1}{2}L_f^2 \,. \end{aligned} \qquad \textbf{5.49}$$

Note that if G_0=1 then the steady ATE input results in an advance ratio independent change to collective whilst the longitudinal cyclic is left unaffected. Similarly if G_1=1 then the sinusoidal ATE input requires a change in longitudinal cyclic which is independent of advance ratio whilst the collective is left unaltered. For a given length of ATE then there exists a location where a steady ATE deflection results in a purely collective response and a separate location where a 1/rev input provides a purely cyclic response. These locations are plotted as a function of ATE length in Figure 5.43.

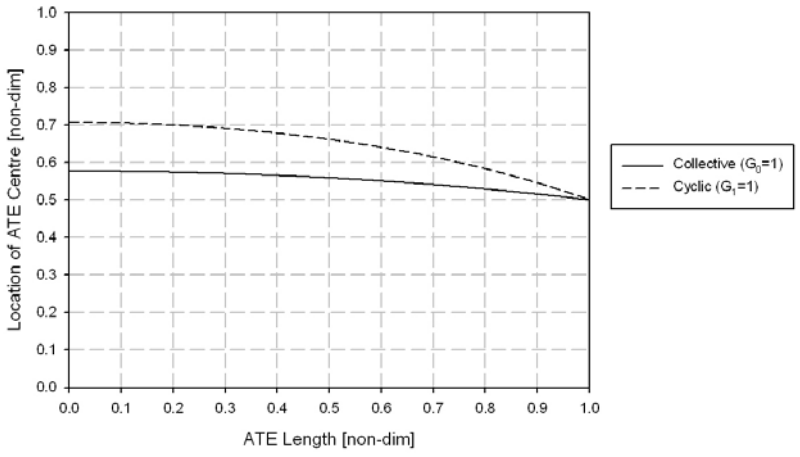

Figure 5.43: ATE location to achieve purely collective or purely cyclic inputs. These locations also achieve independence from the advance ratio.

Recall that the ATEs used in the previous vibration reduction study were located at 40-70% rotor radius, i.e. they were centred at 55% rotor radius. This location is in fact very close to that required for a purely collective input and therefore the inclusion of a constant offset in the deflection of these ATEs, will have minimal effect on the longitudinal cyclic and, therefore, the handling qualities of the aircraft should be maintained.

Perhaps of greater interest is the reduction of the retreating blade pitch angle due to the deflection of the ATE. The pitch change on the retreating side due to the alteration in the control angles is given by $\Delta\theta_0+\Delta B_1$. Summing the equations for these deltas gives a

formula with a term proportional to δ_0 and a term proportional to δ_1. Comparing the two terms then shows the relative effectiveness of the steady and 1/rev input. Figure 5.44 shows, for an ATE of 30% rotor radius, the reduction in the retreating side pitch angle at an advance ratio of 0.35 due to the application of either a constant deflection at the maximum 8.84deg or a 1/rev input varying between 0 and 8.84deg. Clearly the most effective solution is to use an ATE far outboard with a 1/rev input, as suggested by Chan and Brocklehurst (2001). However, if ATEs are located further inboard than 65% radius, such as might be done for vibration reduction and hover performance, then holding the ATE at its maximum deflection is more effective than the 1/rev input. Also, if the ATE is located astride the location where the optimum switches from the 1/rev to the constant input then splitting the total 30% radius ATE into three sections and choosing the best deflection method can further improve the capability in this region. The result of this suggestion is plotted as the line labelled as 'combination'.

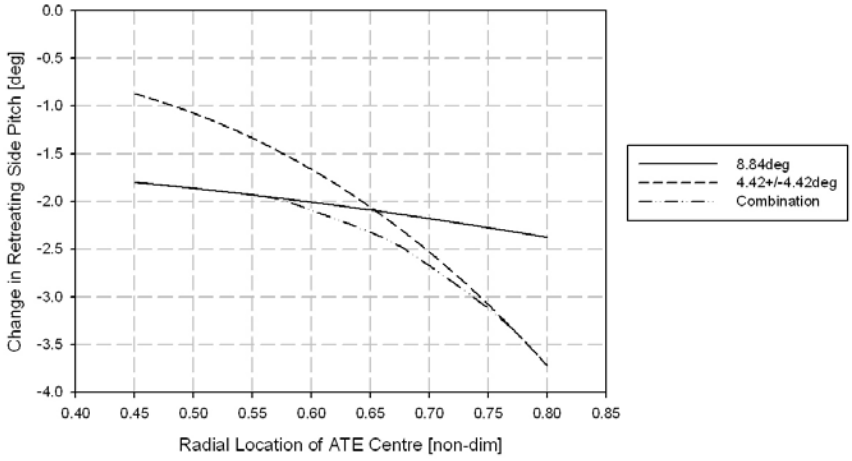

Figure 5.44: Effect on retreating blade pitch angle due to constant or 1/rev ATE inputs for an ATE region of length 30% rotor radius.

Of course the other function of the 1/rev input is to return the advancing side blade to its neutral configuration to avoid large control loads and to minimise the drag rise at higher Mach numbers. These concerns are however mostly associated with outboard ATEs at the very high speed, low loading conditions. In the region of the flight envelope where retreating blade stall is a concern the presence of a constant deflection on an inboard ATE may be more acceptable, particularly if it is delaying the onset of stall. In this case even inboard located ATEs can reduce the retreating blade pitch by 2 degrees and if ATEs further out are included the advantage increases further.

In summary, it has been shown that the retreating blade pitch angle may be reduced considerably using a combination of constant and 1/rev ATE inputs. The addition of the

offset to the 1/rev actuation capability will clearly improve this by making use of the collective, as well as the cyclic, term. The optimum use of collective and cyclic ATE inputs is dependent on the radial location of the ATEs and more benefit is obtained from ATEs further outboard. However, the inclusion of offset means that even if use is made of ATEs located further inboard, which may be more suited to vibration reduction and hover performance, a reduction in the pitch angle of at least 2 degrees is still achievable even with the limited deflection range of the ATEs.

The suggested use of the ATEs to obtain the maximum performance and vibration benefit from the limited deflection range is therefore summarised in Figure 5.45, which assumes the same half-peak-to-peak deflection capability as before.

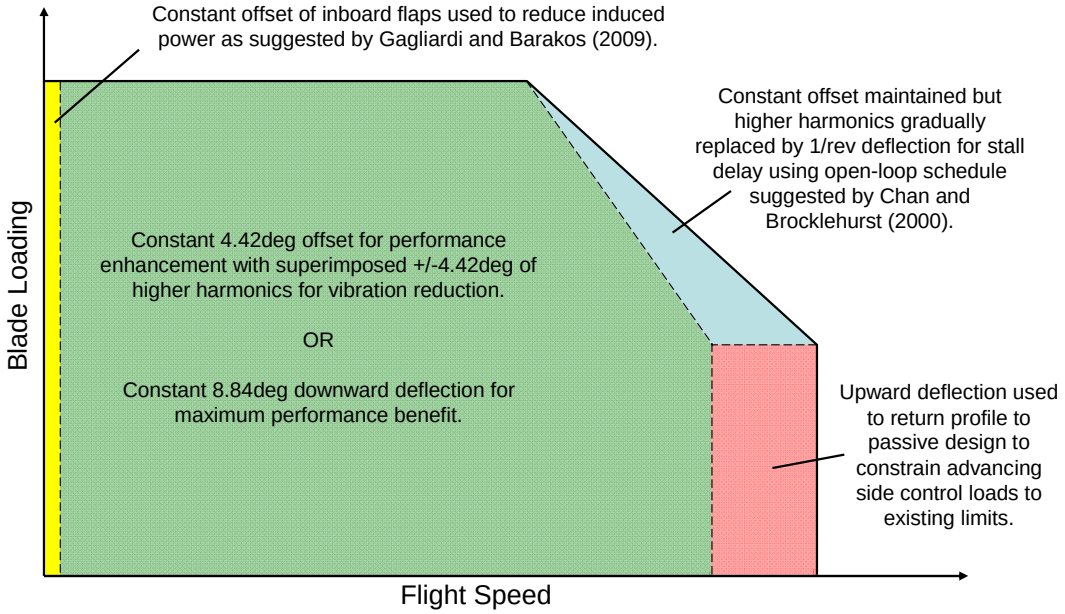

Figure 5.45: Suggested ATE deflections in various flight envelope regions to maximise performance improvement whilst also reducing vibration and constraining advancing side control loads.

The inclusion of the offset therefore acts primarily as an enabler for the performance enhancement algorithms at both the high-speed and low-speed extremes of the flight envelope which may otherwise not be possible within the limited deflection capability of the ATE. Operating the ATE at higher harmonics about this offset then maintains the vibration reduction capability throughout the remainder of the flight envelope.

5.6 Overall Utility of Active Trailing Edges

The concept of the Active Trailing Edge is to provide the advantages of the flight-proven Trailing Edge Flap system whilst improving its reliability and reducing the drag penalty.

This is done by making the ATE an integral part of the trailing edge structure to provide a smooth aerodynamic contour whilst eliminating the exposure of any mechanism to the harsh environments within which rotorcraft often operate.

These aims can be achieved through the use of morphing structures, however with the current level of technology, the achievable deflection ranges may be considerably reduced in comparison to the Trailing Edge Flaps. The development and application of a new aerodynamic model for the ATE to a rotor performance code has however shown that the small differences made by the shape of the trailing edge deflection are sufficient to provide the same levels of vibration reduction associated with the Trailing Edge Flaps with significantly less deflection. Furthermore, this has been demonstrated using the BERP III rotor blade which is stiff in torsion in comparison to the blades used by the Boeing and Eurocopter Deutschland experimental TEF rotor systems thus confirming that the ATE has sufficient authority to directly influence the modes of interest without relying on the servo-effect.

Nevertheless, although this provides evidence to support the use of the ATE for its primary vibration reduction purpose, the use of the TEF for other purposes such as flight envelope expansion is predicted to require much greater deflections. As the adaptability of the TEF to a number of purposes is a clear strength of the technology, the effectiveness of the ATE in this sense has to be considered. Previous studies into the use of the TEF for both hover and forward flight performance improvement have suggested that only downward deflections are required. With this in mind the inclusion of a constant deflection offset, or increased camber, can enable the ATE to achieve downward deflections capable of providing some of the performance benefit, whilst the upward deflection of the ATE can be used to return the aerofoil to a more neutral camber during high-speed flight to minimise the increase in drag and control loads. Furthermore, it has been predicted that the individual optimisation of smaller ATE regions can provide further enhancement over that of a single region as the deflection can be tailored to the specific radial location. In particular this can be used to improve the performance improvement capability of ATEs which may have been located mid-span for vibration reduction whereas inboard and outboard located ATEs are best for hover performance and forward flight performance respectively.

Clearly though, the ATEs cannot achieve the same deflection capability as TEFs and if very large deflections are required for a given purpose, such as the reduction of blade sailing presented in the previous chapter or for primary control in place of the swashplate,

then a solution using TEFs with discrete hinges should be sought although this will come with the disadvantages of increased drag and reduced reliability in the harshest environments. However, if the largest deflections are not required then the ATE is predicted to have sufficient authority to enable its use for the primary purpose of vibration reduction and through careful tailoring of the pre-deflection blade geometry and intelligent choice of radial locations they can also provide worthwhile improvements in hover and high-speed performance along with reduced drag (in comparison to the TEF) at intermediate flight speeds and the potential for improved reliability in harsh environments.

Chapter 6 Concluding Remarks and Future Outlook

The fundamental challenge for the rotorcraft designer is to deliver the best compromise between the requirements for forward and axial flight. The installation of active technologies into the rotor blades promises to remove some of the compromise by adapting the rotor to the specific conditions associated with the portion of the flight envelope in which it resides and to the varying inflow experienced by the blades as they rotate. Furthermore, active devices offer the opportunity to control the blade at higher harmonics of the rotor rotation frequency than is currently done with the conventional swashplate control.

All of the technologies studied in detail in this dissertation can be applied to enhance the high-speed performance of the main rotor system. The predictions presented herein (and in the literature in the case of the Trailing Edge Flap) show that such benefits are relatively small in comparison to those which may be realised through more significant changes to configuration such as the tilt-rotor or by using thrust and/or lift compounding. The application of Air Jet Vortex Generators (AJVGs) to a helicopter rotor can only ever be intended to delay retreating blade stall. It has been shown in Chapter 3 that the AJVGs can successfully perform this function, improving even the performance of an advanced technology baseline, but this high-speed benefit is limited to a very small region of the flight envelope such that the operational gain is minimal. In particular, the lack of influence of the AJVGs over un-stalled conditions means that they cannot have any influence on the all-important range and endurance capability at all but the very highest blade loading.

The sole benefit provided by the AJVGs is therefore in the high-speed dash performance of the aircraft. To provide this relatively small benefit, the AJVGs must be installed near the leading edge of the blade, thus considerably complicating the manufacturing and structural design of the blade which generally has its main load path provided by a leading edge D-spar or C-spar. This fact would also mean that access to the AJVGs for servicing may require access to the spar cavity which will further complicate the structural design of the blade. The jets must be supplied from a source of high-pressure air which would not be readily available and would thus lead to a complication of the rotor hub to supply the air from the fixed-frame or the installation of pumps in the rotating-frame which will clearly come with a considerable mass penalty. Furthermore, the orifices of the jets themselves, being near the leading edge, may be susceptible to icing or sand and dust injection thus bringing the reliability of such a system into question.

Even ignoring all these additional potential problems, given the limited operational benefit offered by the AJVG system, it is the author's opinion that it will never be installed in an operational rotor blade. The installation and maintenance cost of the valves alone is unlikely to be justified by the small operational gain, especially when competing technologies are considered.

The Trailing Edge Flap (TEF) is one such competing technology which has also been predicted to provide a small expansion of the high-speed portion of the flight envelope. Like the AJVGs, the improvement in performance is small in comparison to the cost and complexity of the system and the TEF is unlikely to be installed on a rotor for performance benefits alone. However, unlike the AJVGs, Trailing Edge Flaps are adaptable to many applications; indeed it is their application to secondary, or higher harmonic, control of vibration and noise which has seen most emphasis in the literature.

There are, however, competing technologies which may provide similar benefits. Vibration reduction has been controlled in the fixed-frame by active systems, such as the Active Control of Structural Response (ACSR) system of the EH101, for many years and such fuselage –based methods might be preferred to a rotor-based system simply on the basis of reduced risk. Similarly, noise reduction might be achieved by enabling a variable, or dual, rotor speed or through further optimisation of the passive design. Although TEFs interfere less with the structure of a typical rotor blade than a leading edge device, the incorporation of the structure to support the flap will still bring significant complications and compromises to the design of the blade. The structure must also enable the installation and servicing or replacing of the actuator and the supply of precise control signals to the rotating-frame and along the length of the blade also brings considerable complication in comparison to active systems located in the fixed-frame. Such systems will therefore come with a reasonable cost and maintenance burden.

With such complications, if TEFs are to be employed then maximum use must be made of their multi-function capability and the investigation into any additional applications of the Trailing Edge Flap is considered to be vital by the author as it is the combination of the numerous applications which make it a competitive proposition in comparison to other vibration and noise reduction technologies. In chapter 4 of this dissertation it was predicted that TEFs could provide an expansion to the Ship Helicopter Operational Limit (SHOL) through the control of blade sailing. The investigation showed that whilst very large deflections of large flaps were required for the complete control of blade sailing in the final few rotations of the rotor, much smaller TEF deflections could still provide some

level of control which could mean the difference between sustaining and avoiding damage. Such a capability, in combination with the vibration and noise reduction applications, could lead to the selection of the TEF over a fuselage-based vibration solution which is likely to serve only a single purpose.

Two criticisms of the TEF however arise due to the use of discrete hinges which are generally used as they allow the deflection capability to be maximised and the structure to be simplified. However, the use of such hinges means that the aerodynamic contour of the blade is interrupted, thus leading to a drag penalty. In addition, their exposure to the environment which may include sand, dust or ice gives rise to the risk of reduced reliability and an increased maintenance burden when operating in the harshest environments. The elimination of the hinges by the Active Trailing Edge (ATE) concept therefore promises to reduce the power penalty associated with TEFs whilst also improving the reliability. This, however, might be done at the expense of some of the deflection capability.

The investigation into ATEs in Chapter 5 predicted that, when the subtle changes to the aerodynamic coefficients are considered, the ATE can provide a similar level of vibration reduction to that proven by flight test for the TEF, even with a limited deflection capability. Furthermore, by careful selection of the location of the ATEs and the camber of the baseline aerofoils, the same limited deflection range could also provide worthwhile performance benefits in both the high-speed and hover flight regimes. Clearly, however, if much larger deflections are required, for example, for primary flight control or for the complete control of blade sailing, then the use of the ATE with the current technology may not be suitable. The choice between the TEF and ATE should therefore be governed by the deflection requirement of the primary purpose. If the primary objective is higher harmonic control for vibration reduction with some secondary envelope expansion and power reduction benefits, then the results of Chapter 5 suggest that the deflection capability of the ATE is perfectly adequate and should be selected over the TEF to obtain the benefits of reduced drag and increased reliability, on the other hand if much larger deflections are a requirement then these can only be met by the TEF.

Looking forward, given the author's conclusions regarding the usefulness of AJVGs, there would appear to be little that can be recommended in terms of future work, at least in the rotorcraft context. However, the conclusions have been based on the results from an aerodynamic model for which data was only available for a very limited Mach number. Further investigations using a combination of Computational Fluid Dynamics

and experimental tests could provide significantly more input to the new aerodynamic model which may be used to predict the effects due to AJVGs over a greater azimuth section. Indeed the literature has shown examples of AJVGs being used to good effect at high, as well as low, Mach numbers and their use all around the rotor disc could well increase their effectiveness. However, it should be recalled that the model did not take account of the so-called yawed-flow effect, whereby the blade experiences inflow in the radial direction to varying degrees as it passes around the azimuth. The effect of wing sweep has been shown in the literature to alter the optimum configuration for the AJVGs and therefore the varying yawed-flow effect on a helicopter rotor may reduce their effectiveness away from 90 and 270 degrees azimuth. Therefore if the AJVGs are to be considered for use around the entire azimuth then an investigation into the effect of the rotor rotation should be performed if their impact is to be correctly assessed.

The research suggested above may well lead to the prediction of a greater effectiveness of the AJVGs in the enhancement of the high-speed flight envelope. However, the fact remains that this is all they will ever do for the rotorcraft. AJVGs do not improve the attached-flow aerodynamics of the blade and therefore do not improve on the all-important payload-range characteristic. Neither can they be applied to the higher harmonic control of the blade response. Therefore, regardless of whether future research shows the assumptions made in the current study are overly conservative in the prediction of high-speed flight enhancement, the underlying flaws of the technology in the application to rotorcraft, and therefore the conclusions herein, remain the same. Any future work on AJVGs in the rotorcraft context is therefore expected to provide further confirmation of these conclusions.

The future of the Trailing Edge Flap appears to be more promising but still lies in the justification of its application to a production rotor and the satisfaction of airworthiness authorities. The justification of its selection over competing technologies might be made based on its multi-function capability. Whilst its vibration and noise reduction credentials have been proven in flight, much can be done to further the research into its additional applications. The results of Chapter 4 are encouraging in this respect and suggest that the TEF can significantly reduce blade sailing but further work on this subject is required if the TEF is to be reliably applied to this problem. In particular future research should consider a much wider range of inflow conditions including gusty and turbulent flow, perhaps generated from CFD, wind tunnel or even full-scale data sets. Investigation could also consider improving on the control philosophy. Although the deflection of the TEF based on the feedback of the blade tip velocity worked well in the case study

presented, under wind conditions displaying a greater time dependency a more sophisticated control approach might be necessary and for the relatively stiff blades of modern rotors, the control algorithm might be based on the feedback of blade loads instead of deflections. The current study was also limited to the flap degree of freedom and whilst this has been justified in the literature for the blade sailing of a passive blade, the large pitching moments generated by a TEF may cause the torsion degree of freedom to have a greater influence, particularly for a blade which is soft in torsion. It is therefore recommended that this effect should be investigated in any future research into this topic. However, proof of the concept can only really be provided through testing. Full-scale tests would clearly be prohibitively dangerous and very costly but a model-scale test might be feasible and should be considered.

If such research can justify the application of the TEF to an operational rotor then it remains to turn the demonstration systems into a viable commercial technology which is of low mass, minimum cost and has the highest possible reliability. The latter in particular is an objective of the Active Trailing Edge. The ATE is, however, a relatively immature technology and much can be done to develop it. Clearly the most significant part of this development is structurally related as a large amount of optimisation will be required to provide the maximum possible deflection whilst also ensuring that it can withstand the significant loads associated with rotor blades in limit conditions. From an aeromechanic viewpoint, the model developed by the author has been validated in the steady state, however further validation should include unsteady cases and a greater Mach number range. Whilst the model has been demonstrated here in terms of predicting vibration reduction and control load benefits, the unsteady capability of the model makes it particularly useful in the study of the stability of an ATE. Whilst the stability of a coupled blade-TEF can be improved by including a mass balance forward of its hinge, Shen and Chopra (2001), this is clearly not feasible for the ATE. The inherent stiffness of the ATE and the lack of a discrete hinge may mean that this is not an issue, however the new model may easily be incorporated into a coupled dynamic analysis which could investigate the stability of the active rotor which must be demonstrated before the system could be certified for flight. The impact of the ATE on the blade dynamic properties should also be investigated. In the current investigation, the deflection of the ATE was assumed to have no effect on the stiffness of the blade even though it is much more of an integral part of its structure than the TEF. In reality, the deflection of the ATE could stiffen the blade in the flapwise direction and conversely the flapwise bending of the blade could stiffen the ATE. This will clearly impact on the effectiveness of the system and consideration should be given to modelling this structural coupling.

In summary, the future for active rotor blades looks promising so long as they can be shown to provide a multi-function capability which cannot possibly be provided by passive or fuselage based solutions. Air Jet Vortex Generators fall short of this requirement as they are only intended to serve a single purpose which has been shown in here to have only a limited operational significance, especially when applied to a modern blade such as the BERP III of the EH101 which has already been highly optimised for good retreating blade performance. Any future research into AJVGs in the rotorcraft context would therefore only be expected to further confirm this conclusion. Trailing Edge Flaps on the other hand can perform a multitude of tasks and all benefits to be gained from these systems, such as the application to blade sailing presented here, should continue to be investigated as they could justify their selection over fuselage-based or passive solutions which, whilst being likely to come with significantly less risk, can only perform a single task. The results presented here show promising reductions in blade sailing due to the TEF but further research into this topic is required to ensure that the concept can be applied to an operational aircraft. Finally it has been shown that even with a restricted deflection capability the Active Trailing Edge is a viable alternative to the Trailing Edge Flap for higher harmonic control and with intelligent design can also deliver worthwhile performance benefits. If the promised improvement in reliability and reduction in drag of the ATE is to be realised much research into its structural design and stability is required, however the latter may be facilitated using the model developed herein.

Chapter 7 Appendix: Calculating the Inflow to a Blade Segment

7.1 Uniform Velocity Field

In order to define the blade inflow velocities, some axes systems will first be defined as shown in Figure 7.1. The fuselage axes and hub axes are parallel to each other but the origin of the fuselage axes is at the centre of mass of the fuselage whilst that of the hub axes is at the hub centreline. The disc axes have the same origin as the hub axes but are rotated to take account of any shaft tilt.

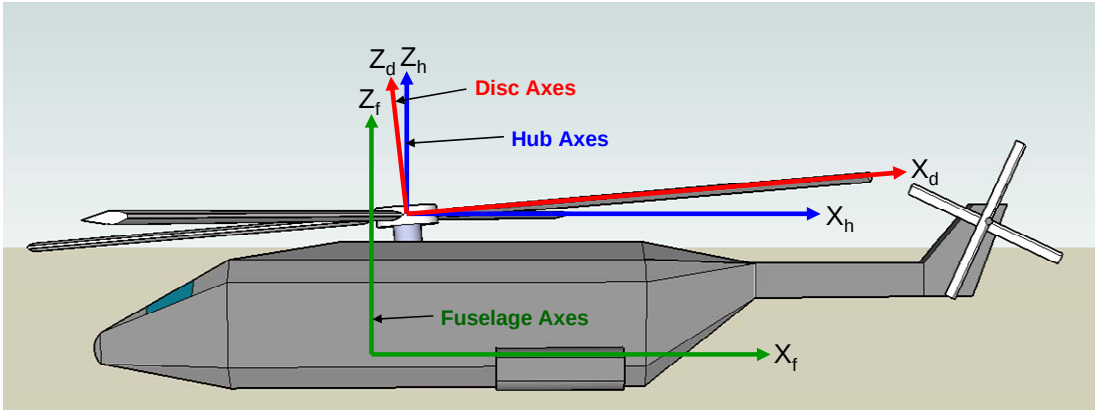

Figure 7.1: Axes systems for the blade sailing program, y-axes are into the page.

Suppose a uniform velocity field is defined in a global axes system (X_v,Y_v,Z_v), which for zero fuselage displacement is equivalent to the fuselage axes system. If the fuselage is allowed to rotate about the X_v and Y_v axes, i.e. if the fuselage has roll and pitch motion but zero yaw motion, then the global axes system may be transformed into the fuselage axes system (X_f,Y_f,Z_f) by a single equivalent rotation, γ_{tilt}, about a line in the (X_v,Y_v) plane, as shown in Figure 7.2. The line about which the rotation is performed is defined by the angle ψ_{tilt} which is dependent upon the relative magnitudes of the rotations about the X_V and Y_V axes.

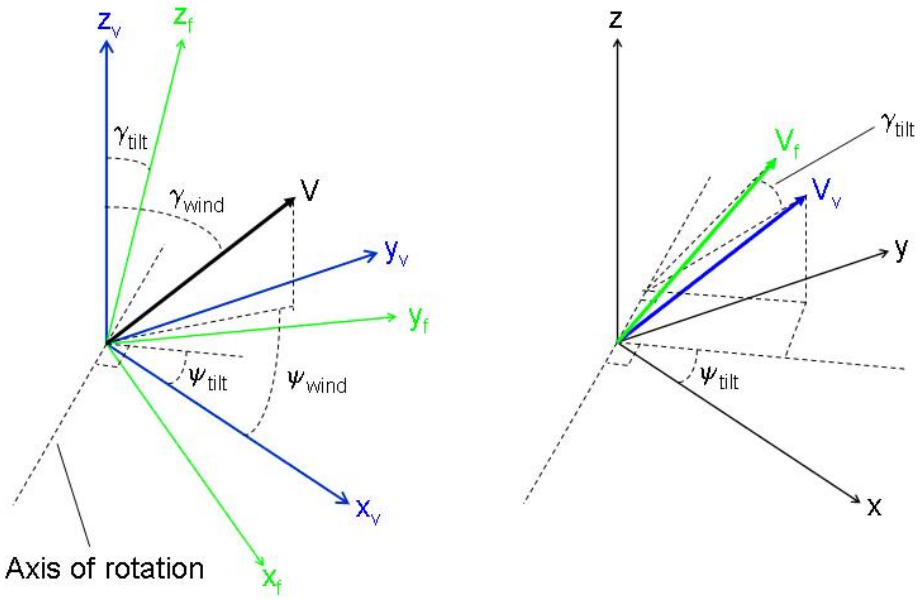

Figure 7.2: Tilting of the fuselage witin a velocity field.

Now suppose that the uniform velocity field is given by the vector $\underline{V}_v$ in the global axes. The velocity vector in the fuselage axes, $\underline{V}_f$, may be obtained by rotating through angle $-\gamma_{tilt}$ about the axis of rotation.

This transformation may be achieved via three rotations about the primary axes as shown in Figure 7.3.

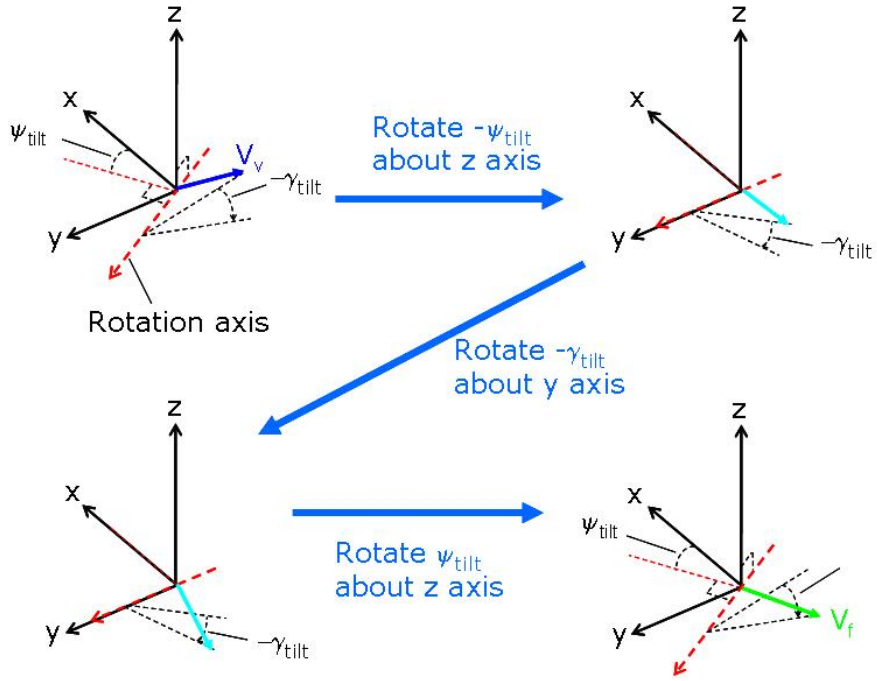

Figure 7.3: Transformation of velocity vector to fuselage coordinates.

If the rotations through an angle θ about the y and z axes, in the sense of a right hand screw, are denoted by $R_y(\theta)$ and $R_z(\theta)$ respectively, then the transformation of the velocity vector to the fuselage axes is given by:

$$\underline{V_f} = \underline{V_v} T_r \left(\psi_{tilt}, -\gamma_{tilt} \right) \tag{7.1}$$

where the rotation transformation matrix is defined by:

$$T_r \left(\theta_1, \theta_2 \right) = R_z \left(-\theta_1 \right) R_y \left(\theta_2 \right) R_z \left(\theta_1 \right). \tag{7.2}$$

For a uniform inflow, no transformation is required from the fuselage axes to the hub axes as the coordinate systems are parallel. The transformation from the fuselage to the disc coordinates however is similar to that from the global to the fuselage coordinates. If the disc is tilted by an angle γ_s about a line perpendicular to ψ_s in the fuselage axes then the velocity field in the disc axes may be written as:

$$\underline{V_d} = \underline{V_f} T_r \left(\psi_s, -\gamma_s \right). \tag{7.3}$$

The transformation from the disc axes to the blade axes is a single rotation about the z-axis, such that the x-axis moves with the blade around the azimuth. Therefore:

$$\underline{V_b} = \underline{V_d} R_z \left(-\psi_b \right). \tag{7.4}$$

Combining equations 7.1, 7.3 and 7.4 gives the overall transformation from the global velocity to the blade velocity as:

$$\underline{V_b} = \underline{V_v} T_r \left(\psi_{tilt}, -\gamma_{tilt} \right) T_r \left(\psi_s, -\gamma_s \right) R_z \left(-\psi_b \right). \tag{7.5}$$

7.2 Non-Uniform Velocity Field

For a distributed non-uniform velocity field, each velocity vector in the global axes, $\underline{V}_v$, also has a position vector, $\underline{P}_v$.

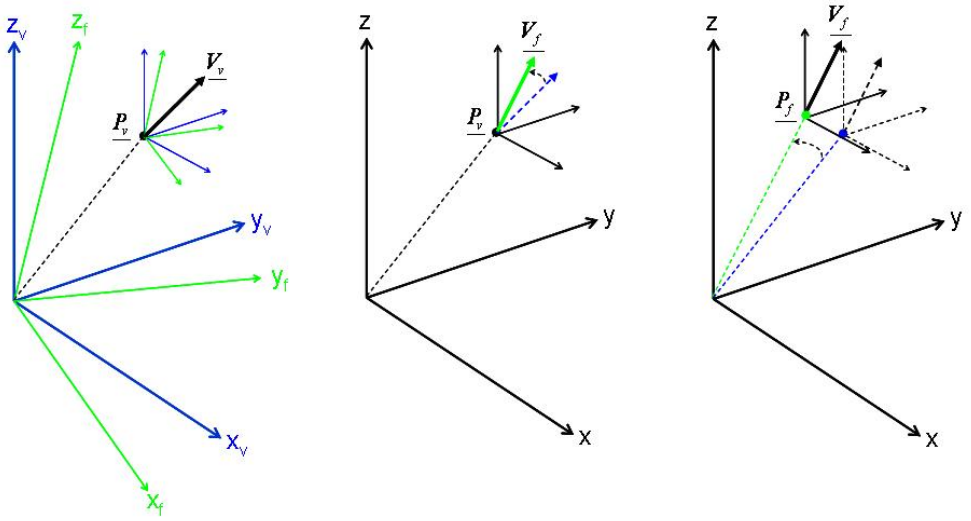

Figure 7.4: Transformation of a velocity vector field.

For each axes transformation, the position vector as well as the velocity vector must be transformed, as shown in Figure 7.4.

The transformation of both the position and velocity vectors is performed in the same manner as for the uniform velocity field in the previous section. Therefore, the velocity vector and the location of each velocity vector are transformed from the global axes to the fuselage axes by:

$$\begin{aligned} \underline{V_f} &= \underline{V_v} T_r \left(\psi_{tilt}, -\gamma_{tilt}\right) \\ \underline{P_f} &= \underline{P_v} T_r \left(\psi_{tilt}, -\gamma_{tilt}\right). \end{aligned} \qquad \textbf{7.6}$$

As the hub coordinate system is parallel to the fuselage system, the velocity vectors in the hub axes are the same as those in the fuselage axes; however the location of the velocity vectors must be translated. Therefore if the hub location in the fuselage coordinates is given by:

$$\underline{P_{f_{hub}}} = \underline{h_f} \qquad \textbf{7.7}$$

then the transformation of the velocity field from the fuselage coordinates to the hub coordinates is given by:

$$\begin{aligned} \underline{V_h} &= \underline{V_f} \\ \underline{P_h} &= \underline{P_f} - \underline{h_f} \,. \end{aligned} \qquad \textbf{7.8}$$

In a similar manner to the global-to-fuselage transformation, the hub coordinate velocity field may then be transformed into disc coordinates by:

$$\begin{aligned} \underline{V_d} &= \underline{V_h} T_r\left(\psi_s, -\gamma_s\right) \\ \underline{P_d} &= \underline{P_h} T_r\left(\psi_s, -\gamma_s\right) \end{aligned} \qquad \textbf{7.9}$$

and the velocity field is further transformed into blade coordinates by:

$$\begin{aligned} \underline{V_b} &= \underline{V_d} R_z\left(-\psi_b\right) \\ \underline{P_b} &= \underline{P_d} R_z\left(-\psi_b\right). \end{aligned} \qquad \textbf{7.10}$$

Combining equations 7.6 to 7.10 gives the overall transformation from global coordinates to blade coordinates as:

$$\begin{aligned} \underline{V_b} &= \underline{V_v} T_r\left(\psi_{tilt}, -\gamma_{tilt}\right) T_r\left(\psi_s, -\gamma_s\right) R_z\left(-\psi_b\right) \\ \underline{P_b} &= \left[\underline{P_v} T_r\left(\psi_{tilt}, -\gamma_{tilt}\right) - \underline{h_f}\right] T_r\left(\psi_s, -\gamma_s\right) R_z\left(-\psi_b\right). \end{aligned} \qquad \textbf{7.11}$$

Therefore, to find the velocity vector at a given point in the blade axes, $\underline{P_b}$, the global flow must be interpolated for the point:

$$\begin{aligned} \underline{P_v} &= \left[\underline{P_b} R_z\left(-\psi_b\right)^{-1} T_r\left(\psi_s, -\gamma_s\right)^{-1} + \underline{h_f}\right] T_r\left(\psi_{tilt}, -\gamma_{tilt}\right)^{-1} \\ \underline{P_v} &= \left[\underline{P_b} R_z\left(\psi_b\right) T_r\left(\psi_s, \gamma_s\right) + \underline{h_f}\right] T_r\left(\psi_{tilt}, \gamma_{tilt}\right). \end{aligned} \qquad \textbf{7.12}$$

Following which the velocity for the point is found using equation 7.11.

7.3 Dynamic Coordinate Systems

If a coordinate system is moving within another coordinate system, through rotation and/or translation, then effective velocities are produced in the direction opposite to the motion. Consider, for example, the fuselage coordinate system moving within the global system at a velocity $\underline{V}_{axes,f}$. As shown in Figure 7.5, this is equivalent to superimposing a uniform velocity of $-\underline{V}_{axes,f}$ onto the velocity field in the global axes.

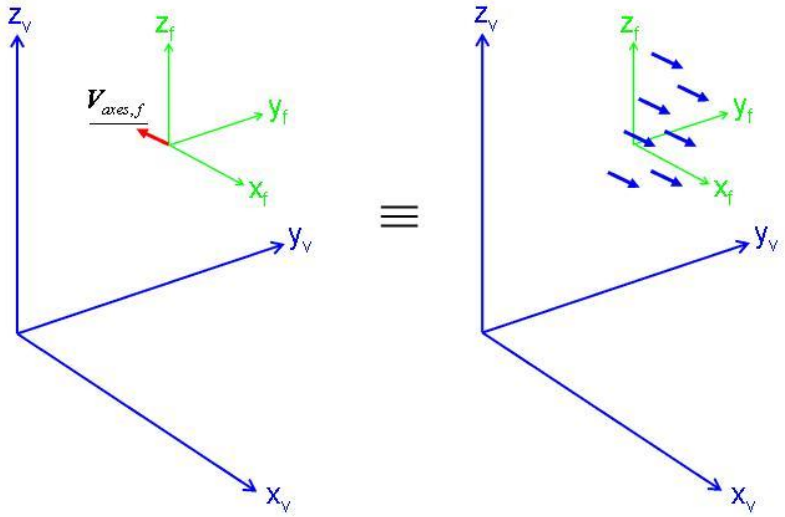

Figure 7.5: Equivalent velocity for a translating axes system.

The velocity in the fuselage axes would then become:

$$\underline{V}_f = \left[\underline{V}_v - \underline{V}_{axes,f}\right] T_r\left(\psi_{tilt}, \gamma_{tilt}\right). \qquad \textbf{7.13}$$

Similarly, if the axes are rotating about a given axis, $\underline{A}_{rot,f}$, as shown in Figure 7.6, then the superimposed velocity in the global axes varies radially from this axis in a direction opposite to the rotation.

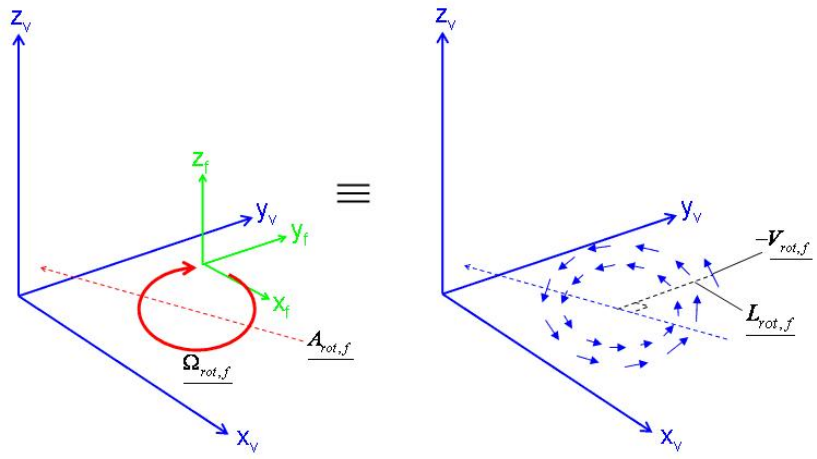

Figure 7.6: Equivalent velocity for a rotating axes system.

If the rotation axis is defined as:

$$\underline{A_{rot,f}} = \underline{A_{1,f}} + \lambda \underline{\hat{A}_{rot,f}} \qquad \textbf{7.14}$$

then for the point, $\underline{P}$, the velocity due to the rotation is:

$$\begin{aligned} \underline{V_{rot,f}} &= \Omega_{rot,f}\left[\underline{\hat{A}_{rot,f}} \times \left(\underline{P} - \underline{A_{2,f}}\right)\right] \\ \underline{A_{2,f}} &= \underline{A_{1,f}} + \lambda_2 \underline{\hat{A}_{rot,f}} \\ \lambda_2 &= \left(\underline{P} - \underline{A_{1,f}}\right) \cdot \underline{\hat{A}_{rot,f}} \,. \end{aligned} \qquad \textbf{7.15}$$

where $\underline{A_{2,f}}$ is the foot of the perpendicular. The velocity at a given point in the fuselage axes then becomes:

$$\underline{V_f} = \left[\underline{V_v} - \underline{V_{rot,f}}\right] T_r\left(\psi_{tilt}, -\gamma_{tilt}\right). \qquad \textbf{7.16}$$

A dynamic translation and rotation may be applied to each system of axes in turn. The rotation of the rotor blade may be accounted for by applying a rotation about the z-axis between the disc axes and the blade axes. However, there are not usually any other dynamic relations between the fuselage and disc axes and the disc and blade axes. Whence, the velocity in the blade axes is given in terms of that in the global axes by:

$$\underline{V_b} = \left\{ \left(\underline{V_v} - \underline{V_{rot,f}} - \underline{V_{axes,f}} \right) T_r\left(\psi_{tilt}, -\gamma_{tilt}\right) T_r\left(\psi_s, -\gamma_s\right) - \underline{V_{rot,b}} \right\} R_z\left(-\psi_b\right). \quad \textbf{7.17}$$

7.4 Angle of Attack at a Blade Segment

Finally, to make use of the inflow, an angle of attack must be generated at each blade segment.

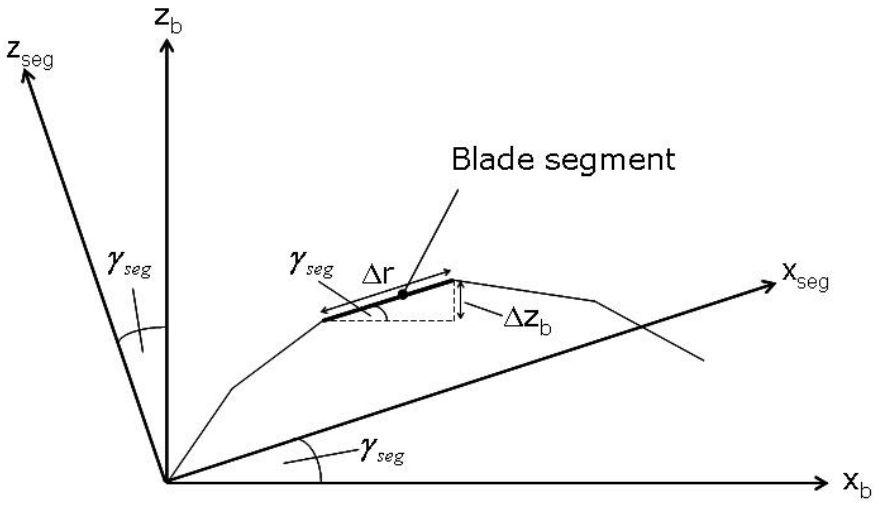

Figure 7.7: Definition of the blade segment axes.

Firstly the flow is transformed into the blade segment axes as shown in Figure 7.7 by rotating around the y-axis by an angle $-\gamma_{seg}$

$$\begin{aligned} \underline{V_{seg}} &= \underline{V_b} R_y\left(-\gamma_{seg}\right) \\ -\gamma_{seg} &= \arcsin\left(\frac{\Delta y}{\Delta r}\right). \end{aligned} \quad \textbf{7.18}$$

The tangential and perpendicular components of velocity are therefore given by:

$$\begin{aligned} U_P &= -V_{seg,z} \\ U_T &= -V_{seg,y}. \end{aligned} \quad \textbf{7.19}$$

Note that at this stage the contribution from the blade flapping velocity must also be added to the perpendicular component. The angle of attack can then be calculated as:

$$\alpha = \theta + \arctan\left(\frac{U_p}{U_T}\right) \qquad \textbf{7.20}$$

where θ is the pitch due to the built-in twist and control angles.

The angle of attack may be fed into an aerodynamic coefficient solver to obtain the aerodynamic forces on the blade segment. These forces however will be in the blade segment coordinates and must be transformed into the blade axes for the dynamic calculations by:

$$\underline{F_b} = \underline{F_{seg}} R_y\left(\gamma_{seg}\right) \qquad \textbf{7.21}$$

where $\underline{F}_b$ and $\underline{F}_{seg}$ are the forces in the blade and segment axes respectively.

7.5 Additional Systems of Axes

If required, additional systems of axes may be defined between the global and fuselage axes. For example the fuselage may undergo motion with respect to a set of deck axes which may in turn undergo motion with respect to the global axes. This may be accounted for simply by adding in additional sets of transformations between each set of axes.

Chapter 8 References

Ahci E., Pfaller R., Structural design, optimization and validation of the integrated active trailing edge for a helicopter rotor blade, Proceedings of the American Helicopter Society 64th Annual Forum, 2008.

Akanni S.D., Henry F.S., Numerical calculations of air-jet vortex generators in turbulent boundary layers, CEAS European forum on High-lift and separation control, Paper 16, 1995.

Altmikus A.R.M., Knutzen B., Trimmed forward flight simulation with CFD featuring elastic rotor blades with and without active control, Proceedings of the American Helicopter Society 63rd Annual Forum, 2007.

Bagai A., Leishman J.G., Rotor Free-Wake Modelling using a Pseudo-Implicit Technique – Including Comparisons with Experimental Data, Journal of the American Helicopter Society, Volume 40, No. 3, 1995.

Bao J., Allen K., Chopra I., Design and test of a mach scale swashplateless rotor using smart trailing-edge flaps, Proceedings of the American Helicopter Society 62nd Annual Forum, 2006.

Bao J., Nagaraj V.T., Chopra I., Bernhard A.P.F., Wind Tunnel Test of Five Sets pf Mach Scale Composite Tailored Rotor with Flap-Bending/Torsion Couplings for Vibration Reduction, Journal of the American Helicopter Society, Volume 53, No. 3, 2008.

Beddoes T.S., A Synthesis of Unsteady Aerodynamic Effects including Stall Hysteresis, Proceedings of the 1st European Rotorcraft Forum, 1975.

Beddoes T.S., A Synthesis of Unsteady Aerodynamic Effects including Stall Hysteresis, Vertica, Volume 1, No. 2, 1976.

Beddoes T.S., A 3-D Separation Model for Arbitrary Planforms, Proceedings of the American Helicopter Society 47th Annual Forum, 1991.

Ben-Zeev O., Chopra I., Advances in the development of an intelligent helicopter rotor employing smart trailing-edge flaps, Smart Materials and Structures, Vol. 5, No. 1, 1996.

Bernhard A.P.F., Chopra I., Trailing edge flap activated by a piezo-induced bending-torsion coupled beam, Journal of the American Helicopter Society, Vol. 44, No. 1, 1999.

Bernhard A.P.F., Wong J., Wind-tunnel evaluation of a sikorsky active rotor controller implemented on the NASA/Army/MIT active twist rotor, Journal of the American Helicopter Society, Volume 50, No. 1, 2005.

Bons J.P., Sondergaard R., Rivir R.B., Turbine separation control using pulsed vortex generator jets, Journal of Turbomachinery, Vol. 123, No. 2, 2001.

Bottasso C.L., Bauchau O.A., Multibody Modelling of Engage and Disengage Operations of Helicopter Rotors, Journal of the American Helicopter Society, Volume 46, No. 4, 2001.

Bridges D.O., Horn J.F., Alpman E., Long L.N., Coupled flight dynamics and CFD analysis of pilot workload in ship airwakes, In proceedings of the AIAA Atmospheric Flight Mechanics Conference, 2007.

Carr L.W., McAlister K.W., McCroskey W.J, Analysis of the Development of Dynamic Stall Based on Oscillating Airfoil Experiments, NASA TN-D-8382, 1977.

Carr L.W., McAllister K.W., The effect of a leading edge slat on the dynamic stall of an oscillating aerofoil, AIAA Paper 1983-2533, Aircraft Design, Systems and Technology Meeting,1983.

Celi R., Stabilisation of helicopter blades with severed pitch links using trailing-edge flaps, Journal of Guidance, Control and Dynamics, Vol. 26, No. 4, 2003.

Centolanza L.R., Smith E.C., Munsky B., Induced-shear piezoelectric actuators for rotor blade trailing edge flaps, Smart Materials and Structures, Vol. 11, No. 1, 2002.

Chan W., Brocklehurst A., Performance enhancement evaluation of an actuated trailing edge flap, The Aeronautical Journal, July 2001.

Chandra R., Chopra I., Actuation of trailing edge flap in a wing model using piezostack device, Collection of Technical Papers - AIAA/ASME/ASCE/AHS/ASC Structures, Structural Dynamics and Materials Conference, 1997.

Charles B.D., Tadghighi H., Hassan A., Higher harmonic actuation of trailing edge flaps for rotor BVI noise control, Proceedings of the American Helicopter Society 52nd Annual Forum, 1996.

Chaudhry Z.A., Wake B.E., Bagai A., Lorber P.F., Collins A.J., Active rotor development for primary and secondary flight control, Proceedings of the American Helicopter Society 65th Annual Forum, Texas, 2009.

Chopra I. Status of application of smart structures technology to rotorcraft systems, Journal of the American Helicopter Society, Vol. 45, No. 4, 2000.

de la Cierva J., Rose D., Wings of Tomorrow: The Story of the Autogiro, Brewer, Warren and Putnam, New York, 1931.

Clement J.W., Brei D., Barrett R., Wind tunnel testing of a high authority airspeed insensitive rotor blade flap, Collection of Technical Papers - AIAA/ASME/ASCE/AHS/ASC Structures, Structural Dynamics and Materials Conference, 1999.

Colucci F., Speedhawk – Phase I, Vertiflite – A Publication of the American Helicopter Society, Volume 53, No. 4, 2007.

Colucci F., Hummingbird hunts for a home, Vertiflite – A Publication of the American Helicopter Society, Volume 54, No. 3, 2008.

Compton D.A, Johnston J.P., Streamwise vortex production by pitched and skewed jets in a turbulent boundary layer, AIAA Journal, Vol. 30, No. 3, 1992.

Copp P., Chopra, I., Continued development of a mach scale swashplateless rotor with integrated trailing edge flaps, Proceedings of the American Helicopter Society 64th Annual Forum, 2008.

Coton F., Final report on smart rotor activities at the University of Glasgow, Rotor Aeromechanics DARP Report D1.26, 2008.

Cribbs R., Friedmann P.P., Actuator saturation and its influence on vibration reduction by actively controlled flaps, Proceedings of the 42nd AIAA/ASME/ASCE/AHS/ASC Structures, Structural Dynamics and Materials Conference, 2001.

Crozier P., Leconte P., Delrieux Y., Gimonet B., Le Pape A., Des Rochettes H.M., Wind-tunnel tests of a helicopter rotor with active flaps, Proceedings of the 32nd European Rotorcraft Forum, 2006.

Davis G.L., Feszty D., Nitzsche F., Trailing edge flow control for the mitigation of dynamic stall effects, Proceedings of the 31st European Rotorcraft Forum, Florence, 2005.

Dawson S., Marcolini M., Booth E., Straub F.K, Hassan A.A., Tadghighi H., Kelly H., Wind tunnel test of an active flap rotor: BVI noise and vibration reduction, Proceedings of the American Helicopter Society 51st Annual Forum, 1995.

Delrieux Yves., Le Pape A., Leconte P., Crozier P., Gimonet B., Des Rochettes H.M., Wind-tunnel assessment of the concept of active flaps on a helicopter rotor model, Proceedings of the American Helicopter Society 63rd Annual Forum, 2007.

Depailler G., Friedmann P.P., Alleviation of dynamic stall induced vibrations using actively controlled flaps, Proceedings of the American Helicopter Society 58th Annual Forum, 2002.

de Terlizzi M., Friedmann P.P., Active control of BVI induced vibrations using a refined aerodynamic model and experimental correlation, Proceedings of the American Helicopter Society 55th Annual Forum, 1999.

Dieterich O., Enenkl B., Roth D., Trailing edge flaps for active rotor control - Aeroelastic characteristics of the ADASYS rotor system, Proceedings of the American Helicopter Society 62nd Annual Forum, 2006.

Drela M., An analysis and design system for low Reynolds number airfoils, Conference on low Reynolds number airfoil aerodynamics, University of Notre Dame, 1989.

Endres G., Gething M., Jane's Aircraft Recognition Guide, Harper Collins Publishers, 2002.

ESDU, Characteristics of Atmospheric Turbulence Near Ground. Part II: Single Point Data for Strong Winds (Neutral Atmosphere), Item No. 85020, ESDU International, 1985.

ESDU, Mean Wind Speed Over Hill and Other Topography, Item No. 91043, ESDU International, 1993.

ESDU, Increments in Aerofoil Lift Coefficient at Zero Angle of Attack and In Maximum Lift Coefficient due to Deployment of a Plain Trailing-Edge Flap, With or Without a Leading-Edge High-Lift Device, at Low Speeds, ESDU Report No. 94028, 1994.

ESDU, Strong Winds in the Atmospheric Boundary Layer. Part II: Discrete Gust Speeds, Item No. 83045, ESDU International, 2002.

Evans W.T., Mort K.W., Analysis of computer flow parameters for a set of sudden stalls in low speed two-dimensional flow, NACA TN-D-85, 1959.

Falls J., Datta A., Chopra I., Integrated trailing-edge flaps and servotabs for helicopter primary control, Proceedings of the American Helicopter Society 62nd Annual Forum, Phoenix, 2006.

Falls J., Datta A., Chopra I., Design and analysis of trailing-edge flaps and servo-tabs for primary control, Proceedings of the American Helicopter Society 63rd Annual Forum, Virginia Beach, 2007.

Fang R., Booij P.J.A., Helicopter-Ship qualification testing - the Dutch clearance process, Proceedings of the American Helicopter Society 62nd Annual Forum, Phoenix, 2006.

Fenn R.C., Downer J.R., Bushko D.A., Gondhalekar V., Ham N.D., Terfenol-D driven flaps for helicopter vibration reduction, Smart Materials and Structures, Vol. 5, No. 1, 1996.

Ferrier B., Duncan J., Carico D., Validation of simulated dynamic interface testing as a tool in the forecasting of air vehicle deck limits and deck landing aids, Proceedings of the American Helicopter Society 63rd Annual Forum, Virginia Beach, 2007.

Feszty D., Gillies E.A., Vezza M., Alleviation of rotor blade dynamic stall via trailing edge flap flow control, AIAA Paper 2003-0020, 41st Aerospace Sciences Meeting and Exhibit, 2003.

Feszty D., Gillies E.A., Vezza M., Alleviation of airfoil dynamic stall moments via trailing-edge flap flow control, AIAA Journal, Vol. 42, No. 1, 2004.

Feszty D., Nitzsche F., Khomutov K., Lynch B.K., Mander A., Ulker F.D., Design and instrumentation of the SHARCS scaled rotor with three independent control systems, Proceedings of the American Helicopter Society 64th Annual Forum, 2008.

Friedmann P.P., Millott T.A., Vibration reduction in rotorcraft using active control: A comparison of various approaches, Journal of Guidance, Control and Dynamics, Vol. 18, No. 4, 1995.

Fulton M.V., Ormiston R.A., Small-scale rotor experiments with on-blade elevons to reduce blade vibratory loads in forward flight, Proceedings of the American Helicopter Society 54th Annual Forum, 1998.

Fulton M.V., Ormiston R.A., Hover testing of a small-scale rotor with on-blade elevons, Journal of the American Helicopter Society, Vol. 46, No. 2, 2001.

Fung Y.C., The Theory of Aeroelasticity, John Wiley & Sons, Inc, 1955.

Gagliardi A., Barakos G.N., Improving hover performance of low-twist rotors using trailing-edge flaps – A computational study, Proceedings of the 32nd European Rotorcraft Forum, Maastricht, 2006.

Gagliardi A., Barakos G.N., Analysis and design of a flap-equipped low-twist rotor for hover, Journal of Aircraft, Vol. 46, No. 1, 2009.

Gerontakos P., Lee T., Dynamic stall flow control via a trailing edge flap, AIAA Journal Vol. 44, No. 3, 2006

Gerontakos P., Lee T., Trailing edge flap control of dynamic pitching moment, AIAA Journal, Vol. 45, No. 7, 2007a.

Gerontakos P., Lee T., Dynamic wing airloads with higher harmonic flap motion, Journal of Aircraft, Vol. 44, No. 3, 2007b.

Gerontakos P., Lee T., PIV study of flow around unsteady airfoil with dynamic trailing edge flap deflection, Experiments in Fluids, Vol. 45, No. 6, 2008.

Geyer W.P., Smith E.C., Keller J.A., Validation and application of a transient aeroelastic analysis for shipboard engage/disengage operations, Proceedings of the American Helicopter Society 52nd Annual Forum, 1996.

Geyer W.P., Smith E.C., Keller J.A., Aeroelastic Analysis of Transient Blade Dynamics During Shipboard Engage/Disengage Operations, Journal of Aircraft, Volume 35, No. 3, 1998.

Gandhi F., Frecker M, Nissly A., Design optimisation of a controllable camber rotor aerofoil, AIAA Journal, Vol. 46, No. 1, 2008.

Ghorashi M., Mikjaniec T., Lynch B., Ulker F.D., Cha M., Mander A., Brassard D.P., Feszty D., Nitzsche F., Preliminary design of a scaled rotor blade with vibration and noise control devices, Proceedings of the 32nd European Rotorcraft Forum, 2006.

Glauert H., The elements of aerofoil and airscrew theory, 2nd edition, Cambridge University Press and Macmillan Co., 1947.

Glaz B., Friedmann P.P., Bagnoud F-X., Liu L., Active/passive vibration reduction and performance enhancement of helicopter rotors at high advance ratios, Proceedings of the American Helicopter Society 64th Annual Forum, Montreal, 2008a.

Glaz B., Friedmann P.P., Bagnoud F-X., Liu L., Vibration and noise reduction of helicopter rotors using an active/passive approach, Proceedings of the American Helicopter Society International Specialists Conference on Aerodynamics, San Francisco, 2008b.

Glaz B., Friedmann P.P., Liu L., Helicopter Vibration Reduction throughout the Entire Flight Envelope Using Surrogate-Based Optimisation, Journal of the American Helicopter Society, Volume 54, No. 1, 2009.

Gotzhein C., Eurocopter highlights its innovation and bluecopter® technology at Heli-Expo 2010 (online), Available online at http://www.eurocopter,com/site/en/ref/Press-Releases_310.html, 2010.

Grohmann B.A., Maucher C., Prunhuber T., Jänker P., Dieterich O., Enenkl B., Bauer M., Ahci E., Altmikus A., Baier H., Multidisciplinary design and optimization of active trailing edge for smart helicopter rotor blade, Mechanics of Advanced Materials and Structures, Vol. 15, No. 3-4, 2008.

Gross A., Fasel H.F., Investigation of low-pressure turbine separation control, AIAA 45th Aerospace sciences meeting, 2007.

Hall S.R., Prechtl E.F., Development of a piezoelectric servoflap for helicopter rotor control, Smart Materials and Structures, Vol. 5, No. 1, 1996.

Hall S.R., Tzianetopoulou T., Straub F., Ngo H., Design and testing of a double X-frame piezoelectric actuator, Proceedings of SPIE - The International Society for Optical Engineering, Vol. 3985, 2000.

Hansford. R.E., A Unified Formulation of Rotor Load Prediction Methods, Journal of the American Helicopter Society, Volume 31, No. 2, 1986.

Hansford R.E., Vorwald J., Dynamics Workshop on Rotor Loads Prediction, Journal of the American Helicopter Society, Volume 43, No. 1, 1998.

Hariharan. N., Leishman. J.G., Unsteady Aerodynamics of a Flapped Airfoil in Subsonic Flow by Indicial Concepts, Journal of Aircraft, Volume 33, No. 5, 1996.

Harrison R., Stacey S., Hansford B., BERP IV – The Design, Development and Testing of an Advanced Rotor Blade, Proceedings of the American Helicopter Society 64th Annual Forum, 2008.

Hasegawa H., Matsuuchi K., Tanaka J., Generating mechanism of longitudinal vortices using pulsed vortex generator jets, JSME International Journal, Vol. 44 No. 3, 2001a.

Hasegawa Y., Katayama N., Kobiki N., Nakasato E., Yamakawa E., Okawa H., Experimental and analytical results of whirl tower test of ATIC full scale rotor system,

Proceedings of the American Helicopter Society 57th Annual Forum, Washington, DC, 2001b.

Hassan A.A., Charles B.D., Tadghighi H., Sanker L.N., Blade-mounted trailing edge flap control for BVI noise reduction, NASA CR 4426, 1992.

Hassan A.A., Sanker L.N., Tadghighi H., Effects of leading and trailing edge flaps on the aerodynamics of airfoil/vortex interactions, Journal of the American Helicopter Society, Vol 39, No. 2, 1994.

Hassan A.A., Applications of Zero-Net-Mass Jets for enhanced rotorcraft aerodynamic performance, Journal of Aircraft, Vol. 38, No. 3, 2001.

He C., Kang H., Carico D., Long K., Development of a Modelling and Simulation Tool for Rotorcraft/Ship Dynamic Interface Testing, Proceedings of the American Helicopter Society 58th Annual Forum, 2002.

Heaslet M.A., Spreiter J.R., Reciprocity relations in aerodynamics, NACA Report 1119, 1952.

Henry F.S., Pearcey H.H., Numerical model of boundary-layer control using air-jet generated vortices, AIAA Journal, Vol. 32, No. 12, 1994.

Hurst D.W., Newman S.J., Wind tunnel measurements of ship induced turbulence and the prediction of helicopter rotor blade response, Proceedings of the 11th European Rotorcraft Forum, 1985.

Innes F., Pearcey H.H., Sykes D.M., Improvements in the performance of a three element high-lift system by the application of airjet vortex generators, Aeronautical Journal, Vol. 99, No. 987, 1995.

James G., Modern Engineering Mathematics, Second Edition, Addison-Wesley Longman, 1996.

Jänker P., Hermle F., Friedl S., Lentner K., Enenkl B., Müller C., Advanced piezoelectric servo flap system for rotor active control, Proceedings of the 32nd European Rotorcraft Forum, 2006.

Jänker P., Hermle F., Friedl S., Lentner K., Grohmann B., Lorkowski T., Recent development on piezoelectric actuation systems for rotor active control, Proceedings of the American Helicopter Society 63rd Annual Forum, 2007.

Johari H., Pacheco-Tougas M., Hermanson J.C., Penetration and mixing of fully modulated turbulent jets in crossflow, AIAA Journal, Vol. 37, No. 7, 1999.

Johari H., Rixon G.S., Effects of pulsing on a vortex generator jet, AIAA Journal, Vol. 41, No. 12, 2003.

John S., Sirohi J., Wang G., Wereley N.M., Comparison of piezoelectric, magnetostrictive, and electrostrictive hybrid hydraulic actuators, Journal of Intelligent Material Systems and Structures, Vol. 18, No. 10, 2007.

Johnson W., Self-tuning regulators for multicyclic control of helicopter vibration, NASA Technical Paper 1996, 1982.

Johnston J.P., Nishi M., Vortex generator jets – Means for flow separation control, AIAA Journal, Vol. 28, No. 6, 1990.

Jones R.T., The unsteady lift of a wing of finite aspect ratio, NACA Report 681, 1940.

Jones M.P., Newman S.J., Vibration reduction of a Lynx aircraft via actively controlled trailing edge flaps, Proceedings of the 32nd European Rotorcraft Forum, 2006.

Jones M.P., Newman S.J., A method of reducing blade sailing through the use of trailing edge flaps, Proceedings of the American Helicopter Society 63rd Annual Forum, 2007.

Kang H., He C., Saberi H., Dynamic Interface Simulation of Rotorcraft Shipboard On-Deck Operation, Proceedings of the American Helicopter Society 58th Annual Forum, 2003.

Kang H., He C., Carico D., Modelling and Simulation of Rotor Engagement and Disengagement during Shipboard Operations, Proceedings of the American Helicopter Society 60th Annual Forum, 2004.

Keller. J.A., Smith. E.C., Experimental and Theoretical Correlation of Helicopter Rotor Blade-Droop Stop Impacts, Journal of Aircraft, Volume 36, No. 2, 1999a.

Keller J.A., Smith E.C., Analysis and control of the transient shipboard engagement behaviour of rotor systems, Proceedings of the American Helicopter Society 55th Annual Forum, 1999b.

Keller J.A., Analysis and control of the transient aeroelastic response of rotors during shipboard engagement and disengagement operations, PhD Thesis, Pennsylvania State University, 2001.

Keller J.A., Smith E.C., Active control of gimballed rotors using swashplate actuation during shipboard engagement operations, Journal of Aircraft, Volume 40, No. 4, 2003.

Kenning O.C., Kaynes I.W., Miller J.V., The potential application of flow control to helicopter rotor blades, 30th European Rotorcraft Forum, Marseilles, 2004.

Klemin A., An introduction to the helicopter, NACA TM 340, 1925.

Kim J-S., Smith E.C., Wang K.W., Active load control of an articulated composite rotor blade via dual trailing edge flaps, Proceedings of the 44th AIAA/ASME/ASCE/AHS/ASC Structures, Structural Dynamics and Materials Conference, 2003.

Kim J-S., Smith E.C., Wang K.W., Helicopter vibration suppression via multiple trailing edge flaps controlled by resonance actuation system, Proceedings of the American Helicopter Society 60th Annual Forum, 2004.

Kim J-S., Smith E.C., Wang K.W., Development of a resonant actuation system for active flap rotors, Proceedings of the American Helicopter Society 61st Annual Forum, 2005.

Kim J-S., Smith E.C., Wang K.W., Helicopter blade loads control via multiple trailing edge flaps, Proceedings of the American Helicopter Society 62nd Annual Forum, 2006.

Kim J-S., Wang K.W., Smith E.C., Development of a resonant trailing edge flap actuation system for helicopter rotor vibration control, Smart Materials and Structures, Vol. 16, No. 6, 2007.

Kobiki N., Yamakawa E., Hasegawa Y., Aeroelastic analysis and design for on-blade active flap, Proceedings of the 20th European Rotorcraft Forum, 1999.

Kobiki N., Shigeru S., Takehito F., Takayoshi K., Design and performance evaluation of full-scale on-board active flap system, Proceedings of the American Helicopter Society 63rd Annual Forum, 2007.

Kobiki N., Shigeru S., Performance evaluation of full-scale on-board active flap system in transonic wind tunnel, Proceedings of the American Helicopter Society 64th Annual Forum, 2008.

Konstanzer P., Decentralised vibration control for active helicopter rotor blades, Proceedings of the 31st European Rotorcraft Forum, 2005.

Koratkar N.A., Chopra I., Analysis and testing of a Froude scaled helicopter rotor with piezoelectric bender actuated trailing edge flaps, Journal of Intelligent Material Systems and Structures, Vol. 8, No. 7, 1997.

Koratkar N.A., Chopra I., Design, fabrication and testing of a Mach scaled rotor model with trailing-edge flaps, Proceedings of the American Helicopter Society 55th Annual Forum, 1999.

Koratkar N.A., Chopra, I., Open-loop hover testing of a smart rotor model, AIAA Journal, Vol. 40, No. 8, 2002a.

Koratkar N.A., Chopra, I., Wind tunnel testing of a smart rotor model with trailing-edge flaps, Journal of the American Helicopter Society, Vol. 47, No. 4, 2002b.

Kostas J., Foucaut J.M., Stanislas M., The flow structure produced by pulsed-jet vortex generators in a turbulent boundary adverse pressure gradient, Flow, Turbulence and Combustion, Vol. 78, No. 3-4, 2007.

Kostas J., Foucaut J.M., Stanislas M., The effects of pulse frequency and duty cycle of the skin friction downstream of pulsed jet vortex generators in an adverse pressure gradient turbulent boundary layer, Aerospace Science and Technology, Vol. 13, No. 1, 2009.

Kouli F, Wall A.S., Langlois R.G., Afagh F.F., Investigation of the feasibility of a proposed hybrid passive and active control strategy for the transient aeroelastic response of helicopter rotor blade during shipboard engage and disengage operations, Proceedings of the American Helicopter Society 64th Annual Forum, 2008.

Krzysiak A., Control of flow separation using self-supplying air-jet vortex generators, AIAA Journal, Vol. 46, No. 9, 2008.

Küssner H.G., Zusammenfassender bericht uber den instationaren auftreib von flugeln, Luftfahrtforschung, Volume 13, No. 12, 1935.

Leconte P., Rapin M., van der Wall, B.G., Main rotor active flaps: Numerical assessment of vibration reduction, Proceedings of the American Helicopter Society 57th Annual Forum, 2001.

Leconte P., des Rochettes H.M., Experimental assessment of an active flap device, Proceedings of the American Helicopter Society 58th Annual Forum, 2002.

Lee T., Chopra I., Design of piezostack-driven trailing-edge flap actuator for helicopter rotors, Smart Materials and Structures, Vol. 10, No. 1, 2001.

Leishman J.G., Beddoes T.S., A Generalised Model for Airfoil Unsteady Aerodynamic Behaviour and Dynamic Stall using the Indicial Method, Proceedings of the American Helicopter Society 42nd Annual Forum, 1986.

Leishman J.G., A two-dimensional model for airfoil unsteady drag below stall, Journal of Aircraft, Volume 25, No. 7, 1987.

Leishman. J.G., Validation of Approximate Aerodynamic Functions for Two-Dimensional Subsonic Flow, Journal of Aircraft, Volume 25, Number 10, 1988

Leishman J.G., Beddoes T.S., A Semi-Empirical Model for Dynamic Stall, Journal of the American Helicopter Society, Volume 34, No. 3, 1989.

Leishman. J.G., Principles of Helicopter Aerodynamics, Cambridge University Press, 2000.

Lewington N.P., Henry F.S., Peake D.J., Singh C., Numerical and experimental investigations of air-jet vortex generators in streamwise pressure gradients, The Aeronautical Journal, Vol. 105, No. 1049, 2001.

Liandrat J., Aupoix B., Cousteix J., Calculation of longitudinal vortices imbedded in a turbulent boundary layer, Proceedings of 5th symposium on turbulent shear flows, Cornell University, 1985.

Liu L., Friedmann P.P., Kim I., Bernstein D.S., Rotor performance enhancement and vibration reduction in presence of dynamic stall using actively controlled flaps, Proceedings of the 32nd European Rotorcraft Forum, 2006a.

Liu L., Friedmann P.P., Kim I., Bernstein D.S., Simultaneous vibration reduction and performance enhancement in rotorcraft using actively controlled trailing edge flaps, Proceedings of the 62nd American Helicopter Society Annual Forum, 2006b.

Liu L., Friedmann P.P., Kim I., Bernstein D.S., Rotor performance enhancement and vibration reduction in presence of dynamic stall using actively controlled flaps, Journal of the American Helicopter Society, Vol. 53, No. 4, 2008a.

Liu L., Friedmann P.P., Bagnoud F-X., Padthe A., Comparison of approximate time domain aerodynamics for flapped airfoils with CFD based results with applications, In proceedings of the American Helicopter Society Specialists Conference on Aerodynamics, 2008b.

Liu X., Nishi M., Numerical study of flow in a conical diffuser with vortex generator jets, Chinese Journal of Mechanical Engineering, Vol. 20, No. 1, 2007.

Lomax H., Heaslet M.A., Fuller F.B., Sluder L., Two- and Three-Dimensional Unsteady Lift Problems in High-Speed Flight, NACA Report 1077, 1952.

Magill J.C., McManus K.R., Exploring the feasibility of pulsed jet separation control for aircraft configurations, Journal of Aircraft, Vol. 38, No. 1, 2001.

Mainz H., Van Der Wall B.G., Leconte P., Ternoy F., Des Rochettes H.M., ABC rotor blades: Design, manufacturing and testing, Proceedings of the 31st European Rotorcraft Forum, 2005.

Malpica C., Celi R., Simulation-based bandwidth analysis of a swashplateless rotor helicopter, Proceedings of the American Helicopter Society 63rd Annual Forum, Virginia Beach, 2007.

McCroskey W., McAlister K., Carr L., Pucci S., Lambert O., Indergrand R., Dynamic Stall on Advanced Airfoil Sections, Journal of the American Helicopter Society, Volume 26, No. 3, 1981.

McManus K.R., Legner H.H., Davis S.J., Pulsed vortex generator jets for active control of flow separation, AIAA Paper 1994-2218, AIAA 25th Fluid Dynamics Conference, Colorado Springs, 1994.

McManus K.R., Joshi P.B., Legner H.H., Davis S.J., Active control of aerodynamic stall using pulsed jet actuators, AIAA Paper 1995-2187, AIAA 26th Fluid Dynamics Conference, San Diego, 1995.

McManus K., Ducharme A., Goldey C., Magill J., Pulsed jet actuators for suppressing flow separation, AIAA Paper 1996-0442, AIAA 34th Aerospace Sciences Meeting and Exhibit, Reno, 1996.

Mehta R.D., An experimental study of a vortex/mixing layer interaction, AIAA Paper 84-1543, 1984.

Mehta R.D., Bradshaw P., Longitudinal vortices imbedded in turbulent boundary layers, Part 2: Vortex pair with common flow upwards, Vol. 188, 1988.

Milgram J., Chopra I., Helicopter vibration reduction with trailing edge flaps, Proceedings of the 36th AIAA/ASME/ASCE/AHS/ASC Structures, Structural Dynamics and Materials Conference and AIAA/ASME Adaptive Structures Forum, 1995.

Milgram J., Chopra I., A comprehensive rotorcraft aeroelastic analysis with trailing-edge flaps: validation with experimental data, Proceedings of the American Helicopter Society 52nd annual forum, 1996.

Milgram J., Chopra I., A parametric study for actively controlled trailing edge flaps, Journal of the American Helicopter Society, Vol. 43, No. 2, 1998a.

Milgram J., Chopra I., Rotors with trailing edge flaps: analysis and comparison with experimental data, Journal of the American Helicopter Society, Vol. 43, No. 4, 1998b.

Millott T.A., Friedmann P.P., Vibration reduction in helicopter rotors using an active control surface located on the blade, AIAA Paper No. 92-2451, 1992.

Millott T.A., Friedmann P.P., The practical implementation of an actively controlled flap to reduce vibration in helicopter rotors, Proceedings of the American Helicopter Society 49th Annual Forum, 1993.

Millott T.A., Friedmann P.P., Vibration reduction in helicopter rotors using an actively controlled partial span trailing edge flap located on the blade, NASA Technical Report No. CR-4611, 1994.

Mishra A., Sitaraman J., Baeder J., Opoku D., Computational investigation of trailing edge flap for control of vibration, Collection of Technical Papers - 25th AIAA Applied Aerodynamics Conference, 2007.

Mishra A., Ananthan S., Baeder J.D., Coupled CFD/CSD prediction of the effects of trailing edge flaps on rotorcraft dynamic stall alleviation, AIAA paper 2009-891, Presented at the 47th AIAA Aerospace Sciences Meeting, 2009.

Moffatt S, Griffiths N., Structural optimisation and aeroelastic tailoring of the BERP IV demonstrator blade, Proceedings of the American Helicopter Society 65th Annual Forum, 2009.

Myrtle T.F., Friedmann P.P., Unsteady compressible aerodynamics of a flapped airfoil with application to helicopter vibration reduction, Proceedings of the 38th AIAA/ASME/ASCE/AHS/ASC Structures, Structural Dynamics and Materials Conference,1997a.

Myrtle T.F., Friedmann P.P., New comprehensive time domain unsteady aerodynamics for flapped airfoils and its application to rotor vibration reduction using active control, Proceedings of the American Helicopter Society 53rd Annual Forum,1997b.

Myrtle T.F., Friedmann P.P., Vibration control in rotorcraft using the actively controlled trailing edge flap and issues related to practical implementation, Proceedings of the American Helicopter Society 54th Annual Forum,1998.

Myrtle T.F., Friedmann P.P., Application of a new compressible time domain aerodynamic model to vibration reduction in helicopters using an actively controlled flap, Journal of the American Helicopter Society, Vol. 46, No. 1, 2001.

Neville T., Dynamic and aerodynamic clearance of the Apache AH Mk1 attack helicopter for embarked operations, Proceedings of the Institution of Mechanical Engineers, Part G: Journal of Aerospace Engineering, Vol. 219, No. 5, 2005.

Newman S.J., Theoretical model for predicting the blade sailing behaviour of a semi-rigid rotor helicopter, Vertica, Volume 14, Issue 4, 1990.

Newman S.J., The application of a theoretical blade sailing model to predict the behaviour of articulated helicopter rotors, Aeronautical Journal of the Royal Aeronautical Society, Volume 96, No. 956, 1992.

Newman. S.J., The Foundations of Helicopter Flight, Arnold, 1994.

Newman S.J., Verification of a theoretical helicopter rotor blade sailing method by means of wind tunnel testing, Aeronautical Journal, Volume 99, Issue 982, 1995a

Newman S.J., An Investigation into the Phenomenon of Helicopter Blade Sailing, PhD Thesis, University of Southampton, 1995b.

Newman S.J., The phenomenon of helicopter rotor blade sailing, Proceedings of the Institution of Mechanical Engineers, Part G: Journal of Aerospace Engineering, Volume 213, Issue 6, 1999.

Newman S.J., The safety of shipborne helicopter operation, Aircraft Engineering and Aerospace Technology, Vol. 76, No. 5, 2004.

Nguyen K., Chopra I., Application of higher harmonic control to rotors operating at high speed and thrust, Journal of the American Helicopter Society, Volume 35, No. 3, 1990.

Nitzsche F., Feszty D., Waechter D., Bianchi E., Voutsinas S., Gennaretti M., Coppotelli G., Ghiringhelli G., The SHARCS project: Smart hybrid active rotor control system for noise and vibration attenuation of helicopter rotor blades, Proceedings of the 31st European Rotorcraft Forum, 2005.

Oliver A., Wootton L.R., Prats J., Use of air jet vortex generators leading to improved energy capture and power regulation of a wind turbine, Proceedings of the 1996 18th Wind Energy Association Conference, 1996.

Oliver A.G., Air jet vortex generators for wind turbines, PhD Thesis, City University, London,1997.

Ortmanns J., Kahler C.J., The effect of a single vortex generator jet on the characteristics of a turbulent boundary layer, International Journal of Heat and Fluid Flow, Vol. 28, No. 6, 2007.

Patt D., Liu L., Friedmann P.P., Rotorcraft vibration reduction and noise prediction using a unified aeroelastic response simulation, Journal of the American Helicopter Society, Vol. 50, No. 1, 2005.

Patt D., Liu L., Friedmann P.P., Simultaneous vibration and noise reduction in rotorcraft using aeroelastic simulation, Journal of the American Helicopter Society, Vol. 51, No. 2, 2006.

Pauley W.R., Eaton J.K., Experimental study of the development of longitudinal vortex pairs embedded in a turbulent boundary layer, AIAA Journal, Vol. 26, No. 7, 1988.

Pearcey H.H., Shock induced separation and its prevention by design and boundary layer control, In boundary layer and flow control, its principle and applications. Vol. 2, Pergamon Press, 1961.

Peters D.A., He C.J., Finite state induced flow models – Part II: Three-dimensional rotor disk, Journal of Aircraft, Volume 32, No. 2, 1995.

Piccirillo V., Castao K.A.L., Ramos R.L.da C.B., Goes L.C.S., Aeroelastic control of helicopter blade sailing in unsteady flow using smart materials, Brazilian symposium of aerospace engineering and applications, 2009.

Postl D., Gross A., Fasel H.F., Numerical investigation of active flow control for low-pressure turbine blade separation, AIAA Paper 2004-0750, AIAA 42nd Aerospace sciences meeting and exhibit, 2004.

Prechtl E.F, Hall S.R., X-Frame-actuator servo-flap actuation system for rotor control, Proceedings of SPIE - The International Society for Optical Engineering, Vol. 3329, 1998.

Prechtl E.F., Hall S.R., Closed-loop vibration control experiments on a rotor with blade mounted actuation, Collection of Technical Papers - AIAA/ASME/ASCE/AHS/ASC Structures, Structural Dynamics and Materials Conference, 2000.

Prince S.A., A summary of the City University experimental and computational investigation of steady and pulsed vortex generating air jet and synthetic jet flow control for application to rotor blade flow control, Rotor Aeromechanics DARP Report D1.26, 2008.

Ramos R.L.da C.B., Andrade D. de, Goes L.C.S., Individual blade root control of helicopter blade sailing for articulated shipboard rotors, Proceedings of the American Helicopter Society 65th Annual Forum, 2009.

Rixon G.S., Johari H., Development of a steady vortex generator jet in a turbulent boundary layer, Journal of Fluid Engineering, Vol. 125, 2003.

Roget B., Chopra I., Individual blade control methodology for a rotor with dissimilar blades, Journal of the American Helicopter Society, Vol. 48, No. 3, 2003.

Roget B., Chopra I., Development and testing of an individual blade controller for a dissimilar rotor, Proceedings of the American Helicopter Society 4th Decennial Specialist's Conference on Aeromechanics, San Francisco, 2004.

Roget B., Chopra I., Wind-tunnel testing of rotor with individually controlled trailing edge flaps for vibration reduction, Journal of Aircraft, Vol. 45, No. 3, 2008.

Roth D., Enenkl B., Dieterich O., Active rotor control by flaps for vibration reduction - Full scale demonstrator and first flight test results, Proceedings of the 32nd European Rotorcraft Forum, 2006.

Samak D.K., Chopra I., Design of high force, high displacement actuators for helicopter rotors, Smart Materials and Structures, Vol. 5, No. 1, 1996.

Sankaran L., Russell D.A., A numerical study of a longitudinal vortex interaction with a boundary layer, AIAA Paper 1990-1630, Fluid Dynamics, Plasma Dynamics and Lasers Conference, 1990.

Schimke P., Janker V., Wendt V., Junker B., Wind tunnel evaluation of a full scale piezoelectric flap control unit, Proceedings of the 24th European Rotorcraft Forum, Marseilles, 1998.

Scholz P., Ortmanns J., Kahler J., Radespiel R., Leading edge separation control by means of pulsed jet actuators, AIAA Paper 2006-2850, AIAA 3rd Flow control conference, San Francisco, 2006.

Scholz P., Casper M., Ortmanns J., Kahler J., Radespiel R., Leading-edge separation control by means of pulsed vortex generator jets, AIAA Journal, Vol. 46, No. 6, 2008.

Schubauer G.B., Spangenburg W.G., Forced mixing in boundary layers, Journal of Fluid Mechanics, Vol. 8, No. 1,1960.

Scruggs R.M., Nash J.F., Singleton R.E., Analysis of Dynamic Stall using Unsteady Boundary-Layer Theory, NASA CR-2462, 1974.

Seifert A., Pack L.G., Oscillatory control of separation at high Reynolds numbers, AIAA Journal, Vol. 37, No. 9, 1999.

Selby G.V., Lin J.C., Howard F.G., Control of low-speed turbulent separated flow using jet vortex generators, Experiments in Fluids, Vol. 12, No. 6, 1992.

Shabaka I.M.M.A., Mehta R.D., Bradshaw P., Longitudinal vortices imbedded in turbulent boundary layers, Part 1: Single vortex, Journal of Fluid Mechanics, Vol. 155, 1985.

Shen J., Chopra I., Aeroelastic stability of smart trailing edge flap helicopter rotors, Proceedings of the 42nd AIAA/ASME/ASCE/AHS/ASC Structures, Structural Dynamics and Materials Conference, AIAA paper No. 2001-1675, 2001.

Shen J., Chopra I., Actuation requirements for a swashplateless helicopter control system with trailing edge flaps, Proceedings of the 43rd AIAA/ASME/ASCE/AHS/ASC Structures, Structural Dynamics and Materials Conference, 2002.

Shen J., Chopra I., Aeroelastic stability of trailing edge flap helicopter rotors, Journal of the American Helicopter Society, Vol. 48, No. 4, 2003.

Shen J., Chopra I., Swashplateless helicopter rotor with trailing-edge flaps, Journal of Aircraft, Vol. 41, No. 2, 2004.

Shen J., Yang M., Chopra I., Swashplateless helicopter rotor with trailing-edge flaps for flight and vibration control, Journal of Aircraft, Vol. 43, No. 2, 2006.

Sheng W., Galbraith R.A.McD., Coton F.N, A new stall-onset criterion for low speed dynamic-stall, Journal of Solar Energy Engineering, Volume 128, 2006.

Sheng W., Galbraith R.A.McD., Coton F.N, A modified dynamic stall model for low Mach numbers, AIAA Paper 2007-0626, 45th AIAA Aerospace Sciences Meeting and Exhibit, 2007.

Shizawa T., Eaton J.K, Turbulence measurements for a longitudinal vortex interacting with a three-dimensional turbulent boundary layer, AIAA Journal, Vol. 30, No. 1, 1992.

Shizawa T., Endo S., Production and diffusion of longitudinal vortices downstream of active vortex generators pairs, AIAA Paper 2007-1422, 45th AIAA Aerospace Sciences Meeting and Exhibit, 2007.

Singh C., Peake D.J., Kokkalis A., Khodagolian V., Coton F.N., Galbraith R.A.McD., Parametric study of an air-jet vortex generator configuration to control rotorcraft retreating blade stall, AIAA Paper 2005-1366, 43rd AIAA Aerospace Science Meeting and Exhibit, 2005.

Singh C., Peake D.J., Kokkalis A., Khodagolian V., Coton F.N., Galbraith R.A.McD., Control of rotorcraft retreating blade stall using air-jet vortex generators, Journal of Aircraft, Vol. 43, No. 4, 2006.

Singh C., Application of airjet vortex generators to control helicopter retreating blade stall, PhD Thesis, City University, London, 2007.

Sirohi J., Chopra I., Design and testing of a high pumping frequency piezoelectric-hydraulic hybrid actuator, Proceedings of SPIE - The International Society for Optical Engineering, 2002.

Spangler R.L., Hall S.R., Piezoelectric actuators for helicopter rotor control, Collection of Technical Papers - AIAA/ASME/ASCE/AHS/ASC Structures, Structural Dynamics and Materials Conference, 1990.

Spencer B.T., Chopra I., Design and testing of a helicopter trailing edge flap with piezoelectric stack actuators, Proceedings of SPIE - The International Society for Optical Engineering, 1996.

Spencer M.G., Sanner R.M., Chopra I., Neurocontrol of simulated full scale rotor vibrations using trailing edge flaps, Collection of Technical Papers - AIAA/ASME/ASCE/AHS/ASC Structures, Structural Dynamics and Materials Conference, 1999.

Stevens P.W., Smith E.C., Active interrogation of helicopter rotor faults using trailing-edge flaps, Proceedings of the international modal analysis conference, Kissimmee, 2001.

Straub F.K., Active flap control for vibration reduction and performance improvement, Proceedings of the American Helicopter Society 51st Annual Forum, 1995.

Straub F.K, Hassan A.A., Aeromechanic considerations in the design of a rotor with smart material actuated trailing edge flaps, Proceedings of the American Helicopter Society 52nd Annual Forum, 1996.

Straub F.K., Merkley, D.J., Design of a smart material actuator for rotor control, Smart Materials and Structures, Vol. 6, No. 3, 1997a.

Straub F.K., Ealey M.A., Schetky L.M., Application of smart materials to helicopter rotor active control, Proceedings of SPIE - The International Society for Optical Engineering, Vol. 3044, 1997b.

Straub F.K., Charles B.D., Comprehensive modelling of rotors with trailing edge flaps, Proceedings of the American Helicopter Society 55th Annual Forum, 1999.

Straub F.K., Charles B.D., Aeroelastic analysis of rotors with trailing edge flaps using comprehensive codes, Journal of the American Helicopter Society, Vol. 46, No. 3, 2001a.

Straub F.K., Ngo H.T., Anand V., Domzalski D.B., Development of a piezoelectric actuator for trailing edge flap control of full scale rotor blades, Smart Materials and Structures, Vol. 10, No. 1, 2001b.

Straub F.K., Kennedy D.K., Stemple A.D., Anand V.R., Birchette T.S., Development and whirl tower test of the SMART active flap rotor, Proceedings of SPIEs international symposium on smart structures and materials, 2004.

Straub F.K., Kennedy D.K., Design, development, fabrication and testing of an active flap rotor system, Proceedings of the American Helicopter Society 61st Annual Forum, 2005.

Straub F.K., Anand V.R., Birchette T.S., Lau B.H., Wind tunnel test of the SMART active flap rotor, Proceedings of the American Helicopter Society 65th Annual Forum, 2009.

Stuller J., The taming of the copter, Air and Space, Volume 5, No. 5, 1992.

Szefi J.T., Mockensturm E., Smith E.C., Wang K-W., Rehrig P., Centolanza L., Development of a novel high authority piezoelectric actuator for rotor blades with trailing edge flaps, Proceedings of the American Helicopter Society 62nd Annual Forum, 2006.

Taylor H.D., The elimination of diffuser separation by vortex generators, United Aircraft Corporation Report No. R-4012-3, 1947.

Theodorsen T., General theory of aerodynamic instability and the mechanism of flutter, NACA report 496, 1935.

Vertiflite Contributors, Vertiflite – A Publication of the American Helicopter Society, Volume 54, No. 3, 2008.

Viswamurthy S.R., Ganguli R., An optimisation approach to vibration reduction in helicopter rotors with multiple active trailing edge flaps, Aerospace Science and Technology, Vol. 8, 2004.

Viswamurthy S.R., Ganguli R., Effect of piezoelectric hysteresis on helicopter vibration control using trailing edge flaps, Journal of Guidance, Control and Dynamics, Vol. 29, No. 5, 2006.

Viswamurthy S.R., Ganguli R., Optimal placement of trailing-edge flaps for helicopter vibration reduction using response surface methods, Journal of Engineering Optimisation, Vol. 39, No. 2, 2007.

Vronsky T., High performance cost-effective large wind turbine blades using air-jet vortex generators, ETSU W/41/00541/REP, 1999.

Wagner H., Uber die entstehung des dynamischen auftriebes von tragflugeln, Zeitschrift fur Angewandte Mathematik und Mechanick, Volume 5, No. 1, 1925.

Wall A.S., Khouli F., Afagh F.F., Langlois R.G., Zan S.J., Modelling helicopter blade sailing: Model validation using experimental data, Proceedings of the American Helicopter Society 64th Annual Forum, 2008.

Wallis R.A., The use of air jets for boundary layer control, Aeronautical Research Laboratories, Australia, Aero Note No. 110, 1952.

Wallis, R.A., A preliminary note on a modified type of air-jet for boundary layer control, Aeronautical Research Council, CP No. 513, 1956.

Wei F-S., Design of soft in torsion rotor systems at Kaman Aerospace Corporation, Proceedings of the American Helicopter Society 58th Annual Forum, 2002.

Wereley N.M., Woodsy B.K.S., Bubert E.A., Kothera C.S., Wind tunnel testing of a trailing-edge flap actuated by pneumatic artificial muscles, Proceedings of the American Helicopter Society 64th Annual Forum, 2008.

You D., Wang M., Mittal R., Moin P., Large-Eddy simulation of longitudinal vortices embedded in a turbulent boundary layer, AIAA Journal, Vol. 44, No. 12, 2006.

Zhang J., Smith E.C., Wang K.W., Active-passive hybrid method for optimisation of rotor blades with trailing edge flaps, Proceedings of the 40th AIAA/ASME/ASCE/AHS/ASC Structures, Structural Dynamics and Materials Conference, St. Louis,1999.

Zhang J., Smith E.C., Wang K.W., Active-passive hybrid optimisation of rotor blades with trailing edge flaps, Journal of the American Helicopter Society, Vol. 49, No. 1, 2004.

Zhang X., Collins M.W., Flow and heat transfer in a turbulent boundary layer through skewed and pitched jets, AIAA Journal, Vol. 31, No. 9, 1993.

Zhang X., Counter-rotating vortices embedded in a turbulent boundary layer with inclined jets, AIAA Journal, Vol. 37, No. 10, 1999.

Zhang X., The evolution of co-rotating vortices in a canonical boundary layer with inclined jets, Physics of Fluids, Vol. 15, No. 12, 2003.